Nonlinear techniques for distributed optical fibre sensing.

Feced, Ricardo

NONLINEAR TECHNIQUES FOR DISTRIBUTED OPTICAL FIBRE SENSING

by

Ricardo Feced

A thesis submitted for the Degree of Doctor of Philosophy

Department of Electronic Engineering

King's College

THE UNIVERSITY OF LONDON

December 1997

ABSTRACT

The most attractive feature of optical fibre sensors is their ability to interrogate many sensing points simultaneously. This thesis studies the application of several nonlinear optical effects to distributed optical fibre sensing. In particular, we will consider sensors based on Raman scattering, Kerr-induced polarisation coupling, and Brillouin scattering in optical fibres.

The first technique examined uses Spontaneous Raman Scattering for mapping temperature distributions with high-spatial resolution. We demonstrate that a time-correlated single photon counting detection scheme gives optimum signal-to-noise ratio for this type of measurement, achieving spatial resolutions in the centimetre range. Also, the application of this technique to Optical Time-Domain Reflectometry (OTDR) overcomes the dead-zone problem that affects conventional OTDR's, offering a practical solution for monitoring short haul networks with high density of components.

Secondly, we examine the fabrication and use of static and dynamic polarisation gratings in high birefringence optical fibres. Permanent static gratings are formed by exposing the optical fibres to blue-green or UV radiation. We have experimentally studied some aspects of the photo-induced anisotropy, demonstrating a method for the fabrication of polarisation filters with tailored spectral response. Dynamic gratings, on the other hand, are created by an intense pump-beam propagating along the fibre through the Kerr effect. The application of transient gratings and pump-probe architectures to distributed sensing is theoretically analysed, showing their potential advantages and limitations.

Finally, we consider the use of Noise-Initiated Brillouin Scattering for simultaneous distributed sensing of strain and temperature. We demonstrate a novel processing technique that discriminates strain from temperature by measuring the spectrum and integrated power of the Brillouin scattered radiation. This technique is able to compensate for the nonlinear growth of the Brillouin signals. The noise limitations for a system based on this principle are also discussed.

To my parents

TABLE OF CONTENTS

ACKNOWLEDGEMENTS

Many people have contributed to the realisation of this thesis. Firstly, I would like to thank my supervisor, Dr. V.A. Handerek, for his continuous support, encouragement and guidance. I am specially grateful to M. Farhadiroushan, who shared with me not only his knowledge and experience, but also the excitement of many hours in the lab. I would also like to acknowledge and thank the help received from: S.E. Kanellopoulos, for his support and teachings during the initial stages of this research; T.R. Parker, for involving me in the exciting research on Brillouin scattering; and the rest of the Optoelectronics Group at King's College London: N. Nicola, J.A. Croucher, P. Rodriguez, A. Munoz, K.W. Raine, J. Zhang, L. Gomez-Rojas and J. Xu. I would also like to express my gratitude to Prof. A.J. Rogers for his positive reaction when I first decided to come to King's College, and also for his helpful comments and advice during these years.

This thesis would not have been possible without generous economic support from BICC Cables. I would like to thank BICC for sponsoring my studentship, and also for permitting me the use of their facilities at the Helsby Technology Centre. In particular, I would like to thank my industrial supervisor, Dr. R. Linton, and also M. Edwards, N. Taylor, B. Butler, A. Blythe, J. McCormack, T. Elders, J. Latchem, I. Cook, N. Heigh and M. Harrop.

I would also like to remember here the Photonics Group at Madrid Polytechnic University, where I started my postgraduate studies. I am particularly grateful to my former supervisor, Prof. M.A. Muriel, and also to Dr. I. Matias, Prof. M. Lopez-Amo and Prof. J. Capmany. I also wish to thank the Consejeria de Educacion y Cultura (Comunidad de Madrid) for providing financial support during that period.

Finally, I would like to acknowledge the constant support received from my parents and the rest of my family, specially from my aunt Maria Diaz-Portas. I am also grateful to Carmen, for her encouragement to finish this thesis.

PREFACE

Optical fibre technology is a very active research field due to the vast range of applications that it spans. This thesis mainly focuses on the use of optical fibres for distributed sensing. The ability of optical fibre sensors to perform fully distributed measurements is one of their most distinctive features. I have examined three techniques, based on the Raman, Kerr and Brillouin nonlinear optical effects, that enable distributed measurements along the fibre.

Although distributed sensing constitutes the main stream of the thesis, I will also present some results in the area of photosensitivity of optical fibres. The possibility of tailoring the dielectric properties of the glass by exposure to UV (or blue-green) radiation has permitted the fabrication of many all-fibre new grating devices with a great variety of potential applications. I have studied some aspects of the fabrication of birefringence gratings and also mechanical effects of this fabrication procedure.

My PhD research work at King's College London begins in August of 1994 and has been funded by BICC Plc. The activity on distributed sensing was motivated by a European Community project called FORMS (Fibre Optics for Remote Monitoring of Structures) in which BICC is a partner. The objective of this project was to design and build a high spatial resolution distributed temperature sensor that could operate at elevated temperatures. The particular application selected for the sensor was the life-time assessment and detection of hot spots along the steam-pipes of power generating plants. Initially, we considered various possible distributed sensing techniques and identified the strengths and limitations of each of them. In order to achieve the stringent specifications of the project, the solution adopted was to measure the Raman scattered radiation along the fibre by means of a photon counting technique. Several aspects related to the performance of the sensor were investigated (Chapter 2), and a laboratory prototype that satisfied the project specifications was built. Presently this sensor is being installed in a power plant in Portugal (run by Electricidad De Portugal) for its evaluation in a real environment.

I have also contributed to the understanding of two other distributed sensing techniques by carrying out detailed analyses of their principles of operation and theoretically expected performance. In the case of the Kerr-based sensor, the sensing technique relies on the measurement of a frequency modulated signal that arises as a result of a Kerr-induced polarisation coupling between two counter-propagating beams. In my study, I have evaluated

the efficiencies of the nonlinearly-induced coupling and the magnitude of the derived frequencies in the detector, studying also several possible system architectures and the noise limitations of this technique (Chapter 4).

In the Brillouin case, the interest was focused on the simultaneous distributed measurement of strain and temperature. The sensing technique relies on the discrimination of strain and temperature by measuring both the frequency shift and the integrated power of the noise-initiated Brillouin scattering along the fibre. In the theoretical analysis, apart from predicting the strain and temperature dependence of the Brillouin scattered power, I derived a normalisation procedure that permits the accurate measurement of Brillouin signals, correcting against their nonlinear growth. I also identified the noise limitations of the technique, highlighting the contribution due to the statistics of the scattered field (Chapter 5). Several experiments that demonstrated the principle of operation of the sensor were carried out at King's College by Tom Parker and Mahmoud Farhadiroushan. These experiments, which are described in Section 5.4, showed good agreement with the theoretical analysis.

As previously mentioned, the thesis also presents some results on the photosensitivity properties of optical fibres (Chapter 3). The first topic considered is related to the understanding and control of photoinduced anisotropy in high birefringence optical fibres. I have experimentally tested several aspects of the depletion model for photoinduced anisotropy, demonstrating also a method to fabricate polarisation gratings with tailored coupling spectra (Sections 3.3 and 3.4).

The second objective was to evaluate the effect that the fabrication of fibre gratings by exposure to UV light has on the mechanical properties of the fibre (Section 3.5). This study was motivated by the growing interest in the use of fibre gratings for strain sensing, where the mechanical properties of the device could be a critical issue. We carried out two sets of experiments. The first one, in collaboration with the National Physical Laboratory, aimed to measure the change of the internal stress distribution in the fibre after exposure to UV radiation. The stress profiles that appear in Section 3.5.1 were measured by Ken Raine at NPL. In a second set of experiments, we evaluated the strength degradation of UV exposed optical fibres. I would like to thank Merrion Edwards, from BICC, for providing the facilities and helping me to carry out this experiment.

London, December 1997.

LIST OF ABBREVIATIONS

ADC:	Analogue to Digital Converter
APD:	Avalanche Photo-Diode
ASE:	Amplified Spontaneous Emission
BOTDA:	Brillouin Optical Time Domain Analysis
BOTDR:	Brillouin Optical Time Domain Reflectometry
CFD:	Constant Fraction Discriminator
CW:	Continuous Wave
DART:	Distributed AntiStokes Raman Thermometry
DFB:	Distributed Feed-Back
DOFS:	Distributed Optical Fibre Sensor
EDFA:	Erbium Doped Fibre Amplifier
FET:	Field Effect Transistor
FP:	Fabry-Perot
FSR:	Free Spectral Range
FWHM:	Full-Width-Half-Maximum
GODC:	Germanium Oxygen Deficient Centre
IGD:	Intermodal Group Delay
MCA:	Multi-Channel Analyser
MCP:	Micro-Channel Plate
NA:	Numerical Aperture
NEP:	Noise-Equivalent Power
NIBS:	Noise-Initiated Brillouin Scattering
OFDR:	Optical Frequency Domain Reflectometry
OTDR:	Optical Time Domain Reflectometry
PMT:	Photo-Multiplier Tube
SNR:	Signal-to-Noise Ratio
SPAD:	Single-Photon Avalanche Diode
SSRE:	Spontaneous Stokes Raman Emission
TAC:	Time-to-Amplitude Converter
TC-SPC:	Time Correlated Single Photon Counting
UV:	Ultra-Violet
WDM:	Wavelength Division Multiplexing

Chapter 1

INTRODUCTION

This chapter introduces the basic principles of distributed optical fibre sensing and outlines the various topics investigated in this thesis.

1.1 OPTICAL FIBRE SENSORS

Optical fibre sensors have received great interest in recent years due to their unique capabilities [1]. However, their potential has not translated yet into a wide range of commercially available fibre optic based sensors. Considerable research effort is still necessary and the objective of this thesis is to contribute to the development of this promising technology.

In an optical fibre sensor, the propagation properties of light in the optical fibre are influenced by the measurand field. The use of optical fibres as transducers has several well known advantages. Firstly, when properly coated and cabled, their high resistance allows sensing in hazardous environments, like those subject to high temperatures or chemically active substances. Secondly, their electrical passivity makes them immune to electromagnetic interference in contrast with other electronic based sensors. Finally, the high bandwidth of optical fibres enables the possibility of simultaneous measurement of multiple locations along the fibre network, facilitating the attractive concept of smart structures.

The potential for simultaneous interrogation of multiple sensing points is the most distinctive feature of optical fibre sensors. There have been two main approaches for the practical implementation of this idea. The first one, called quasi-distributed sensing, was to multiplex a number of optical fibre point-sensors. Several techniques, such as wavelength, time or coherence division multiplexing, have been explored to achieve this objective. An alternative approach, which constitutes the main topic of this thesis, was to perform fully distributed measurements along the optical fibre. The low loss of optical fibres permits the measurement of long sensing lengths with good spatial resolution. The simplicity and elegance of this solution provides clear advantages over the complicated multiplexing schemes that would be necessary in competing technologies.

These unique features of optical fibre sensors make them suitable for a great number of specialised applications, as for example:

- Chemical and process control industry (temperature monitoring in ovens, leak detection)
- Electrical power industry (transformers hot spots, pipe-work life assessment)
- Construction industry (stress monitoring in dams and mines to avoid catastrophic failure)
- Seismic data acquisition

- Smart structures in vehicles and buildings
- Medical applications

1.2 OTDR PRINCIPLE FOR DISTRIBUTED MEASUREMENTS

Optical Time Domain Reflectometry (OTDR) [2] is the most popular technique to carry out distributed measurements in optical fibres. The first demonstrations of this technique [3-5] showed its potential for mapping losses and locating faults along optical fibre links. Its principle of operation is described in Figure 1. An intense laser pulse is launched into the optical fibre and, as it propagates along it, some of its photons will be scattered due to the Rayleigh scattering mechanism and some others will suffer Fresnel reflections. Part of the scattered and reflected radiation is recaptured by the fibre and guided towards the launching end, where it is detected and monitored as a function of time.

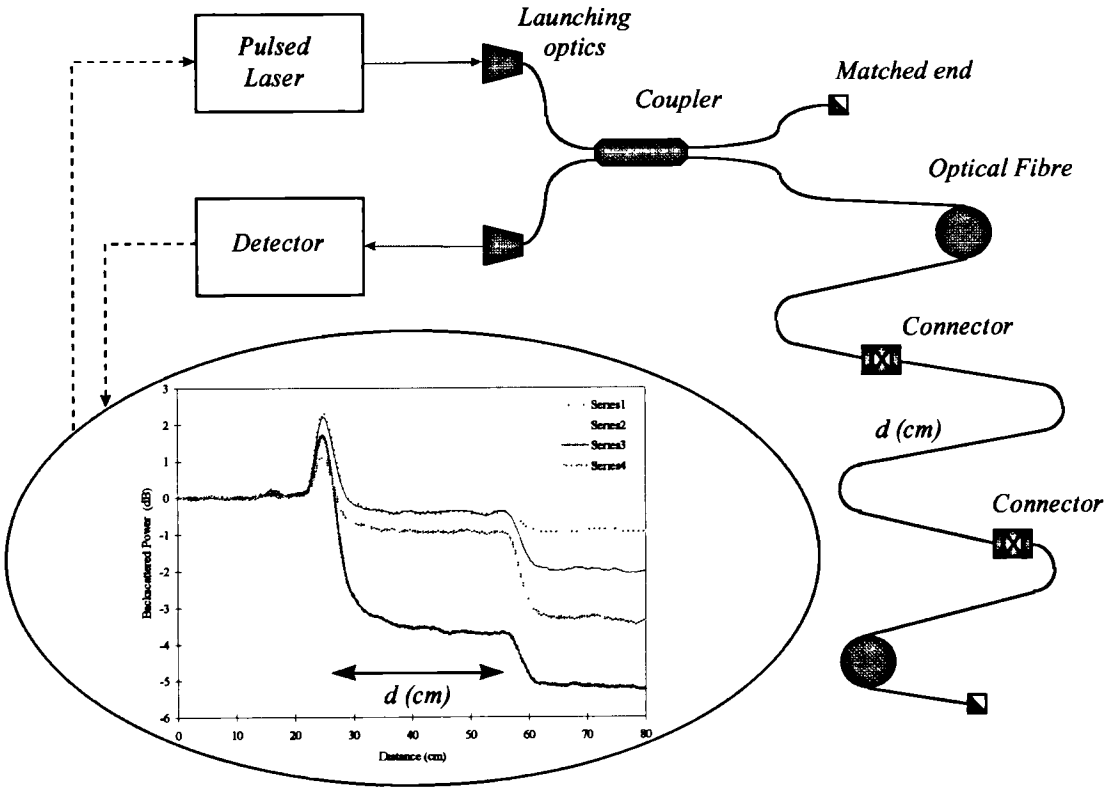

Figure 1. Schematic diagram of an OTDR system.

As can be appreciated, two ingredients are essential in any distributed optical fibre measurement system. First, a scattering mechanism which provides some information about the local state of the fibre and, second, a procedure to resolve the scattered radiation to be able to

locate its origin along the fibre. From the space-time diagram represented in Figure 2, it can be observed that in an OTDR system the light scattered at the spatial position z is detected at a time t related to z through the expression:

$$z = \frac{v}{2} t \qquad (1)$$

where v is the speed of the light in the fibre.

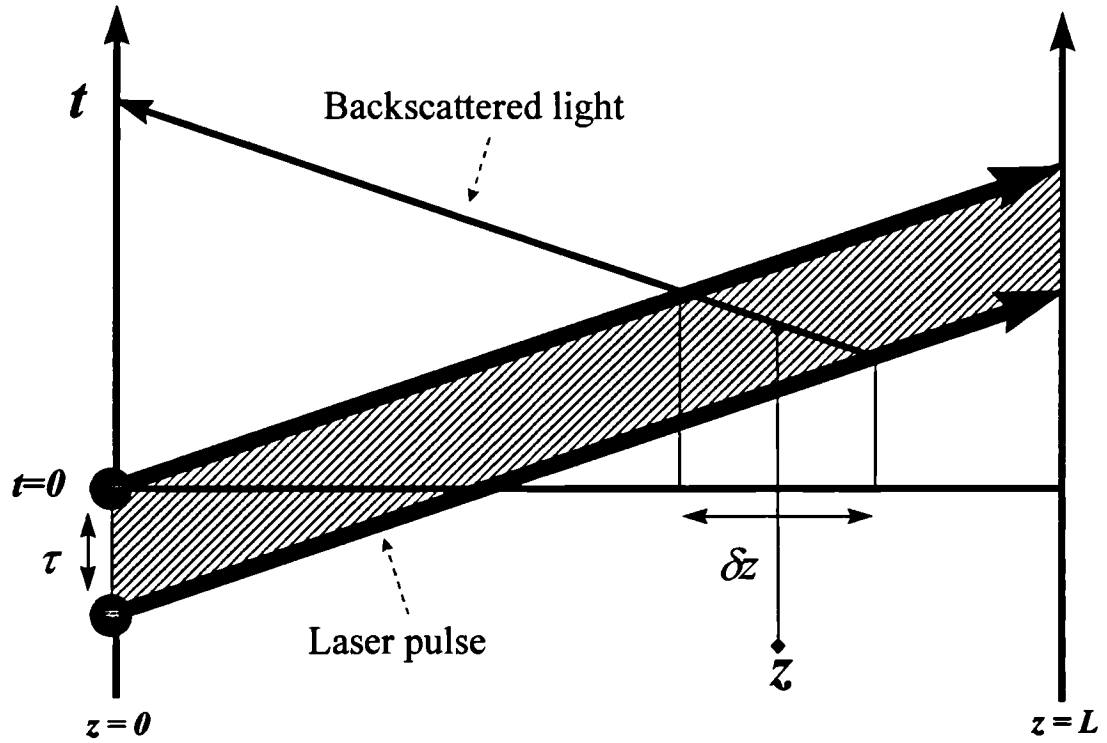

Figure 2. Space-time diagram that illustrates the OTDR principle

An important parameter of a distributed optical fibre measurement system is its spatial resolution. Figure 2 shows that the spatial resolution δz of the OTDR technique is ultimately limited by the finite pulse-width of the laser τ according to the relation:

$$\delta z = \frac{v}{2} \tau \qquad (2)$$

However, the spatial resolution of an OTDR depends in general not only on the finite pulse-width of the laser τ, but also on the bandwidth of the detection system B. The timing resolution T_R achieved by a detection system with a limited bandwidth B is given by [6]:

$$T_R \approx \frac{1}{2B} \tag{3}$$

In order to optimise the spatial resolution and the signal-to-noise ratio performance of OTDR schemes, the detection time resolution T_R is usually matched to the laser pulse-width τ:

$$T_R \approx \tau \tag{4}$$

Another important consideration for the performance of an OTDR system is the level of backscattered radiation received at the detector. The received signal is proportional to the energy of the laser pulse sent into the fibre and also depends on the scattering features of the fibre. The Rayleigh backscattered photon flux ϕ (photons·s^{-1}) obeys the famous OTDR formula [7]:

$$\phi(t) = \phi_{inc}\, \tau \frac{v}{2} \alpha_R\, \kappa\, e^{-2\alpha z(t)} \tag{5}$$

where ϕ_{inc} is the peak photon flux of the laser pulse and τ its pulse-width; α_R is the Rayleigh scattering coefficient; κ is the fibre capture fraction; α is the overall loss coefficient of the fibre; and z(t) is given by equation (1). This formula can be generalised to calculate the scattered power levels due to other scattering mechanisms. For short laser pulses and long measured distances, equation (5) shows that the backscattered flux ϕ becomes very weak, being difficult for direct analogue detection. Other detection schemes like coherent detection [8,9] and photon-counting [10] have enabled a substantial increase in the measurement sensitivity.

Finally, it is worth mentioning that alternative techniques for performing distributed measurements of Rayleigh scattering and/or Fresnel reflections along optical fibres have been proposed. One of them, called Optical Frequency Domain Reflectometry (OFDR) [11,12], involves first the measurement of the scattered power at different radio-frequency modulation frequencies [11] or wavelengths (coherent OFDR) [12], and then subsequent calculation of its

time distribution by means of a Fourier transform. Another technique, based on low coherence interferometry, is well suited for analysis of fibre devices of very small dimensions [13].

1.3 CLASSIFICATION OF DISTRIBUTED OPTICAL FIBRE SENSORS

Distributed Optical Fibre Sensors (DOFS) can be classified in two groups according to their configuration architecture: backscattering and pump-probe systems. Pump-probe configurations have attracted quite a lot of interest due to their potentially better signal-to-noise ratio performance. However, the only commercially available DOFS to date are based on the backscatter architecture.

1.3.1 Backscattering architectures

In backscattering architectures, a laser pulse launched into the fibre is scattered as it propagates along it due to various possible scattering mechanisms. A fraction of the scattered radiation is recaptured by the fibre and detected at the launching end. The OTDR scheme described in the previous section belongs to this group. The average backscattered photon flux is given by an expression similar to (5), where the Rayleigh scattering coefficient is substituted by that corresponding to the relevant scattering mechanism. As the backscattered photon flux is usually low, the sensitivity and noise performance of the detection scheme has to be optimised to achieve a good signal-to-noise ratio. Also, as scattered fields are due to contributions from many independent random scatterers, they usually obey gaussian statistics. This means that the noise induced by the random nature of the field can be non negligible, specially if the scattered radiation has a narrow spectrum.

The first proposed method to perform backscattered distributed sensing measurements was called Polarisation OTDR. It relied on mapping the birefringence along a polarisation preserving optical fibre by mixing the Rayleigh backscattered light from the two polarisation modes of the fibre [14,15]. The birefringence of fibres is sensitive to many measurand fields, for example strain or temperature. A different approach consisted in the measurement of the Rayleigh scattering coefficient along a liquid-core optical fibre with a conventional OTDR configuration [16]. Due to the thermal fluctuations of the liquid's density, the Rayleigh scattering coefficient correlates with the temperature distribution along the fibre.

Measurement of the spontaneous Raman backscattered light has been shown to be a very powerful technique to monitor temperature distributions [17,18]. As Raman scattering is due to the interaction of light with the thermal optical phonons in the medium, its cross-section is very temperature sensitive. Several commercial systems are based on this principle. Finally, distributed sensors based on spontaneous Brillouin scattering have been recently demonstrated [19,20]. The Brillouin scattering process involves interaction of light with the acoustic phonons in the medium and is both temperature and strain sensitive.

1.3.2 Pump-probe configurations

Pump-probe configurations are those in which a continuous-wave (CW) laser probe-beam counter-propagates against an intense pump laser pulse. The interaction between the pump and probe beams occurs by means of a nonlinear optical effect and is influenced by the relevant measurand field. The spatial information is retrieved by monitoring the evolution of the probe beam as the laser pulse propagates along the fibre. Pump-probe schemes usually lead to improved signal-to-noise ratios because the probe field is in a coherent state and its detection can in principle reach the fundamental shot-noise limit.

The first proposed pump-probe configuration for DOFS relied on the Raman stimulated emission process [21]. The Raman gain that a CW probe experiences due to its interaction with an intense pump pulse depends on their relative polarisation states which, in turn, are dependent on the strain distribution along the fibre. In a second approach, the birefringence along a polarisation preserving fibre was mapped by means of phase matched coupling between the polarisation modes of the CW probe beam. This coupling was induced by the laser pump pulse through the optical Kerr effect [22]. Recently, various systems that rely on Brillouin stimulated emission and can measure strain or temperature distributions have been successfully demonstrated [23, 24]. Their principle of operation relies on mapping the evolution of the Brillouin frequency shift along the fibre.

1.4 OBJECTIVES AND OUTLINE OF THE THESIS

As we have discussed in previous sections, optical fibre sensing is a field of growing interest due to the unique ability of optical fibres to act both as transducers and signal carrier in multiplexed and distributed measurements. This thesis studies the application of several nonlinear optical effects to distributed optical fibre sensing.

In Chapter 2, we will investigate the application of spontaneous Raman scattering for distributed optical fibre measurements. Our aim will be to demonstrate a DOFS system capable of performing distributed measurement of temperature with very high spatial resolution. We will show that the use of the time-correlated single photon-counting technique allows measurement of temperature distributions with a high spatial resolution (10 cm) and good temperature accuracy (2 °C) within a reasonable integration time (1 minute) [25,26]. We will also investigate the problem of measuring distributions of high temperatures (550 °C) with specially coated optical fibres [27-29] and the different trade-offs and noise limitations of our system. Finally, we will demonstrate that the measurement of Raman scattering by means of the time-correlated single photon-counting technique constitutes an attractive solution to overcome the dead-zone problem that affects most conventional OTDR systems [30,31].

Chapter 3 and 4 will examine the formation and applications of static (photosensitive) and dynamic (Kerr) polarisation gratings in high birefringence optical fibres. Chapter 3 will treat photosensitive polarisation gratings in high birefringence fibres. Permanent static gratings are fabricated by exposing optical fibres to green or ultraviolet (UV) light. Our objective will be to study some aspects related to the polarisation dependence of the photo-induced birefringence and, as a consequence, to demonstrate a method for tailoring the spectral response of polarisation filters [32,33]. Also, we will study the mechanical effects that the fabrication process has on these devices and its consequences for their performance as sensors [34,35]. Although static gratings are not suitable for fully-distributed sensing, they can be multiplexed to implement quasi-distributed sensing systems.

In Chapter 4, we will analyse Kerr-induced polarisation gratings in high birefringence fibres. Dynamic gratings are created through the Kerr effect by means of an intense pump-beam propagating along the fibre. These transient gratings can induce phase matched coupling between the polarisation modes of a counter-propagating CW probe beam, and can be used for mapping the birefringence along a polarisation preserving fibre. The application of transient gratings and pump-probe architectures to distributed sensing will be theoretically analysed, showing its potential advantages and limitations [36-38].

In Chapter 5, we will study the application of Noise-Initiated Brillouin Scattering (NIBS) to distributed sensing. We will show that a combined monitoring of the Brillouin frequency shift and backscattered power allows simultaneous distributed measurement of strain and

temperature. We will also consider the problem of measuring Brillouin powers in the nonlinear regime of the NIBS growth, proposing and demonstrating a novel normalisation method. Finally, the noise limitations of the technique will be discussed [39-42].

REFERENCES

[1] J. Dakin, B. Culshaw. "Optical fiber sensors: principles and components". Artech House, 1988.

[2] M. Tateda, T. Horiguchi. "Advances in optical time-domain reflectometry". Journal of Lightwave Technology, Vol. 7, No. 8, pp. 1217-1224, August 1989.

[3] M.K. Barnorski, M.D. Rourke, S.M. Jensen, R.T. Melville. "Optical time domain reflectometer". Applied Optics, Vol. 16, No. 9, pp. 2375-2379, September 1977.

[4] S.D. Personick. "Photon probe: an optical-fiber time-domain reflectometer". Bell System Technical Journal, Vol. 56, No. 3, pp. 355-366, March 1977.

[5] B.S. Kawasaki, K.O. Hill, D.C. Johnson. "Optical time domain reflectometer for single-mode fiber at selectable wavelengths". Applied Physics Letters, Vol. 38, No. 10, pp. 740-742, May 1981.

[6] A.B. Carlson, "Communication Systems", pp. 101-103. McGraw Hill International, 1986.

[7] E. Brinkmeyer. "Analysis of the backscattering method for single-mode optical fibres". Journal of the Optical Society of America, Vol. 70, No. 8, August 1980.

[8] P. Healey. "Fading in heterodyne OTDR". Electronics Letters, Vol. 20, No. 1, pp. 30-32, January 1984.

[9] J.P. King, D.F. Smith, K. Richards, P. Timson, R.E. Epworth, S. Wright. "Development of a coherent OTDR instrument". Journal of Lightwave Technology, Vol. 5, No. 4, pp. 616-623, April 1987.

[10] P. Healy, P. Hensel. "Optical time domain reflectometry by photon counting". Electronics Letters, Vol. 16, No. 16, pp. 631-633, July 1980.

[11] R.I. MacDonald. "Frequency domain optical reflectometer". Applied Optics, Vol. 20, No. 10, pp. 1840-1844, May 1981.

[12] W. Eickhoff, R. Ulrich. "Optical frequency domain reflectometry in single-mode fiber". Applied Physics Letters, Vol. 39, No. 9, pp. 693-695, November 1981.

[13] K. Takada, I. Yohohama, K. Chida, J. Noda. "New measurement system for fault location in optical waveguide devices based on an interferometric technique". Applied Optics, Vol. 26, No. 9, pp. 1603-1606, May 1987.

[14] A.J. Rogers. "Polarization-optical time domain reflectometry: a technique for the measurement of field distributions". Applied Optics, Vol. 20, No. 6, 1060-1074, March 1981.

[15] M. Nakazawa, M. Tokuda, N. Uchida. "Analysis of optical time domain reflectometry for single mode fibers and of polarization optical time domain reflectometry for polarization-maintaining fibers". Optics Letters, Vol. 8, No. 2, pp. 130-132, February 1983.

[16] A.H. Hartog. "A distributed temperature sensor based on liquid-core optical fibers". Journal of Lightwave Technology, Vol. 1, No. 3, pp. 498-509, September 1983.

[17] J. P. Dakin, D. J. Pratt, G. W. Bibby, J. N. Ross. "Distributed optical fibre Raman temperature sensor using a semiconductor light source and detector". Electronics Letters, Vol. 21, No. 13, pp. 569-570, June 1985.

[18] A. H. Hartog, A. P. Leach, M. P. Gold. "Distributed temperature sensing in solid-core fibres". Electronics Letters, Vol. 21, No. 23, pp. 1061-1062, November 1985.

[19] T. Kurashima, T. Horiguchi, H. Izumita, S. Furukawa, Y. Koyamada. "Brillouin optical-fiber time domain reflectometry". IEICE Transactions Communications, Vol. E76-B, No. 4, pp. 382-389, April 1993.

[20] P.C. Wait, T.P. Newson. "Landau-Placzek ratio applied to distributed fibre sensing". Optics Communications, Vol. 122, pp. 141-146, 1996.

[21] M.C. Farries, A.J. Rogers. "Distributed sensing using stimulated Raman action in a monomode optical fibre". Proceedings of the 2nd International Conference on Optical Fibre Sensors, pp. 121-132, Stuttgart 1984.

[22] F. Parvaneh, L.C.G. Valente, V.A. Handerek, A.J. Rogers. "Forward-scatter frequency-derived distributed optical-fibre sensing using the optical Kerr effect". Electronics Letters, Vol. 28, No. 12, pp. 1080-1082, June 1992.

[23] T. Horiguchi, K. Shimizu, T. Kurashima, M. Tateda, Y. Koyamada. "Development of a distributed sensing technique using Brillouin scattering". Journal of Lightwave Technology, Vol. 13, No. 7, pp. 1296-1302, July 1995.

[24] X. Bao, D.J. Webb, D.A. Jackson. "Characteristics of Brillouin gain based distributed temperature sensors". Electronics Letters, Vol. 29, No. 17, pp. 1543-1544, August 1993.

[25] R. Feced, M. Farhadiroushan, V.A. Handerek, A.J. Rogers. "Advances in high resolution distributed sensing using the time-correlated single photon counting technique". IEE Proceedings in Optoelectronics, Vol. 144, No. 3, pp. 183-188, June 1997.

[26] R. Feced, M. Farhadiroushan, P. Rodriguez, V.A. Handerek, A.J. Rogers. "Advances in high resolution distributed sensing using a time-resolved photon counting technique". SPIE 2838, pp. 105-113 (1996). Denver (USA), August 1996.

[27] R. Feced, M. Farhadiroushan, V.A. Handerek, A.J. Rogers. "A high spatial resolution distributed optical fiber sensor for high temperature measurements". Review of Scientific Instruments (AIP), Vol. 68, No. 10, pp. 3772-3776, October 1997.

[28] R. Feced, M. Farhadiroushan, V.A. Handerek, A.J. Rogers. "High temperature testing of a high spatial resolution distributed optical fibre temperature sensor". Optical techniques for smart structures and structural monitoring. IEE, London, February 1997.

[29] R. Feced, M. Farhadiroushan, V.A. Handerek, A.J. Rogers. "Evaluation of a high spatial resolution distributed optical fiber sensor for high temperatures applications". 12th Optical Fiber Sensors Conference, Williamsburg, Virginia (USA). October 1997.

[30] R. Feced, M. Farhadiroushan, V.A. Handerek. "Zero dead-zone OTDR with high spatial resolution for short haul applications". IEEE Photonics Technology Letters, Vol. 9, No. 8, pp. 1140-1142, August 1997.

[31] R. Feced, M. Farhadiroushan, V.A. Handerek. "A high spatial resolution zero dead-zone OTDR". 4th Optical fibre measurement conference. NPL, Teddington (UK), October 1997.

[32] V.A. Handerek, S.E. Kanellopoulos, R. Feced, J.Croucher. "Evaluation of shape-birefringent fibres for sensing systems employing photogenerated polarization couplers". Optical fibre gratings and their applications. IEE, London, January 1995.

[33] R. Feced, S.E. Kanellopoulos, R.A. Griffin, V.A. Handerek. "Polarization dependence of photo-induced birefringence and its application to fabrication of tailored polarization filters". Bragg grating, Photosensitivity, and Poling in Glass Fibers and Waveguides Topical Meeting (OSA), Williamsburg, Virginia (USA). October 1997.

[34] R. Feced, M.P. Edwards, S.E. Kanellopoulos, N.H. Taylor, V.A. Handerek. "Mechanical strength degradation of UV exposed optical fibres". Electronics Letters Vol. 33, No. 2, pp. 157-159, January 1997.

[35] K. Raine, R. Feced, S.E. Kanellopoulos, V.A. Handerek, A. Parker. "High resolution stress profiling of UV exposed optical fibres". 4th Optical fibre measurement conference. NPL, Teddington (UK), October 1997.

[36] R. Feced, S.E. Kanellopoulos, M. Farhadiroushan, V.A. Handerek, A.J. Rogers. "Analysis of optical Kerr effect induced coupling among polarization modes in high-birefringence optical fibers". Optics Communications, Vol. 143, pp. 268-278, November 1997.

[37] F. Parvaneh, M. Farhadiroushan, R. Thomas, R. Feced, V.A. Handerek, A.J. Rogers. "Demonstration and potential of distributed temperature sensors using the frequency derived

technique". Progress in optical fibre sensors and their applications. IEE, London, November 1995.

[38] F. Parvaneh, M. Farhadiroushan, R. Thomas, R. Feced, V.A. Handerek, A.J. Rogers. "Recent progress in distributed temperature sensing using the frequency derived technique". Optical Fiber Sensors (OFS-11), Sapporo (Japan), May 1996.

[39] T.R. Parker, M. Farhadiroushan, R. Feced, V.A. Handerek, A.J. Rogers. "Simultaneous distributed measurement of temperature and strain from noise-initiated Brillouin scattering in optical fibres". Accepted for publication in IEEE Journal of Quantum Electronics (April 1998).

[40] R. Feced, T.R. Parker, M. Farhadiroushan, V.A. Handerek, A.J. Rogers. "Power measurement of noise-initiated Brillouin scattering in optical fibres for sensing applications". Accepted for publication in Optics Letters (January 1998).

[41] T.R. Parker, M. Farhadiroushan, R. Feced, V.A. Handerek, A.J. Rogers. "Simultaneous distributed strain and temperature sensing using noise-initiated Brillouin scattering ". 12th Optical Fiber Sensors Conference, Williamsburg, Virginia (USA). October 1997.

[42] T.R. Parker, R. Feced, M. Farhadiroushan, V.A. Handerek, A.J. Rogers. "Linearisation of noise-initiated Brillouin backscattered power for simultaneous strain and temperature measurement". 4th Optical fibre measurement conference. NPL, Teddington (UK), October 1997.

Chapter 2

RAMAN SCATTERING FOR HIGH SPATIAL RESOLUTION DISTRIBUTED MEASUREMENTS

In this chapter, we examine the application of spontaneous Raman scattering for high spatial resolution distributed measurements in optical fibres. In Section 1, the phenomenon of Raman scattering in optical fibres is introduced. Section 2 discusses the optimum technique to measure the weak backscattered Raman signals with high spatial resolution. It is shown that the time-correlated single photon-counting (TC-SPC) technique combines a high sensitivity with an excellent time resolution for distributed measurements. In Section 3, we implement a distributed temperature sensor that achieves a high spatial resolution of 10 cm and 2 °C temperature resolution for a measurement time of 1 minute [1,2]. Section 3 examines the critical issues for measurement of high temperatures (550 °C) with the previous system, in particular the thermal behaviour of specially coated fibres [3-5]. Finally, in Section 5 we describe a high resolution OTDR system that overcomes the dead zone problem that affects most Rayleigh based OTDR's. The system relies on the detection of the spontaneous Stokes Raman emission by means of the TC-SPC architecture [6,7].

2.1 RAMAN SCATTERING IN OPTICAL FIBRES

2.1.1 Raman effect

Raman scattering is a nonlinear optical process in which the incident electromagnetic radiation is scattered and frequency shifted due to its interaction with the vibrational modes of the scattering medium [8]. The scattering system could be a gas of molecules, a liquid or a solid. This phenomenon can be explained from a classical point of view in terms of the electromagnetic radiation generated by the electric dipoles that the incident radiation induces in the scattering system. As the electronic polarizability of the medium can be modulated in time by the nuclear vibrational modes, part of the scattered radiation will suffer a shift of frequency with respect to the frequency of the incident radiation [9]. The study of the vibrational modes of molecules, liquids or solids through the analysis of the spectrum of the Raman scattered light is called Raman spectroscopy.

Raman scattering is more rigorously explained by means of the quantum mechanical formalism [10], where the scattering processes are viewed as particle-like interactions among photons and optical phonons (which are the quanta of the electromagnetic and of the vibration fields respectively). There are two types of Raman scattering processes. The first one is the Stokes process, in which an incident photon is scattered into a frequency downshifted Stokes photon, with concomitant creation of an optical phonon (Figure 1). The scattering cross-section of this process is proportional to:

$$\sigma_S \propto n_L\,(n_S+1)(n_V+1) \qquad (1)$$

where n_L is the number of photons in the incident radiation mode, n_S is the number of photons in the scattered Stokes mode and n_V is the number of phonons in the relevant vibrational mode. If initially there are no photons in the Stokes scattered radiation mode (n_S=0), the process is called spontaneous Raman scattering. If, on the other hand, n_S is not null, the scattering cross section increases and the process is called stimulated Raman scattering.

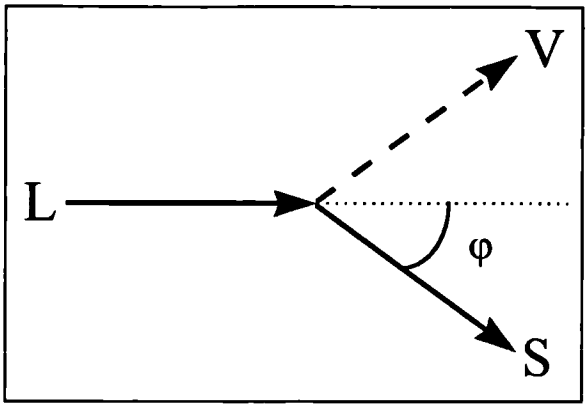

Figure 1. Illustration of Stokes Raman scattering process. L: incident photon, S: Stokes photon, V: optical phonon and φ, scattering angle.

The second type of Raman scattering process is the antiStokes interaction, in which the incident photon is scattered into a frequency upshifted antiStokes photon with concomitant annihilation of an optical phonon (Figure 2). The scattering cross-section of this process is proportional to:

$$\sigma_S \propto n_L (n_A + 1) n_V \qquad (2)$$

where it can be observed that the difference with respect to the Stokes case is in the term which involves the optical phonons. It is important to realise that in the stimulated scattering regime the processes inverse to those represented in Figures 1 and 2 have to be considered to explain the dynamics of the Stokes and antiStokes photons.

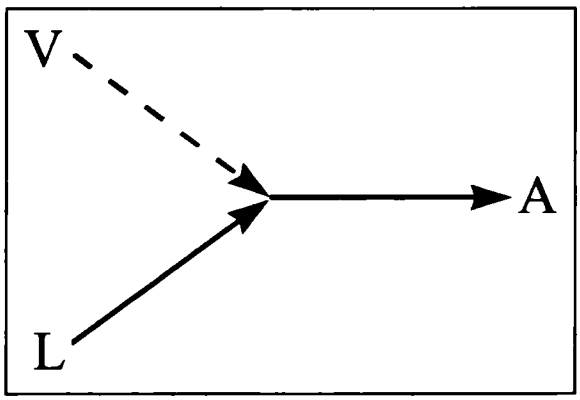

Figure 2. Illustration of antiStokes Raman scattering process. L: incident photon, A: antiStokes photon, V: optical phonon.

Isolated molecules have a discrete number of vibrational modes, each with a characteristic frequency. The vibrational modes that satisfy certain symmetry selection rules are able to induce periodic variations in the molecular electronic polarisability and are said to be Raman active. The Raman spectrum of gases and liquids is formed by the characteristic frequencies of the Raman active modes. In solids, on the contrary, the nuclei vibrational modes are not confined to particular molecules [11]. The vibrational modes are collective vibrations of the lattice, with frequencies spread into bands which create a continuum. The vibrational modes that intervene in Raman scattering are those which belong to the optical vibration branch, which is reminiscent of the internal molecular vibrations [12]. If many of the vibrational modes in the optical branch are Raman active, then the Raman spectrum will extend continuously over a broad range. This is the case in amorphous materials like glass [13].

The first measurement of the spontaneous Stokes Raman scattering cross-section spectrum in silica was performed by Stolen [14,15]. The Raman spectrum was very broad, extending from 20 cm^{-1} to 500 cm^{-1}, with a maximum at 440 cm^{-1} (Figure 3). Galeener [16] has studied the Raman scattering cross-sections of other glass formers like GeO_2, B_2O_3 and P_2O_5, reaching the conclusion that their cross-sections were from 5 to 10 times bigger than that of silica. Also, their corresponding Raman spectra were very different from one another. GeO_2, for example, exhibited the maximum scattering cross-section at 420 cm^{-1}. These experiments suggested that glasses formed from a mixture of several conveniently selected glass formers could have a very broad Raman scattering band. A mixture of GeO_2 and P_2O_5 provided, for example, a scattering band of 1300 cm^{-1} approximately. Raman scattering is very suitable for high spatial resolution distributed measurements in optical fibres because its broad band spectrum translates into a very fast response time.

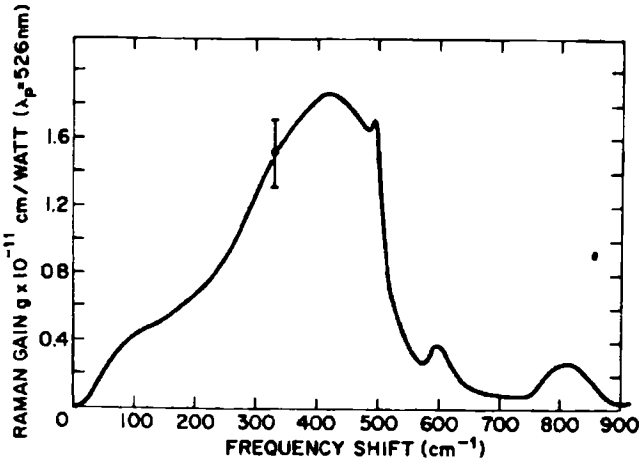

Figure 3. Raman gain of fused quartz plotted as a function of frequency shift, after [15].

2.1.2 Applications and limitations of Raman scattering in optical fibres

Most of the applications of Raman scattering in optical fibres are related to the gain experienced by an optical probe signal with a frequency within the Stokes band of a copropagating intense optical pump signal. This optical amplification is a consequence of the stimulated Raman scattering process described in Figure 1 (together with its inverse process). Raman optical amplification in optical fibres was first proposed [14] and demonstrated [15] by Stolen and coworkers, who were also the first to demonstrate Raman lasers in both Fabry-Perot [14] or ring configurations [17]. The broad band of the Raman spectrum enabled the possibility of wide band optical amplification and of long range tunability in Raman lasers.

On the other hand, stimulated Raman scattering sets a limitation to the optical power handling capacity of optical fibres [18]. Intense optical radiation that propagates in an optical fibre can be seriously depleted due to the scattering of its energy into the Stokes band. The seed for the exponential growth of the Stokes radiation is provided by some initial spontaneously scattered photons. The dynamics of pump depletion due to Raman scattering has been studied by Yariv [19]. Raman scattering can also have a negative effect in communication systems based on wavelength division multiplexing (WDM) because it acts as a source of cross-talk among the channels [20].

2.1.3 Distributed temperature sensing based on Raman effect

Spontaneous Raman scattering has been successfully applied to distributed measurements of temperature along optical fibres [21,22]. The principle of operation of Raman thermometry was first proposed by Dakin [21] and relies on the temperature dependence of the Stokes and antiStokes scattering processes. This dependence arises from the thermally excited phonon population of the vibrational modes involved in the scattering, which follows a Bose-Einstein distribution. The average number of phonons in one of these modes is:

$$\langle n_V \rangle = \frac{1}{\exp\left(\frac{hc\tilde{\nu}}{kT}\right) - 1} \tag{3}$$

where h is the Planck constant; c is the speed of light in vacuum; k is the Boltzmann constant; T is the local fibre temperature; and $\tilde{\nu}$ is the mode wavenumber (which corresponds to the Raman frequency shift, 440 cm^{-1} for silica).

The Stokes scattering process (1) is only slightly temperature sensitive due to the fact that $1 >> n_v$ for usual temperatures. On the other hand, the antiStokes process (2) is much more temperature sensitive because it involves the annihilation of a vibrational optical phonon. Usually, Distributed AntiStokes Raman Thermometry (DART) systems normalise the antiStokes scattered signal with the Stokes scattered signal in order to compensate against propagation losses along the fibre. Taking into account the wavelength dependence of the electrical dipole emission ($\propto 1/\lambda^4$) , the ratio R between the antiStokes ϕ_{AS} and Stokes ϕ_S photon fluxes is given by:

$$R = \frac{\phi_{AS}}{\phi_S} = \frac{\lambda_S^4}{\lambda_{AS}^4} \exp\left(-\frac{hc\tilde{\nu}}{kT}\right) \tag{4}$$

where λ_S and λ_{AS} are the wavelengths of the Stokes and antiStokes scattered radiation respectively. The temperature sensitivity of this ratio is:

$$S_T = \frac{1}{R}\frac{\delta R}{\delta T} = \frac{hc\tilde{\nu}}{kT^2} \tag{5}$$

which is clearly temperature dependent. At 300 K, the temperature sensitivity S_T is 0.7 % $^{\circ}C^{-1}$.

In a standard DART sensor, an intense laser pulse is launched into the sensing fibre and, as it propagates, some of its photons are spontaneously Raman scattered into the Stokes and antiStokes bands. A fraction of these scattered photons is captured in guided modes of the fibre and then propagate back to the launching end where they are detected by a fast photodetector as in a typical OTDR scheme. The flux of Raman backscattered photons (photons per second) $\phi_{AS,S}$ is proportional to the incident laser pulse energy and also to the Raman scattering cross-section, which is three orders of magnitude smaller than the Rayleigh scattering cross-section. $\phi_{AS,S}$ are given by the OTDR formula described in Chapter 1 [23]:

$$\phi_{AS,S} = \phi_{inc}\, \tau \frac{v}{2} \alpha_{AS,S}\, \kappa\, \Gamma \tag{6}$$

where ϕ_{inc} is the peak photon flux and τ the pulse-width of the incident laser pulse. The product $\phi_{inc} \cdot \tau$ gives the total number of photons in the laser pulse. v is the speed of light in the fibre; $\alpha_{AS,S}$ are the Raman scattering coefficients. κ is the fibre capture fraction, which is given by the expression [23]:

$$\kappa = \frac{1}{4} \frac{NA^2}{n^2} \tag{7}$$

where NA is the numerical aperture of the fibre and n the refractive index of the fibre core. Finally, Γ is a measure of the power throughput of the system and accounts for losses in its different components and for the attenuation of the fibre.

In the first experimental demonstrations of the DART principle [21,22], the sensor system was implemented with semiconductor pulsed lasers emitting in the 900 nm wavelength region as sources, and silicon avalanche photodiodes (APD) followed by low noise transimpedance amplifiers as detectors. The fibres used were multimode with core sizes of 50 μm in [21] and 100 μm in [22], and corresponding NA of 0.2 [21] and 0.3 [22]. The fibres were germanium doped to maximise the Raman scattering cross-section. Dakin's system [21] achieved a temperature resolution of 10 °C, with 3 m spatial resolution and 1 km of total sensing range for a measurement time of 40s. Hartog's system [22] traded off temperature resolution for spatial

resolution, achieving 1 °C temperature resolution with 7.5 m spatial resolution for a total sensing length of 1km and a measurement time of 25 s.

Nowadays there exist several commercially available DART systems based on semiconductor sources and fast APD detectors operating in the 900 nm wavelength region. They achieve a typical performance of 1°C temperature resolution, with 1m spatial resolution for a sensing length of several kilometres and a measurement time below 1 minute. Both the high fibre attenuation at 900 nm and the limitation in the maximum permissible laser pulse power set by the threshold of stimulated Raman scattering are the main reasons that prevent the extension of the sensing range over distances longer than 10 km. Recently, it has been shown that this limit can be overcome by implementing a system that operates in the low attenuation window of 1.55μm [24]. This system achieved a temperature resolution of 2.3 °C and a spatial resolution of 6.5 m for a total sensing length of 30 km in a measurement time of 11 minutes.

It is worth mentioning two other proposed Raman sensor architectures that are different from the standard OTDR architecture described so far. The first one [25] uses spread spectrum techniques to try to improve the detection signal-to-noise ratio. In this case, the laser is modulated with a pseudo-random bit sequence and the Raman scattered signal is correlated with a delayed version of this sequence. The other architecture [26] is based on the concept of a self-starting passively mode locked fibre ring laser, where the sensing length of fibre is part of the ring laser. The main advantage of this implementation would be its power efficiency, because large intracavity power can be generated with modest pump powers.

All the systems described so far have in common that they are well suited for long range applications with coarse spatial resolution (>1m). However, there are some applications where higher spatial resolutions are needed. In the following section we discuss why the performance of the previously described systems is degraded when we try to improve their spatial resolution and what would be the optimum system design to achieve high spatial resolution distributed measurements in optical fibres.

2.2 OPTIMISATION OF THE SIGNAL-TO-NOISE RATIO IN HIGH SPATIAL RESOLUTION DISTRIBUTED MEASUREMENTS: THE TIME-CORRELATED SINGLE PHOTON COUNTING TECHNIQUE

In this section, we will first discuss the reasons for the performance deterioration of OTDR systems based on analogue detection schemes as their spatial resolution is gradually improved. We will show that this performance degradation can be minimised with a digital detection technique: the time-correlated single photon-counting technique (TC-SPC). Finally, we will describe some aspects related to the technology available for the practical implementation of this technique and also we will review the state of the art regarding to its application to distributed optical fibre measurements.

2.2.1 Analogue detection schemes

In an analogue detection scheme, the flux of Raman backscattered photons $\phi_{AS,S}$ is detected by a fast photodetector, usually an avalanche photodiode APD, followed by a low noise transimpedance amplifier. Every detected photon generates a current pulse whose total charge depends on the detector internal gain and its extension in time T_R is inversely proportional to the detection bandwidth B (Chapter 1):

$$B = \frac{1}{2T_R} \tag{8}$$

All the current pulses add together to produce a current proportional to the detected photon flux. In order to compare the signal-to-noise ratio achieved by analogue and digital (photon-counting) detection schemes, it is convenient to define the random variable m, which is equal to the number of photons detected (or photoelectrons) in the photodiode during the characteristic time T_R [27]. The probability of detecting m photons in the time interval T_R when a random photon flux $\phi(t)$ impinges on a detector of quantum efficiency η obeys the Mandel formula [28]:

$$p(m, T_R) = \left\langle \frac{1}{n!} W^n e^{-W} \right\rangle \tag{9}$$

where the brackets stand for ensemble average over realisations of the random variable $\phi(t)$ and W is a random variable given by the expression:

$$W = \int_{t}^{t+T_R} \eta \, \phi(t) \quad dt \tag{10}$$

The average value of m is given by:

$$\overline{m} = \overline{W} = \eta \, \overline{\phi} \, T_R \tag{11}$$

while its variance σ_m^2 is:

$$\sigma_m^2 = \overline{m} + \sigma_W^2 \tag{12}$$

The first term in (12) gives the fundamental noise limitation due to the quantum nature of the photon field and the photodetection process, the well known shot noise. The second term accounts for the excess noise due to the randomness of the field and it is null when the field is in a coherent state. In this case, m will follow the Poisson statistics. However, scattered fields usually obey gaussian statistics because they result from the contributions of many random independent scatterers. This means that σ_W^2 could be non null and that m could depart from the Poisson statistics of coherent light. The actual value of σ_W^2 in the case of gaussian light depends on the ratio between the characteristic measurement time T_R and the coherence time of the detected light τ_C. If T_R is much bigger than τ_C, as is the case for the broad band Raman scattering, the fluctuations of the field intensity are averaged in time (or more precisely, averaged over many longitudinal propagation modes), giving rise to an almost null σ_W^2 [30]. Consequently, we can safely assume that the number of Raman scattered photons detected in T_R follows a Poisson distribution.

In analogue detection schemes, there are two additional noise sources. The first one is associated with the random multiplication factor of photoelectrons in devices with internal gain, such as the APD. The second one is the circuit noise, including the dark current of the photodiode, thermal noise of resistors and other dissipative elements, etc. Following Saleh [31], the overall signal-to-noise ratio SNR of the current generated is given by the expression:

$$SNR = \frac{\overline{G}^2 \overline{m}^2}{F\overline{G}^2 \overline{m} + \sigma_q^2} \tag{13}$$

where $\overline{G}$ is the average internal gain of the APD, F is the corresponding excess noise factor ($F \equiv \overline{G^2} / \overline{G}^2$), and σ_q is a dimensionless circuit noise parameter whose value depends on each particular detection scheme. σ_q^2 is inversely proportional to the detection bandwidth B for a resistance limited design, proportional to B in a FET based design and independent of B in a bipolar transistor based design [31]. The signal-to-noise ratio in (13) increases linearly if the measurements from successive repetitions of the experiment (excitation cycles) are averaged.

The spatial resolution of an OTDR is determined, as we discussed in Chapter 1, by the laser pulse-width τ and the detection bandwidth B ($=1/2T_R$). Usually, the resolution time of the circuit T_R is matched to the laser pulse-width ($T_R \approx \tau$). From (13) we can observe how the signal-to-noise ratio degrades when trying to improve the spatial resolution. To improve the resolution by one order of magnitude, both τ and T_R should each decrease by one order of magnitude. Consequently, the backscattered photon flux ϕ (6) will decrease by one order of magnitude and $\overline{m}$ will decrease by two orders of magnitude (11). From (13), we see that the signal scales with the fourth power of the spatial resolution, falling to very low levels as we try to reduce the resolution under 1 m. As the circuit noise σ_q^2 can increase or decrease by one order of magnitude depending on the detection circuit used, the signal-to-noise ratio falls between three and five orders of magnitude if we neglect the shot noise component. The overall signal-to-noise ratio can be partially improved by increasing the detector's gain while ensuring that the excess noise F does not amplify the shot noise above the circuit noise. From the preceding discussion, it can be appreciated that both the circuit noise σ_q^2 and the excess noise factor F are the main causes that prevent the achievement of the fundamental noise limitation given by (11) and (12), deteriorating considerably the signal-to-noise ratio when the detection bandwidth is increased. Qualitatively new techniques are needed to achieve better spatial resolutions in distributed optical fibre measurements.

2.2.2 Digital time-correlated single photon-counting

We have seen that, as we try to increase the spatial resolution of the DART sensor, the backscattered photon flux ϕ becomes very weak. Ideally, to optimise the signal-to-noise ratio we should use a detection technique in which the circuit noise σ_q would be negligible and the excess noise factor F would be equal to 1. Then, the only source of noise would be that associated with the photon statistics. A digital time-correlated single photon counting technique (TC-SPC) [32] that satisfies these two conditions has been proposed to improve the spatial resolution and sensitivity in optical fibre distributed measurements. The technique consists in the repetitive measurement of the delay time between the first detected Raman backscattered photon and the laser trigger signal. As the backscattered photon flux is very weak, the probability of detecting one photon or more per launched laser pulse is small. A detector with very high gain (a photomultiplier, for example) will produce a current pulse when a photon is detected. If the gain is high enough, the circuit noise would be negligible compared to the current pulse and the time of the pulse detection could be determined precisely. For every laser pulse (or repetition of the measurement), either no photon is detected or we detect only one photon and time it within a resolution interval T_R (time channel or slot). We see that this digital technique has eliminated both the circuit noise σ_q and the randomness of the gain F just by detecting one photon at a time. Consequently, the signal-to-noise ratio for one such measurement would be very near $\overline{m}$ for each channel (see equation 13), which is the fundamental limit. By repetitive measurements, a histogram of number of counts (detected photons) versus time can be built. The signal to noise ratio will increase linearly with the number N of repetitions of the measurement (excitation cycles) to become $N\overline{m}$.

Practical single photon-counting detectors, however, do not achieve this ideal performance because they are subjected to dark counts and background light counts that contribute some noise. Dark counts result usually from thermally driven processes and can be minimised by cooling the detector. If the average number of noise counts (s^{-1}) is R_B, the signal-to-noise ratio of a channel that corresponds to a time interval T_R would be (after N measurements) [33]:

$$SNR = N\frac{\overline{m}^2}{\overline{m} + T_R R_B} \qquad (14)$$

where it was assumed that the different noise sources were statistically independent and followed Poisson statistics. Usually $\overline{m} >> T_R R_B$ and the TC-SPC scheme approaches the ideal performance. Equation (14) will be useful to calculate the ultimate sensitivity of a particular TC-SPC system by equating the SNR to unity.

The probability that a photon-counting detector registers a count in a channel i (that corresponds to a time interval T_R) when it is exposed to an incident photon flux ϕ_i can be calculated from (9) by adding the probabilities of detecting one or more photons:

$$p_i(T_R) = \sum_{m=1}^{\infty} p(m, T_R) = 1 - e^{-m} \tag{15}$$

We see that, strictly speaking, the number of counts in the different channels follows a binomial distribution that can be approximated to a Poisson distribution because $\overline{m}$ is much less than unity. After N measurements, the average number of counts in the channel i will be:

$$N_i = N\, p_i = N\,(1 - e^{-m}) \approx N\,\overline{m} \tag{16}$$

However, the number of counts N_i^{exp} measured in the different channels (time-slots) after a TC-SPC experiment differs from the former N_i in (16) due to the fact that only one photon is detected per repetition of the process. Those photons that arrive first to the photodetector have higher probability of being detected, making the experimental counts N_i^{exp} unfaithful representations of the photon flux incident at each particular time-slot. This distortion is negligible if the overall probability of detecting a photon in the whole time range is small (<0.02). In this case N_i^{exp} is approximately equal to N_i. Coates [34] has devised an algorithm that corrects this "pile-up" effect in the general case of high overall detection probabilities, showing that the N_i (16) can be recovered from the experimental N_i^{exp} through the formula:

$$N_i = N \frac{N_i^{exp}}{N - \sum_{j=1}^{i-1} N_j^{exp}} \tag{17}$$

From (17), the values of the photon fluxes ϕ_i at each particular time-slot can be recovered through (16) and (11).

The high sensitivity of TC-SPC permits the achievement of very high spatial resolutions when the technique is implemented with picosecond laser sources and fast photodetectors. The overall time resolution of a TC-SPC system is given by the convolution of the laser pulse-width, the transit time spread of the photodetector and other additional jitter in the electronics. Time resolutions in the hundred picoseconds range can be achieved, permitting OTDR measurements with spatial resolution in the centimetre range.

2.2.3 Technology for the implementation of the TC-SPC technique

The design of a TC-SPC system with time resolution in the picosecond range requires the use of state of the art technology. First, the laser has to able to generate short and stable pulses, in the range of 50 to 500 ps. An attractive solution is the use of gain switched semiconductor lasers due to the wide range of wavelengths that they cover and their portability. For our application, peak powers of the order of hundreds of milliwatts, which are commonly achieved by semiconductor lasers, will be necessary.

One of the most critical parts of the system is the single photon-counting detector. There are several options available depending on the wavelength of the optical radiation and the time resolution required. Photomultipliers tubes (PMT) provide a high quantum efficiency (5-30%) for detection of light in the visible range of the spectrum (<650 nm). Special photocathodes with low work functions (multi-alkali or S-1) can extend the use of PMTs into the infrared region of the spectrum (<900 nm). The dark counts of PMTs are the result of thermal emission of electrons by the photocathode and can be specially problematic for the infrared sensitive PMTs. The dark count rate can be minimised by an adequate cooling of the PMT and also by pulse height discrimination of the current pulses. Typical values of dark counts are in the range of 10^2-10^3 s^{-1}. Another spurious effect that causes signal deterioration are the "after pulses", which are delayed current pulses generated by the collision of accelerated ions in the residual gas with the photocathode.

The multiplication stages of PMTs (dynodes) provide gains of the order of 10^6 but also, due to the randomness of the process, cause some spread in the transit time of the secondary electrons. This transit time spread limits the time resolution of the detector, which is typically several

hundred picoseconds for commercial devices. Special designs in which the secondary electrons are focused by static electric and magnetic fields have achieved time resolutions of 50ps [35]. A particular type of PMT called a micro-channel plate (MCP) has been shown to have very low transit time spread, of the order of tens of picoseconds [36]. In these devices the secondary electrons are multiplied inside small glass capillaries (10-20 μm of diameter) which are coated with emissive material and form arrays of millions of channels. In spite of their short transit time spreads (≈50 ps), the residual charge in the channels after the passage of the electronic current causes a fall tail in their response function that extends for hundreds of picoseconds.

An alternative solution for the single photon detector is the single-photon avalanche photodiode (SPAD) which offers enhanced sensitivity for detection of infrared radiation. The SPADs are avalanche photodiodes that are operated in Geiger mode, i.e. biased slightly over the breakdown voltage. In these conditions, the detection of a single photon is enough to trigger a self-sustained avalanche that is quenched either passively (by a resistor) or actively (by an external active circuit). Passive quenching gives rise to long dead times, of the order of several microseconds. Active quenching [37,38], on the other hand, reduces considerably the dead time, a typical figure being 100 ns. The wavelength sensitivity of SPADs depends on the semiconductor used for their fabrication. Devices based on silicon [37,38], InGaAs.InP [39], and germanium [40] have been reported. The last two could operate at wavelengths in the 1.5μm range. The overall quantum efficiency of SPADs depends on their optical quantum efficiency and also on the probability of breakdown initiation, which is a function of the reverse bias voltage. Usually, quantum efficiencies in excess of 10% can be attained. The dark count rate also increases with the reverse bias voltage and in many situations cooling of the photodetector is necessary.

The fundamental limit for the time resolution of SPADs is given by the transit time of carriers across the depletion layer. However, their time response usually exhibits a long tail due to the diffusion of carriers into the depletion layer once they have been photogenerated in the neutral regions. An epitaxial SPAD has been designed to minimise this effect [38], providing a time resolution of 30 ps. Also, carrier traps can have the negative effect of producing "after pulses" when the trapped carriers are freed.

The first OTDR photon-counting systems timed the detection of photons very coarsely by use of gates either in the detector or in the counting circuit [41]. The measurement time resolution improved with the development of multichannel scalers, in which each channel counted the

number of events in a time slot. These systems did not really implement the TC-SPC technique, because for each full scan more than one event could be counted. The time reference in multichannel scalers is provided by an oscillator clock and the time resolution has improved from 1μs [39] to 4 ns [42]. There are commercially available systems with a time resolution of 5 ns and virtually no dead time between channels. Multichannel scalers have been implemented for OTDR and DART applications [43], achieving good spatial resolutions (≈0.5 m) and relatively short measurement times due to their multiphoton counting capability.

However, in order to achieve higher spatial resolutions (<10cm), a more accurate timing procedure is necessary. In the TC-SPC technique (see Figure 4) the delay time between the first backscattered photon and the triggering of the laser is measured by a time to amplitude converter (TAC). A TAC is simply a capacitor that is charged by a constant current source during a time interval limited by a START and STOP signals, producing a final voltage proportional to the duration of the time interval. The main sources of distortion and timing errors in a TAC are due to nonlinerities in the voltage ramp.

The START and STOP signals, especially the signal coming from the single photon detector, have to be adequately discriminated and conditioned prior to their action on the TAC. This is achieved by constant fraction discriminators (CFD), that are able to measure accurately the time positions of pulses with independence of their amplitudes as long as their pulse shape remains unaltered.

The final TAC voltage level is digitised in an analogue to digital converter (ADC) and the corresponding channel in the memory of a multichannel analyser (MCA) increases then its count by one unit. It is clear that this technique only detects one photon per laser pulse but that its timing resolution is much superior to previous ones. All the electronic circuits should have high stability, excellent linearity and low time jitter.

Photon counting schemes were first used for OTDR measurements of Rayleigh backscattered light due to their great sensitivity. Initially, Healy [41] demonstrated a system based on gate-timing and SPAD detection that operated at 850nm. Later, Levine [39] demonstrated an improved system based on a multichannel scaler and also SPAD detection that could operate at 1.3 μm and 1.5 μm. The high spatial resolution capability of the TC-SPC technique for OTDR measurements was first reported by Cova [44-46], who demonstrated a system with centimetre spatial resolution and 10^{-15} W sensitivity using a silicon SPAD photodetector.

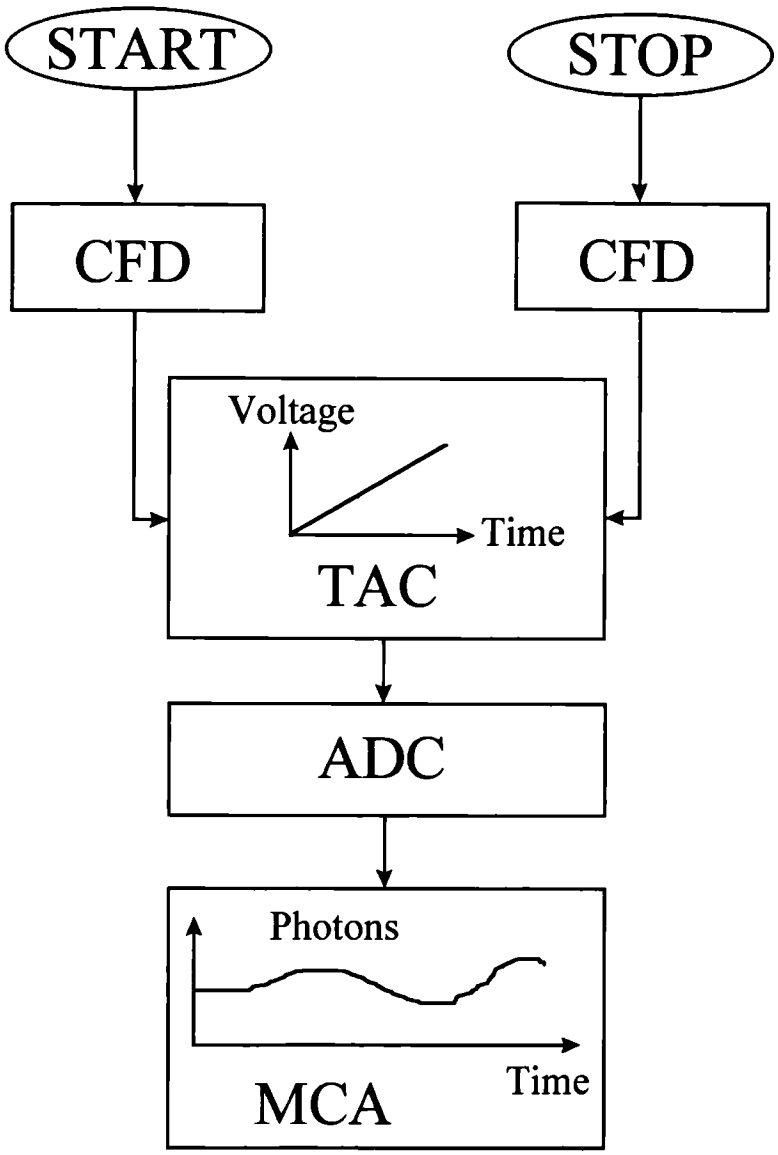

Figure 4. Schematic diagram of the TC-SPC technique. START and STOP are the synchronisation signals; CFD, constant fraction discriminator; TAC, time to amplitude converter; ADC, analogue to digital converter; MCA, multichannel analyser.

The first experimental implementation of the TC-SPC technique in a DART sensor is due to Stierlin [47] who achieved a spatial resolution of 30 cm over a range of 30 m. The measurement time needed to achieve a temperature resolution of 4 °C was 3 minutes. More recently, an experimental system by Thorncraft [48] using a frequency-doubled mode-locked Nd:YAG laser showed the potential of the TC-SPC technique for distributed temperature measurement with very high spatial resolutions of 10 cm. However, in this experiment the measurement range was limited to 90cm and a long measurement time of 6 minutes was needed to achieve a temperature resolution of 6°C. The applications that we are addressing are those

that require measurement of temperature distributions with very high spatial resolution (10cm) in a short measurement time (1 minute). The typical temperature resolution needed would be around 2 °C and the sensing range would extend for several tens of metres. A great improvement over the performance of previous systems is necessary to meet these specifications.

2.3 DEVELOPMENT OF A HIGH SPATIAL RESOLUTION DISTRIBUTED TEMPERATURE SENSOR

In this section we present an optimised distributed sensor that provides a practical solution for high spatial resolution temperature monitoring [1,2]. As the system aims at short haul applications where the loss in the fibre is not a critical issue, visible semiconductor lasers and compact PMTs have been selected to take advantage of the enhanced Raman scattering cross section at shorter wavelengths.

2.3.1 System description

The experimental system is shown in Figure 5. The laser was a semiconductor gain switched laser that emitted at a central wavelength of 635 nm. The laser pulses were adjustable approximately from 100 ps to 500 ps (FWHM) by control of the current pulses generated by a laser driver. The peak power of the optical pulses scaled with their pulse width. The average power for the pulse width used in our application (approximately 200 ps) was 0.15 mW at a 5MHz repetition rate, giving a peak power of 150 mW. The repetition rate, 5MHz, was limited by the total length of the sensor, 20 m. The spectrum of the laser had a FWHM of 1.5 nm and exhibited a long tail towards the short wavelengths that extended for 8 nm. The jitter of the laser pulses with respect to their synchronisation signal was 25 ps.

These laser pulses were launched through a fibre coupler into 20 m of a multimode graded index fibre. The fibre was GeO_2 doped, had a numerical aperture NA of 0.2 and the dimensions of the core and cladding diameters were 62.5 μm and 125 μm respectively. The fibre losses at 633 nm were 12 dB/km.

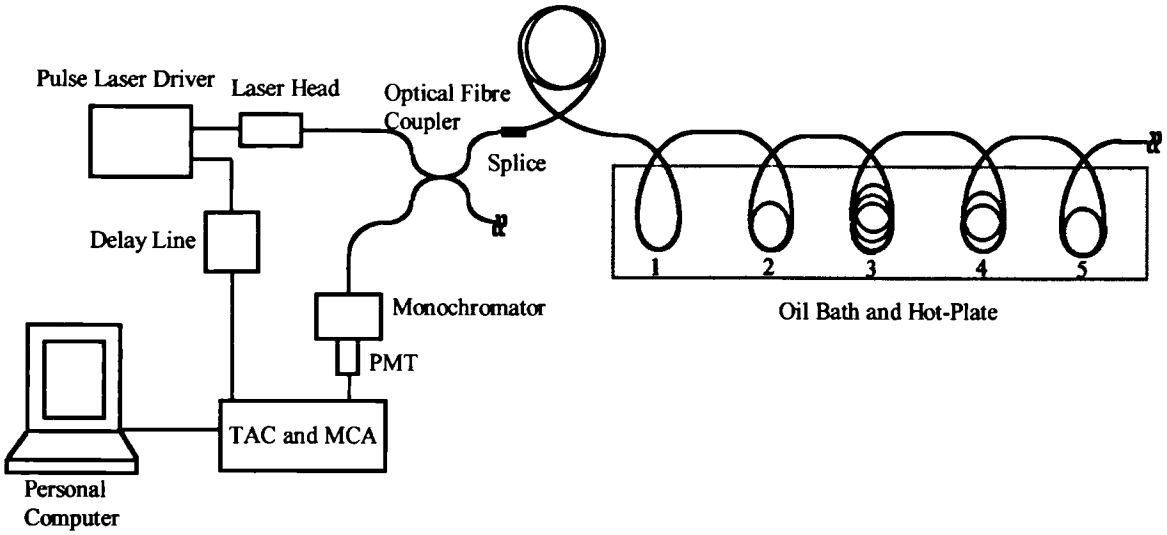

Figure 5. Experimental set up for high spatial resolution distributed optical fibre sensor. The lengths of the sensing fiber heated in section (1), (2), (3), (4), and (5) are 15cm, 25cm, 100cm, 50cm and 25cm, respectively. In the figure: PMT, photomultiplier tube; TAC, time-amplitude converter; MCA, multichannel analyser.

As the laser pulse propagates along the fibre, both antiStokes and Stokes Raman scattered photons are generated. A small fraction of these (0.5%) is guided back towards the launching end and is spectrally filtered by a 2 nm bandwidth monochromator to select the antiStokes or Stokes band. The separation of the peaks of the spontaneous Raman emission from the central wavelength of the laser is about 17 nm. The compact monochromator had a Czerny-Turner configuration, with F/3.9 and a focal distance of 74 mm. This monochromator was substituted at a later stage by a set of interference filters, as will be described in Sections 2.4 and 2.5.

Some of the spectrally filtered Raman scattered photons are then detected by a compact PMT with 4% quantum efficiency at 635 nm. Its photocathode was multialkali and the multiplication stage had a gain of $3 \cdot 10^5$. The transit time spread of the PMT was 280 ps (FWHM).

Both the PMT and the laser synchronisation signals feed a time-correlated single photon-counting board, which consisted of a constant fraction discriminator (CFD), a time to amplitude converter (TAC), an analogue to digital converter (ADC), and a multichannel analyser (MCA). The PMT pulses are discriminated in the CFD, which worked under the principle of subtracting a delayed version of the pulse and detecting the zero crossover. The time uncertainty of this operation is less than 100 ps even if the amplitude of the signal changes by a factor of 10. The discriminated PMT signal sets then the START of the voltage ramp in

the TAC. The TAC had a very short dead time (recovering time), 200 ns, which allowed count rates higher than 2 Mcounts·s^{-1}. The laser synchronisation signal STOPS the TAC ramp, and the final voltage is digitised by a 12 bit ADC. One important feature of the system was that the nonlinearities of the TAC and ADC characteristics were partially corrected by statistically dithering one with respect to the other. Finally, the content of the MCA memory address that corresponds to the ADC output is increased by one unit.

This mode of operation in which the scattered photon sets the START of the TAC and the laser synchronisation signal STOPS it is called "reversed mode" and allows higher count rates than normal operation. The reversed mode of operation, the short dead time of the TAC and the high laser repetition rate are essential to optimise the measurement time in a distributed temperature sensor.

2.3.2 Experimental results

In order to test the temperature sensing features of the system, five sections of fibre were looped and immersed in an oil bath (Figure 5). The lengths of the sections were 15 cm, 25 cm, 100 cm, 50 cm and 25 cm respectively. The last section was close to the end of the fibre. The laser pulse width was adjusted to be about 200ps. AntiStokes and Stokes backscattered photon distributions were measured for different temperatures of the oil bath. The temperature was increased from room temperature (20 °C) up to 115 °C in steps of 10°C. The measurement time for each temperature was 1 minute. Figure 6 shows the antiStokes traces that were obtained. The average count rate was 200 kcounts s^{-1} in the antiStokes channel and 500 kcounts s^{-1} in the Stokes channel.

2.3.2.a Raman scattering coefficient

The photon flux backscattered by the Raman effect into the antiStokes band is given by the OTDR formula (6). For our experiment, the total number of photons in the laser pulse ($\phi_{inc}\tau$) was roughly 10^8 (photons); α_{AS} would be the Raman scattering coefficient for an antiStokes band of 2 nm; and κ is the fibre capture fraction (0.5% in our case). Γ is a measure of the power throughput of the system that takes into account the launching efficiency into the fibre, the splitting ratio of the fibre coupler and the monochromator and fibre losses. Its value, 0.015, corresponds to an overall attenuation of 18 dB.

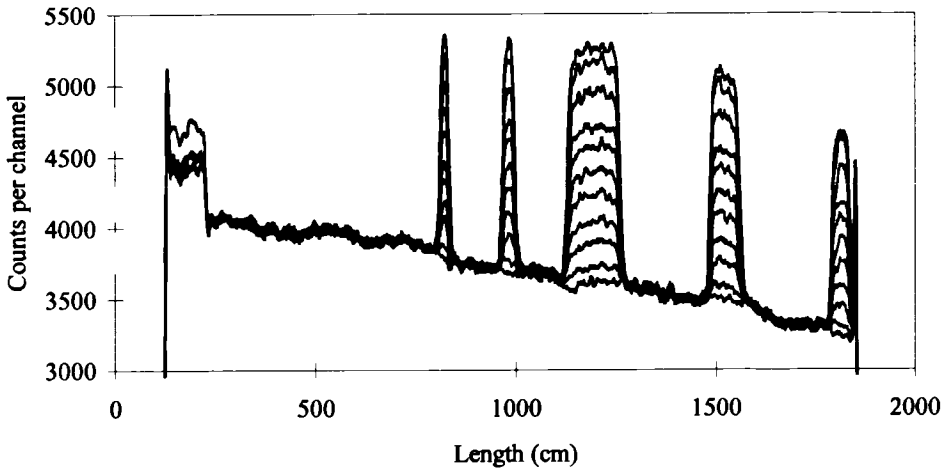

Figure 6. AntiStokes traces for several temperatures (20°C, 25°C, 35°C, 45°C, 55°C, 65°C, 75°C, 85°C, 95°C, 105°C and 115 °C).

As the number of counts per second in the antiStokes band ($\phi\eta$) was 200 kcounts s^{-1} and the detector quantum efficiency η is 4%, the flux of antiStokes photons ϕ was $5 \cdot 10^6$ photons s^{-1}. Substituting this value in equation (6), we calculate the antiStokes scattering coefficient, giving a value of $6 \cdot 10^{-6}$ m^{-1} (for a 2 nm spectral bandwidth). This is about three orders of magnitude lower than the Rayleigh scattering coefficient ($2.7 \cdot 10^{-3}$ m^{-1}).

It was observed that the ratio between the antiStokes and the Stokes signals was 0.35 instead of the theoretical 0.15. This is due to the differential spectral response of the various components of the system, mainly the PMT and monochromator and, also, to the cross-talk of Rayleigh backscattered light into the Stokes and antiStokes signals. It is interesting to note that the power of the backscattered signals was optimised for an asymmetric splitting ratio in the multimode fibre coupler. Multimode couplers behave as "non reciprocal" devices because the backscattered light can be guided in different modes compared to the forward propagating pulse.

2.3.2.b Pile-up effect and signal processing

Both antiStokes and Stokes traces showed a pronounced negative slope (Figure 6). This is due to two factors: losses along the fibre and the pile-up effect [34]. This latter effect arises

because, for each repetition of the experiment (excitation cycle), only one event is detected at most, so that the photons scattered at the front end of the sensing fibre have higher probability of being detected than those scattered at the back end (Section 2.2.2). If the overall detection probability per repetition of the experiment is very small, this effect is negligible. In our case, approximately one photon was detected for every ten laser pulses, which gives a relatively high detection probability per incident laser pulse (0.1). Consequently, the number of counts in one channel becomes dependent on the counts of all the channels that precede it.

The traces were processed in the following steps. First, we applied the pile-up correction described by equation (17) to both the antiStokes and Stokes traces. They were then digitally filtered (averaged over 8 cm) and corrected for losses by normalising the antiStokes trace with respect to Stokes. Finally, the normalised signal was filtered again (over 6 cm) to reduce the division noise and to obtain a spatial resolution of 10 cm. The differential losses between Stokes and antiStokes signals can be neglected for such a short range at moderate temperatures (see Section 2.4). Figure 7 shows the processed temperature distributions along the fibre. Some of the signal irregularity in the heated sections is due to temperature inhomogeneities in the oil bath.

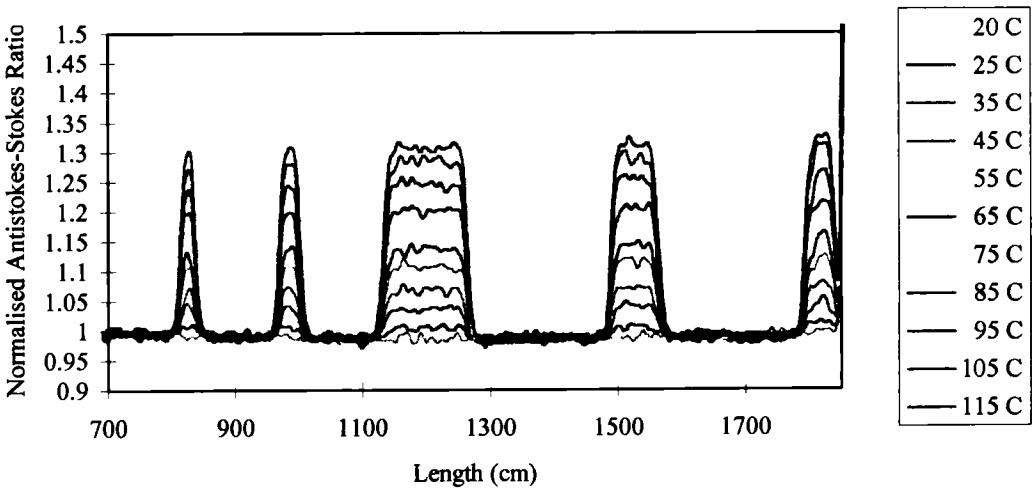

Figure 7. Normalised and processed antiStokes-Stokes ratio for several temperatures (20°C, 25°C, 35°C, 45°C, 55°C, 65°C, 75°C, 85°C, 95°C, 105°C and 115 °C).

2.3.2.c Spatial resolution

The theoretically expected spatial resolution of the system is given by the convolution of half the laser pulse width (because it is a backscattering arrangement), the spatial uncertainty corresponding to the transit time spread of the PMT (which in our case is 280 ps FWHM), and minor contributions from the time jitter in both the photon and synchronisation channels and from the nonlinearities of the TAC and ADC conversions. Dispersion effects within each of the Raman bands can be safely ignored for short lengths of fibre. The material dispersion at 635 nm is 230 ps/nm·km, which for a band of 2 nm and a length of 40 m (round trip) gives rise to a time spread of 18.4 ps. The modal dispersion of a typical graded index fibre, 125 ps/km, would give rise to 5 ps of time spread. These figures are negligible with respect to the rest of the time uncertainties of the system.

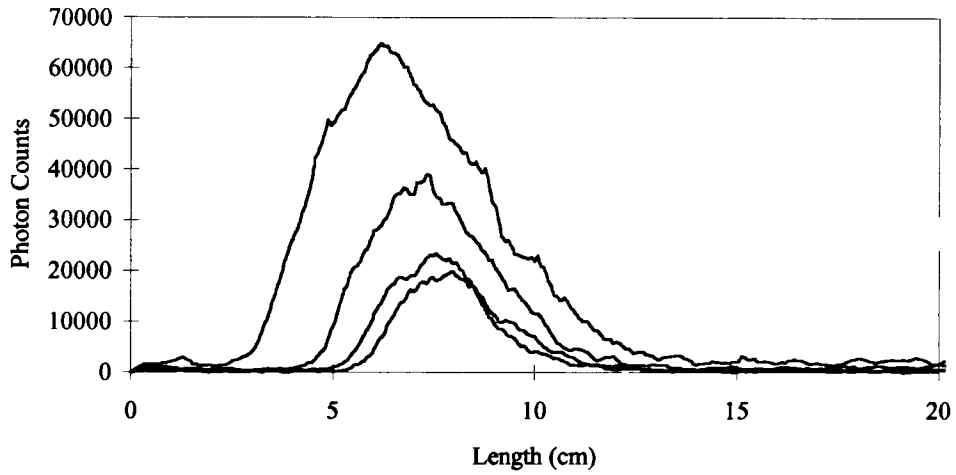

Figure 8. Response of the system to the reflected light from a reflective splice for several laser pulse widths ranging from 100 to 500 ps. The different curves correspond to estimated laser pulse widths of 100ps, 200ps, 300ps and 450ps.

A resolution better than 10 cm is expected. In order to measure the spatial resolution, the system was configured in an OTDR arrangement by removing the wavelength selective components and reducing the laser peak power. The impulse response function of the system was measured by monitoring the reflection from a slightly-reflective splice for the various pulse widths that our laser was able to produce (ranging from 100 to 500 ps). Figure 8 shows that the FWHM of the system response varies from 2.7 cm to about 5 cm. These responses match well the values expected from the convolution of the laser pulse widths with the transit time

spread of the PMT. The overall instrument time response (squared) is given by the sum of the squares of all the time uncertainties in the system. For short laser pulse widths, the instrument time response is limited by the transit time spread of the PMT to an approximate value of 280ps (which is equivalent to 2.8 cm FWHM spatial resolution). As the laser pulse widths become comparable to this value, the instrument impulse response broadens. For the longest pulses produced by the laser (estimated to be 450 ps), the spatial resolution was about 5 cm.

In the distributed temperature sensing experiments the pulse width of the laser was approximately fixed at 200ps and the traces were processed as previously explained. If the spatial resolution is defined as the rise time from 10% to 90% in an abrupt temperature step, then this transition occurs in approximately 10 cm for some of the heated sections. Figures 9 and 10, for example, show the evolution of the antiStokes-Stokes ratio along the 15 cm and 25 cm heated sections. The sharpness of the measured temperature transitions is also slightly reduced because the temperature evolution along the fibre for each heated section does not follow an ideal squared function as a result of temperature gradients inside the oil bath.

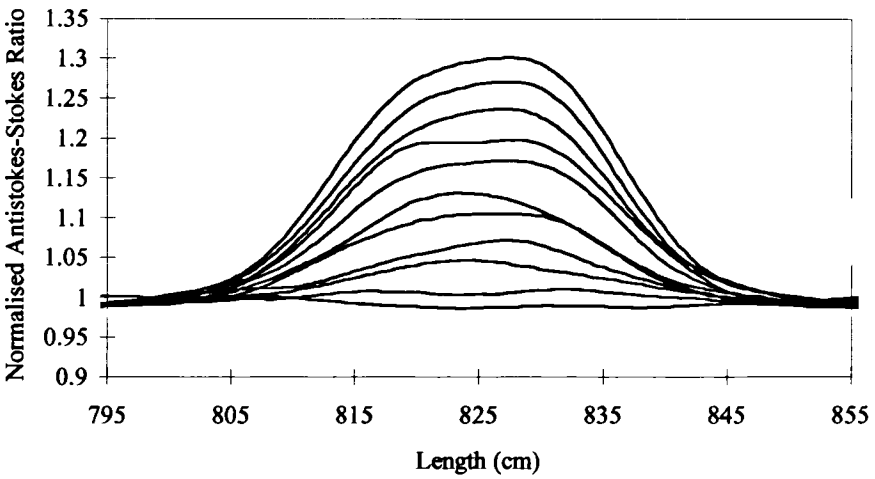

Figure 9. Zoom of the normalised AntiStokes-Stokes ratio in the 15 cm heated section (first section).

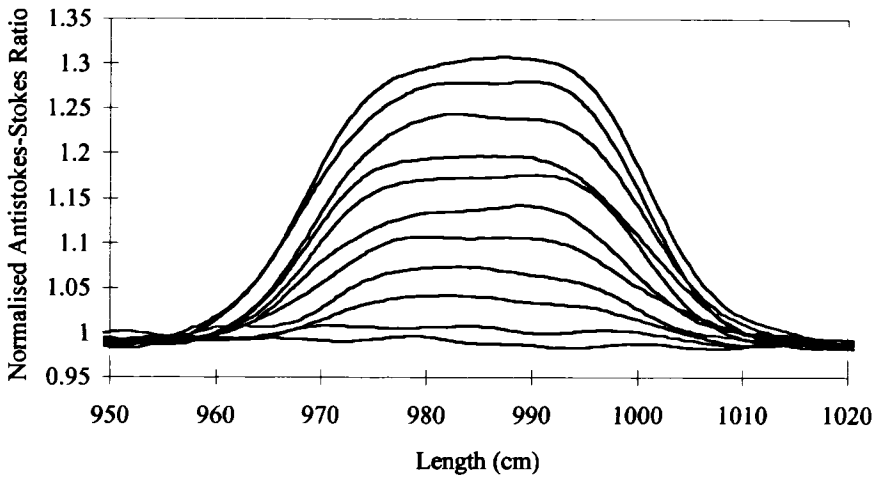

Figure 10. Zoom of the normalised AntiStokes-Stokes ratio in the 25 cm heated section (second section).

2.3.2.d Temperature resolution

The temperature resolution is limited by the signal-to-noise ratio in the different time channels. Our multichannel analyser (MCA) has 4096 channels (12 bits) so that, for an overall time range of 200 ns (20m), each time slot corresponds to 0.05 ns (0.5 cm). We can group the channels in sets of 20 adjacent ones (adding their counts) while still retaining a spatial resolution of 10 cm. This is equivalent to a smoothing of the trace, in which time resolution is traded against signal-to-noise ratio. In our experiment, after 1 minute of measurement time with a laser repetition rate of 5 MHz, the number of counts in a channel was $4 \cdot 10^3$, so that the number of counts which correspond to a 10 cm section (20 channels) would be $8 \cdot 10^4$ counts. Assuming that the number of counts in these sets of channels can be associated with Poisson random variables, the signal-to-noise ratio ($N\overline{m}$) also will be $8 \cdot 10^4$ (49 dB).

To determine the temperature resolution achieved experimentally, we selected the central 80 cm of the 1m heated section and calculated, for each temperature, the mean and standard deviation of the normalised antiStokes-Stokes ratio. The maximum standard deviation for all the traces was 0.6% while the average of the standard deviations was 0.45%. As the temperature sensitivity exhibited by this ratio was 0.33 $\%^{\circ}C^{-1}$, the temperature resolution in this temperature range is 2°C.

The experimental temperature sensitivity of the antiStokes-Stokes ratio (0.33 $\%^{\circ}C^{-1}$) is lower than the $0.7\%^{\circ}C^{-1}$ theoretically expected due, probably, to cross-talk from the Rayleigh backscattered light into the antiStokes and Stokes signals. The achieved temperature resolution translates into a signal-to-noise ratio of 2.7 10^4 (44 dB), which is slightly lower than that ideally predicted by Poisson statistics (49 dB). Other sources of noise such as dark counts and after-pulse effects in the photomultiplier, nonlinearities in the TAC or ADC conversion, or laser spectrum broadening and insufficient Rayleigh-scattered light filtering, could be responsible for this reduction in the signal-to-noise ratio.

2.3.3 SYSTEM PERFORMANCE: FIGURE OF MERIT FOR TC-SPC DART SENSORS

The performance of a DART system is described in terms of four quality parameters: spatial resolution (δz), temperature resolution (δT), measurement time (t) and total sensor length (L). We can define a Figure of Merit (F_m) for a DART system which involves these four performance parameters:

$$F_m = \frac{L}{(\delta z\, \delta T)^2\, t} \tag{18}$$

so that the higher F_m is, the better the performance attained by the system. Systems with equal F_m have equivalent performance except for a trade off among the former parameters. Equation (18) shows that the spatial resolution can be traded off linearly with the temperature resolution but quadratically with respect to the other two quality parameters: measurement time and total sensor length. If we fix a spatial resolution (δz) for the DART, the Figure of Merit (F_m) will depend only on the features of the optical and electronic components of the system. This dependence, which is derived in the Appendix by calculating the number of averages needed to improve the measurement signal-to-noise ratio so as to achieve the specified temperature resolution, can be expressed as a function of three design parameters (p, t_d, and S_T) (Appendix):

$$F_m = \frac{S_T^2\, p}{1 + p\, \delta z\, t_d} \tag{19}$$

where p is a measure of the optical power throughput of the system and is proportional to the detected flux of antiStokes photons ($p = \phi_{inc}\, \alpha_{AS}\, \kappa\, \Gamma\, \eta$). S_T is the temperature sensitivity of the antiStokes-Stokes ratio, and has a value at room temperature of 0.7 %°C^{-1} . t_d is the dead time for the electronics, i.e. the time needed by the system to recover after the detection of a photon. Figure 11 represents F_m as a function of p with t_d as a parameter for a fixed δz. It can be seen that t_d limits the Figure of Merit, setting a maximum value which does not depend on the power throughput parameter p. Equation (19) holds for the optimum system design, where the only source of noise associated with the measurement is given by the photon statistics (Section 2.2). In practice, there exist additional sources of noise and, therefore, higher values of the p parameter than those predicted by (19) are needed to achieve a system performance described by the figure of merit F_m.

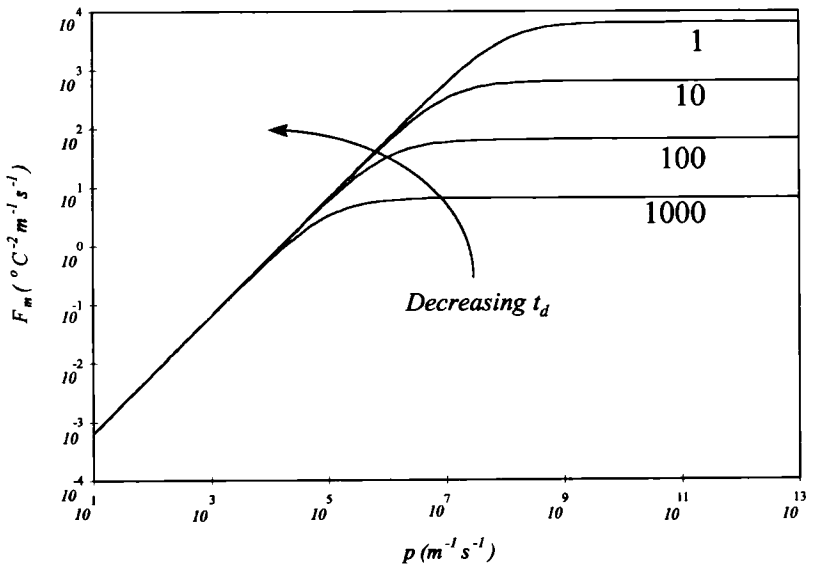

Figure 11. Saturation of the Figure of Merit as a function of p with $\delta z \cdot t_d$ as a parameter. The values of the product $\delta z \cdot t_d$ corresponding to the different curves (1, 10, 100 and 1000) are in cm·μs.

Let us compare now the present system with previously reported [47,48] TC-SPC based DART systems. This comparison is illustrated in Figure 12. Both of the previous systems have an electronics dead time t_d of 10μs, but the system in reference [48] attains higher spatial resolution (10 cm). Due to the low values of the parameter p, neither system is limited by the electronics dead time. Their Figures of Merit are 10^{-1} °C^{-2}m^{-1}s^{-1} [47] and 10^{-2} °C^{2}m^{-1}s^{-1} [48] respectively. The system presented here was optimised by increasing the value of p and

reducing the electronics dead time (t_d =200 ns) to delay the saturation of F_m. The Figure of Merit achieved, 8 $°C^{-2}m^{-1}s^{-1}$, is two to three orders of magnitude better than previously reported systems.

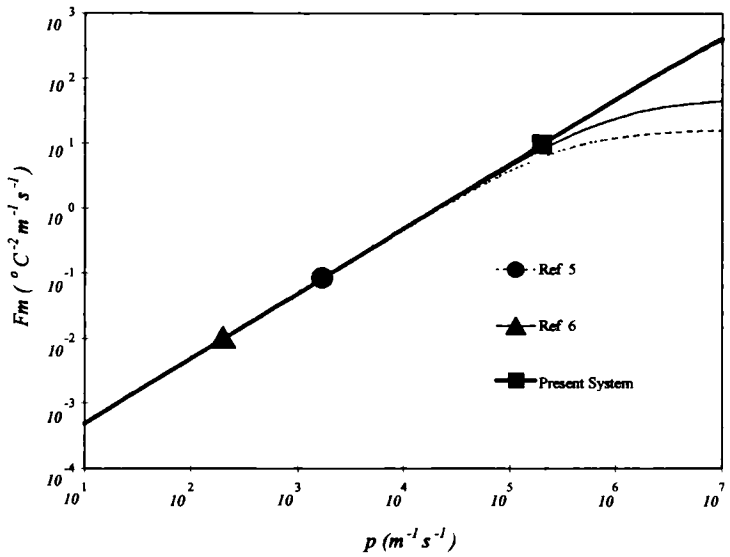

Figure 12. Comparison of the Figure of Merit for three reported TC-SPC DART sensors.

To improve the system performance further, the way to proceed is to increase the value of p while ensuring that the electronics dead time t_d does not saturate F_m. However, this procedure cannot continue indefinitely because the detection probability of a photon per launched pulse increases with p. If this probability becomes too high, the system will not operate in the single photon counting regime, causing important distortions in the spatial evolution of the antiStokes and Stokes traces (pile-up effect). These distortions can be partially corrected with the pile-up correction algorithm described in (17). However, the use of pile-up correction algorithms to process the traces induces an additional source of noise which is small as long as the photon detection probability per excitation cycle is kept at a moderate value (<0.2) [34]. Our system, which has a detection probability per pulse of 0.1, is near the optimum performance which can be expected from a DART sensor based on the TC-SPC technique.

2.4 HIGH TEMPERATURE TEST OF THE HIGH SPATIAL RESOLUTION DISTRIBUTED TEMPERATURE SENSOR

In the last section we have demonstrated an improved DART sensor based on TC-SPC that operated in a temperature range that extended from room temperature to 115 °C. This reduced temperature range was mainly due to the acrylate coating that provided mechanical reliability to the fibre. Extension of the temperature range to higher temperatures requires the use of specially coated fibres. In this section, we investigate the performance of the DART TC-SPC system for high temperature measurements. Two main problems are found as the operating temperature is increased. The first one, inherent to Raman thermometry, is a progressive decrease in the temperature sensitivity, which translates into a reduced temperature resolution. The second one is related to the special high temperature resistant coatings, which are used to provide mechanical protection for the fibre. In particular, we will study the temperature dependence of losses in carbon and gold coated fibres and show how differential losses between the antiStokes and Stokes channels act as an added source of errors in temperature measurements [3-5].

2.4.1 Experiments

The experimental arrangement, shown in Figure 13, was very similar to that described in Section 2.3.1. The main difference is the use of interference filters, instead of the compact monochromator, to limit the laser spectral emission and to filter the antiStokes and Stokes scattered photons. The interference filters had a band-pass (FWHM) of 10 nm and provided a rejection of 30 dB at a wavelength separation equivalent to the Raman shift. Several of these filters were stacked together when necessary. This design improved the temperature sensitivity, which approached to that theoretically expected. Also, the present system incorporated a signal router that permitted simultaneous measurement of the Stokes and antiStokes channels. The fibres studied, which had similar optical properties to that previously used, were protected by special coatings that could withstand high temperatures. A hot plate was used to control the temperature of a few metres of these fibres.

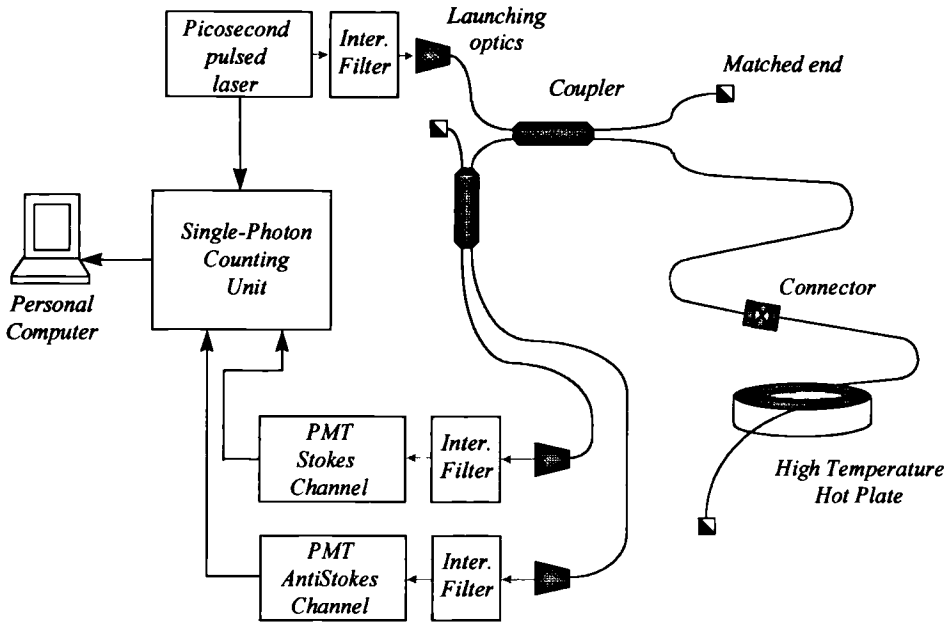

Figure 13. Experimental set-up for high spatial resolution distributed optical fiber sensor.

Two specially coated fibres were tested: carbon-coated and gold-coated. Both coatings belong to the family of non-polymeric hermetic coatings. Hermetic coatings improve the mechanical reliability of fibres by protecting them from moisture attacks that would cause the growth of flaws and, consequently, material fatigue [49]. These coatings also withstand higher temperatures than polymeric coatings. The carbon-coated fibre tested had a thin layer of glassy carbon of less than 1 μm thickness. A thermo-gravimetric analysis carried out on this fibre [50] showed that the coating remained stable in an inert atmosphere at temperatures as high as 600°C. However, oxidation of the coating occurs if the purity of the atmosphere is not controlled adequately. Metal coatings, on the other hand, have been reported to increase the fibre mechanical reliability compared to non-metallic coatings [51]. The gold coating, in particular, is very appropriate for high temperature applications because it withstands temperatures above 700°C [52]. Metal coatings are usually thicker than carbon coatings. For our fibre, the thickness of the gold coating was about 20 μm.

Sections of the two specially coated fibres were heated from room temperature (24°C) to a very high temperature (550 °C) and then cooled down to room temperature again. The evolution of the antiStokes and Stokes signals was monitored along this temperature cycle. From these

measured traces, the changes of the fibre losses due to thermal effects were calculated. We proceeded as follows. First, we corrected the traces against the pile-up effect [34], which is inherent to the TC-SPC technique and would translate into errors in the loss measurement (Section 2.2.2 and 2.3.2.b). We slightly modified the simple correction formula (17) to accommodate it to the present multiplexing scheme. In the present case, the correction formula for the number of counts in one channel (time-slot) has to consider the total number of both Stokes and antiStokes photons counted in all the previous channels. The only modification needed in (17) is the inclusion of an extra term in its denominator to account for the extra photons counted in the complementary Raman scattering band. The correction was very small because we deliberately reduced the laser peak power to minimise this effect. Then, we calculated the fibre loss coefficients from the slope of the corrected traces. Taking into account that the Raman backscattered photons have a different wavelength than that of the laser pulses, two effective loss coefficients, $\alpha_{as}^{eff}(T)$ and $\alpha_{s}^{eff}(T)$, were defined for the antiStokes and Stokes traces respectively:

$$\alpha_{as}^{eff}(T) = \frac{1}{2}\left(\alpha(\lambda_{as}, T) + \alpha(\lambda_{l}, T)\right)$$
$$\alpha_{s}^{eff}(T) = \frac{1}{2}\left(\alpha(\lambda_{s}, T) + \alpha(\lambda_{l}, T)\right) \qquad (20)$$

where $\alpha(\lambda_{as},T)$, $\alpha(\lambda_{l},T)$ and $\alpha(\lambda_{s},T)$ are the fibre loss coefficients at the antiStokes, laser and Stokes wavelengths respectively, and T stands for temperature.

A length of 10 m of the carbon-coated fibre was thermally cycled as previously discussed. Although the coating oxidised as expected, the bare fibre survived the temperature cycle. The antiStokes traces can be seen in Figure 14. The thicker lines in Figure 14 correspond to traces measured when the fibre was cooling down. The effective antiStokes losses of the fibre were calculated from these traces and can be seen in Figure 15. These losses were 10 dB/km at room temperature and only increased slightly during the heating stage. They remained almost constant along the cooling stage.

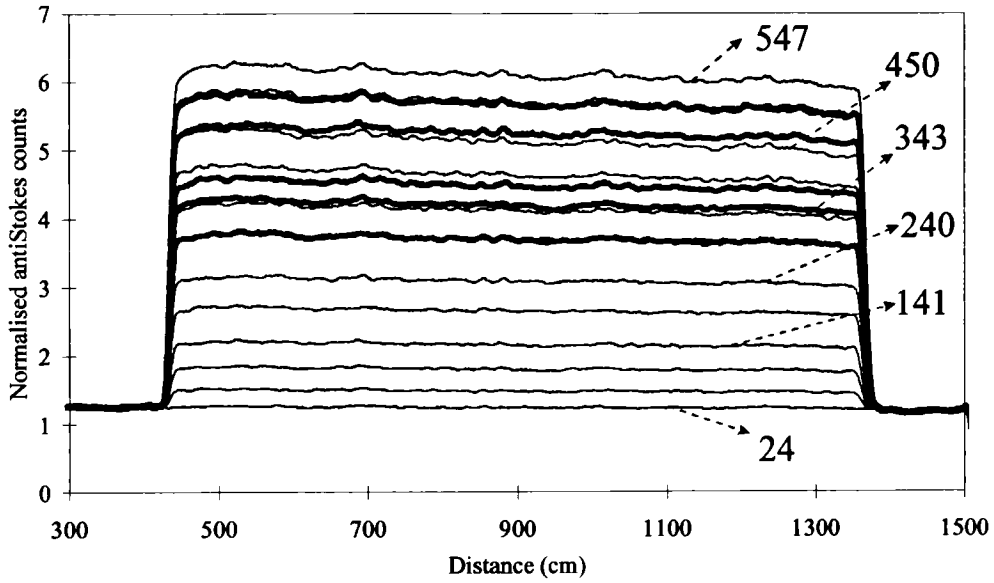

Figure 14. Evolution of the antiStokes signal in the carbon-coated fibre when it is heated from room temperature to 550 °C and cooled back to 300 °C. The thicker lines correspond to the cooling stage. Temperatures are in °C.

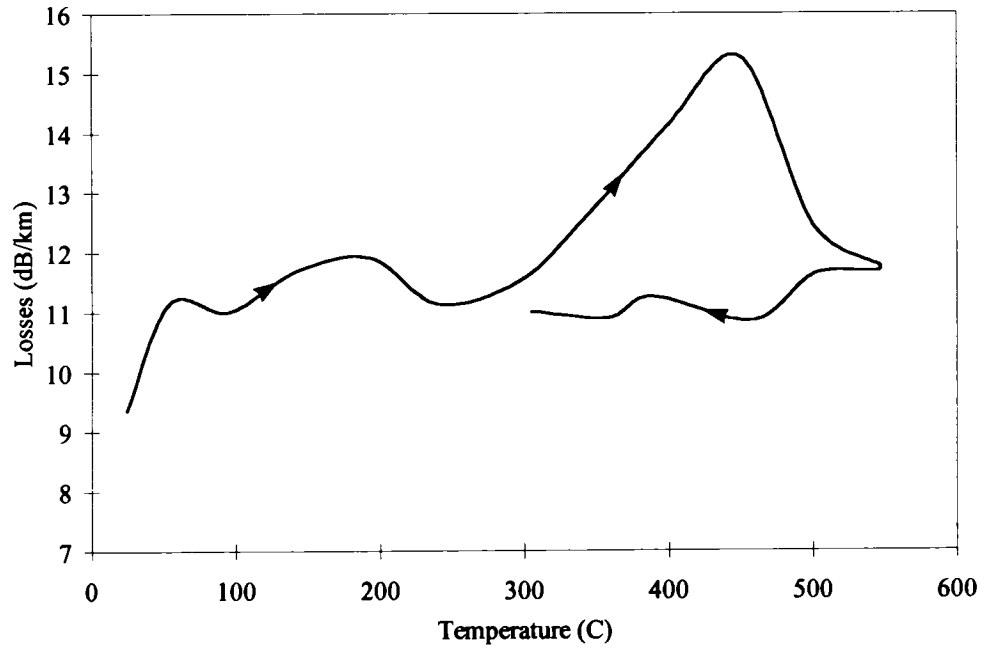

Figure 15. Evolution of effective antiStokes losses (α_{as}^{eff}) with temperature for carbon-coated fibre.

The gold-coated fibre was 6 metres long and behaved very differently. This fibre showed high effective losses at room temperature (50 dB/km) and it was found that the losses were very temperature and wavelength dependent. The antiStokes traces for one temperature cycle are shown in Figures 16 and 17. Figure 16 shows the heating part of the cycle while Figure 17 shows the cooling stage. It can be appreciated that the slope of the traces changed substantially in the initial part of the heating stage due to an increase in the fibre losses. At high temperatures, however, the traces became more horizontal showing a reduction of losses (Figure 16). The losses remained fairly constant in the cooling stage (Figure 17). According to data supplied by the gold-coated fibre manufacturer, as the fibre is heated microbending losses are initially enhanced due to the difference in thermal expansion coefficients between gold and silica. At high temperatures, however, gold enters the plastic regime, releasing stresses, and reducing the microbending losses. This behaviour can be appreciated in Figure 18, which shows the evolution of losses with temperature. A second temperature cycle showed a similar trend, but the maximum losses during the heating stage were reduced from 120 dB/km to 60dB/km. The coating resisted well the two temperature cycles.

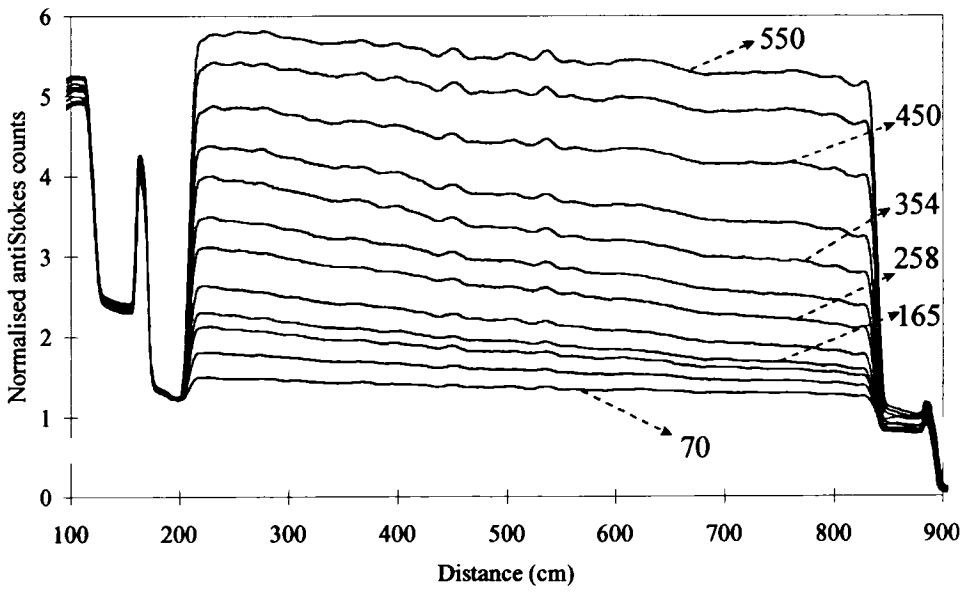

Figure 16. Evolution of the antiStokes signal in the gold-coated fibre when it is heated from room temperature to 550 °C. Temperatures are in °C.

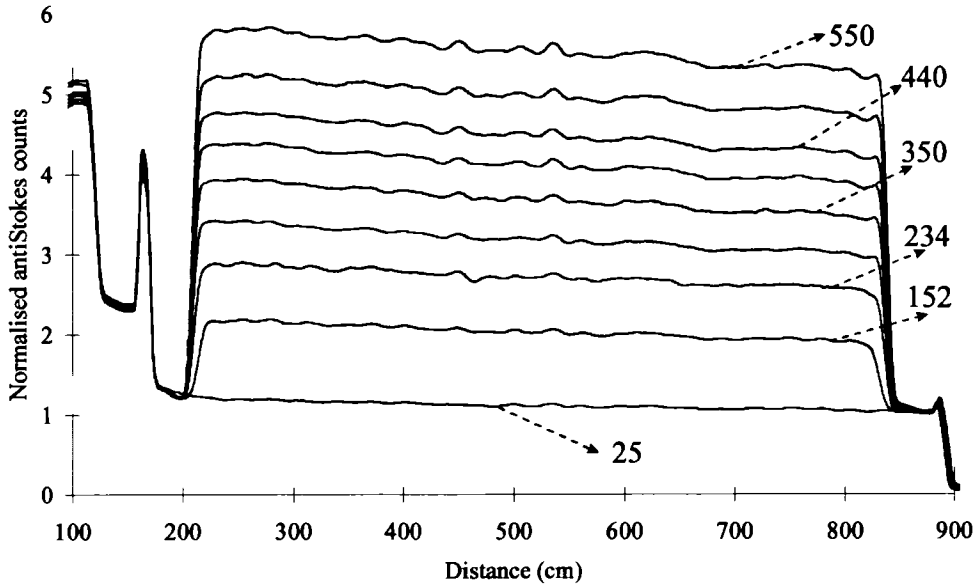

Figure 17. Evolution of the antiStokes signal in the gold-coated fibre when it is cooled from 550°C to room temperature. Temperatures are in °C.

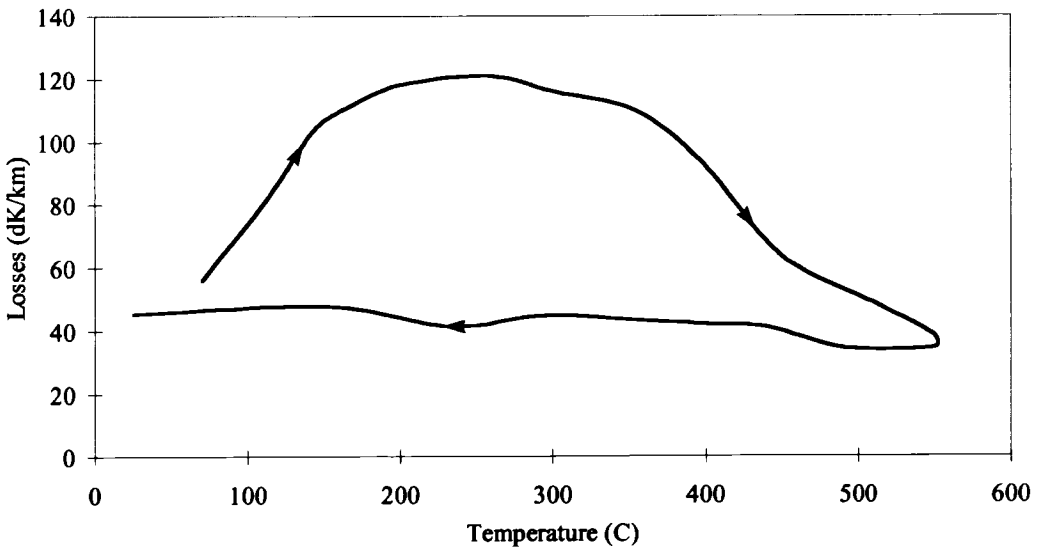

Figure 18. Evolution of effective antiStokes losses (α_{as}^{eff}) with temperature for the first cycle of the gold-coated fibre.

The differential losses between antiStokes and Stokes traces were calculated. Using equation (20), we define the effective differential losses as:

$$\Delta\alpha = \alpha_{as}^{eff} - \alpha_{s}^{eff} = \frac{1}{2}\left(\alpha(\lambda_{as}) - \alpha(\lambda_{s})\right) \qquad (21)$$

For the carbon-coated fibre, the differential losses $\Delta\alpha$ remained below 1-2 dB/km (our measurement resolution) for the whole temperature range, which means that their contribution to temperature errors is small. For the gold-coated fibre, it was found that $\Delta\alpha$ has a value of -4 dB/km at room temperature, indicating that the Stokes signal suffered more loss than the antiStokes. This is not surprising because microbending losses are very wavelength dependent. At 550 °C the differential loss tends to 0 dB/km. The evolution of this differential loss during the first cycle follows the pattern shown in Figure 19. Its fluctuation from minimum to maximum can be as large as 17dB/km. However, during the second cycle this differential loss was considerably reduced, remaining below 4-5 dB/km over the full temperature range and approaching 0 dB/km at high temperatures (Figure 19). The effect of differential loss on the temperature resolution of the system will be discussed in the next paragraph.

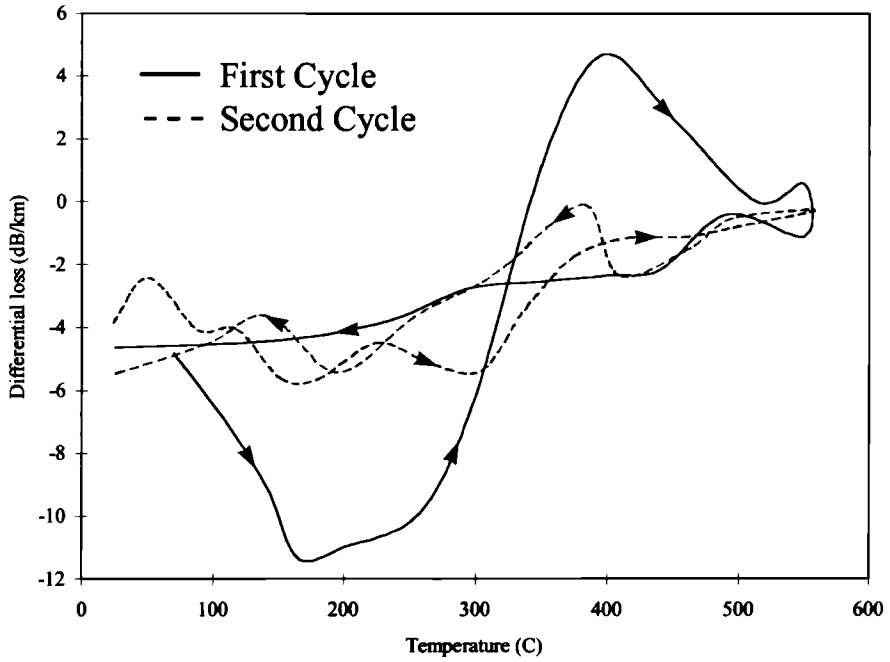

Figure 19. Effective differential losses ($\Delta\alpha$) between antiStokes and Stokes signals for the first (-) and second (--) temperature cycles of the gold-coated fiber.

2.4.2 Temperature resolution in high temperature measurements

The performance of a DART system based on the TC-SPC technique can be quantified through the figure of merit F_m (18). The figure of merit is useful to examine the degradation of the performance of TC-SPC based DART systems when the operational temperature is increased. In equation (19), both S_T and p are temperature dependent. On one hand, the temperature sensitivity of the antiStokes signal S_T (5) is given by the fractional change of the phonon population with temperature. S_T is, in theory, inversely proportional to the square of the absolute temperature, decreasing from 0.7% at room temperature to 0.15% at 550°C. The evolution of the measured sensitivity during the second temperature cycle of the gold-coated fibre, which agreed with the theoretical prediction, is shown in Figure 20. On the other hand, the p parameter is proportional to the antiStokes scattering coefficient, which depends on temperature through the Bose-Einstein distribution for phonons (3). Theoretically, the ratio between the antiStokes scattering coefficient at 550°C and at room temperature should be 6. The results obtained for the carbon-coated fibre (Figure 14), and for the gold-coated fibre (Figures 16 and 17), show good agreement with this value.

From equations (18) and (19), it can be observed that the deterioration in temperature resolution (δT) due to the decreased sensitivity (S_T) at high temperatures is partly compensated by the enhanced signal level for the antiStokes emission (p). If the rest of the parameters are kept fixed, the temperature resolution should degrade by a factor of 2 at 550°C compared to room temperature. We have measured the evolution of the DART temperature resolution for the second temperature cycle of the gold-coated fibre (Figure 20). For temperatures below 150°C, a temperature resolution of 2°C was achieved with 10 cm spatial resolution for a measurement time of 4 minutes. The temperature resolution was reduced to 4.5 °C at 550 °C as expected from the previous discussion. Consequently, the figure of merit F_m decreases by a factor of 5 at high temperatures. The collection time in present experiments is longer than that reported in previous experiments, 1 minute, due to our attempt to reduce the system power throughput to minimise the pile up effect.

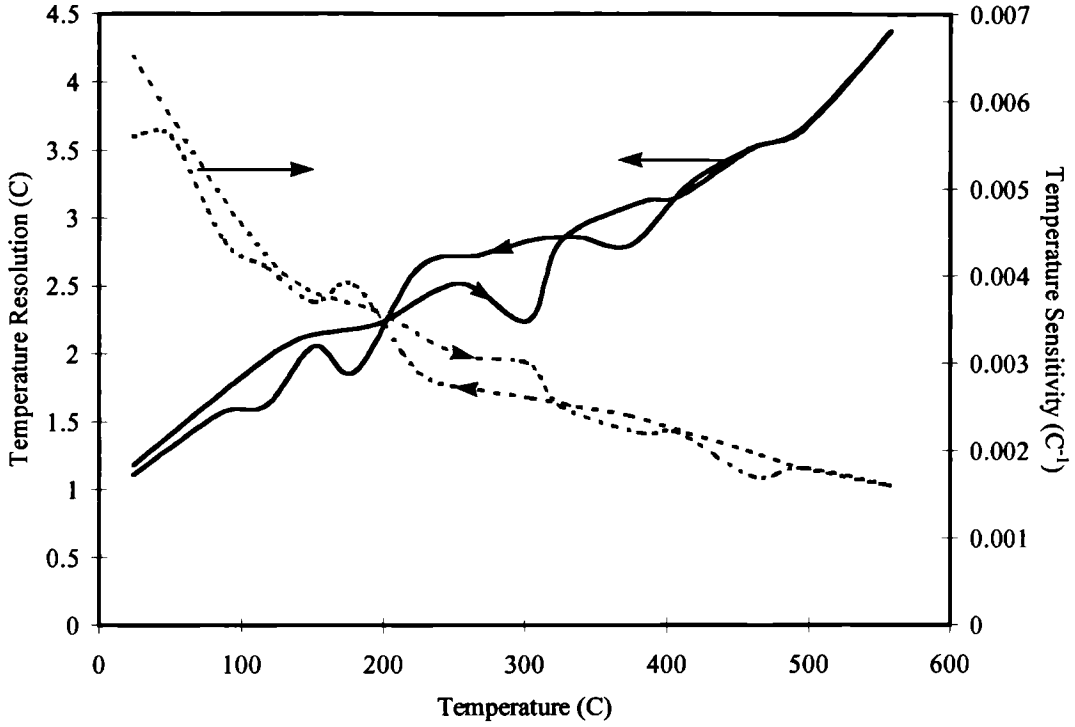

Figure 20. Evolution of the temperature resolution (δT) and the antiStokes temperature sensitivity (S_T) for the second temperature cycle of the gold-coated fiber.

The second main source of temperature errors is the variation of the antiStokes-Stokes differential losses with temperature. DART systems normalise the antiStokes traces with respect to the Stokes ones to correct against common losses along the fibre. As we have seen, differential losses can be important in gold-coated fibres. For a single-ended measurement, the error in the temperature measurement due to this effect can be expressed as:

$$\delta T = 0.46 \frac{\Delta\alpha(\mathrm{dB/km})L(\mathrm{km})}{S_T} \qquad (22)$$

where L is the sensing length, S_T is the temperature sensitivity and $\Delta\alpha$ the effective antiStokes-Stokes differential losses defined in (21). This effect can become predominant. If we assume, for example, 10 dB/km for the differential loss, a temperature error of 5°C could result from (22) for a sensing length of only 5m. However, our experiments show that the differential losses are considerably reduced if the gold-coated fibre is annealed, giving rise to an improved temperature accuracy. It should be mentioned that the differential loss problem could be

overcome with a more involved double-ended measurement system with a small section of fibre at a reference temperature. However, access to both ends of the sensing fibre is required in this case and the advantages of a single-ended measurement would be lost. Also, a dual wavelength system design could overcome the differential loss problem. In this case, access to only one end of the fibre would be necessary at the expense of a more complex system with two laser sources.

2.5 ZERO DEAD-ZONE OTDR WITH HIGH SPATIAL RESOLUTION

Optical Time Domain Reflectometry (OTDR) [53-55,23] is an important diagnostic tool for location of faults, mapping losses, or accurately locating components along fibre-based optical networks. However, present commercial systems suffer from the existence of dead-zones along the network due to intense Fresnel reflections generated by connectors or other optical components. The large difference of power between these reflections and the Rayleigh backscattered light (around 50 dB) gives rise to saturation of the receiver and, consequently, to a dead-zone equivalent to the receiver's recovery time. This problem can be severe in short haul applications with a large density of optical components, such as local area networks in buildings or vehicles and sensor arrays for smart structures. In this section, we show that the Time-Correlated Single Photon Counting (TC-SPC) technique overcomes the dead-zone limitation by monitoring the Spontaneous Stokes Raman Emission (SSRE) to avoid the intense Fresnel reflections [6,7].

The use of the TC-SPC technique for OTDR applications offers important advantages. Firstly, the high sensitivity of photon-counting detection [41,39,44] permits a considerable improvement in the OTDR loss budget. Secondly, very high spatial resolution can be achieved when TC-SPC is implemented with picosecond lasers and fast single-photon detectors [45]. Minimum dead-zone OTDR measurements have been reported using TC-SPC by attenuating the optical signals to avoid the distortions introduced by strong Fresnel reflections [56]. However, this results in a significant reduction of the signal to noise ratio for the Rayleigh signal and requires a deconvolution of the OTDR traces in the vicinity of the reflection peaks. As the spontaneous Raman scattering is proportional to the energy of the pulse of light propagating along the optical network, SSRE could be used instead of the Rayleigh scattering in an OTDR scheme. This would only introduce a small error in the loss measurement of 0.0035 dB/°C due to the SSRE temperature sensitivity. Spectral selection of the SSRE with an optical band-pass filter leads to a complete rejection of both the Fresnel reflected and the Rayleigh backscattered light, solving the dead-zone problem.

2.5.1 System description

The experimental arrangement is shown in Figure 21. Laser pulses from a gain-switched semiconductor laser operating at 635 nm are filtered to limit their spectrum and are then launched into a fibre-based optical network through a fibre coupler. Their pulse width was set

to the minimum pulse width that the laser could produce (about 100 ps FWHM) and their peak power was 24.7 dBm. The optical network consisted of several patch cords of multimode graded-index fibre joined with mechanical splices. As the laser pulse propagates along the network, some photons will be scattered due to the Rayleigh or Raman scattering mechanisms and some others will suffer Fresnel reflections. Part of the scattered and reflected photons are recaptured by the fibre and guided back towards the launching end, where they are divided into two channels. The Fresnel channel attenuates the photon flux before detection by a photomultiplier (PMT). The Stokes channel spectrally filters the photon flux by means of four stacked interference filters prior to detection by a second PMT. Each interference filter has a bandpass of 10 nm centered at 656 nm to match the spectrum of the SSRE and also to provide a rejection of 30 dB at the central wavelength of the laser. The remainder of the system is as described in Section 2.3.1. By repetitive measurements, a histogram of number of counts (detected photons) versus time can be built for both the Fresnel and the SSRE signals.

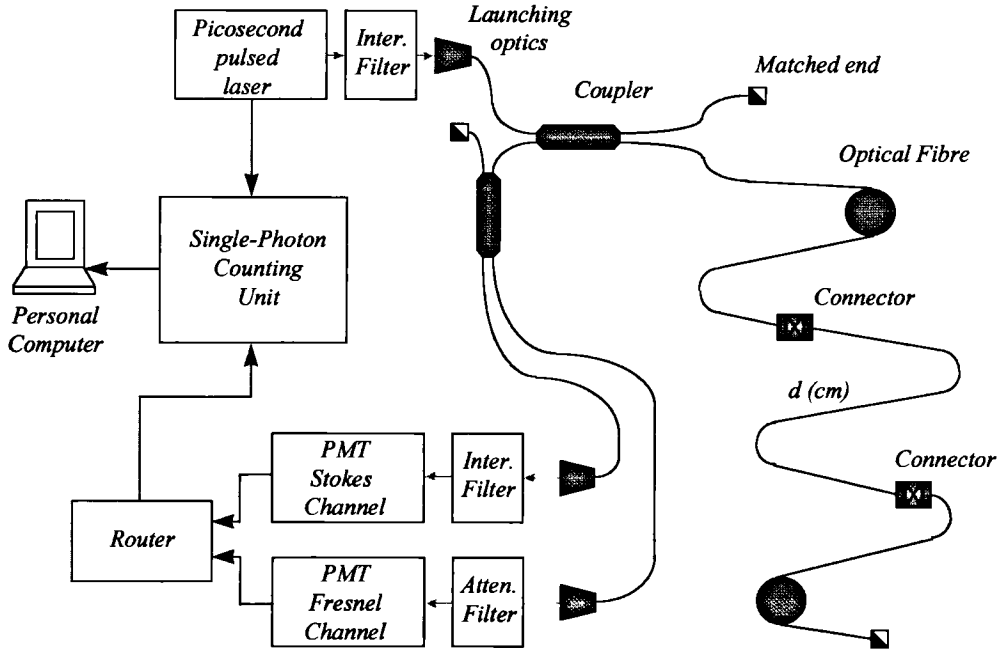

Figure 21. Experimental set-up of the OTDR system.

The SSRE is 20 to 30 dB weaker than the Rayleigh scattering in optical fibres. This will translate into a reduced OTDR loss budget. To assess the practicality of the proposed system, we have to evaluate the signal levels available and also the noise limitations. The photon fluxes (photons·s^{-1}) in the Stokes and Fresnel channels, $P_{S(or\,F)}$, are given by the equations:

$$P_{S(or\,F)} = P_i\, C_{S(or\,F)}\, L^2\, K_{S(or\,F)} \qquad (23)$$

where P_i is the peak photon flux of the laser pulse. $C_{S(or\,F)}$ are the losses inside the OTDR instrument due to filters, couplers and launch optics. C_S was -25.7 dB and C_F was -13.7 dB. L is the one-way loss along the optical network from its beginning until the point at which the SSRE or the Fresnel reflection is detected. K_S measures the efficiency of the generation and capture of SSRE [1] and its value was -85.3 dB. K_F is the Fresnel reflectivity of the monitored point. The Stokes and Fresnel photon fluxes are detected by two PMTs with a quantum efficiency η, giving rise to photon count-rates $R_{S(or\,F)}$ $(=\eta P_{S(or\,F)})$. After N repetitions of the measurement, the number of counts in a channel corresponding to a time interval τ will be $N\tau R_{S(or\,F)}$.

The TC-SPC technique is quantum noise limited except for the noise contribution of a small additional independent count-rate (R_B) due to dark events and background-light detection (Section 2.2.2). Assuming that all of these random processes follow Poisson statistics, the signal-to-noise ratio achieved after N repetitions of the measurement with a time resolution τ will be (14):

$$SNR = N\,\tau\,\frac{R_{S(or\,F)}^2}{R_{S(or\,F)} + R_B} \qquad (24)$$

The maximum sensitivity of the system is calculated by equating the SNR to unity in (24) and then finding the minimum detectable count-rate $R_{S(or\,F)min}$. If sufficient repetitions N of the measurement are allowed, R_B becomes predominant in the denominator ($R_B >> R_{S(or\,F)min}$). The calculated minimum count-rate $R_{S(or\,F)min}$ translates into a corresponding minimum photon flux before detection $P_{S(or\,F)min}$. The substitution of $P_{S(or\,F)min}$ in (23) permits the calculation of the loss budget L for the system.

2.5.2 Experiments

Three experiments were carried out to evaluate the performance of the system. The first experiment was intended to assess its spatial resolution. The time resolution of our TC-SPC instrument has already been discussed in 2.3.2.c. The two parameters commonly used to

specify the spatial resolution of OTDR systems are the two-point resolution and the single-point spatial resolution. The two-point spatial resolution is defined as the minimum distance between two adjacent reflective points that the system is able to resolve. The one-point spatial resolution refers to the uncertainty in the location of a single reflective point. We monitored the response of the Fresnel channel as the distance *d* between the two mechanical splices (Figure 21) was progressively reduced. Figure 22 shows that one centimetre two-point resolution is achievable. Also, it can be observed in this figure that a reflective event can be resolved along the fibre with millimetre one-point resolution.

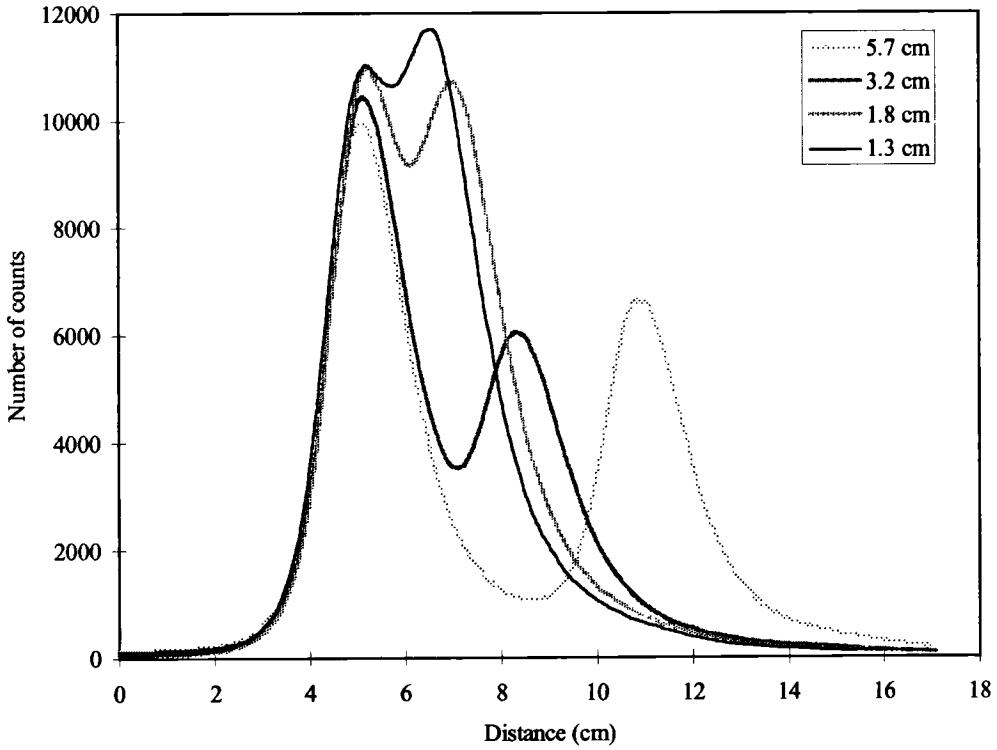

Figure 22. Fresnel traces for testing two-point spatial resolution.

The aim of the second experiment was to show that the dead-zone of this OTDR is negligible in the presence of Fresnel reflections. The total length of fibre used in this experiment was 5 m and the measurement time was one minute. The distance between the two mechanical splices was set to 30cm. The first splice was deliberately poorly matched in order to produce a Fresnel reflected signal in excess of -30 dB. The second splice was matched, but misaligned to enhance the losses. Figures 23 and 24 show the Fresnel and Stokes channels for different connection losses in the splices. In all the cases considered, the Stokes channel resolved the losses in the

second splice in spite of the strong Fresnel reflection in the first one. It is interesting to note that the Stokes trace exhibits a peak in the first splice due to the Fresnel reflection of the forward scattered Stokes photons which copropagate with the laser pulse. This effect does not produce a dead-zone because the power of the reflected and backscattered Stokes photon fluxes are comparable. However, it distorts the traces in a region which extends less than 10 cm. Deconvolution of the traces could be performed to correct for this effect.

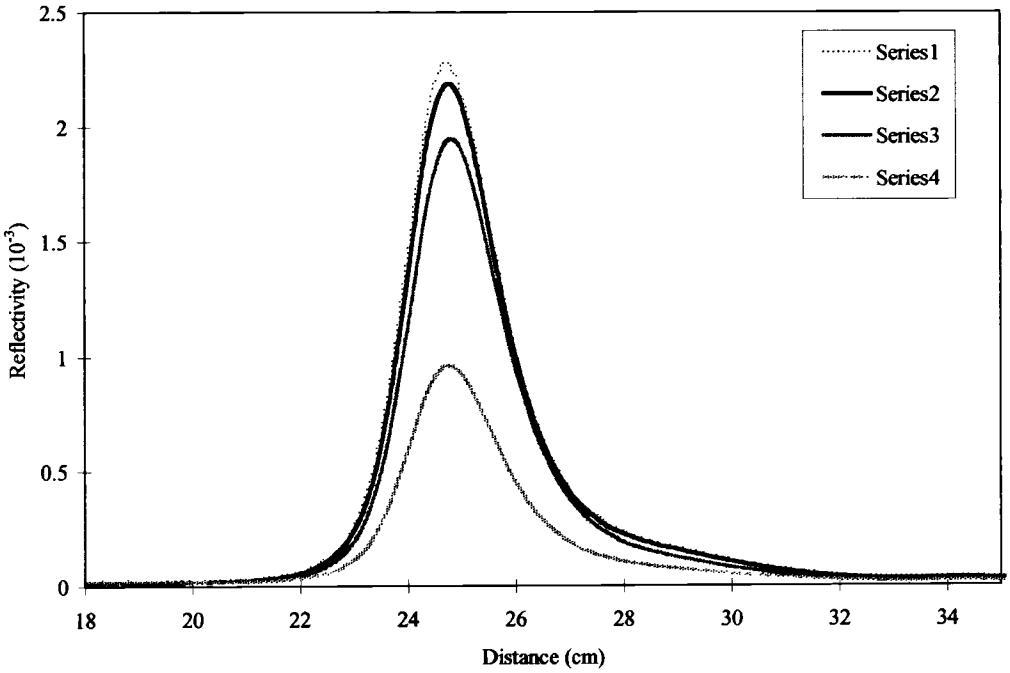

Figure 23. Zoom of the first mechanical splice in the Fresnel trace showing its reflectivity (second experiment).

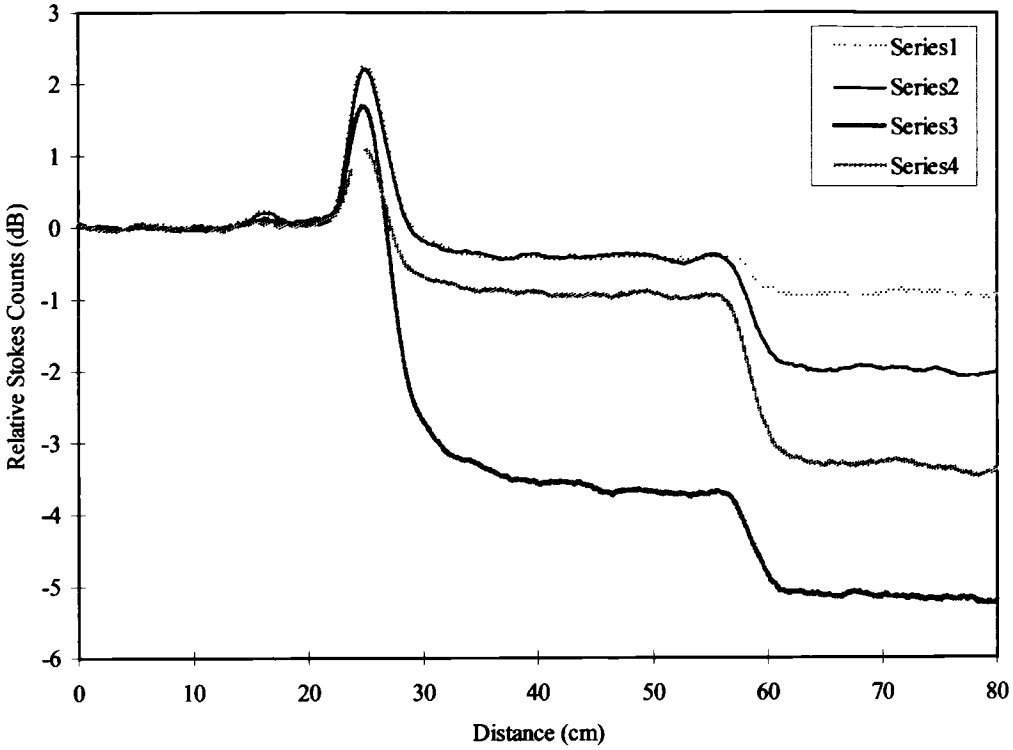

Figure 24. Stokes (SSRE) traces showing immunity to Fresnel reflections (second experiment).

In the third experiment, we investigated the loss budget of the system. We connected the OTDR system to 14 m of fibre and measured the background noise R_B. Figure 25 shows a Stokes trace collected in two minutes after it was processed by subtracting the average of the background level. R_B was measured to be 1500 s^{-1}. As the size τ of the time channels was set to 0.5 ns (equivalent to 5 cm spatial resolution) and the number of repetitions N was $6 \cdot 10^8$, using (24) we calculate a minimum count-rate R_S of 70 s^{-1} which corresponds to a system sensitivity P_s (translated into power) of -122.6 dBm. The two-way loss budget L^2 is then calculated from (23) to be -36 dB. The result shown in Figure 25 agrees well with these calculations. The OTDR system, consequently, has an insertion loss budget (Stokes channel) of 18 dB and a return loss budget (Fresnel channel) of 133 dB in the considered case.

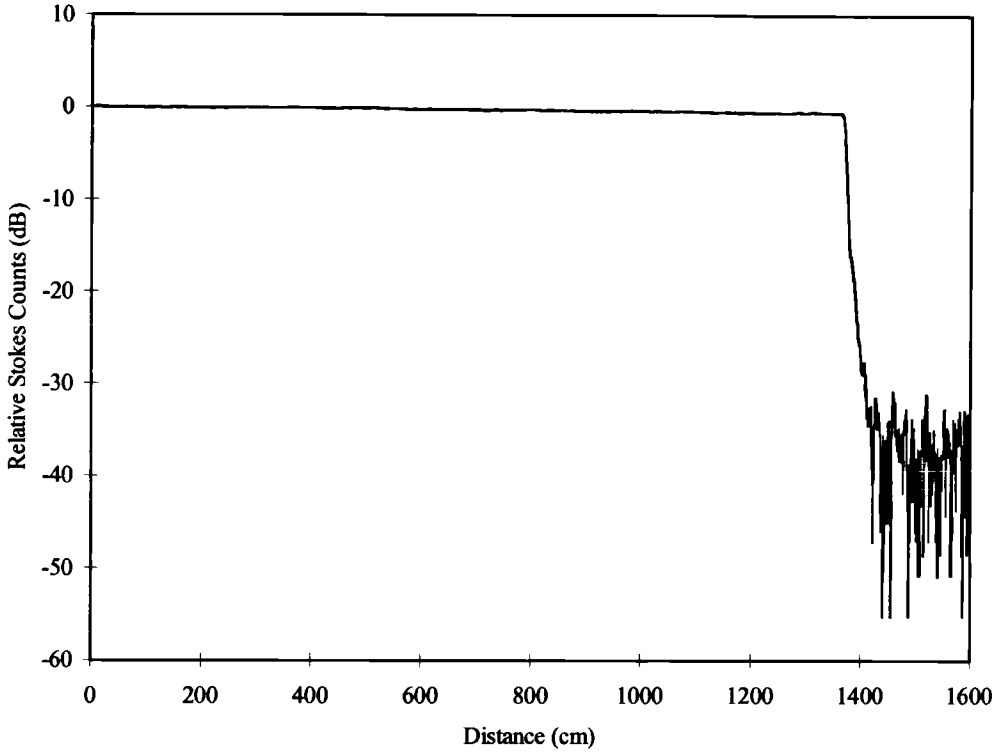

Figure 25. Stokes (SSRE) trace showing the system-sensitivity and the loss budget.

2.6 CONCLUSIONS

In conclusion, we have demonstrated a distributed optical fibre temperature sensor for high spatial resolution and high temperature applications. The system is based on Raman thermometry and the time-correlated single photon counting technique. Optimisation of the power throughput along the system together with the use of very fast electronics permits the measurement of temperature distributions with very high spatial resolution (<10cm) and good temperature resolution (2 °C) in short measurement times (1 minute). This sensor offers a practical solution for temperature monitoring in some specialised applications where the viability of competing technology is questionable. Some of these situations arise, for example, when monitoring the temperature profile along processing ovens of chemical plants, steam pipes in power plants, oil wells or electrical transformers.

We have also presented a zero dead-zone OTDR system with millimetre single-point location resolution and centimetre two-point spatial resolution. The system is based on the use of the TC-SPC technique to monitor the spontaneous Stokes Raman scattering, avoiding dead-zones induced by Fresnel reflections. The high spatial resolution and loss budget achieved make this technique very attractive for short haul applications with a large density of optical components.

APPENDIX

In this appendix, we are going to derive the relation between the Figure of Merit and several system design parameters that appear in equations (18) and (19).

Let us assume that the system is optimised so that the laser pulse-width τ matches the time slots of the multichannel analyser so that the spatial resolution δz is given by:

$$\delta z = \tau \frac{v}{2} \tag{A1}$$

where v is the speed of light in the fibre. The probability of detecting a photon in one such time slot would be equal to $\overline{m}$ (11):

$$\overline{m} = \eta \, \phi \, \tau \tag{A2}$$

where ϕ is the average flux of antiStokes photons. The overall SNR of the processed traces will be limited by the SNR of the antiStokes signal because the average flux of backscattered photons in the antiStokes band is weaker than that corresponding to the Stokes band. After N repetitions of the measurement (N laser shots or excitation cycles), the signal-to-noise ratio SNR in one channel will be for an optimum system without dark counts (14):

$$SNR = \frac{\overline{m}^2}{\sigma_m^2} = \frac{(N\overline{m})^2}{N\overline{m}} = N\overline{m} \tag{A3}$$

Let us now relate the number of useful laser shots N with the measurement time t and the total length of the fibre L. The probability of detecting a photon per shot of the laser P_S is given by the expression:

$$P_S = \eta\phi \frac{L}{v/2} \tag{A4}$$

If a photon is detected, the TAC is triggered and the time consumed by the system before it is ready to detect the next photon would be given by the addition of the laser pulse round trip along the fibre and the electronics dead time t_d:

$$\text{Time when a photon is detected} = \frac{L}{v/2} + t_d \tag{A5}$$

If, on the other hand, no photon is detected, the consumed time would only be given by the laser pulse round trip. Taking into account both cases, the average time consumed per laser shot would be:

$$\text{Average time} = \frac{L}{v/2}(1 - P_S) + \left(\frac{L}{v/2} + t_d\right)P_S \tag{A6}$$

And the total time t after N measurements (or laser shots) is:

$$t = N\frac{L}{v/2}(1 + \eta\,\phi\,t_d) \tag{A7}$$

The temperature resolution δT is related to the signal to noise ratio (A3) through the expression:

$$(S_T \delta T)^2 = \frac{1}{SNR} \tag{A8}$$

Finally, using (6), (A1), (A2), (A3), (A7), (A8) and defining a design parameter p as:

$$p = \phi_{inc}\,\alpha_{AS}\,\kappa\,\Gamma\,\eta \tag{A9}$$

we obtain the sought relation:

$$F_m = \frac{L}{(\delta z\,\delta T)^2\,t} = \frac{S_T^2\,p}{1 + p\,\delta z\,t_d} \tag{A10}$$

REFERENCES

[1] R. Feced, M. Farhadiroushan, V. A. Handerek, A. J. Rogers. "Advances in high resolution distributed temperature sensing using the time-correlated single photon counting technique". IEE Proceedings in Optoelectronics, Vol. 144, No. 3, pp. 183-188, June 1997.

[2] R. Feced, M. Farhadiroushan, Pablo Rodriguez, V. A. Handerek, A. J. Rogers. "Advances in high resolution distributed temperature sensing using a time-resolved single counting technique." SPIE Vol. 2838, pp. 105-113, August 1996.

[3] R. Feced, M. Farhadiroushan, V. A. Handerek, A. J. Rogers. "A high spatial resolution distributed optical fibre sensor for high temperature measurements". Review of Scientific Instruments (AIP), Vol. 68, No. 10, pp. 3772-3776, October 1997.

[4] R. Feced, M. Farhadiroushan, V.A. Handerek, A.J. Rogers. "High temperature testing of a high spatial resolution distributed optical fibre temperature sensor". Optical techniques for smart structures and structural monitoring. IEE, London, February 1997.

[5] R. Feced, M. Farhadiroushan, V.A. Handerek, A.J. Rogers. "Evaluation of a high spatial resolution distributed optical fiber sensor for high temperatures applications". 12th Optical Fiber Sensors Conference, Williamsburg, Virginia (USA). October 1997.

[6] R. Feced, M. Farhadiroushan, V. A. Handerek. "Zero dead-zone OTDR with high spatial resolution for short haul applications". IEEE Photonics Technology Letters, Vol. 9, No. 8, pp. 1140-1142, August 1997.

[7] R. Feced, M. Farhadiroushan, V.A. Handerek. "A high spatial resolution zero dead-zone OTDR". 4th Optical fibre measurement conference. NPL, Teddington (UK), October 1997.

[8] D.A. Long. "Raman Spectroscopy", pp. 1. McGraw-Hill International, 1977.

[9] D.A. Long. "Raman Spectroscopy", pp. 41-43. McGraw-Hill International, 1977.

[10] A. Yariv. "Quantum electronics", pp. 462. John Wiley & Sons, 1988.

[11] D. Marcuse. "Principles of quantum electronics", pp. 390. Academic Press, 1980.

[12] A.S. Davidov. "Teoria del solido", pp. 48. Editorial Mir Moscu, 1981.

[13] G.P. Agrawal. "Nonlinear fiber optics", pp. 219. Academic Press, 1989.

[14] R. H. Stolen, E. P. Ippen, A.R. Tynes. "Raman oscillation in glass optical waveguide". Applied Physics Letters, Vol. 20, No. 2, pp. 62-64, January 1972.

[15] R. H. Stolen, E. P. Ippen. "Raman gain in glass optical waveguides". Applied Physics Letters, Vol. 22, No. 6, pp. 276-278, March 1973.

[16] F. L. Galeener, J.C. Mikkelsen, R. H. Geils, W. J. Mosby. "The relative Raman cross sections of vitreous SiO_2, GeO_2, B_2O_3, and P_2O_5". Applied Physics Letters, Vol. 32, No. 1, pp. 34-36, January 1978.

[17] R.H. Stolen, C. Lin, J. Shah, R.F. Leheny. "A fiber Raman ring laser". IEEE Journal of Quantum Electronics, Vol. 14, No. 11, pp. 860-862, November 1978.

[18] R.G. Smith. "Optical power handling capability of low loss optical fibers as determined by stimulated Raman and Brillouin scattering". Applied Optics, Vol. 11, No. 11, pp. 2489-2494. November 1972.

[19] J. Auyeung, A. Yariv. "Spontaneous and stimulated Raman scattering in long low loss fibers". IEEE Journal of Quantum Electronics, Vol. 14, No. 5, pp. 347-352, May 1978.

[20] G.P. Agrawal. "Nonlinear fiber optics", pp. 235. Academic Press, 1989.

[21] J. P. Dakin, D. J. Pratt, G. W. Bibby, J. N. Ross. "Distributed optical fibre Raman temperature sensor using a semiconductor light source and detector". Electronics Letters, Vol. 21, No. 13, pp. 569-570, June 1985.

[22] A. H. Hartog, A. P. Leach, M. P. Gold. "Distributed temperature sensing in solid-core fibres". Electronics Letters, Vol. 21, No. 23, pp. 1061-1062, November 1985.

[23] E. Brinkmeyer. "Analysis of the backscattering method for single-mode optical fibres". Journal of the Optical Society of America, Vol. 70, No. 8, August 1980.

[24] T. Wakami, S. Tanaka. "1.55 μm long-span fiber-optic distributed temperature sensor". 10th Optical Fibre Sensors Conference, pp. 134-137, 1994.

[25] J.K.A. Everard, R. Thomas. "Distributed optical fibre temperature sensor using spread-spectrum techniques". Electronics Letters, Vol. 25, No. 2, pp. 140-142, January 1989.

[26] P.C. Wait, S. Gaubicher, J.M. Sommer, T.P Newson. "Raman backscatter distributed temperature sensor based on a self-starting passively modelocked fibre ring laser". Electronics Letters, Vol. 32, No. 4, pp. 388-389, February 1996.

[27] B.E.A. Saleh, M.C. Teich. "Fundamentals of Photonics", pp. 675. John Wiley & Sons, 1991.

[28] L. Mandel, E. Wolf. "Optical coherence and quantum optics", pp. 449-450. Cambridge University Press, 1995.

[29] B. Crosignani, P. Di Porto, M. Bertolotti. "Statistical properties of scattered light", pp. 134. Academic Press, 1975.

[30] B.E.A. Saleh, M.C. Teich. "Fundamentals of Photonics", pp. 420. John Wiley & Sons, 1991.

[31] B.E.A. Saleh, M.C. Teich. "Fundamentals of Photonics", pp. 685. John Wiley & Sons, 1991.

[32] D.V. O'Connor, D. Phillips. "Time-correlated single photon counting". Academic Press, 1984.

[33] P. Healy. "Optical time domain reflectometry- a performance comparison of the analogue and photon counting techniques". Optical and Quantum Electronics, Vol. 16, pp. 267-276, 1984.

[34] P. B. Coates. "The correction of photon pile-up in the measurement of radiative lifetimes". Journal of Scientific Instruments (Journal of Physics E), Series 2, Vol. 1, pp. 878-879, 1968.

[35] D. Bebelaar. "Time response of various types of photomultipliers and its wavelength dependence in time-correlated single-photon counting with an ultimate resolution of 47 ps FWHM". Review of Scientific Instruments, Vol. 57, No. 6, pp. 1116-1125, June 1986.

[36] D.V. O'Connor, D. Phillips. "Time-correlated single photon counting", pp. 124. Academic Press, 1984.

[37] S. Cova, A. Longoni, A. Andreoni. "Towards picosecond resolution with single-photon avalanche photodiodes". Review of Scientific Instruments, Vol. 52, No. 3, pp. 408-412, March 1981.

[38] S. Cova, A. Lacaita, M. Ghioni, G. Ripamonti. "20-ps timing resolution with single-photon avalanche diodes". Review of Scientific Instruments, Vol. 60, No. 6, pp. 1104-1110, June 1989.

[39] B. F. Levine, C. G. Bethea, J. C. Campbell. "1.52 μm room-temperature photon-counting optical time domain reflectometer". Electronics Letters, Vol. 21, No. 5, pp. 194-196, February 1985.

[40] I. Prochazka, K. Hamal, B. Greene, H. Kunimori. "Large-aperture germanium detector package for picosecond photon counting in the 0.5-1.6 μm range". Optics Letters, Vol. 21, No. 17, pp. 1375-1377, September 1996.

[41] P. Healy, P. Hensel. "Optical time domain reflectometry by photon counting". Electronics Letters, Vol. 16, No. 16, pp. 631-633, July 1980.

[42] M. Hobel, M. Wuthrich, J. Ricka, T. Binkert. "A fast multi-time-interval analyzer with real-time processing capability". Review of Scientific Instruments, Vol. 65, No. 6, pp. 2123-2129, June 1994.

[43] M. Hobel, J. Ricka, M. Wuthrich, T. Binkert. "High-resolution distributed temperature sensing with the multiphoton-timing technique". Applied Optics, Vol. 34, No. 16, pp. 2955-2967, June 1995.

[44] G. Ripamonti, S. Cova. "Optical time domain reflectometry with centimetre resolution at 10^{-15} W sensitivity". Electronics Letters, Vol. 22, No. 15, pp. 818-819, July 1986.

[45] C. G. Bethea, B. F. Levine, S. Cova, G. Ripamonti. "High-resolution and high-sensitivity optical time-domain reflectometer". Optics Letters, Vol. 13, No. 3, pp. 233-235, March 1988.

[46] G. Ripamonti, M. Ghioni, S. Vanoli. "Photon timing OTDR: a multiphoton backscattered pulse approach". Electronics Letters, Vol. 26, No. 19, pp. 1569-1571, September 1990.

[47] R. Stierlin, J. Ricka, B. Zysset, R. Battig, H. P. Weber, T. Binkert, W. J. Borer. "Distributed fibre optic temperature sensor using single photon counting detection". Applied Optics, Vol. 26, No. 8, pp. 1368-1370, April 1987.

[48] D. A. Thorncraft, M. G. Sceats, S. B. Poole. "An ultrahigh resolution temperature sensor." Conference proceedings, 8th Optical Fibres Sensors Conference, Monterey, CA., pp. 258-260, 1992.

[49] N. Yoshizawa, Y. Katsuyama. "High-strength carbon-coated optical fiber". Electronics Letters, Vol. 25, No. 21, pp. 1429-1431, October 1989.

[50] R.S. Linton, BICC Cables, Private communication.

[51] V.A. Bogatyrjov, M.M Bubnov, E.M. Dianov, S.D. Rumyantzev, S.L. Semjonov. "Mechanical reliability of polymer-coated and hermetically coated optical fibers based on proof testing". Optical Engineering, Vol. 30, No. 6, pp. 690-699. June 1991.

[52] K.T.V. Grattan, A.W. Palmer, Z. Zhang. "Development of a high-temperature fiber-optic thermometer probe using fluorescent decay." Review Scientific Instruments, Vol. 62, No. 5, pp. 1210-1213. May 1991.

[53] M.K. Barnorski, M.D. Rourke, S.M. Jensen, R.T. Melville. "Optical time domain reflectometer". Applied Optics, Vol. 16, No. 9, pp. 2375-2379, September 1977.

[54] S.D. Personick. "Photon probe: an optical-fiber time-domain reflectometer". Bell System Technical Journal, Vol. 56, No. 3, pp. 355-366, March 1977.

[55] B.S. Kawasaki, K.O. Hill, D.C. Johnson. "Optical time domain reflectometer for single-mode fiber at selectable wavelengths". Applied Physics Letters, Vol. 38, No. 10, pp. 740-742, May 1981.

[56] G. Ripamonti, M. Ghioni, A. Lacaita. "No dead-space optical time-domain reflectometer". Journal of Lightwave Technology, Vol. 8, No. 9, pp. 1278-1283, September 1990.

Chapter 3

STATIC POLARISATION GRATINGS

This chapter studies static (photosensitive) polarisation gratings generated by exposing the optical fibres to blue-green or ultraviolet (UV) radiation. Sections 3.1 and 3.2 introduce the fundamental ideas about polarisation preserving fibres and propagation in periodically perturbed polarisation waveguides. Section 3.3 reviews the different mechanisms proposed to explain the photosensitivity of optical fibres. In Section 3.4 we will study some aspects related to the photo-induced birefringence in optical fibres and, as a consequence, we will demonstrate a fabrication method for tailoring the spectral response of polarisation filters [1,2]. Finally, in Section 3.5 we will investigate the mechanical effects produced by the UV irradiation of optical fibres [3,4]. Although static gratings are not suitable for distributed sensing applications, the concepts introduced in Sections 3.1 and 3.2 will be useful for the analysis of dynamic Kerr-induced polarisation gratings [5-7]. The study of this type of gratings and their application to distributed sensing will be deferred to the next chapter.

3.1 POLARISATION MAINTAINING FIBRES

In this chapter we are going to study several applications of polarisation maintaining fibres. Single mode optical fibres with circular cores support two fundamental modes (HE_{11}^{x} and HE_{11}^{y}) with identical propagation constants but orthogonal polarisations. Due to this modal degeneracy, random perturbations along the fibre induce coupling between them, leading to a random evolution of the polarisation state along the fibre [8]. This unpredictability of the polarisation state of the light can be problematic in some applications such as, for example, those based on fibre interferometers or coherent detection schemes. Considerable effort [9-14] has been devoted to the development of high birefringence fibres that overcome these limitations.

In a high birefringence fibre, the degeneracy between the fundamental polarisation modes is lifted, and each of these modes preserves its identity during propagation. The degree of non-degeneracy among the modes is measured through a parameter called beatlength, L_B, that is inversely proportional to the difference between their propagation constants $\Delta\beta$:

$$L_B = \frac{2\pi}{\Delta\beta} \tag{1}$$

Alternatively, an effective birefringence Δn can be defined by normalising $\Delta\beta$ with respect to the vacuum propagation constant k_o ($=\omega/c$):

$$\Delta n = \frac{\Delta\beta}{k_o} = \frac{\Delta\beta}{\omega / c} \tag{2}$$

3.1.1 Types of high birefringence fibres

The two most important mechanisms responsible for birefringence in optical fibres are stress induced birefringence [9,10] and geometrically induced birefringence [11]. High birefringence fibres based on both of these mechanisms have been shown to attain beatlengths in the millimetre range, which are sufficient to preserve the polarisation modes along the fibre.

Fibres with stress induced birefringence have their cores subjected to a transverse thermal stress caused by a mismatch between the expansion coefficients of different regions of the fibre. This stress introduces an anisotropy in the refractive index of the core through the photo-elastic effect. Several designs that generate thermal stress along the fibre-core are represented in Figure 1. A first approach was to fabricate fibres with elliptical claddings [9]. More recently, fibres that contain stress elements with cylindrical or bow-tie shapes have shown better performance [13]. The materials used as stress elements have higher expansion coefficients than silica and are typically B_2O_3 and P_2O_5. The final birefringence induced in the fibre, Δn, is proportional to this difference between the expansion coefficients of the stress element and silica $\Delta\alpha$, and also proportional to the difference between the glass fictive temperature and the operational temperature of the fibre ΔT:

$$\Delta n \propto \Delta\alpha\, \Delta T \qquad (3)$$

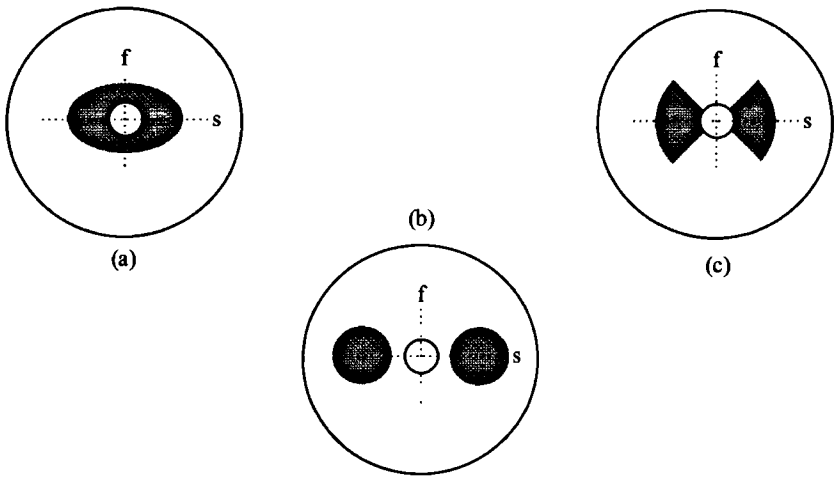

Figure 1. Three types of stress birefringence fibres: (a) elliptical cladding, (b) Panda fibre (stress elements with cylindrical shape), (c) bow-tie fibre. The slow and fast axes are indicated with s and f respectively.

Fibres with geometrical birefringence are those whose core has an elliptical shape or, in general, a non-circular shape (Figure 2). As glass is an isotropic material, geometrical birefringence is a purely wave-guide effect. The geometrically induced birefringence [11] turns out to be proportional to the square of the refractive index difference between core and cladding (n_{co}-n_{cl}), and also proportional to a parameter related to the ellipticity of the core:

$$\Delta n \propto (n_{co} - n_{cl})^2 \left(\frac{a}{b} - 1\right) \tag{4}$$

where a is the semi-major axis and b the semi-minor axis of the core ellipse. From equation (4), its is clear that the two ways to increase the birefringence of an elliptical core fibre are either to increase the refractive index difference between the core and the cladding or to increase the fibre ellipticity.

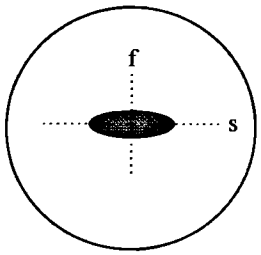

Figure 2. Elliptical core fibre. The slow and fast axes are indicated with s and f respectively.

An interesting difference between stress birefringent fibres and elliptical-core fibres is the wavelength dependence of their beatlength, i.e. their different birefringence dispersion. Due to its wave-guide origin, the beatlength of elliptical-core fibres does not exhibit a linear dependence with respect to wavelength. The dispersion of the birefringence Δn as a function of the normalised frequency V:

$$V = k_o b \sqrt{n_{co}^2 - n_{cl}^2} \tag{5}$$

can be observed in Figure 3 [11]. On the contrary, the beatlength of stress birefringent fibres varies almost linearly with wavelength. This difference has an important impact in the design of polarisation filters as we will see in Section 3.4. As most of the work carried out in this chapter is based on elliptical core fibres, we will restrict the discussion to this type of fibre in the rest of the chapter.

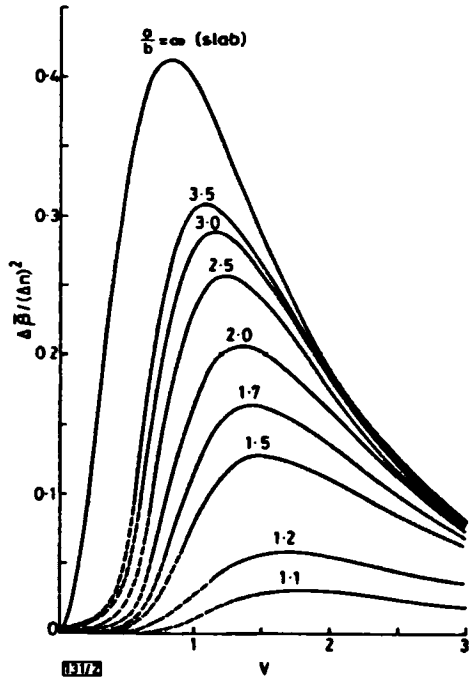

Figure 3. Dispersion of the birefringence Δn ($=\Delta\tilde{\beta}$) with respect to the normalised frequency V, for different values of the ratio between the major and minor axes of the elliptical core fibre (a/b). Δn in the Figure refers to the core-cladding refractive index difference (after [11]).

3.1.2 Modes in elliptical core fibres

In a circular-core fibre, the first higher order modes consist of a group of four modes designated as TM_{01}, TE_{01} and HE_{21} (which is two-fold degenerate). In the weakly guiding approximation (i.e. small n_{co}-n_{cl}), these four modes are degenerate and have a common cut-off normalised frequency V_c equal to 2.4 [15]. By combining adequately the former first higher order modes, we can form an alternative set of four modes with linearly polarised (LP) field distributions. These modes are designated as the even-$LP_{11}^{x,y}$ (that obey a $\cos\phi$ angular field pattern dependence) and odd-$LP_{11}^{x,y}$ (with a $\sin\phi$ angular field dependence). The linearly polarised LP modes are not true eigenmodes of a circular core fibre when the weakly guiding approximation is not valid. In this case, the cut-off frequency of the HE_{21} pair is slightly higher than that of the TM_{01}, TE_{01} pair, and the two pairs of modes are non-degenerate. The linearly polarised LP modes are, however, the natural modes of birefringent waveguides and are very useful for the mode description in elliptical core fibres.

In an elliptical-core fibre, the four first higher order modes can be split into two groups according to their cut-off frequency [16]. The group with lowest cut-off frequency is the even-LP_{11}, and its normalised cut-off frequency V_c varies from 2.4 when the fibre core is circular, to 0 in the limit of a highly elliptical core fibre. The second group is the odd-LP_{11}, with a cut-off frequency varying from 2.4 (circular core) to $\pi/2$ (highly elliptical core case). The field patterns of the fundamental and first higher order modes of an elliptical-core fibre are represented in Figure 4. From the preceding discussion, it can be observed that in elliptical-core fibres there is a wavelength range in which only the fundamental modes (HE_{11} or LP_{01}) and the first pair of higher order modes (the even-LP_{11}) can propagate. This bimodal regime has been successfully used in many applications, for example for sensing [17] or optical switching [18].

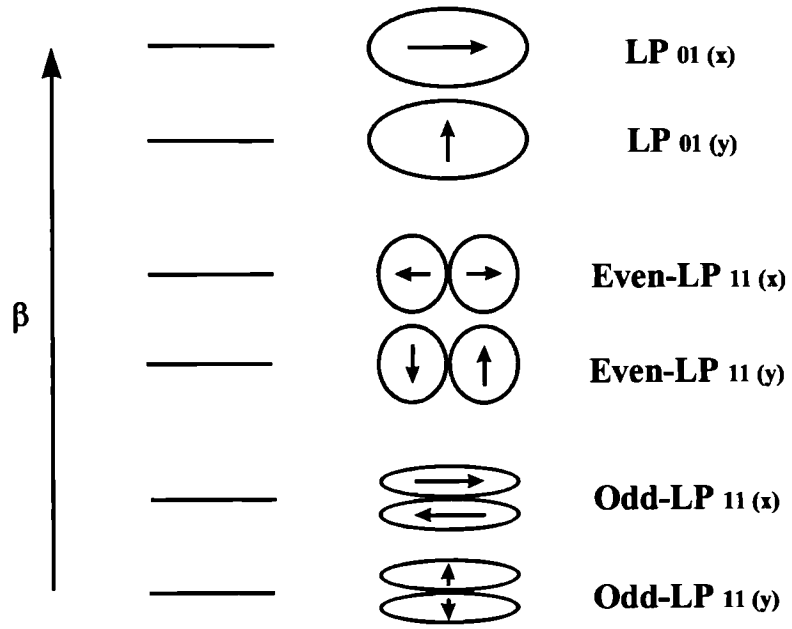

Figure 4. Field patterns of the fundamental and first higher order modes of an elliptical core fibre. β is the propagation constant of the modes.

A characteristic beatlength can be associated with every pair of modes represented in Figure 4. As we have seen in the last section, the beatlength between polarisation modes ($LP_{01}^x \leftrightarrow LP_{01}^y$, for example) ranges from one millimetre to several centimetres in elliptical core fibres. On the other hand, the beatlength due to spatial-mode non-degeneracy (for example, between $LP_{01}^x \leftrightarrow \text{even} - LP_{11}^x$) has typical values in the range of hundreds of micrometres. These small beatlength values are responsible for the good mode holding capability of elliptical core fibres. Another interesting property associated with every pair of modes is their intermodal group

delay (IGD), which is a measure of the difference between their group velocities. The IGD gives rise to walk-off among the modes as they propagate along the fibre. IGD is very dependent on the wavelength and there is usually an optimum wavelength for which it is null, so that different polarisation modes [11] or different spatial modes [19] propagate with the same group velocity. A typical figure for the IGD between polarisation modes is 2 ns/km. In the case of different spatial modes, the IGD can be as large as 10 ns/km if the operational frequency is far from the optimum null point.

The total electric field that propagates along an elliptical core fibre can be represented mathematically as a sum over all the modes sustained by it:

$$\bar{e}(t,x,y,z) = \Re e\left\{\sum_m \tilde{B}_m(t,z)\,\bar{\Gamma}_m(x,y)\,e^{j\omega t}\right\} \qquad (6)$$

where $\bar{\Gamma}_m(x,y)$ is the normalised transverse field pattern of mode m, ω is the angular frequency of the field; and $\tilde{B}_m(t,z)$ are field amplitudes that for a stationary field do not depend on time (t):

$$\tilde{B}_m(z) = \tilde{A}_m\, e^{-j\beta_m z} \qquad (7)$$

where β_m is the propagation constant of mode m, z is the direction of propagation, and $\tilde{A}_m$ is a constant field amplitude. This field representation will be used in the following sections.

3.2 PROPAGATION IN PERIODIC MEDIA

As we have seen in the last section, optical waveguides support electromagnetic modes with characteristic field patterns and propagation constants. These modes do not exchange power as they propagate unless their propagation constants are almost degenerate. In this case, small random perturbations can induce significant mode coupling and power redistribution among degenerate modes. This effect is minimised in elliptical core fibres, where the propagating modes are very non-degenerate and maintain their identity along the fibre.

In many applications, however, it is necessary to have an efficient and controlled transfer of power between modes with different propagation constants. This is usually achieved by

introducing a periodic perturbation in the properties of the waveguide. When the periodicity of the waveguide perturbation is equal to the beatlength between two modes, efficient phase-matched coupling is produced between them. As this condition can only be satisfied for a restricted wavelength range, periodic media have been used extensively for spectral filtering applications.

3.2.1 Propagation in perturbed waveguides

In this section, we will introduce the standard mathematical tools that are used to analyse mode coupling in perturbed waveguides [20]. The basic idea is to describe the electromagnetic field in terms of the relevant field amplitudes $\widetilde{A}_m$ (7), and assume that these amplitudes change along the fibre (z) as a result of mode coupling induced by the waveguide perturbations. If the periodicity of the perturbation is long enough to neglect contradirectional coupling, then the system of equations that the $\widetilde{A}_m(z)$ satisfy are [20]:

$$\frac{d}{dz}\widetilde{A}_k(z) = -\frac{j\omega}{4}\sum_m \langle k|\Delta\varepsilon|m\rangle\, \widetilde{A}_m(z)\, e^{j(\beta_k-\beta_m)z} \tag{8}$$

where $\Delta\varepsilon$ is the perturbation of the dielectric permitivity tensor in the waveguide, and $\langle k|\Delta\varepsilon|m\rangle$ is the coupling function (dependent on z):

$$\langle k|\Delta\varepsilon|m\rangle = \int \overline{\Gamma}_k^*(x,y)\, \Delta\varepsilon(x,y,z)\, \overline{\Gamma}_m(x,y)dxdy \tag{9}$$

Equation (8) can also be written in terms of the amplitudes $\widetilde{B}_m(z)$ (7):

$$\frac{d}{dz}\widetilde{B}_k(z) = -j\beta_k\widetilde{B}_k(z) - \frac{j\omega}{4}\sum_m \langle k|\Delta\varepsilon|m\rangle\, \widetilde{B}_m(z) \tag{10}$$

In the next sections, we will be mainly concerned with the case in which only the two fundamental polarisation modes of an elliptical core fibre are excited (HE_{11}^x and HE_{11}^y). From equation (9), we see that a perturbation with non null $\Delta\varepsilon_{xy}$ is necessary to couple efficiently these modes. Several physical mechanisms could be used to induce a non null $\Delta\varepsilon_{xy}$ in an optical fibre. Among them, we could mention the photoelastic, electrooptic, magnetooptic, fibre

photosensitivity, and optical Kerr effects. We will study the use of the last two mechanisms for this purpose.

From equation (8) we can find the phase matching condition necessary for efficient mode coupling. This condition relates the perturbation periodicity Λ to the beatlength between the coupled modes. If we assume that only the nondiagonal components $\Delta\varepsilon_{xy}\,(=\Delta\varepsilon_{yx}^{*})$ of the perturbed permittivity are not null, we can rewrite (9) as:

$$\frac{4}{\omega}\left\langle HE_{11}^{x}\left|\Delta\varepsilon_{xy}\right|HE_{11}^{y}\right\rangle = \kappa\, e^{-jKz} + \text{c.c.} \qquad (11)$$

where K is equal to $2\pi/\Lambda$, κ is a coupling constant independent of z and c.c. stands for complex conjugated. Efficient coupling will only be produced if the exponential term in (8) is null, giving rise to the phase matching condition:

$$\beta_x - \beta_y - K = 0 \qquad (12)$$

Due to the wavelength dispersion of the beatlength, this condition is only satisfied in the vicinity of a characteristic coupling wavelength.

3.2.2 Bloch modes in periodic media

As we have seen in the last section, the fundamental modes of an elliptical core fibre are no longer the true propagation eigenmodes if there is a periodic perturbation $\Delta\varepsilon_{xy}(z)$ along the fibre. The natural modes that describe propagation in a periodic medium are the Bloch modes, which have the particularity of being formed by many space harmonics [21]. However, it has been shown that a good approximation to the Bloch modes can be achieved by considering only two space harmonics (or partial waves), each space harmonic corresponding to one of the original fundamental modes of the fibre [22].

By inserting equation (11) in (10) we arrive at the following system of equations in terms of the $\tilde{B}_{x,y}$ field amplitudes:

$$\frac{d}{dz}\begin{bmatrix}\tilde{B}_x\\ \tilde{B}_y\end{bmatrix}=-j\begin{bmatrix}\beta_x & \kappa\, e^{-jKz}\\ \kappa^* e^{+jKz} & \beta_y\end{bmatrix}\begin{bmatrix}\tilde{B}_x\\ \tilde{B}_y\end{bmatrix} \tag{13}$$

The Bloch theorem, in the approximation of two space harmonics, states that the Bloch modes can be written according to the expression:

$$V_B(z)=\begin{bmatrix}B_x^o\, e^{-jKz}\\ B_y^o\end{bmatrix}e^{-jk_B z} \tag{14}$$

where the term in brackets has the medium periodicity and k_B is the propagation constant of the Bloch wave. Substitution of (14) in (13) permits the calculation of the two Bloch modes and also of the dispersion relation for k_B. This dispersion relation is:

$$k_B=\frac{(\beta_x-K)+\beta_y}{2}\pm\sqrt{\left(\frac{(\beta_x-K)-\beta_y}{2}\right)^2+|\kappa|^2} \tag{15}$$

k_B has been represented in Figure 5 as a function of the vacuum propagation constant k_o. It can be observed that far from the resonance condition the Bloch modes correspond to the elliptical core fundamental modes. However, near the resonance condition, the dispersion diagram shows a gap, and the Bloch modes are a mixture of the two fundamental modes of the unperturbed waveguide.

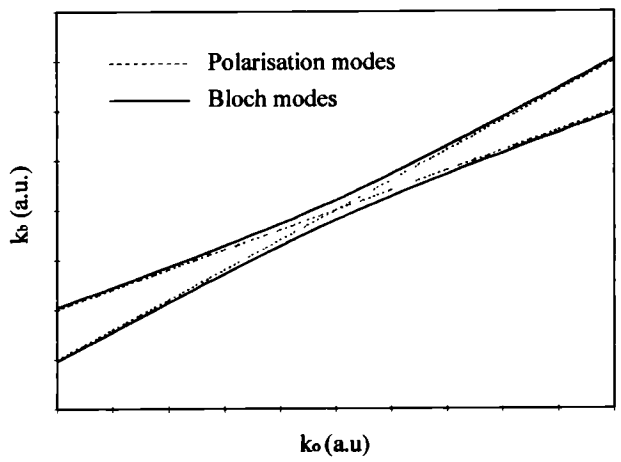

Figure 5. The two branches of k_B (Bloch modes) as a function of the vacuum propagation constant k_o.

The Bloch approach, in the approximation of two space harmonics, is completely equivalent to the coupled mode formalism previously described.

3.2.3 Solution of the coupled mode equations

The amount of power exchanged between the two fundamental polarisation modes in a periodic medium is normally calculated by solving the coupled equations (8). Taking into account (11), equation (8) can be rewritten:

$$\frac{d}{dz}\begin{bmatrix}\tilde{A}_x\\ \tilde{A}_y\end{bmatrix}=\begin{bmatrix}-j\kappa\, e^{+j\Delta\tilde{\beta}z}\,\tilde{A}_y\\ -j\kappa^{*}\, e^{-j\Delta\tilde{\beta}z}\,\tilde{A}_x\end{bmatrix} \tag{16}$$

where $\Delta\tilde{\beta}$ is:

$$\Delta\tilde{\beta}=\beta_x-\beta_y-K \tag{17}$$

The general solution for the fields $\tilde{A}_x$ and $\tilde{A}_y$ of (16) is given by the matrix relation [20]:

$$\begin{bmatrix}\tilde{A}_x(z)\\ \tilde{A}_y(z)\end{bmatrix}=\begin{bmatrix}\left(\cos(sz)-j\frac{\Delta\tilde{\beta}}{2s}\sin(sz)\right)e^{j\frac{\Delta\tilde{\beta}}{2}z} & -j\frac{\kappa}{s}\sin(sz)\,e^{j\frac{\Delta\tilde{\beta}}{2}z}\\ -j\frac{\kappa^{*}}{s}\sin(sz)\,e^{-j\frac{\Delta\tilde{\beta}}{2}z} & \left(\cos(sz)+j\frac{\Delta\tilde{\beta}}{2s}\sin(sz)\right)e^{-j\frac{\Delta\tilde{\beta}}{2}z}\end{bmatrix}\begin{bmatrix}\tilde{A}_x(0)\\ \tilde{A}_y(0)\end{bmatrix} \tag{18}$$

where:

$$s^2=|\kappa|^2+\left(\frac{\Delta\tilde{\beta}}{2}\right)^2 \tag{19}$$

From (18) we can calculate the fraction of power η coupled from the mode HE_{11}^{x} to the mode HE_{11}^{y} by a polarisation grating of total length L when initially only the first mode is excited ($\tilde{A}_y(z=0)=0$):

$$\eta(\Delta\tilde{\beta}) = \frac{|\kappa|^2}{s^2}\sin^2(sL) \qquad (20)$$

where it can be appreciated that total power transfer is possible if the phase matching condition (12) is satisfied and $\sin^2(|\kappa|L)$ equals 1. The transfer function $\eta(\Delta\tilde{\beta})$ is represented in Figure 6 for several values of the parameter $|\kappa|$.

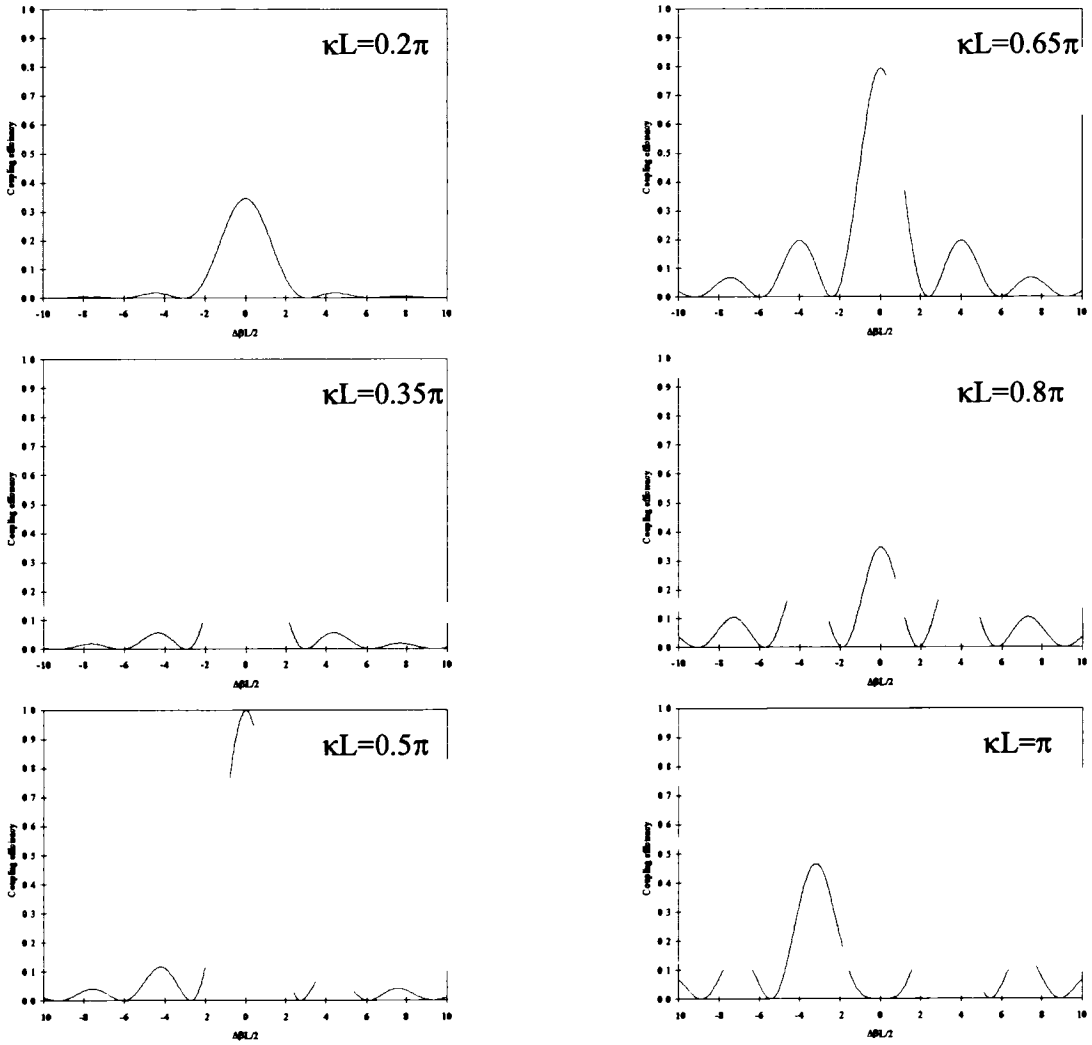

Figure 6. Transfer function $\eta(\Delta\tilde{\beta})$ for several values of the parameter $|\kappa|L$.

The analysis carried out so far is useful to describe coupling in uniform periodic media, where κ is constant along the structure. In the next sections we are going to consider more general situations. Firstly, by use of the photosensitivity properties of optical fibres, we are going to demonstrate a technique to fabricate structures where κ is no longer constant, varying along z: $\kappa(z)$. This fabrication technique will be useful for the synthesis of polarisation filters with tailored spectral response. Secondly, by use of the optical Kerr effect, we will show that transient gratings can be created along an optical fibre. In this case, the coupling function will not only depend on the position variable z, but also on the time variable t: $\kappa(z,t)$. These transient gratings will be theoretically analysed by an adequate extension of the previous mathematical treatment. Its application for distributed sensing will also be discussed.

3.3 PHOTOSENSITIVITY IN OPTICAL FIBRES AND PHOTOINDUCED BIREFRINGENCE

Recently, it was discovered that the electrical properties of optical fibres could be perturbed when they are exposed to visible [23] or ultraviolet (UV) [24] radiation. This phenomenon, called photosensitivity, has been used extensively to generate periodic structures in fibres. When a fibre is exposed to blue-green or UV radiation, a small change is induced in its dielectric permittivity. Although most of this change is isotropic, it has been shown that a small fraction of it is anisotropic, permitting the generation of controlled birefringence in the fibre [25]. Many different fibre devices based on the photosensitivity effect have been developed. Their applications include spectral filtering, pulse compression, compensation of the fibre dispersion, fibre lasers and switching or sensing among others. In this section, we will first review the physical mechanisms involved in the photosensitivity of optical fibres, focusing at a later stage on the phenomenon of photoinduced birefringence.

3.3.1 Photosensitivity in optical fibres

The photosensitivity of optical fibres was discovered by Hill [23] during the exposure of germanium doped silica fibres to core-launched visible light from an argon-ion laser. The observation of a pronounced attenuation in the transmission of the fibre was attributed to the formation of a contradirectional Bragg grating. The growth dynamics of these gratings were satisfactorily explained [26,27] by assuming that the instantaneous change in the refractive index was proportional to the square of the local field intensity. Physically, this meant that a two-photon absorption process was responsible for the index perturbation. The final variation in the core refractive index achieved by Hill was in the range of 10^{-6} to 10^{-5}.

After this first demonstration of the photosensitivity properties of fibres, the next major advance was the creation of gratings by means of transverse UV exposure from the side of the fibre. An interference pattern formed with an intense UV laser source was shown to produce an index modulation in the fibre core [24]. The main advantage of this approach was a significant enhancement (10^6) in the efficiency of the writing process, because now a one-photon absorption process is responsible for the index perturbation. Also, flexibility for the selection of the resonance wavelength and of the grating's internal structure are added advantages of the transverse UV exposure technique. The first side-written fibre Bragg grating was demonstrated

by means of a split beam interferometer by Meltz [24]. Other interferometers, such as the prism interferometer [28], have relaxed the stringent stability requirements of mirror interferometers.

A more recent development to fabricate fibre Bragg gratings is the use of diffractive optical phase-mask gratings with nearly suppressed zero-order transmission. In this case, an interference fringe pattern with a periodicity equal to one half of the mask periodicity is formed by the UV radiation after passing through the phase mask [29,30]. The phase-mask greatly simplifies the fibre grating fabrication set-up, reducing also the temporal coherence requirements for the UV laser source. Finally, a technique in which the grating is transversely written point by point by accurately controlling the position and spot size of the UV beam has been demonstrated [31]. Due to the difficulty of controlling submicron periodic pitches, the grating was written at a longer pitch and operated in the third order diffraction mode.

Many mechanisms are thought to play a role in the interaction between the blue-green or UV radiation and the amorphous glass network. However, as the bandgap of silica is around 9-10eV and the photon energy of the UV radiation usually employed in photosensitive experiments is only of the order of 5 eV (240 nm), it is thought that glass defects that introduce electronic levels in the middle of the bandgap play a key role in these mechanisms. Due to the high photosensitivity of germanium doped silica, these defects have been associated with wrong bonds in the glass network due to the germanium. It is now generally accepted that germanium oxygen deficient centres (GODC) act as precursors for most of the photosensitive mechanisms, providing a way to channel the UV energy radiation into the glass network [32,33]. Two main UV optical absorption bands are related to the GODC defects. The first one is situated at 240nm (5eV) and corresponds to a singlet to singlet transition (Figure 7). The associated triplet state gives a forbidden transition at 330 nm [33-37]. The second GODC-induced absorption band is due to a different variety of GODC and its peak occurs at 185 nm (6.6 eV) [33].

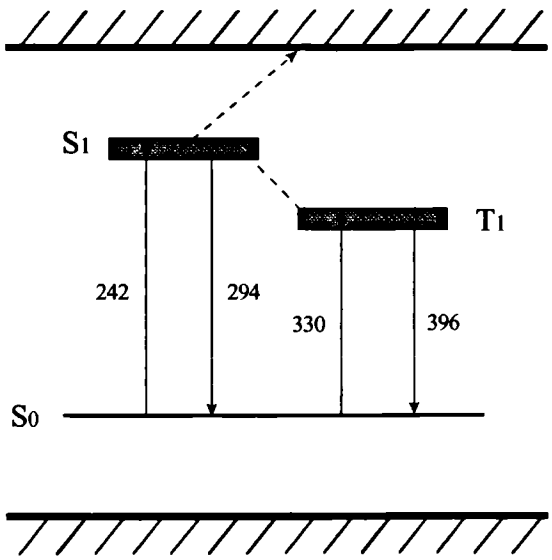

Figure 7. Mid-band electronic states associated with the 240nm (5eV) UV optical absorption band (related to the GODC defects). S_0 is the fundamental singlet state, and S_1 and T_1 are the excited singlet and triplet states respectively (after [33]).

3.3.1.a Colour centre model

The colour centre model, first proposed by Russell [38], relies on the fact that UV radiation induces colour centres in the glass as a result of its interaction with GODC [32]. The generation of colour centres gives rise to a change in the absorption band structure, which translates into a variation of the refractive index through the Kramers-Kronig relations. While the absorption bands associated with the GODC are bleached, other bands associated with the created colour centres will grow [34-37]. The generally accepted model for this process is represented in Figure 8 and consists in the transformation of a GODC into a GeE' and Ge(1) or Ge(2) colour centres. The GeE' corresponds to an absorption band at 195 nm (6.2 eV), while the Ge(1) and Ge(2) are associated with absorption bands at 281 nm (4.4. eV) and 213 nm (5.8 eV) respectively. Kramers-Kronig calculations have shown that changes in the refractive index as large as $3 \cdot 10^{-4}$ could be accounted for with the colour centre model for fibres exposed to 248nm [37].

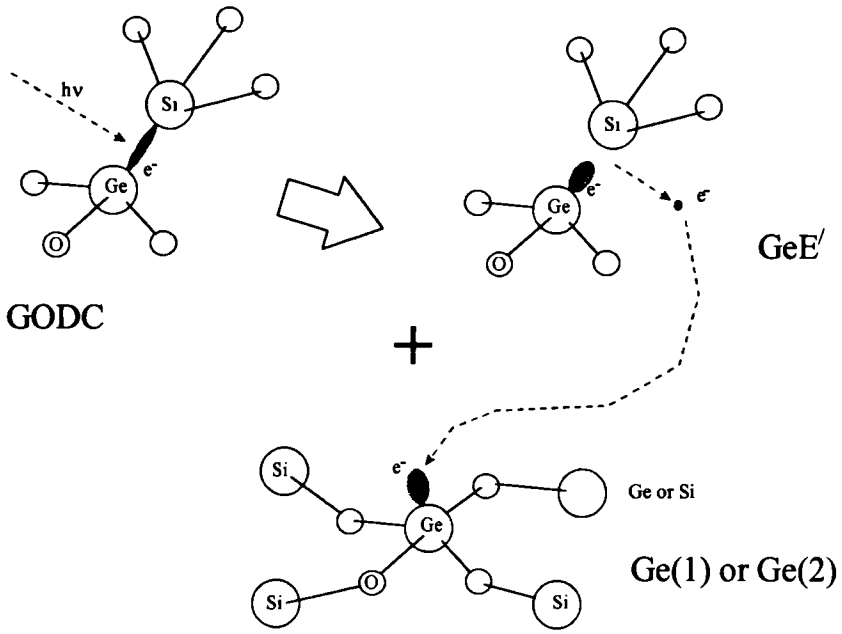

Figure 8. Colour centre model: the optical radiation interacts with a GODC generating the colour centres GeE' and Ge(1) (or Ge(2)) according to the process represented in the picture.

3.3.1.b Glass network compaction

Glass compaction as a mechanism to explain the refractive index changes of UV exposed glass was first suggested by Lawandy [39]. This model has been supported by some recent experimental evidence. Corrugations in the surface of UV exposed glasses have been observed by means of atomic force microscopes [40] and interferometric miscoscopes [41]. The rearrangement of the electron subsystem associated with the GODC is thought to trigger transformations in the chemical bonds, producing the shrinkage of the initially loose metastable packing of the glass [42].

The UV induced compaction of the glass has two main consequences with respect to its final physical properties. Firstly, the glass density increases and, consequently, its refractive index also increases. Secondly, the glass structure is subjected to higher internal stresses, as was experimentally observed by Limberger [43]. This important observation invalidated other models that relied on a stress relief of the glass structure [44]. In his work, Limberger found a linear relationship between the change of refractive index and the increase of axial stress in the fibre core. A theoretical model that explains this relation by means of the correlation between the increase of axial stress and the compaction of the structure has been developed by Poumellec [45], reaching a reasonable agreement with experimental data. It is important to note

that the Kramers-Kronig causality relations between the real and imaginary part of the refractive index are of general validity, so that the compaction of the glass structure should also manifest itself through changes in the UV absorption spectrum. Digonnet has suggested that compaction introduces a shift in the UV absorption band edge [46], making it difficult to discern its contribution from that of some colour centres like the GeE'.

In section 3.5 of this chapter, we will present some experiments that corroborate that UV exposed optical fibres exhibit structural changes. In a first set of experiments we measured the stress changes in the core of UV exposed fibres, confirming the previously reported increase in the axial stress in the fibre's core [3]. A further consequence of the increased internal stress of UV exposed fibres is that its mechanical reliability should degrade. In a second set of experiments, we corroborated this prediction and quantified the mechanical strength degradation of UV exposed fibres.

3.3.1.c Methods to enhance the photosensitivity

The photosensitive mechanisms reviewed so far are dominant when the fibre is exposed to moderate fluences per UV laser pulse (<1 J/cm^2) and also moderate total accumulated fluences. They are usually referred as type I mechanisms. In order to enhance the photosensitivity of germanium doped fibres, several techniques have been proposed. Their objective is usually to increase the number of GODC in the fibre core. Refractive index changes of the order of 10^{-3} are routinely achieved with these methods.

A first method to photosensitise an optical fibre consisted in heating it with a hydrogen flame to a temperature of 1700 °C [47]. This procedure thermally excites a number of GODC, increasing considerably their corresponding UV absorption bands. Photoinduced refractive index changes of 10^{-3} have been reported with this technique.

A different and extremely efficient way to enhance the fibre photosensitivity is to load it with high pressure molecular hydrogen (20-750 Atm) at low temperatures [48,49]. The concentration of molecular hydrogen (H_2) loaded into the glass can reach 3% (mol). When the fibre is exposed to UV radiation, initially there is a reaction in which the molecular hydrogen is incorporated to the glass network as hydroxyl groups (OH^-), generating a GODC. Subsequently, the generated GODC are bleached by the type I mechanisms described previously. Lemaire [48] has reported refractive index changes of $5 \cdot 10^{-3}$ with this technique.

Another way to increase the photosensitivity of optical fibres is to add codopants to the germanosilica fibre core. Kashyap [50] has demonstrated that boron codoped fibres with high germanium concentration (15%) reached saturated refractive index changes of the order of 10^{-3} for accumulated fluences one order of magnitude smaller than equivalent germanium doped fibres without boron. Investigation of the UV absorption band indicated that the addition of boron does not increase the 240 nm absorption band. This perhaps means that the effect of the boron is not to increase the number of GODC precursors but to enhance mechanical transformations of the network once the process has been triggered.

Finally, the possibility of using shorter wavelength UV radiation to enhance the photoinduced transformations has been explored. A new photosensitive mechanism was discovered by Malo when exposing a lightly germanium doped fibre to 193 nm UV radiation [51,52]. The dependence of the grating growth rate with respect to the laser pulse fluence indicated that this mechanism consisted in the direct excitation of valence band electrons over the whole bandgap by a two-photon absorption process. Subsequently, these electrons are trapped by defect states in the middle of the bandgap. As this process does not rely on any precursor, its saturation is delayed and high refractive index changes can be achieved (10^{-3}). It is thought, however, that germanium related defects play an important role in the trapping of the excited electrons. Low germanium concentration fibres are necessary to observe this effect in order to avoid significant UV absorption in the core of the fibre, which would make the two photon absorption process very inefficient compared to one photon absorption processes. It is interesting to note that this was not the first time that high refractive index changes were induced in low germanium concentration silica fibres. Limberger [53] has reported changes of 10^{-3} irradiating low Ge silica fibres with 240 nm UV laser radiation. Although from their measurements it can not be proved, it is not unrealistic to think that a similar two-photon absorption mechanism was also responsible in this case.

3.3.1.d Type II photosensitivity mechanisms

New photosensitivity mechanisms have been reported to appear when the exposure fluences are increased. The first one [54] occurs when the accumulated UV exposure of highly germanium doped fibres (>18% mol) is extended to the range of several kJ/cm^2, while keeping a moderate fluence per laser pulse (<0.5 J/cm^2). In these conditions, a second and still unexplained mechanism has been shown to generate gratings with a negative refractive index perturbation.

This process is referred to as type IIa photosensitivity. The growth dynamics of the negative grating have been explained by assuming that there is a second independent mechanism, slower than the type I process, that has a delayed saturation and continues growing when the type I process reaches its saturation. This behaviour has also been reported in boron codoped germanosilica fibres exposed to 193 nm UV radiation, where gratings with a refractive index change of $-3 \cdot 10^{-4}$ were created with an overall fluence of 2.5 kJ/cm^2 [55]. One important characteristic of type IIa gratings is that they are stable at temperatures of the order of 500 °C.

Another interesting photosensitivity mechanism (Type IIb) occurs when the fluence of the UV laser pulse is increased over 1 J/cm^2. In this regime, thermal breakdown at the core-cladding interface, due to the absorption of the intense UV radiation, gives rise to a heating of the lattice with consequent melting or fracture of the material. Very large changes of refractive index can be induced by this mechanism ($>10^{-3}$), permitting the fabrication of gratings with a single UV laser shot [56,57]. Type IIb gratings have also been demonstrated with 193 nm UV radiation [58]. The two most distinctive features of type IIb gratings are: first, that they couple light efficiently to radiation modes at short wavelengths due to the nonuniform refractive index change across the core; and second, that they are thermally stable at temperatures as high as 800 °C, which is approximately the temperature induced in the fibre during the thermal breakdown process.

3.3.1.e Thermochemical gratings

Recently, a new type of photosensitive effect has been discovered [59]. A germanium doped and fluorine codoped optical fibre is initially loaded with high pressure and low temperature molecular hydrogen. The loaded fibre is then exposed to UV radiation, triggering the reaction that incorporates the molecular hydrogen to the glass network as a hydroxyl radical (OH^-). Subsequent annealing at elevated temperatures (1000 °C) induces a second reaction which combines the previously dissociated H^+ with the F^- dopant to produce hydrofluoric acid HF, which rapidly outdiffuses from the fibre, giving rise to a change of refractive index in the UV exposed regions. The main advantage of these gratings is their excellent stability at elevated temperatures (800 °C).

3.3.2 Photoinduced birefringence

The exposure of optical fibres to polarised blue-green or UV light can result in an anisotropic change of its dielectric permittivity. This phenomenon was first observed by Parent when studying the reflectivity of Bragg gratings written with polarised green light by the Hill method [60]. The reflected light was maximum when the reading beam had the same polarisation as that of the writing beam [60,61]. Other experiments have also demonstrated permanent changes of birefringence in fibres exposed to blue-green light [62-64].

The control of the fibre's birefringence by means of blue-green or UV light exposures has permitted the fabrication of polarisation rocking filters in polarisation preserving fibres. The first polarisation rocking filter was demonstrated by Russell [62], who wrote a rocking filter in a stress birefringent fibre by launching 488 nm blue radiation with a linear polarisation oriented at 45° with respect to the fibre birefringence axes. As the polarisation state of the light evolves periodically along the fibre, a periodic perturbation of $\Delta\varepsilon_{xy}$ was induced in the core, giving rise to the formation of a polarisation coupler (section 3.2). The authors suggested that the photoinduced changes in the birefringence were aligned with the major axis of the local polarisation state along the fibre. The coupling efficiency of this first rocking filter, 10%, corresponded to a change of birefringence of 10^{-6}. Polarisation rocking filters with efficiencies of 100% were first demonstrated by Kanellopoulos [64], who wrote rocking filters with 488 nm and 514 nm laser radiation in elliptical-core fibres doped with very high germanium concentrations (25-30% mol). This study also showed that the induced birefringence perturbation had a reduced thermal stability, being erased at temperatures of 240 °C. The growth of rocking filters by internal propagation of blue-green light along the fibre core is a self-organised process with complex dynamics. A theoretical model for this process, based on two-photon preferential bleaching of glass defects, was first proposed by Sipe [65].

The possibility of inducing birefringence changes by exposing optical fibres to UV radiation was first shown by Hill [66]. He demonstrated a new method to fabricate rocking filters that consisted in the external point by point exposure of the fibre to polarised UV radiation with the linear polarisation oriented at 45° with respect to the axes of the fibre. Rocking filters with 100% efficiency and photoinduced birefringence in the 10^{-6}-10^{-5} range can be fabricated with this technique, which has an efficiency 10^6 times superior to that of the blue-green light internal method [67]. The photoinduced anisotropy has been shown to be enhanced by high germanium concentrations in the core and also by molecular hydrogen loading of the fibre [63,68]. It is

interesting to mention that the exposure of hydrogenated elliptical core fibres to 248 nm UV radiation leads to a nonmonotonic response of the photoinduced anisotropy with respect to the accumulated UV fluence. At high fluences, the photoinduced birefringence seems to reverse its sign [68]. Also, it has been shown that 193 nm UV radiation is more efficient than 248 nm to induce changes of birefringence [69]. The highest photoinduced birefringence reported had a value of $7 \cdot 10^{-5}$ and was induced in a low birefringence hydrogenated fibre exposed to 248 nm UV radiation [70].

Rocking filters have found applications in areas such as sensing or optical communications. Several schemes that employ rocking filters have been demonstrated for the simultaneous measurement of strain and temperature [71,72]. Also, demultiplexing of serial data has been achieved by pulse switching induced by cross-phase modulation in rocking filters [73].

3.3.2.a Physical mechanisms of photoinduced anisotropy

The most successful model to explain the photoinduced birefringence in optical fibres is the preferential depletion model, which is based on the colour centre photosensitivity model discussed in 3.3.1.a. However, the overall picture is not complete yet, and the role of other effects, including stresses and compaction, in the photoinduced anisotropy has to be clarified.

The depletion model has been proposed by several authors [74-78]. It is based on the fact that although the germanosilica glass is isotropic on a macroscopic scale, the individual molecular bonds are, on the contrary, very anisotropic, with much higher polarisability along the direction parallel to the bond. As we have seen in section 3.3.1, blue-green and UV light can interact strongly with certain glass defective bonds, the GODC. Photoinduced anisotropy is thought to be due to the preferential excitation (and depletion) of those anisotropic defects (GODC) whose polarisability is aligned with the polarisation of the incident electric field, causing a reduction of polarisability along that direction. The excited electron is then trapped isotropically, giving rise to a different electronic defect that contributes mainly to the positive isotropic refractive index change (colour centre model).

Theoretical expressions have been derived to explain the functional dependence of the photoinduced changes in the permittivity tensor on the electric fields of the blue-green or UV radiation [75,78]. For the case of exposure to blue-green light (i.e. two-photon absorption

process) and assuming that z is the axis of the optical fibre and that the light is polarised along the XY plane, the change in the permittivity tensor induced by the electric fields E_x and E_y is:

$$\begin{aligned}\Delta\varepsilon_{xx} &= -C \quad \left\{5|E_x|^4 + |E_y|^4 + 4|E_x|^2|E_y|^2 + \left(E_x^2 E_y^{*2} + \text{c.c.}\right)\right\} \\ \Delta\varepsilon_{xy} &= -2\,C \quad \left(|E_x|^2 + |E_y|^2\right)\left(E_x E_y^* + \text{c.c.}\right)\end{aligned} \tag{21}$$

where C is a constant that depends on the material and the time of exposure. $\Delta\varepsilon_{yy}$ will follow a symmetric relation with respect to $\Delta\varepsilon_{xx}$. In this derivation, it was assumed that the GODC are isotropically oriented and that the material is far from saturation so that (21) is only valid for the initial moments of exposure.

The corresponding equations in the case of UV exposure (i.e. one-photon absorption process) are:

$$\begin{aligned}\Delta\varepsilon_{xx} &= -C' \quad \left(3|E_x|^2 + |E_y|^2\right) \\ \Delta\varepsilon_{xy} &= -C' \quad \left(E_x E_y^* + \text{c.c.}\right)\end{aligned} \tag{22}$$

Equations (21) and (22) can be used in conjunction with (8) and (9) to predict the behaviour of photogenerated polarisation gratings in optical waveguides.

There are some experimental results that support this model. In an experiment carried out by Poirier [76] it was observed that the luminescence induced by polarised UV radiation was independent of that induced by an orthogonally polarised UV beam, as if different sets of defects were involved in these processes. In another experiment, Albert [77] observed differential absorption between the two orthogonal polarisations (dichroism) in a sample of ion implanted silica exposed to polarised UV light.

However, there are also experimental observations that cannot be fully accounted for by the previous model. Russell [74], for example, observed that stress birefringent fibres show very different photoinduced birefringence depending on whether they are exposed to light polarised along the fast or slow axis. When green light is launched into the fibre polarised along the fast axis, no significant change in birefringence is produced. It has been argued that this is probably due to the role of stress in the alignment of the glass defects (either the precursor GODC or the

photogenerated defects). Also, compaction and stress changes are more likely to occur in stressed fibres like this [79,80]. However, no full explanation is still available.

A less dramatic asymmetry between the slow and fast axes has been observed in elliptical core fibres [75]. Green light launched into the fibre had a tendency to end up polarised along the fast axis, with independence of the launched polarisation state. A possible reason for this behaviour was the existence of an anisotropic distribution of GODC between the two axes. However, luminescence experiments [76] indicated that this was not the case, and that the distribution of GODC was uniform. Again, stress and compaction of the glass network were claimed as possible reasons for this asymmetry.

Low birefringence fibres exhibit reversible birefringence changes when exposed along different directions [74,81]. The photoinduced changes in the fibre's birefringence can be erased and created again many times by means of two orthogonally polarised blue-green or UV beams. When the two orthogonal beams are switched, initially there is a very fast change of birefringence (transient regime), followed by a further slower growth. This behaviour could be explained if we assume that the defects photogenerated after breakage of the GODC have also some anisotropy, and can be rapidly reoriented according to the polarisation of the incident beam. The experimentally observed relaxation of the photoinduced birefringence when the blue-green or UV beam is blocked could also be explained as a reorientation of a small fraction of these defects. However, these hypotheses have not been experimentally confirmed.

Finally, apart from the mechanisms so far discussed, a new mechanism has been suggested to contribute to the final photoinduced birefringence [82]. An asymmetric absorption of UV light across the core can give rise to an also asymmetric refractive index profile and, consequently, to waveguide birefringence. This mechanism would be insensitive to the polarisation of the UV light employed. Presently, it has been firmly established that the polarisation dependent mechanisms are the most important for the generation of photoinduced birefringence. However, this residual contribution could be important for some special UV exposure geometries.

3.4 FABRICATION OF POLARISATION FILTERS WITH TAILORED RESPONSE

Most of the polarisation filters presented so far in the literature have a uniform structure and can be described by equation (16). In this section, we are going to demonstrate a method to fabricate rocking filters with nonuniform coupling coefficients c(z):

$$c(z) = \kappa(z)\, e^{-jKz} + c.c. \tag{23}$$

where K is equal to $2\pi/\Lambda$, and Λ is the average periodicity of the structure. In this case, the equations verified by the propagating fields will be a modified version of (16). If we assume that the beatlength between the two polarisation modes can vary along the fibre, these equations will be:

$$\frac{d}{dz}\begin{bmatrix}\tilde{A}_x \\ \tilde{A}_y\end{bmatrix} = \begin{bmatrix} -j\kappa(z)\, e^{+j\int_0^z \left(\frac{2\pi}{L_B(\lambda,z')}-K\right)dz'} & \\ & -j\kappa(z)^*\, e^{-j\int_0^z \left(\frac{2\pi}{L_B(\lambda,z')}-K\right)dz'} \end{bmatrix} \begin{bmatrix}\tilde{A}_y \\ \tilde{A}_x\end{bmatrix} \tag{24}$$

where $L_B(\lambda,z)$ is the local beatlength at position z and wavelength λ.

Polarisation filters with tailored coupling spectra will be necessary for practical applications, for instance, filters with apodised sidelobes. The function c(z) that yields a particular coupling spectrum can be calculated with the use of inverse scattering techniques. The fabrication of these filters will require an accurate control of the coupling coefficient c(z) along the filter. In section 3.4.1, we will present some experiments that suggest that the coupling coefficient can be adequately controlled by means of the angle between the birefringence axes of the fibre and the polarisation of the radiation that induces the birefringence changes. These experiments, carried out with blue-green radiation, will also serve to confirm some aspects of the depletion model previously discussed. In section 3.4.2 we will demonstrate the technique by writing a Moiré polarisation grating with UV radiation [2].

3.4.1 Polarisation dependence of photoinduced birefringence

In order to characterise the polarisation dependence of the photoinduced birefringence, we wrote rocking filters by the internal method launching linearly polarised continuous-wave green light (514.5 nm) from an argon-ion laser at different angles ϕ with respect to the major axis of an elliptical core fibre. The experimental set-up is described in Figure 9.

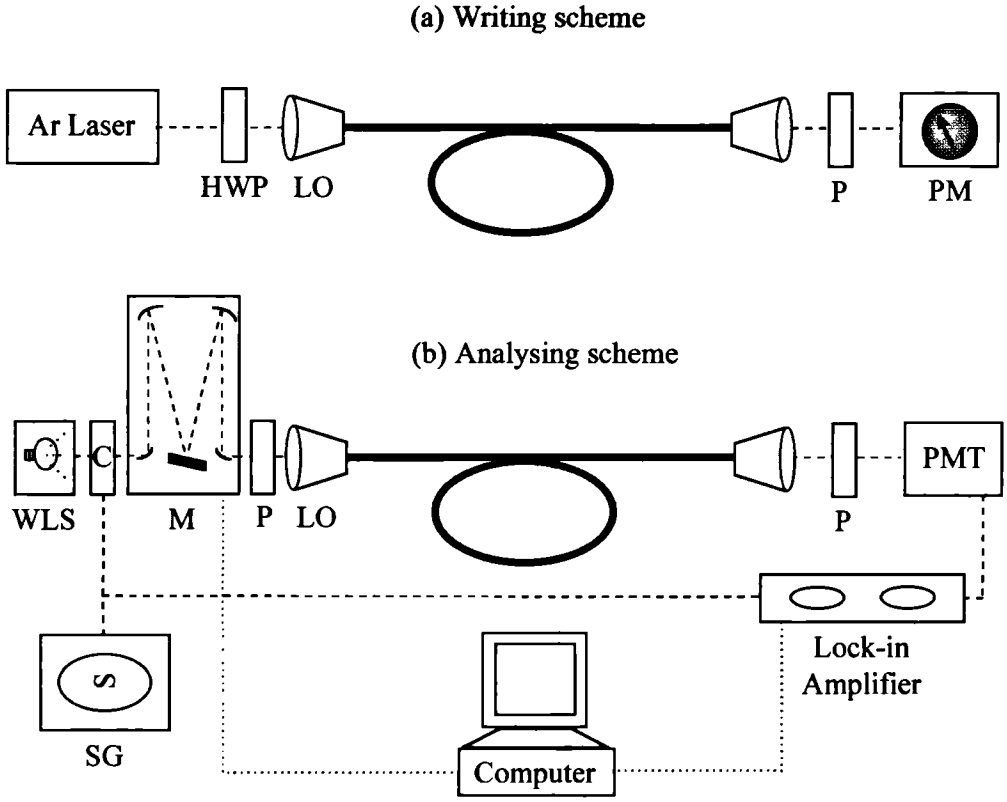

Figure 9. Experimental set-up. (a) Writing scheme. Ar: Argon-ion, HWP: half-wave plate, LO: launching optics, P: polariser, PM: power-meter. (b) Analysing scheme: WLS: white-light source, C: chopper, M: monochromator, P: polariser, LO: launching optics, PMT: photomultiplier tube, SG: signal generator.

In the writing set-up, the angle ϕ between the polarisation of the laser light and the axes of the fibre was controlled by means of a half wave plate. For the spectral characterisation of the rocking filters, the set-up consisted of a white light source modulated in intensity by a chopper, and a photomultiplier detector connected to a lock-in amplifier. A polariser was used in conjunction with an analyser to interrogate the transfer of power between the two polarisation modes.

The elliptical core fibre, manufactured by Andrew Corporation, had core dimensions of 1x2μm, a core-cladding index difference of 0.03 and was single mode at 514 nm. The total length of the filters was 132 beatlengths, each beatlength being 4.5 mm at 514 nm. The fibres were exposed to 140 mW for 15 minutes.

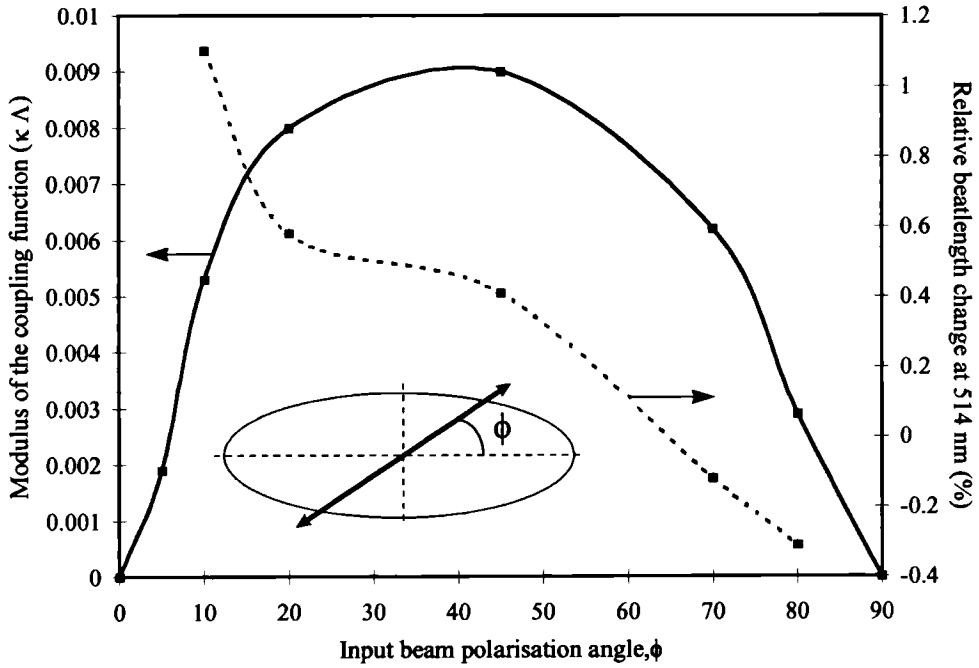

Figure 10. Angular dependence of photoinduced birefringence. κΛ is the coupling strength per beatlength (20); and $\delta L_B/L_B$ (relative change of beatlength) is related to the shift of the resonance wavelength δλ through equation (25).

After the exposure, we monitored the coupling spectrum of each filter, observing their maximum coupling efficiency and also the position of these resonant coupling wavelengths. The results for one set of experiments can be seen in Figure 10. Other sets of experiments were carried out with slightly different exposure conditions, but the results had the same general features as those represented in Figure 10.

The first interesting feature of these results is that the resonance wavelength of the filters depended on the angle ϕ. Filters written with angles near the slow axis were blue shifted with respect to those written with angles near the fast axis. This can be observed, for instance, in Figure 12, which shows the coupling spectrum of two rocking filters, one written for ϕ equal to

20° and the other for a ϕ equal to 70°. The reason for these shifts is that a change in the background birefringence of the fibre is produced during the writing process due to the imbalance of power between the slow and fast axes. This effect is adequately described by the first expression in equation (21). When the light is polarised mainly along the slow axis there is a reduction in the background birefringence, giving rise to a blue shift. Conversely, when the light is mainly polarised along the fast axis, the background birefringence increases, giving rise to a red shift.

The shifts can be approximately related to the changes in birefringence (or beatlength) according to the following reasoning. Let us assume that initially the fibre birefringence is Δn (2), and that at the end of an exposure with a writing wavelength of λ_W the final birefringence is $\Delta n+\delta n$, where δn is the photoinduced contribution to the background birefringence. The written rocking filter will have an average periodicity that corresponds to a beatlength $\lambda_W/(\Delta n+(1/2)\delta n)$. The resonance wavelength in the reading process λ_R will be shifted by $\delta\lambda$ with respect to λ_W according to the equation:

$$\delta\lambda \approx \lambda_R - \lambda_W \approx \frac{\lambda_W}{\Delta n}\frac{\delta n}{2} \approx -\frac{1}{2}\frac{\delta L_B}{\partial L_B / \partial \lambda} \qquad (25)$$

where δL_B is the shift in beatlength corresponding to a $\delta\lambda$ shift of resonance wavelength. δL_B has been represented in Figure 10. It is important to realise that the signs of the shifts of the resonance wavelengths are in agreement with those predicted by the depletion model (negative birefringence).

As a further proof of the resonance wavelength shifts and their relation to the background changes in birefringence, we exposed again (post-exposed) rocking filters written with ϕ equal to 45° to green light polarised along the fast and slow axes. The results, shown in Figure 11, reinforce the previous experiments. Postexposure along the slow and fast axes gives rise to blue and red shifts respectively. Also, a partial erasure of the rocking filters was produced during this process due to the interaction of the green light with the previously written rocking filter. Similar type of shifts of the resonance wavelength have also been seen during the inscription of Bragg gratings [83].

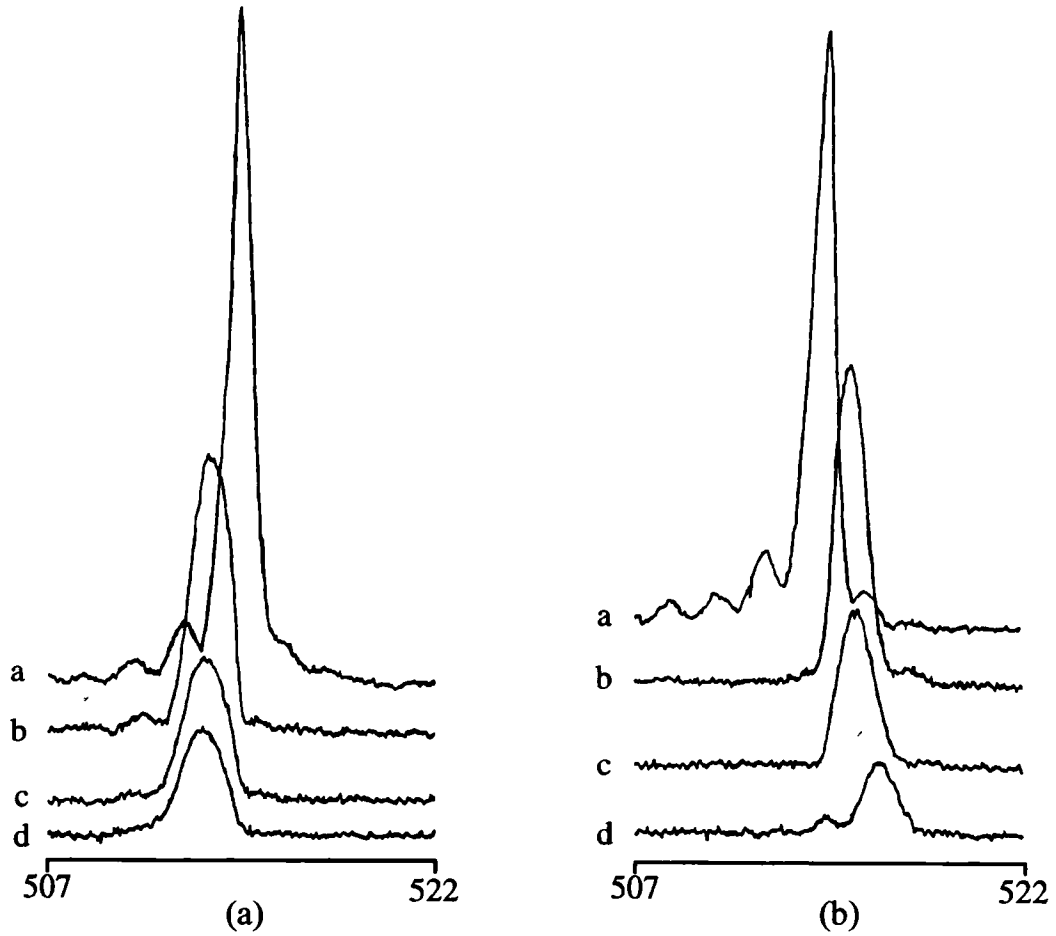

Figure 11. Double exposure experiments. The rocking filter in (a) was initially written with ϕ equal to 45° and then post-exposed to green light polarised along the slow axis. Analogously, the rocking filter in (b) was initially written with ϕ equal to 45° and then post-exposed to green light polarised along the fast axis.

A second feature of the angular experiments was the dependence of the coupling efficiency on the inscription angle ϕ. It can be observed in Figure 10 that the maximum efficiency is produced for ϕ near to 45° and that the efficiency was almost null for angles near the axes. This result can be explained from the second expression in equation (21), that states that κ is a function of ϕ, varying as:

$$\kappa(\phi) \propto \sin 2\phi \tag{26}$$

We will make use of this fact to control the coupling efficiency of nonuniform filters in the next section.

A careful observation of Figure 10 shows that the experimental $\kappa(\phi)$ exhibits a slight angular asymmetry in comparison with the symmetric behaviour described in (26). Rocking filters written at angles near the slow axis had stronger coupling efficiencies than those written at angles near the fast axis with similar exposure conditions (Figure 12). This observation can be related to a previous observation by Lauzon [75], who reported that green light launched into an elliptical core fibre had a strong tendency to end up polarised along the fast axis with independence of the incident angle ϕ. We have monitored the fraction of power polarised along the fast axis at the exit of the couplers represented in Figure 12 (a) during the writing process, confirming this observation. This power evolution is also shown in Figure 12 (b).

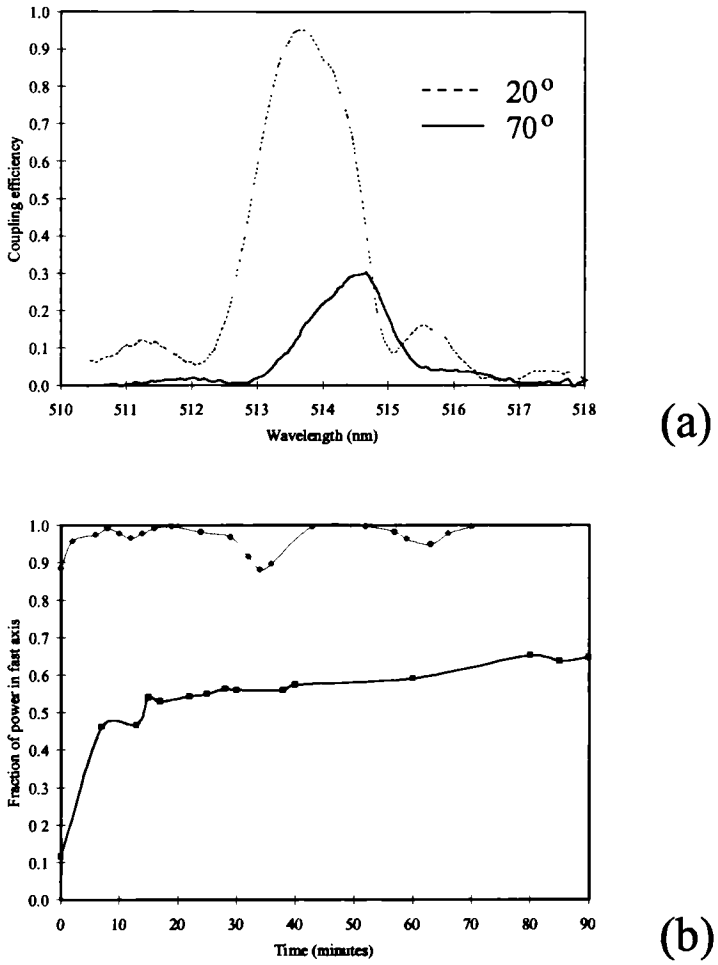

Figure 12. (a) Coupling spectra of rocking filters written at angles ϕ of 20° and 70° with respect to the slow axis. (b) Evolution of the fraction of power in the fast axis during the writing process of the previous couplers (the lower curve corresponds to ϕ equal 20°).

The observed asymmetry cannot be explained with the model described by equation (21). This model predicts that when the launched power is not balanced between the two polarisation modes, the polarisation of the light at the exit of the filter evolves towards the axis that initially had more power, due to a dynamic interaction of the light with the rocking filter [65]. This behaviour would be symmetric with respect to ϕ=45°, in contrast to the experimental observations. The redistribution of power between the two polarisation modes is the result of a mismatch between the instantaneous fibre beatlength and the periodicity of the written rocking filter (due to background changes of the birefringence). The observed asymmetry in the power redistribution process was initially explained in terms of an anisotropy in the GODC angular distribution [75]. However, this hypothesis was experimentally proved not to be valid [76]. The most probable reason for the observed behaviour seems to be additional contributions to the background birefringence due to compaction and stress variations in the fibre [76], but an experimental confirmation is still lacking.

As a summary, we have seen that the depletion model can explain the general features of the described experiments. For exposures with radiation polarised near the slow (or fast) axis, a reduction (or increase) of the background birefringence are respectively induced. Also, the filters with maximum coupling efficiency are created for incident linear polarisations at 45° with respect to the axes, decreasing the efficiency as the incident linear polarisation becomes parallel to the axes. Finally, we have observed an asymmetry in the angular dependence of the coupling efficiency of the rocking filters, that can be correlated with a previously reported asymmetry [76] in the evolution of the power distribution between the two polarisation modes.

3.4.2 Polarisation filters with tailored response: UV experiments

The usual procedure to write rocking filters that operate at long wavelengths is to externally expose the fibre point by point to UV polarised light. In our set-up, the UV beam is polarised perpendicularly to the plane defined by the fibre and the incident beam; and the axes of the elliptical core fibre form an angle ϕ (usually 45°) with respect to the UV polarisation. The experimental set-up is shown in Figure 13.

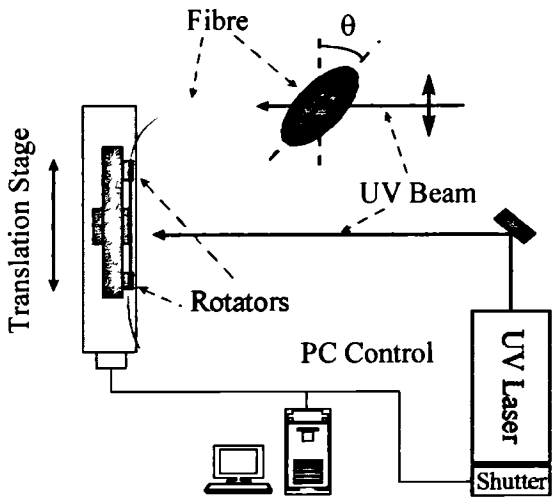

Figure 13. U.V. experimental set-up for the fabrication of tailored rocking filters.

The fabrication of polarisation rocking filters with tailored coupling spectrum requires an accurate control of the phase and modulus of $\kappa(z)$ (33). The phase of $\kappa(z)$ can be easily controlled by changing the distance between adjacent points of exposure. The modulus of $\kappa(z)$, on the other hand, could be in principle tailored by monitoring the total fluence delivered to each exposed point. However, this method is not very reliable because of the nonlinear fibre response due to saturation of the photo-induced birefringence. Besides, it has also been shown that for high fluences the fibre response could be non-monotonic [68]. From the previous experiments with green light, it is clear that an alternative procedure could be to control accurately the angle ϕ between the fibre's major axis and the polarisation of the UV beam. $\kappa(z)$ would then be proportional to $F \cdot \sin(2\phi)$, where F is a function of the total fluence of the exposure. It can also be appreciated that the sign of c(z) in (23) will depend both on the angle of exposure ϕ ($\sin 2\phi \gtrless 0$) and on the position of exposure (phase of $\kappa(z)$).

To demonstrate this fabrication method, we have built a polarisation Moiré grating, which is an example of a device that needs control of the coupling coefficient along its length. Contradirectional Bragg Moiré gratings have been previously demonstrated by two stage exposures, each of them generating a grating with a slightly different periodicity [84]. We have carried out several experiments during this work which indicate that double exposure techniques fail in the fabrication of polarisation Moiré gratings. We think that the reason is that, due to the reversibility of the photo-induced birefringence [74,81], the final change of birefringence after the second exposure is not the linear sum of the changes induced in each individual exposure.

The coupling function c(z) for a polarisation Moiré grating is:

$$c(z) \propto \cos\left(\frac{\pi z}{L}\right) \sin\left(\frac{2\pi z}{\Lambda}\right) \tag{27}$$

where L is the total length of the filter. To achieve this perturbation of birefringence with the present technique, the axes of the fibre were uniformly twisted from an angle ϕ equal to 45° at the beginning of the filter (z=0) to an angle of -45° at the filter's end (z=L) during the UV exposure. The elliptical core fibre used, made by Andrew Corporation, had a beatlength of 4.4 mm at 658 nm. It was exposed to 240 nm UV radiation in 40 equidistant points with one beatlength separation between adjacent points. Each point had a longitudinal exposed length of 2 mm and received a total fluence of 11 J/cm^2.

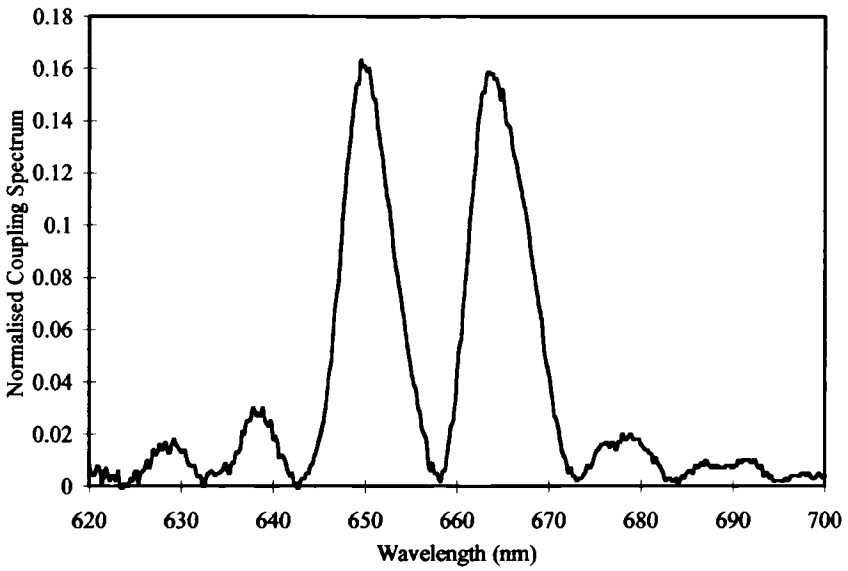

Figure 14. Coupling spectrum of the polarisation Moiré filter.

The coupling spectrum of the polarisation Moiré grating is shown in Figure 14. The phase of the filter response was also retrieved by launching light polarised at 45° with respect to the axes and monitoring the interference signal that appears after a polariser aligned to one of the fibre axes. From the filter's modulus and phase response, we calculated, in first order Born approximation, the modulus and phase of the coupling function $\kappa(z)$ along the filter. This is represented in Figure 15. It can be observed that the modulus of $\kappa(z)$ is maximum at the

beginning and end of the filter, where ϕ was 45° and -45° respectively. Also, there is an abrupt change of π in the coupling phase as the angle ϕ passes through 0°.

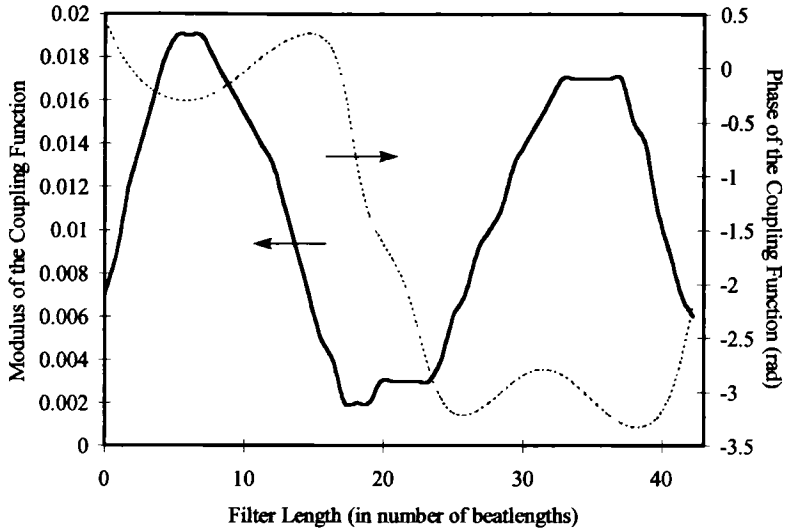

Figure 15. Modulus and phase of the coupling function $\kappa(z)\Lambda$

As a conclusion, we have demonstrated that the angle ϕ between the axes of an elliptical core fibre and the polarisation of the UV radiation can be used to control the polarisation coupling coefficient and, consequently, to fabricate rocking filters with tailored spectral response.

3.5 MECHANICAL EFFECTS IN UV EXPOSED OPTICAL FIBRES

The irradiation of optical fibres to UV light induces changes in their optical properties than can be used to fabricate a great variety of grating devices. In the last section, for instance, we have studied the fabrication of birefringence gratings by exposing polarisation-preserving fibres to polarised UV light. We have also discussed in Section 3.3.1.b that the exposure of optical fibres to UV radiation leads to structural transformations in the glass network. These mechanical modifications probably play an important role in the photosensitivity of optical fibres. In this section, we are going to study experimentally some of the mechanical properties of UV exposed optical fibres. This study will help to understand some aspects of the photosensitivity effect, and also will be useful to assess the mechanical reliability of devices fabricated by exposure to UV radiation.

3.5.1 Photoinduced stress in UV exposed optical fibres

3.5.1.a Stresses in unexposed optical fibres

Unexposed optical fibres support internal stresses which usually have two different origins. The first are thermally-induced stresses, due to the mismatch between the thermal expansion coefficients of different regions of the fibre (core and cladding) [85]. The axial thermal stress σ_z^{th} varies along the radial direction r according to the expression:

$$\sigma_z^{th}(r) = \frac{Y}{1-\nu}\left(\alpha(r) - \langle\alpha\rangle\right)\left(T_s - T_r\right) \qquad (28)$$

where Y is the Young's modulus, ν is the Poisson ratio, $\alpha(r)$ is the expansion coefficient at the radial distance r, $\langle\alpha\rangle$ is the average expansion coefficient over a transverse section of the fibre, and $(T_s\text{-}T_r)$ is the difference between the fibre setting temperature (from which the fibre behaves elastically) and the room temperature.

The second source of stresses in optical fibres are mechanically-induced due to the force F applied to the fibre during the drawing process [86,87]. As the cladding usually has higher viscosity than the core, it takes most of the drawing tension. When the drawing tension is

finally released, the axial stress in the cladding is reduced and the core is compressed. An approximate expression for the axial stress due to the drawing process σ_z^d is:

$$\sigma_z^d(r) = \frac{F}{A}\left(\frac{\eta(r) - \langle\eta\rangle}{\langle\eta\rangle}\right) \tag{29}$$

where F is the drawing force, A is the transverse section of the fibre, $\eta(r)$ is the viscosity at position r, and $\langle\eta\rangle$ is the average viscosity over the transverse section of the fibre. From (28) and (29), it can be appreciated that $\langle\sigma_z^{th}\rangle = \langle\sigma_z^d\rangle = 0$.

The overall axial stress in the fibre, $\sigma_z(r)$, would be calculated by adding the thermal $\sigma_z^{th}(r)$ and drawing $\sigma_z^d(r)$ contributions. Taking into account the axial symmetry of the problem, the rest of the stress components are obtained from $\sigma_z(r)$ by means of the expressions:

$$\begin{aligned} \sigma_r(r) &= \frac{1}{2}\frac{1}{A(r)}\int_{A(r)} \sigma_z(r)\, dA \\ \sigma_\theta(r) &= \sigma_z(r) - \sigma_r(r) \end{aligned} \tag{30}$$

where $A(r)$ is equal to πr^2.

3.5.1.b Measurement of the axial stress in optical fibres

The information about the stress distribution across an optical fibre is usually obtained by exploiting the photoelastic effect. In a typical measurement system [88,89], a linearly polarised beam from a He-Ne laser is focused onto the fibre sample with the plane of polarisation at 45° with respect to the fibre axis (Figure 16). Due to the photoelastic effect, the two orthogonal field components experience a relative retardation. Subsequently, the light passes through a quarter waveplate (oriented at 45° with respect to the fibre axis) that converts its state of polarisation back to linear again. By means of a polariser, the polarisation rotation angle is measured and, from this, the retardation R can be calculated. By scanning vertically across the fibre (x axis), the function R(x) can be found. The axial stress $\sigma_z(r)$ is then calculated from R(x) using the Abel transform [88,89]:

$$\sigma_z(r) = -\frac{1}{\pi C}\int_r^{R_f} \frac{dR(x)/dx}{\sqrt{x^2 - r^2}}dx \qquad (31)$$

where C is the stress optical coefficient and R_f the fibre radius.

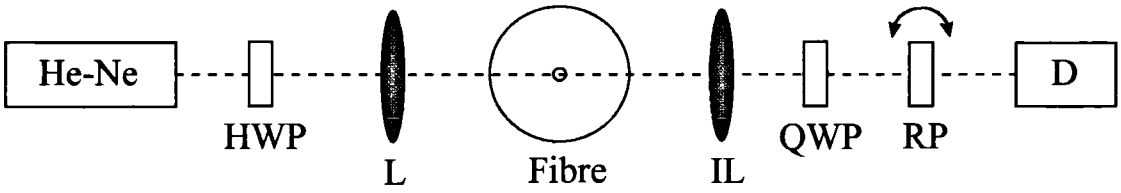

Figure 16. Stress measurement system. He-Ne: Helium-Neon laser, HWP: half-wave plate, L: lens, IL: imaging lens, QWP: quarter-wave plate, RP: rotating polariser, D: detector.

The system used for the stress measurements presented in the next section was fabricated at the National Physics Laboratory (NPL) and had significant improvements over the basic system described before [90]. The measurement of retardations was made through the half-shade technique, that overcomes the insensitivity of the analyser to small rotations near the minimum intensity position. The main idea is to measure the difference of two field intensities proportional to $(1+\cos(\delta_S+\delta_R))$ and $(1+\cos(\delta_S-\delta_R))$ respectively, where δ_S is the so called half-shade angle and δ_R is the phase retardation sought. These fields are generated by first dividing the incident beam in two halves with linear polarisations that form an angle of $2\delta_S$ between them, and then imaging these fields to the output plane through an optical system very similar to that previously described in Figure 16. The difference of intensity between the two halves of the imaged beam is proportional to $\sin\delta_S \cdot \sin\delta_R$, which is a function very sensitive to small variations of the retardation δ_R. The best phase measurement accuracy of the system is about 0.005°, which translates into a stress error of less than 10 MPa.

The spatial resolution of the system depends on the microscope objectives used. Resolutions of 0.5 μm and 0.3 μm can be achieved with objectives of numerical apertures 0.8 (x50) and 1.3 (x100) respectively. This high spatial resolution allows an accurate mapping of the stress distribution along photogenerated fibre devices. For more details about the stress measurement system the reader is referred to reference [90].

3.5.1.c Stress changes in UV exposed optical fibres

The exposure of optical fibres to UV radiation induces an increase in the axial stress of the fibre core. This observation was first reported by Limberger [43,91], who also showed that a linear correlation existed between the positive changes in refractive index and the induced variations in the axial stress. However, none of these variables scaled linearly with the accumulated UV fluence used in the fibre exposures. Both the refractive index and the axial stress increased faster at the beginning of the exposure, reaching saturation at high fluences.

The increase of stress in the fibre core indicates that the glass network transforms under UV irradiation into a more compact configuration with, consequently, higher refractive index (section 3.3.1.b). The photoelastic contribution to the overall refractive index, which is negative, is of smaller magnitude than the positive changes due to compaction.

In this section, we will firstly present some measurements that support the previously reported observations. Secondly, and as a result of the high spatial resolution of our measurement system, we will report the direct observation of stress modulations along the longitudinal direction of a photogenerated fibre Bragg grating [3].

The fibre used in these experiments was a photosensitive germanium doped and boron codoped silica fibre. The core-cladding refractive index difference was 0.0065 and the core had a radius of 5 μm (Figure 17). The estimated concentrations of germanium dioxide and boron oxide were 8% (weight) and 12% respectively. The fibres were exposed to UV radiation from an excimer laser that could operate either at 193 nm (ArF) or at 248 nm (KrF).

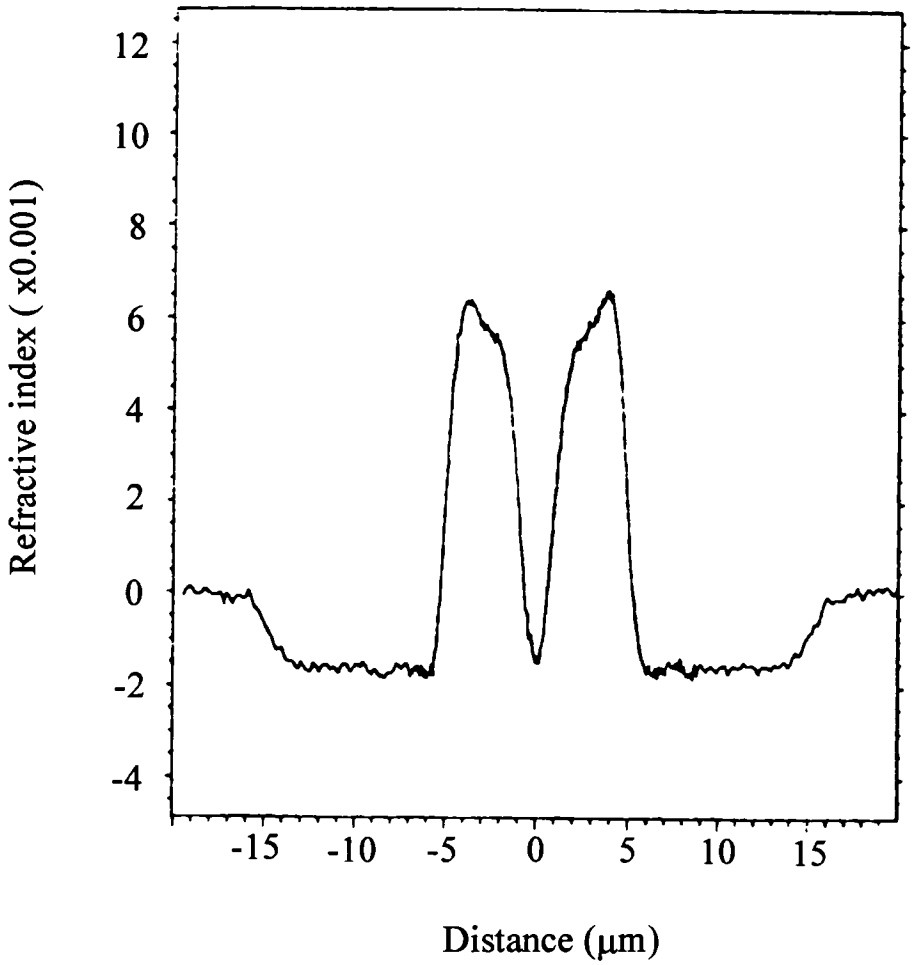

Figure 17. Refractive index profile of the boron-germanosilica fibre used in the experiments.

First we measured the axial stress profile due to thermal effects and the drawing process in a fresh sample of fibre (Figure 18). It can be appreciated that this stress profile correlates with the refractive index profile of the fibre (Figure 17). The maximum axial stress σ_{max}(fresh) in the core was 155 MPa.

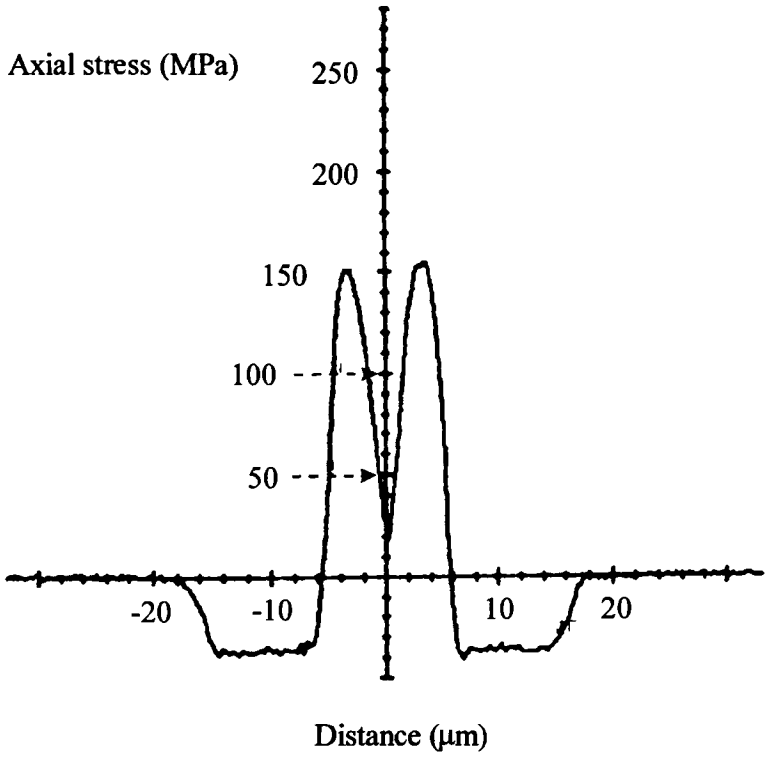

Figure 18. Axial stress profile of a fresh sample of fibre.

Several samples of the fibre were exposed to UV radiation and then analysed with the stress profiler (set at a coarse spatial resolution). In all cases the fluence per laser shot was in the range 300-600 mJ/cm^2. When the fibre was exposed to an accumulated fluence of 400 J/cm^2 with 193 nm UV radiation, the peak of the axial stress σ_{max}(193nm,400J/cm^2) increased to 270MPa, as can be observed in Figure 19. The relative increase of axial stress with respect to the unexposed fibre $\Delta\sigma$ (193nm,400J/cm^2) was 115 MPa. When the accumulated exposure was reduced to 40 J/cm^2, σ_{max}(193nm,40J/cm^2) was 200 MPa and the corresponding change in the peak stress $\Delta\sigma$ (193nm,40J/cm^2) was 45 MPa.

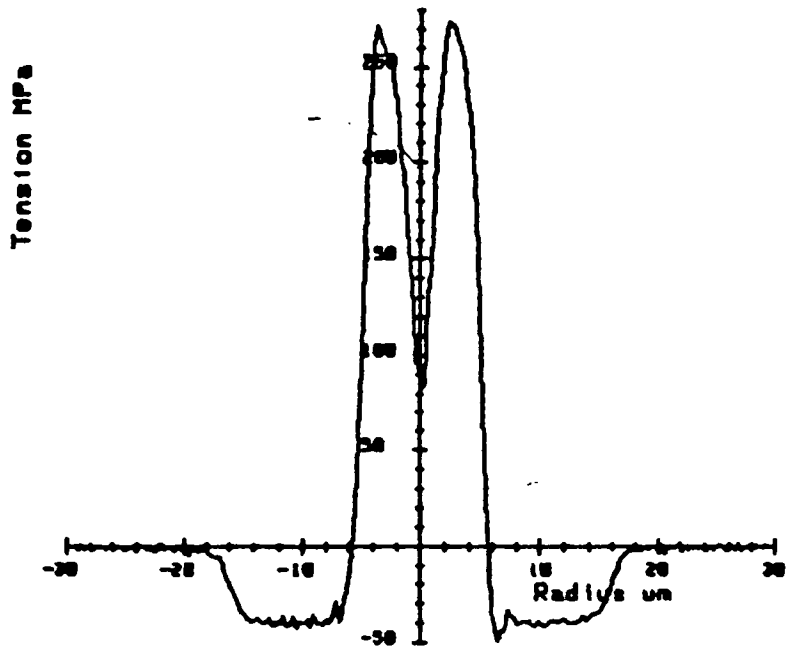

Figure 19. Axial stress profile of a sample of fibre exposed to an accumulated fluence of 400J/cm^2 with 193 nm UV radiation

Similar experiments were carried out with 248 nm UV radiation. An exposure of 500 J/cm^2 led to a maximum tensile stress σ_{max}(248nm,500J/cm^2) of 230MPa, that corresponds with an increase $\Delta\sigma$(248nm,500J/cm^2) of 75 MPa. Finally, when the exposure was reduced to 50 J/cm^2, σ_{max}(248nm,50J/cm^2) was 190 MPa and $\Delta\sigma$(248nm,50J/cm^2) was 35 MPa. All these results are summarised in Table 1:

	σ_{max}(MPa)	$\Delta\sigma$(MPa)
Unexposed	155	0
193 nm, 40 J/cm^2	200	45
193 nm, 400 J/cm^2	270	115
248 nm, 50 J/cm^2	190	35
248 nm, 500 J/cm^2	230	75

Table 1. Summary of the stress changes induced in UV exposed fibres (σ_{max} is the peak value of axial stress in the core, and $\Delta\sigma$ is the increment of σ_{max} due to the UV exposure).

Although we only have two experimental points, it is worthwhile to plot the increase in the axial stress $\Delta\sigma$ versus the accumulated fluence of the UV exposure. This is shown in Figure 20, where the nonlinear response due to saturation effects can be clearly seen.

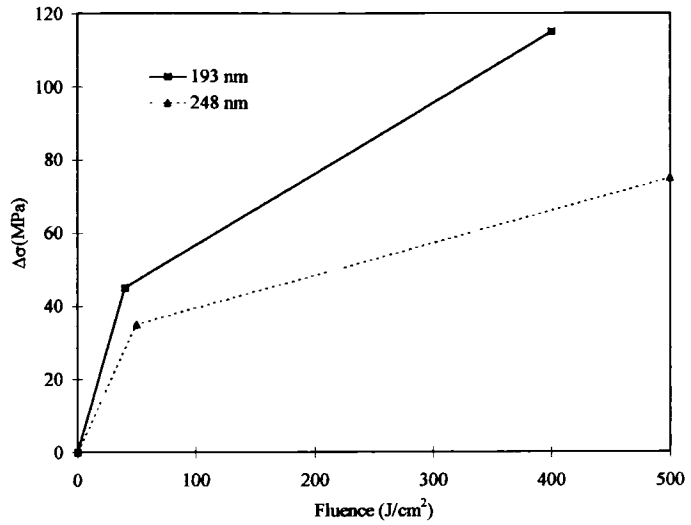

Figure 20. Increase in the axial stress $\Delta\sigma$ versus the accumulated fluence of the UV exposure.

Two fresh samples were again exposed to similar fluences of 193 nm UV radiation, but now the exposure was made through a phase-mask to generate a Bragg grating in the core of the fibre. The phase mask had a periodicity of 1 μm and was designed to suppress the transmission of the zero order diffracted field. The gratings had a length of 10 mm and a reflectivity of 96% and 67% at a wavelength of 1.5 μm for total fluences of 400 J/cm^2 and 40 J/cm^2. These reflectivities correspond to a peak to peak perturbation of the refractive index of $2.2 \cdot 10^{-4}$ and $1.1 \cdot 10^{-4}$ respectively. If we represent these refractive index changes δn against the increments of the core axial stress $\Delta\sigma$ (Figure 21), we observe a fairly linear relation between them, in agreement with the results previously reported [43,91].

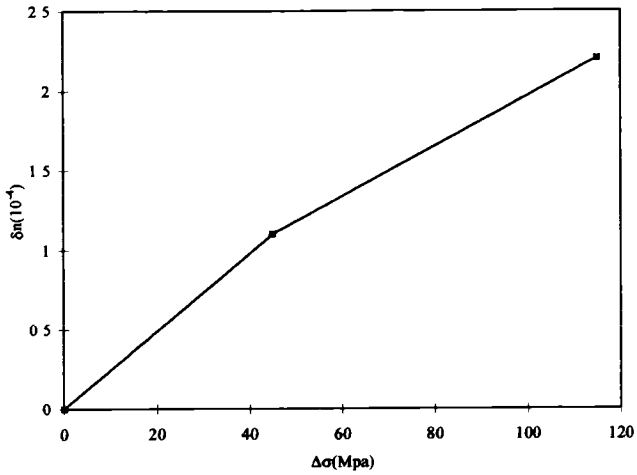

Figure 21. Refractive index changes δn against the increments of the core axial stress Δσ.

The slope of this curve is approximately $2 \cdot 10^{-6}$ MPa^{-1}, which is comparable to the figure reported in references [43,91]: $8 \cdot 10^{-6}$ MPa^{-1}. The differences in the experimental conditions, including the nature of the fibre and the wavelength of the UV radiation are responsible for this mismatch. Although we have not carried out an extensive number of measurements, our results seem to show the same trends as those reported by Limberger [43,91].

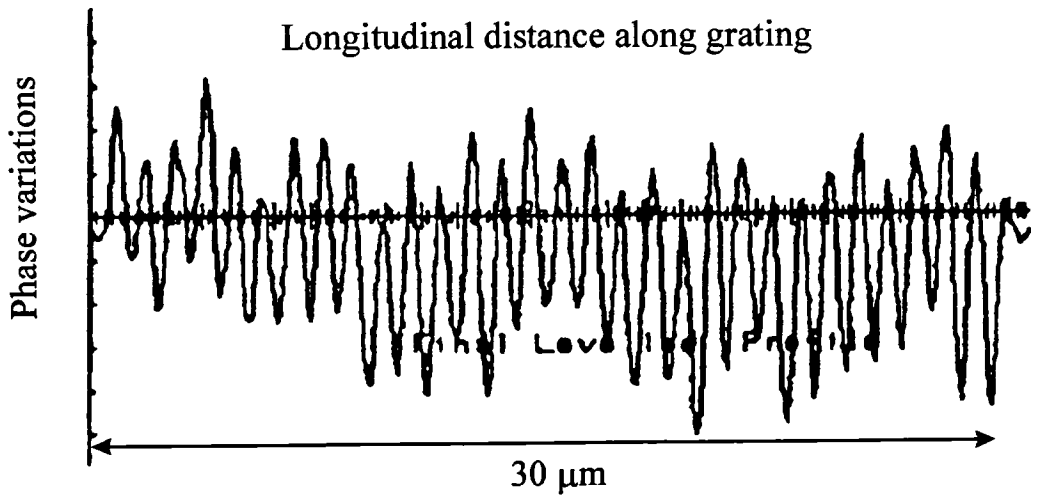

Figure 22. Longitudinal stress profile of the Bragg grating.

Subsequently, we set the stress measurement system to its maximum spatial resolution (0.3μm), and mapped the longitudinal stress profile of the Bragg grating exposed to 400 J/cm^2

with 193nm UV radiation. This measurement is shown in Figure 22. In this figure, it can be appreciated that the periodicity of the stress perturbations is about 1μm, i.e. equal to the periodicity of the phase-mask. This result is surprising in principle, because we would have expected this periodicity to be half of that of the phase-mask (due to the interference pattern of the first diffraction orders). Our measurement system, with a spatial resolution of 0.3μm, would tend to average out this fundamental periodicity at 0.5 μm, but it clearly shows that there is a very strong periodicity at 1μm. By carefully positioning the sampling lines of the measurement system, it was possible to measure the transverse stress profiles at the points of maximum and minimum photoinduced stress. These transverse profiles are shown in Figures 23 and 24. The visibility of the axial stress modulation compared to the average increase of axial stress yielded a value of 20%.

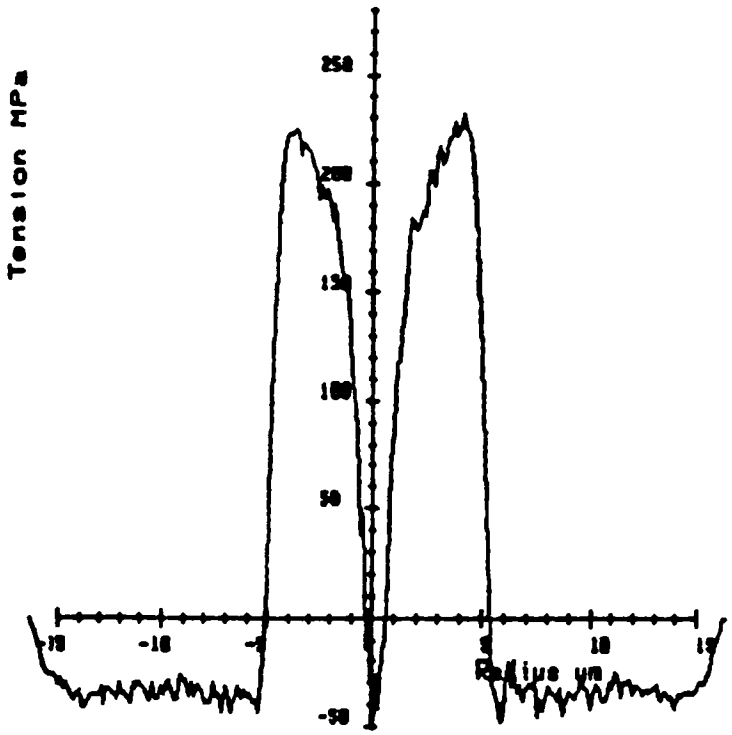

Figure 23. Transverse stress profile at a minimum of the Bragg grating.

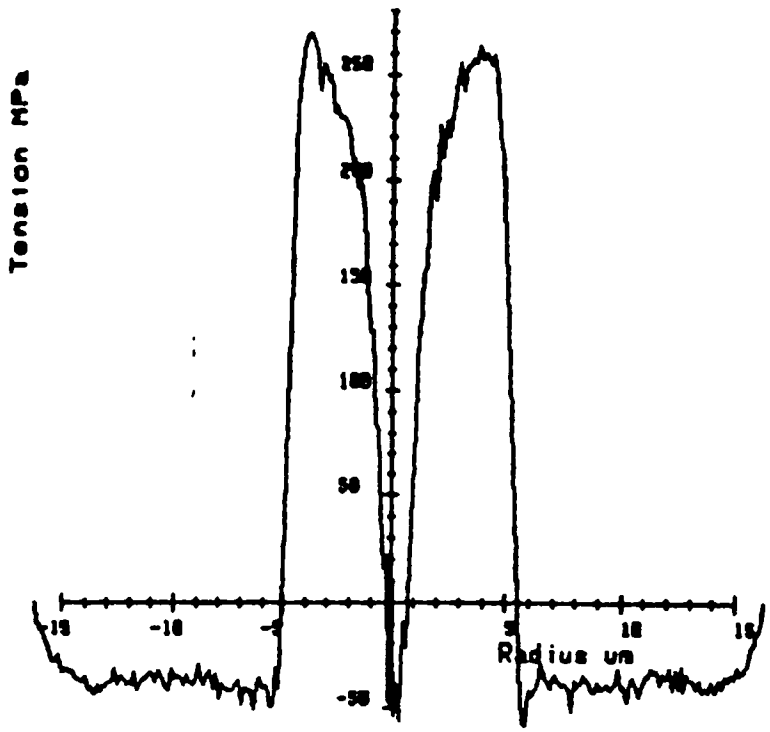

Figure 24. Transverse stress profile at a maximum of the Bragg grating.

The appearance of a dominant periodicity with a pitch of 1μm has been observed before in exposures to UV radiation of various wavelengths (248nm and also 193nm) [57,92,93]. It has been attributed to the combined effect of an interference between the first diffraction orders and the partially unsuppressed zero diffraction order of the phase-mask, together with a threshold-type photosensitive mechanism. In particular, exposure to 193 nm UV radiation has been shown to lead to a reduced threshold for type II processes compared to that at 248 nm [58]. The larger absorption coefficient at this wavelength coupled to an incubation effect in which the damage threshold is reduced with increased number of pulses, permits the rapid formation of gratings with modest fluence levels [58]. In these conditions, the writing efficiency would be optimised if a phase mask with a periodicity of 0.5 μm (half of the usual 1 μm pitch) is used [58].

As a conclusion, these experiments have confirmed the increase of the axial stress in the fibre core after UV exposure, and have also shown good agreement with some previously reported observations [43,91]. The increase of axial stress in the fibre core together with its correlation

to the refractive index changes indicates that the contribution of compaction to the photoinduced changes in refractive index can be significant.

3.5.2 Degradation of the mechanical reliability of UV exposed optical fibres

Optical fibres have a relatively high strength (several GPa) due to the pure nature of the silica used in their manufacture. However they behave as brittle materials, with a sharp transition between the elastic behaviour and catastrophic failure without an intermediate plastic deformation regime. In the last section, we have seen that exposure of optical fibre to UV light gives rise to structural changes in the glass network. In this section, we will investigate the effect of these structural modifications on the mechanical strength of optical fibres [4]. This issue is of practical importance for the assessment of the mechanical reliability of photoinduced fibre devices.

3.5.2.a Strength of optical fibres

Silica optical fibres are both elastic and brittle materials. Their elastic behaviour is characterised by a Young's modulus of 73 GPa. When the applied axial stress exceeds a certain limit, catastrophic failure or fracture occurs. In a perfect glass, the final stress limitation is given by the strength of the Si-O bond, which is of the order of 10 GPa. However, manufactured optical fibres suffer fracture when subjected to stresses of several GPa due to the existence of flaws that reduce their mechanical strength. Some of these flaws can be associated with defects in the glass structure inside the fibre, and others are due to surface microcracks, commonly introduced by fibre handling processes. These flaws act as stress intensifiers, causing the local stress field in their vicinity to be amplified proportionally to the stress intensity factor K_{si} [94]:

$$K_{si} = Y\sigma\sqrt{a} \qquad (32)$$

where σ is the external stress to which the fibre is subjected, a is the size of the flaw, and Y is a geometrical factor of order 1. When the stress intensity factor reaches a critical value K_{si}^{crit} then fracture occurs.

In (32), it can be observed that the stress of failure depends on the size of the flaw involved in the fracture. When a fibre is manufactured, it has a distribution of flaws and, correspondingly, a statistical distribution of failure stresses. It has been empirically shown that the cumulative probability of failure $F(\sigma)$ usually follows a Weibull distribution:

$$F(\sigma) = Prob(\sigma_{FAILURE} < \sigma) = 1 - \exp\left[-\frac{L}{L_o}\left(\frac{\sigma}{\sigma_o}\right)^m\right] \qquad (33)$$

where L is the length of fibre involved and L_o, σ_o and m are constants for a particular fibre. The m parameter of the Weibull distribution gives information about the spread of the failure stress. A good quality optical fibre has an m value in excess of 20 (even bigger than 100 in some cases). In order to ensure that a length of fibre does not incorporate any flaw with low failure stress, optical fibres are proof-tested to stresses in the range of 0.3-0.7 GPa depending on the specifications of each particular application.

The flaw distribution varies with time as a result of the fatigue phenomenon, which causes a degradation of the fibre's mechanical reliability. The material's fatigue is essentially due to the growth of the flaw size a. The usual hypothesis is that the growth obeys the power law:

$$\frac{da}{dt} = A\, K_{si}^n \qquad (34)$$

where A is a proportionality constant and K_{si} is the stress intensity factor (32). The n parameter is indicative of the speed of the process: the higher n is, the slower the crack growth. A usual value for n is 20. The physical mechanism behind the crack growth has been attributed to stress corrosion. In this process, the reaction of water molecules with the glass network results in the rupture of stressed Si-O bonds. The presence of stress is essential to enhance this chemical process. It can be appreciated that fatigue is an effect mainly due to the environment. Hermetic coatings that isolate the optical fibre from its environment have been developed to combat stress corrosion [96].

There are several methods for the strength characterisation of optical fibres [95]. They can be classified into dynamic and static methods. In a dynamic method, many samples of an optical fibre are strained at a uniform rate until fracture. This test provides an assessment of the strength and the strength distribution of the optical fibre. By use of Weibull plots, it also

permits the calculation of the m parameter. In static fatigue tests, the optical fibre samples are subjected to a constant load and the time at which failure occurs is monitored. These tests give information about the growth of flaws and the n parameter. It is interesting to note that both types of tests are not independent, and that information about the n parameter can also be recovered from several dynamic tests at different strain rates. The relations between dynamic and static strength tests could be calculated from expressions (32) and (34).

The dynamic mechanical strength of an optical fibre is measured by the median failure strength of a number of fibre samples which have been strained to failure at a given rate of increasing strain. Weibull statistics are used to plot the probability of failure against the failure strength. The slope of this plot determines the m-value of the fibre for this rate of strain, and this provides a measure of the density of the distribution of the flaws in the fibre.

3.5.2.b Mechanical strength degradation of UV exposed optical fibres

In the last sections it has been shown that exposure to UV light modifies the mechanical properties of the glass. In section 3.5.1, we saw that exposure to relatively low UV fluences per pulse gives rise to an increase in the axial stress of the fibre and, consequently, to a compaction of its structure. Also, in section 3.3.1.d, we discussed that exposure to higher UV fluences per pulse can result in a localised thermal breakdown at the core-cladding interface, that causes mechanical damage in the core. This means that UV exposure probably introduces additional flaws to the glass structure which will translate into a reduced strength and mechanical reliability. Bragg gratings have immense potential as point sensors of strain and temperature. However, if the UV irradiation used to photoinduce Bragg gratings reduces fibre strength, the usefulness of gratings for sensors will be diminished. In this section, we assess the effect that UV irradiation has on the tensile strength of two types of fibre. In particular, the fibres are exposed to UV radiation at 248 nm or 193 nm and significant differences in the resulting tensile strengths are observed.

The single-mode optical fibres used in our investigations were Corning's SMF-28 (3 mol% of germanium), and a highly photosensitive germanium and boron co-doped fibre (10 mol% of germanium) from the University of Southampton. For each fibre, 3 batches of 15 samples were prepared for the exposure and subsequent tensile strength tests by chemically stripping a 5 cm length of the coating from the central section of the fibre. Of the three batches of each fibre type, two were exposed to UV radiation from an excimer laser, while the third was retained as

an unexposed control. Each fibre in the first batch was exposed to a single pulse of 248 nm radiation with a fluence of 1 J/cm^2 while the fibres in the second batch were exposed to a single pulse of 193 nm radiation with the same fluence. In all exposures the beam was apertured to give an exposed length of 5 mm, centred in the stripped region.

A dynamic strength test, in which the fibres were individually stretched at a rate of 50mm/min until failure, was carried out for each of the 6 batches. Prior to testing, the samples were acclimatised at 23°C and 50% humidity for 24 hours. The gauge length was set to 10cm with the stripped section of fibre centralised within this length.

Figures 25 and 26 show the Weibull plots of the data acquired from the SMF-28 and B co-doped fibre, respectively. Table 2 summarises the significant statistical parameters for each fibre:

Corning SMF28	**Unexposed**	**Exposure at 248 nm, 1J/cm^2**	**Exposure at 193 nm, 1J/cm^2**
Mean (Gpa)	0.92	0.69	0.84
Median (GPa)	0.93	0.71	0.86
σ (GPa)	0.38	0.18	0.34
m-value	2.4	3.9	2.0

Ge-B doped fibre	**Unexposed**	**Exposure at 248 nm, 1J/cm^2**	**Exposure at 193 nm, 1J/cm^2**
Mean (Gpa)	0.53	0.41	0.5
Median (GPa)	0.56	0.40	0.52
σ (GPa)	0.14	0.15	0.16
m-value	3.7	2.7	3.1

Table2. Mechanical Weibull statistical parameters of UV exposed fibres. The mean and median represent stress values at failure and σ represents the standard deviation.

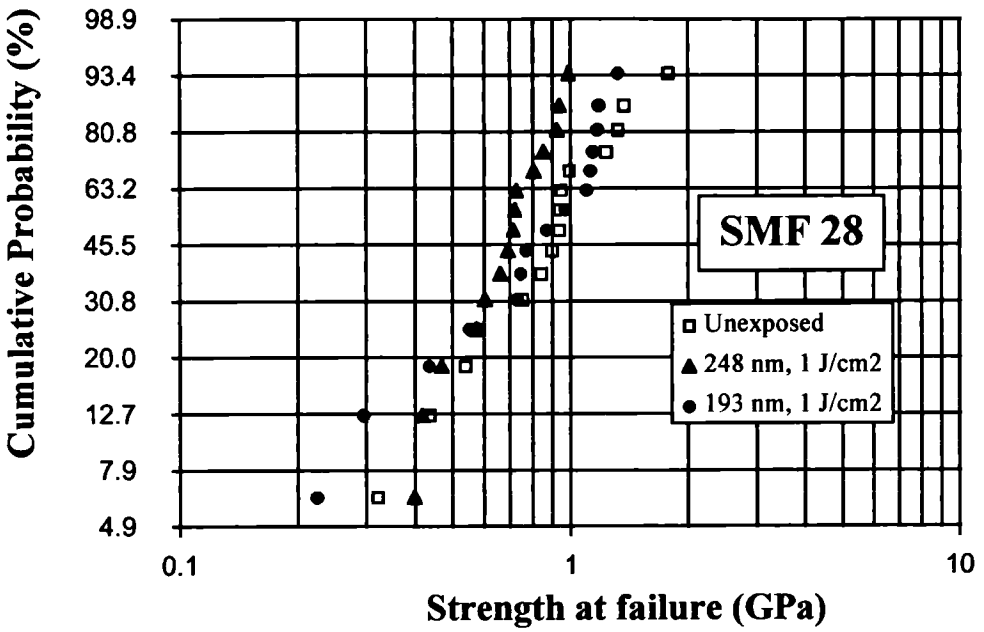

Figure 25. Weibull Plot for Corning SMF 28 fibre.

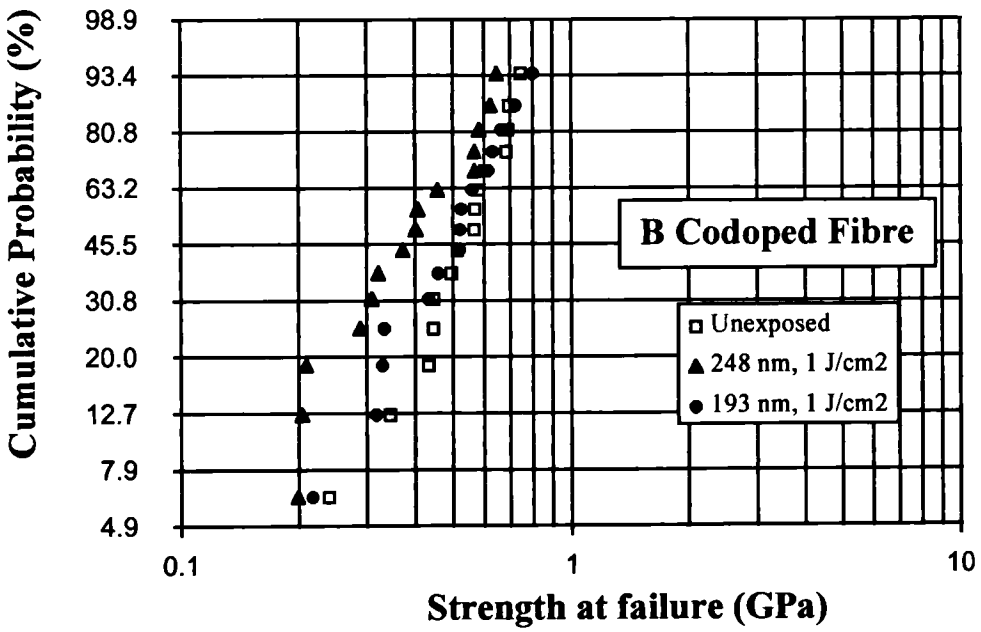

Figure 26. Weibull Plot for Ge-B co-doped fibre.

The exposed fibre samples were examined for physical damage under a microscope and by looking for light scattered into the cladding from a He-Ne laser launched into the fibre core. No evidence of mechanical damage in the fibre was found in spite of the high UV exposure fluences. The data in Table 1 indicates that both types of fibre were affected by exposure in a

similar manner. The median strength of the unexposed fibres was higher for the SMF-28 (0.93 GPa) than for the B co-doped fibre (0.56 GPa). These reduced strengths for the unexposed fibres together with the low value for the m parameter (<4) indicate that in spite of the chemical stripping and the careful handling of the fibres, some extrinsic surface microcracks have been introduced during the experiments. The exposure to a fluence of $1J/cm^2$ of 248 nm UV radiation reduced the median failure strength of the SMF-28 by 24% to 0.71 GPa and that of the B co-doped by 29% to 0.40 GPa. The data acquired for exposure to 193 nm with a fluence of $1J/cm^2$ indicate that the median strength of the SMF-28 and the B co-doped fibre is reduced by about 8% for both fibres.

3.5.2.c Conclusion

The main conclusion to be drawn from these experiments is that UV exposure causes a reduction of the mechanical strength of optical fibres. The differences in the strength reduction between the exposures to 193 nm and 248 nm wavelengths is not well understood and does not seem to correlate with the axial stress measurements presented in the last section. Also, as the absorption at 193nm is usually higher than at 248 nm (except for low germanium concentration fibres) [35,36], larger structural modifications would have been expected for 193nm wavelength irradiation. Recent experiments carried out with 240 nm UV radiation seem to confirm the strength reduction of UV exposed optical fibres [97,98]. Varelas [97] has reported that fibres irradiated with continuous wave UV radiation exhibit minimum strength reduction compared to those exposed to pulsed radiation. However, many sensing applications that require thermal stability at high temperatures will probably rely on type IIb gratings generated through high fluence pulsed sources. In these cases, our study indicates that it will be essential to assess the additional degradation of the fibre strength and mechanical reliability due to the UV exposure.

REFERENCES

[1] V.A. Handerek, S.E. Kanellopoulos, R. Feced, J.Croucher. "Evaluation of shape-birefringent fibres for sensing systems employing photogenerated polarization couplers". Optical fibre gratings and their applications. IEE, London, January 1995.

[2] R. Feced, S.E. Kanellopoulos, R.A. Griffin, V.A. Handerek. "Polarization dependence of photo-induced birefringence and its application to fabrication of tailored polarization filters". Bragg grating, Photosensitivity, and Poling in Glass Fibers and Waveguides Topical Meeting (OSA), Williamsburg, Virginia (USA). October 1997.

[3] K. Raine, R. Feced, S.E. Kanellopoulos, V.A. Handerek, A. Parker. "High resolution stress profiling of UV exposed optical fibres". 4th Optical fibre measurement conference. NPL, Teddington (UK), October 1997.

[4] R. Feced, M.P. Edwards, S.E. Kanellopoulos, N.H. Taylor, V.A. Handerek. "Mechanical strength degradation of UV exposed optical fibres". Electronics Letters Vol. 33, No. 2, pp. 157-159, January 1997.

[5] F. Parvaneh, M. Farhadiroushan, R. Thomas, R. Feced, V.A. Handerek, A.J. Rogers. "Demonstration and potential of distributed temperature sensors using the frequency derived technique". Progress in optical fibre sensors and their applications. IEE, London, November 1995.

[6] F. Parvaneh, M. Farhadiroushan, R. Thomas, R. Feced, V.A. Handerek, A.J. Rogers. "Recent progress in distributed temperature sensing using the frequency derived technique". Optical Fiber Sensors (OFS-11), Sapporo (Japan), May 1996.

[7] R. Feced, S.E. Kanellopoulos, M. Farhadiroushan, V.A. Handerek, A.J. Rogers. "Analysis of optical Kerr effect induced coupling among polarization modes in high-birefringence optical fibers". Optics Communications, Vol. 143, pp. 268-278, November 1997.

[8] F.P. Kapron, N.F. Borrelli, D.B. Keck. "Birefringence in dielectric optical waveguides". IEEE Journal of Quantum Electronics, Vol. 8, No. 2, pp. 222-225, February 1972.

[9] R.H. Stolen, V. Ramaswamy, P. Kaiser, W. Pleibel. "Linear polarization in birefringent single-mode fibers". Applied Physics Letters, Vol. 33, No. 8, pp. 699-701, October 1978.

[10] I.P. Kaminow, V. Ramaswamy. "Single polarization optical fibers: slab model". Applied Physics Letters, Vol. 34, No. 4, pp. 268-270, February 1979.

[11] R.B. Dyott, J.R. Cozens, D.G. Morris. "Preservation of polarisation in optical-fibre waveguides with elliptical cores". Electronics Letters, Vol. 15, No. 13, pp. 380-382. June 1979.

[12] D.N. Payne, A.J. Barlow, J.J. Ramskov Hansen. "Development of low- and high-birefringence optical fibers". IEEE Journal of Quantum Electronics, Vol. 18, No. 4, pp. 477-487, April 1982.

[13] S.C. Rashleigh. "Origins and control of polarization effects in single-mode fibres". Journal of Lightwave Technology, Vol. 1, No. 2, pp. 312-331, June 1983.

[14] J. Noda, K. Okamoto, Y. Sasaki. "Polarization maintaining fibers and their applications". Journal of Lightwave Technology, Vol. 4, No. 8, pp. 1071-1089, August 1986.

[15] C. Yeh. "Guided-wave modes in cylindrical optical fibers". IEEE Transactions on Education, Vol. 30, No 1, pp. 43-51, February 1987.

[16] R.B. Dyott. "Composition of LP_{11} modes in elliptical cored fibre". Electronics Letters, Vol. 30, No. 12, pp. 993-994, June 1994.

[17] S.Y. Huang, J.N. Blake, B.Y. Kim. "Perturbation effects on mode propagation in highly elliptical core two-mode fibers". Journal of Lightwave Technology, Vol. 8, No. 1, pp. 23-33, January 1990.

[18] H.G. Park, C.C. Pohalski, B.Y. Kim. "Optical Kerr switching using elliptical-core two-mode fiber". Optics Letters, Vol. 13, No. 9, pp. 776-778, September 1988.

[19] W.V. Sorin, B.Y. Kim, H.J. Shaw. "Phase-velocity measurements using prism output coupling for single and few-mode optical fibers". Optics Letters, Vol. 11, No. 2, pp. 106-108. February 1986.

[20] A. Yariv, P. Yeh. "Optical waves in crystals", pp. 425-439. John Wiley and Sons, 1984.

[21] C. Elachi. "Waves in active and passive periodic structures: a review". Proceedings of the IEEE, Vol. 64, No. 12, pp. 1666-1698, December 1976.

[22] P.St.J. Russell. "Bloch wave analysis of dispersion and pulse propagation in pure distributed feedback structures". Journal of Modern Optics, Vol. 38, No. 8, pp. 1599-1619, 1991.

[23] K.O. Hill, Y. Fuji, D.C. Johnson, B.S. Kawasaki. "Photosensitivity in optical fiber waveguides: application to reflection filter fabrication". Applied Physics Letters, Vol. 32, No. 10, pp. 647-649, May 1978.

[24] G. Meltz, W.W. Morey, W.H. Glenn. "Formation of Bragg gratings in optical fibers by a transverse holographic technique". Optics Letters, Vol. 14, No. 15, pp. 823-825, August 1989.

[25] P.St.J. Russell, D. P. Hand. "Rocking filter formation in photosensitive high birefringence optical fibres". Electronics Letters Vol. 26, No. 22, pp. 1846-1848, October 1990.

[26] V. Mizrahi, S. LaRochelle, G.I. Stegeman, J.E. Sipe. "Physics of photosensitive-grating formation in optical fibers". Physical Review A, Vol. 43, No. 1, pp. 433-438, January 1991.

[27] S. An, J.E. Sipe. "Universality in the dynamics of phase grating formation in optical fibers". Optics Letters, Vol. 16, No. 19, pp. 1478-1480, October 1991.

[28] R. Kashyap, J.R. Armitage, R. Wyatt, S.T. Davey, D.L. Williams. "All fibre narrowband reflection grating at 1500 nm". Electronics Letters, Vol. 26, No.11, pp. 730-732, May 1990.

[29] K.O. Hill, B. Malo, F. Bilodeau, D.C. Johnson, J. Albert. "Bragg gratings fabricated in monomode photosensitive optical fiber by UV exposure through a phase mask". Applied Physics Letters, Vol. 63, No. 10, pp. 1035-1037, March 1983.

[30] D.Z. Anderson, V. Mizrahi, T. Erdogan, A.E. White. "Production of in-fibre gratings using a diffractive optical element". Electronics Letters, Vol. 29, No. 6, pp. 566-568, March 1993.

[31] B. Malo, K.O. Hill, F. Bilodeau, D.C. Johnson, J. Albert. "Point-by-point fabrication of micro-Bragg gratings in photosensitive fibre using single excimer pulse refractive index modification techniques". Electronics Letters, Vol. 29, No. 18, pp. 1668-1669, September 1993.

[32] T.E. Tsai, D.L. Griscom, E.J. Friebele. "On the structure of Ge-associated defect centers in irradiated high purity GeO_2 and Ge-doped SiO_2 glasses". Diffussion and Defect Data, Vol. 53-54, pp. 469-476, 1987.

[33] V.B. Neustruev. "Colour centres in germanosilicate glass and optical fibres". Journal of Physics: Condensed Matter, Vol. 6, pp. 6901-6936, 1994.

[34] D.L. Williams, S.T. Davey, R. Kashyap, J.R. Armitage, B.J. Ainslie. "Ultraviolet absorption studies on photosensitive germanosilica preforms and fibers". Applied Physics Letters, Vol. 59, No. 7, pp. 762-764, August 1991.

[35] R.M. Atkins, V. Mizrahi. "Observation of changes in UV absorption bands of single mode gernamosilicate core optical fibres on writing and thermally erasing refractive index gratings". Electronics Letters, Vol. 28, No. 18, pp. 1743-1744, August 1992.

[36] R. M. Atkins, V. Mizrahi, T. Erdogan. "248 nm induced vacuum UV spectral changes in optical fibre preform cores: support for a colour centre model of photosensitivity". Electronics Letters, Vol. 29, No. 4, pp. 385-387, February 1993.

[37] L. Dong, J.L. Archembault, L. Reekie, P.St.J. Russell, D.N. Payne. "Photoinduced absorption change in germanosilicate preforms: evidence for the colour centre model of photosensitivity". Applied Optics, Vol. 34, No. 18, pp. 3436-3440, June 1995.

[38] D.P. Hand, P.St.J. Russell. "Photoinduced refractive index changes in germanosilicate fibers". Optics Letters, Vol. 15, No. 2, pp. 102-104, January 1990.

[39] J.P. Bernardin, N.M. Lawandy. "Dynamics of the formation of Bragg gratings in germanosilicate optical fibres". Optics Communications, Vol 79, No. 3-4, pp. 194-199, October 1990.

[40] M. Douay, D. Ramecourt, T. Taunay, P. Bernage, P. Niay, A. Dacosta, C. Mathieu, J.F. Bayon, B. Poumellec. "Microscopic investigations of Bragg gratings photowritten in germanosilicate fibers". Proceedings of the Photosensitivity and quadratic nonlinearity in glass waveguides, pp. 48-51. September 1995, Portland, Oregon.

[41] I. Riant, S. Borne, P. Sansonetti, B. Poumellec. "Evidence of densification in UV written Bragg gratings in fibres". Proceedings of the Photosensitivity and quadratic nonlinearity in glass waveguides, pp. 52-55. September 1995, Portland, Oregon.

[42] V.M. Marchenko. "Photoinduced transformations of oxygen-deficient centers in silica and germanosilicate glasses". Glass Physics and Chemistry, Vol. 21,No. 4, pp. 263-272, 1995.

[43] P.Y. Fonjallaz, H.G. Limberger, R.P. Salathe, F. Cochet, B. Leuenberger. "Tension increase correlated to refractive index change in fibres containing UV-written Bragg gratings". Optics Letters, Vol. 20, No. 11, pp. 1346-1348, June 1995.

[44] M.G. Sceats, G.R. Atkins, S.B. Poole. "Photolytic index changes in optical fibres". Annual Review Material Science, Vol. 23, pp. 381-410, 1993.

[45] B. Poumellec, P. Niay, M. Douay, J.F. Bayon. "The UV-induced refractive index grating in Ge:SiO_2 preforms: additional CW experiments and the macroscopic origin of the change in index". Journal of Physics D: Applied Physics, Vol. 29, pp. 1842-1856, 1996.

[46] M.J.F. Digonnet. "A Kramers-Kronig analysis of the absorption change in fiber gratings". Proceedings of the SPIE conference on Doped Fiber Devices, SPIE Vol. 2841, pp. 109-120, Denver, Colorado, August 1996.

[47] F. Bidoleau, J. Albert, B. Malo, D.C. Johnson, K.O. Hill, Y. Hibino, M. Abe, M. Kawachi. "Photosensitization of optical fiber and silica-on-silicon/silica waveguides". Optics Letters, Vol. 18, No. 12, pp. 953-955, June 1993.

[48] P.J. Lemaire, R.M. Atkins, V. Mizrahi, W.A. Reed. "High pressure H_2 loading as a technique for achieving ultrahigh UV photosensitivity and thermal sensitivity in GeO_2 doped optical fibers". Electronics Letters, Vol. 29, No. 13, pp. 1191-1193, June 1993.

[49] R.M. Atkins, P.J. Lemaire, T. Erdogan, V. Mizrahi. "Mechanisms for enhanced photosensitivity via hydrogen loading in germanosilicate glasses". Electronics Letters, Vol. 29, No. 14, pp. 1234-1235, July 1993.

[50] D.L. Williams, B.J. Ainslie, J.R. Armitage, R. Kashyap, R. Campbell. "Enhanced UV photosensitivity in boron codoped germanosilicate fibres". Electronics Letters, Vol. 29, No. 1, pp. 45-47, January 1993.

[51] B. Malo, J. Albert, K.O. Hill, F. Bilodeau, D.C. Johnson, S. Thériault. "Enhanced photosensitivity in lightly doped standard telecommunication fibre exposed to high fluence ArF excimer laser light". Electronics Letters, Vol. 31, No. 11, pp. 879-880, May 1995.

[52] J. Albert, B. Malo, K.O. Hill, F. Bilodeau, D.C. Johnson. "Comparison of one-photon and two-photon effects in the photosensitivity of germanium-doped silica optical fibers exposed to intense ArF excimer laser pulses". Applied Physics Letters, Vol. 67, No. 24, pp. 3529-3531, December 1995.

[53] H.G. Limberger, P.Y. Fonjallaz, R.P. Salathe. "Spectral characterisation of photoinduced high efficient Bragg gratings in standard telecommunication fibres". Electronics Letters, Vol. 29, No. 1, pp. 47-49, January 1993.

[54] P. Niay, P. Bernage, S. Legoubin, M. Douay, W. X. Xie, J.F. Bayon, T. Georges, M. Monerie, B. Poumellec. "Behaviour of spectral transmissions of Bragg gratings written in germania-doped fibres: writing and erasing experiments using pulsed or CW UV exposure". Optics Communications, Vol. 113, pp. 176-192, 1994.

[55] L. Dong, W.F. Liu, L. Reekie. "Negative-index gratings formed by a 193 nm excimer laser". Optics Letters, Vol. 21, No. 24, pp. 2032-2034, December 1996.

[56] J.L. Archambault, L. Reekie, P.St.J. Russell. "100% reflectivity Bragg reflectors produced in optical fibres by single excimer laser pulses". Electronics Letters, Vol. 29, No. 5, pp. 453-455, March 1993.

[57] B. Malo, D.C. Johnson, F. Bilodeau, J. Albert, K.O. Hill. "Single-excimer-pulse writing of fibre gratings by use of a zero-order null phase-mask: grating spectral response and visualization of index perturbations". Optics Letters, Vol. 18, No. 15, pp. 1277-1279, August 1993.

[58] P.E. Dyer, R.J. Farley, R. Giedl, K.C. Byron, D. Reid. "High reflectivity fibre gratings produced by incubated damage using a 193 nm ArF laser". Electronics Letters, Vol. 30, No. 11, pp. 860-862, May 1994.

[59] M.A. Fokine, B.E. Sahlgren, R. Stubbe. "High temperature resistant Bragg gratings fabricated in silica optical fibres". Bragg grating, Photosensitivity, and Poling in Glass Fibers and Waveguides Topical Meeting (OSA), Williamsburg, Virginia (USA). October 1997.

[60] M. Parent, J. Bures, S. Lacroix, J. Lapierre. "Proprietes de polarisation des reflecteurs de Bragg induits par photosensibilite dans les fibres optique monomodes". Applied Optics, Vol. 24, No. 3, pp. 354-357, February 1985.

[61] S. E. Kanellopoulos, L. C. G. Valente, V. A. Handerek, A. J. Rogers. "Polarisation properties of permanent and nonpermanent photorefractive gratings in Hi-Bi fibers". IEEE Photonics Technology Letters, Vol. 3, No. 4, pp. 345-347, April 1991.

[62] P.St.J. Russell, D. P. Hand. "Rocking filter formation in photosensitive high birefringence optical fibres". Electronics Letters Vol. 26, No. 22, pp. 1846-1848, October 1990.

[63] F. Ouellette, D. Gagnon, M. Poirier. "Permanent photoinduced birefringence in a Ge-doped fibre". Applied Physics Letters Vol. 58, No. 17, pp. 1813-1815, April 1991.

[64] S. E. Kanellopoulos, L. C. G. Valente, V. A. Handerek, A. J. Rogers. "Photorefractive polarisation couplers in elliptical core fibres". IEEE Photonics Technology Letters, Vol. 3, No. 6, pp. 806-809, September 1991.

[65] S. An, J.E. Sipe. "Polarisation aspects of two-photon photosensitivity in birefringent optical fibres". Optics Letters, Vol. 17, No. 7, pp. 490-492, April 1992.

[66] K.O. Hill, F. Bilodeau, B. Malo, D.C.Johnson. "Birefringent photosensitivity in monomode optical fibre : Application to external writing of rocking filters". Electronics Letters, Vol. 27, No. 17, pp. 1548-1550, August 1991.

[67] S.E. Kanellopoulos, V.A. Handerek, A. J. Rogers. "Photoinduced polarisation couplers in elliptical core optical fibres written using 532 and 266 nm sources". Electronics Letters, Vol. 28, No. 16, pp. 1558-1560, July 1992.

[68] D.C. Psaila, F. Ouellette, C. Martijn de Sterke. "Characterization of photoinduced birefringence change in optical fiber rocking filters". Applied Physics Letters, Vol 68, No.7, pp. 900-902, February 1996.

[69] D.C. Psaila, C. Martijn de Sterke, F. Ouellette. "Fabrication of rocking filters at 193nm". Optics Letters, Vol. 21, No. 19, pp. 1550-1552, October 1996.

[70] T. Erdogan, V. Mizrahi. "Characterisation of UV-induced birefringence in photosensitive Ge-doped silica optical fibres". Journal Optical Society of America B, Vol. 11, No. 10, pp. 2100-2105, October 1994.

[71] S.E. Kanellopoulos, V.A. Handerek, A.J. Rogers. "Simultaneous strain and temperature sensing employing photogenerated in-fibre gratings". Optics Letters, Vol. 20, No. 3, pp. 333-335, February 1995.

[72] S.E. Kanellopoulos, V.A. Handerek, A.J. Rogers. "Simultaneous strain and temperature sensing employing a photogenerated polarisation coupler and low-order modes in an elliptically cored optical fibre". Electronics Letters, Vol. 30, No. 21, pp. 1786-1787, October 1994.

[73] C.G. Krautschik, P. Wigley, G.I. Stegeman, R.H. Stolen. "Demonstration of demultiplexing with a rocking filter fibre". Applied Physics Letters, Vol. 63, No. 7, pp. 860-862, August 1993.

[74] S. Bardal, A. Kamal, P.St.J. Russell. "Photoinduced birefringence in optical fibres: a comparative study of low birefringence and high birefringence fibres", Optics Letters, Vol. 17, No. 6, pp. 411-413, March 1992.

[75] J. Lauzon, D. Gagnon, S. LaRochelle, A. Blouin, F. Ouellette. "Dynamic polarisation coupling in elliptical-core photosensitive optical fibre". Optics Letters, Vol 17, No. 23, pp. 1664-1666, December 1992.

[76] M. Poirier, S. Thibault, J. Lauzon, F. Ouellette. "Dynamic and orientational behaviour of UV-induced luminescence bleaching in Ge-doped silica optical fibre". Optics Letters, Vol. 18, No. 11, pp. 870-872, June 1993.

[77] J. Albert, B. Malo, D.C. Johnson, F. Bilodeau, K.O. Hill, J.L. Brebner, G. Kajrys. "Dichroism in the absorption spectrum of photobleached ion-implanted silica". Optics Letters, Vol. 18, No. 14, pp. 1126-1128, July 1993.

[78] A. Kamal, P.St.J. Russell. "Physical origins and general dielectric tensor of photoinduced anisotropy in optical fibres and bulk glasses". Journal Optical Society of America B, Vol. 11, No. 9, pp. 1576-1584, September 1994.

[79] D. Wong, S.B. Poole, M.G. Sceats. "Stress-birefringence reduction in elliptical-core fibres under ultraviolet irradiation". Optics Letters, Vol. 17, No. 24, pp. 1773-1775, December 1992.

[80] K.S. Chiang, M.G. Sceats, D. Wong. "Ultraviolet photolytic-induced changes in optical fibres: the thermal expansion coefficient". Optics Letters, Vol. 18, No. 12, pp. 965-967, June 1993.

[81] T. Meyer, P.A. Nicati, P.A. Robert, D. Varelas, H.G. Limberger, R.P. Salathe. "Reversibility of photoinduced birefringence in ultralow-birefringence fibers". Optics Letters, Vol. 21, No. 20, pp. 1661-1663, October 1996.

[82] D. Inniss, Q. Zhong, A.M. Vengsarkar, W.A. Reed, S.G. Kosinski, P.J. Lemaire. "Atomic force microscopy study of UV-induced anisotropy in hydrogen-loaded germanosilicate fibres". Applied Physics Letters, Vol. 65, No. 12, pp. 1528-1530, September 1994.

[83] E. Fertein, S. Legoubin, M. Douay, S. Canon, P. Bernage, P. Niay, J.F. Bayon, T. Georges. "Shifts in resonance wavelengths of Bragg gratings during writing or bleaching experiments by UV illumination within germanosilicate optical fibre". Electronics Letters, Vol 27, No. 20, pp. 1838-1839, September 1991.

[84] S. Legoubin, E. Fertein, M. Douay, P. Bernage, P. Niay, F. Bayon, T. Georges. "Formation of Moiré grating in core of germanosilicate fibre by transverse holographic double exposure method". Electronics Letters, Vol 27, No. 21, pp. 1945-1946, October 1991.

[85] P.K. Bachmann, W. Hermann, H. Wehr, D.U. Wiechert. "Stress in optical waveguides. 1:Preforms". Applied Optics, Vol. 25, No. 7, pp. 1093-1098, April 1986.

[86] P.L. Chu, T. Whitbread. "Measurement of stresses in optical fiber and preform". Applied Optics, Vol. 21, No. 23, pp. 4241-4245, December 1982.

[87] P.K. Bachmann, W. Hermann, H. Wehr, D.U. Wiechert. "Stress in optical waveguides. 2: Fibers". Applied Optics, Vol. 26, No. 7, pp. 1175-1182, April 1987.

[88] P.L. Chu, T. Whitbread. "Measurement of stresses in optical fiber or preform". Electronics Letters, Vol. 18, No. 1, pp. 28-29, January 1982.

[89] R.B. Calligaro, D.N. Payne, R.S. Anderssen, B.A. Ellem. "Determination of stress profiles in optical fibre preforms". Electronics Letters, Vol. 18, No. 11, pp. 474-475, May 1982.

[90] K.W. Raine. "A microscope for measuring axial stress profiles in optical fibres with high spatial resolution and low noise". Proceedings of the Optical Fiber Measurement Conference (OFMC) 97, pp. 269-272, National Physics Laboratory, Teddington, UK.

[91] H.G. Limberger, P.Y. Fonjallaz, R.P. Salathe, F. Cochet, B. Leuenberger. "Compaction and photoelastic induced index changes in fiber Bragg gratings". Applied Physics Letters, Vol. 68, No. 22, pp. 3069-3071, May 1996.

[92] P.E. Dyer, R.J. Farley, R. Giedl. "Analysis of grating formation with excimer laser irradiated phase masks". Optics Communications, Vol. 115, pp. 327-334, 1995.

[93] P.E. Dyer, R.J. Farley, R. Giedl, C. Radgale, D. Reid. "Study and analysis of submicron-period grating formation on polymers ablated using a KrF laser irradiated phase mask". Applied Physics Letters, Vol. 64, No. 25, pp. 3389-3391, June 1994.

[94] J.P. Schaffer, A. Saxena, S.D. Antolovich, T.H. Sanders, S.B. Warner. "The science and design of engineering materials", Chapter 9. Irwin, 1995.

[95] Fredrick Bacon. "The mechanical strength of silica optical fibers". 3M Application Note. June 1995.

[96] V.A. Bogatyrjov, M.M Bubnov, E.M. Dianov, S.D. Rumyantzev, S.L. Semjonov. "Mechanical reliability of polymer-coated and hermetically coated optical fibers based on proof testing". Optical Engineering, Vol. 30, No. 6, pp. 690-699. June 1991.

J.D. Helfinstine. "Delayed failure or subcritical crack growth in glass". Proceedings of the 28th Symposium on the Art of Glassblowing, 1983.

[97] D. Varelas, H.G. Limberger, R.P. Salathe. "Enhanced mechanical performance of single mode optical fibres irradiated by a CW UV laser". Electronics Letters, Vol. 33, No. 8, pp. 704-705, April 1997.

[98] D. Varelas, H.G. Limberger, R.P. Salathe, C. Kotrotsios. "UV induced degradation of optical fibres". Electronics Letters, Vol. 33, No. 9, pp. 804-806, April 1997.

Chapter 4

DYNAMIC POLARISATION GRATINGS

In this chapter, we will examine the applications of dynamic polarisation gratings created through the Kerr effect by means of an intense pump-pulse propagating along the fibre. These transient gratings can induce phase matched coupling between the polarisation modes of a counter-propagating CW probe beam, and can be used for mapping the birefringence along a polarisation preserving fibre (Sections 4.1 to 4.3). The application of transient gratings and pump-probe architectures to distributed sensing will be theoretically analysed (Sections 4.3 and 4.4), showing the potential advantages and limitations [1-3].

4.1 DYNAMIC GRATINGS: INTRODUCTION

The first technique proposed to measure the variations of birefringence along optical fibres was Polarisation Optical Time Domain Reflectometry (POTDR) [4]. However, back-scattering architectures like POTDR suffer the disadvantage of low signal level in the detector, which translates into long measurement times. In order to overcome this problem, new pump-probe architectures have been suggested [5,6]. As we discussed in Chapter 1, the idea is to enhance the signal by launching a counter-propagating continuous probe wave with respect to the pump pulse. The variations of a propagation property along the fibre due to an external perturbation are imprinted on the probe as a result of a nonlinear action of the pump on the probe. Several nonlinear mechanisms have been considered so far: Raman [5,6], Kerr [7-11] and Brillouin [12,13].

In this chapter, we will focus on pump-probe configurations where the action is due to the optical Kerr effect. The principle of operation, shown schematically in Figure 1, is described as follows. A circularly polarised, intense pump pulse is launched into the high birefringence fibre, so as to equally excite the two fundamental polarisation modes. Due to the Kerr effect, a dynamic birefringence grating resulting from the interference of the launched pump modes is generated. As the grating moves along the fibre, it induces coupling among the similarly launched modes of a continuous-wave counter-propagating probe beam [14].

If the pump and probe wavelengths are different, a frequency modulated signal is produced when one of the probe polarisation modes is detected through a polariser. The beat signal is the result of the interference between the small fraction of the probe light that has suffered coupling from one polarisation mode to the other and the rest of the probe light which has propagated without suffering any scattering (Figure 1). As the instantaneous frequency of the signal is proportional to the local birefringence along the fibre, the scheme has applications for distributed sensing measurement [8,9]. This type of sensor has clear advantages over intensity based sensors because the sensed parameters are related to a frequency that is immune to intensity transmission variations. Recently, a distributed sensor based on this effect with 1 m spatial resolution and 6 °C of temperature resolution has been demonstrated [9].

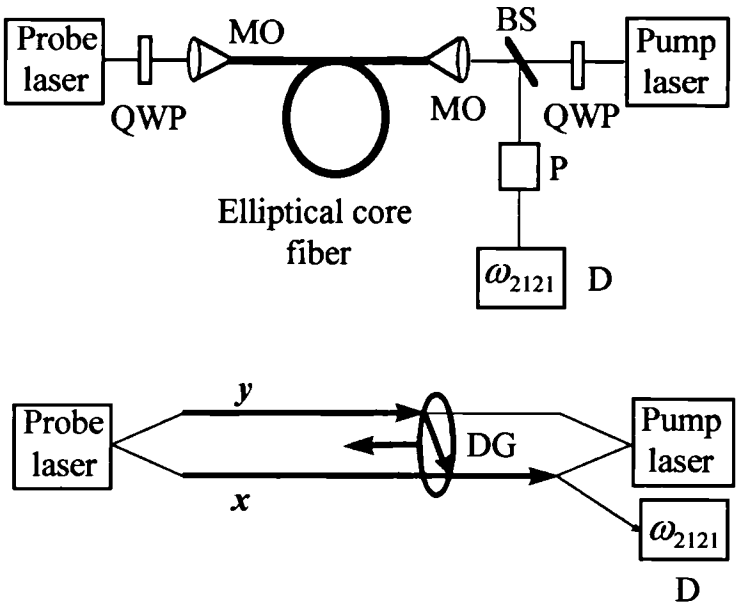

Figure 1. Schematic diagram of a pump-probe configuration. The polariser is aligned parallel to one of the optical axes of the birefringent fibre. QWP, quarter-waveplate; MO, microscope objective; BS, beamsplitter; P, polariser; D, detector; *x*, x polarisation; *y*, y polarisation; DG, dynamic grating created by the pump pulse.

In Section 4.2, we present the theoretical analysis of the Kerr induced coupling in a high birefringence fibre, giving expressions for the coupling coefficients and the derived frequencies. In Section 4.3, we first examine the simplest use of this principle [7,8] in which only the two fundamental polarisation modes propagate along the fibre. This will be extended to the case in which several low order modes are excited in both the pump and probe waves. Finally, Section 4.4 analyses the application of nonlinearly induced coupling to distributed sensing from a global system point of view, studying its signal-to-noise ratio performance.

4.2 ANALYSIS OF THE PUMP-PROBE KERR INTERACTION

In this section, we analyse the nonlinear coupling induced by an intense pump pulse on the modes of a counter-propagating continuous probe wave in a high birefringence optical fibre. A great variety of physical behaviours is possible depending on the time and length scales of the problem, and also depending on the parameters of the fibre. The following considerations will help us to frame the analysis. The temporal width of the pump pulse determines the spatial resolution of the distributed sensor and will be typically several nanoseconds. The birefringence of the fibre will have to be large enough to avoid random coupling among the polarisation

modes. Also, the inter-modal group delay must be low to prevent significant walk-off between the modes along the length of the sensor. Pump and probe powers will be high in order to induce significant Kerr index modulation, but they have to be maintained below the threshold of polarisation instability and other unwanted competing nonlinear effects, specially stimulated Raman (for the pump) and Brillouin scattering (for the probe). Another important parameter is the total length of the sensor, which will be typically limited to less than one kilometre. As the Kerr action of the pump on the probe relies on a coherent interference process, the finite line-width of the lasers will be taken into account in the analysis.

The analysis starts by studying the propagation of the pump pulse. The action of the pump on the probe is then described through a nonlinear polarisation source term in the Maxwell propagation equation for the probe. This equation will be solved by a perturbative scheme, and the appearance of the frequency modulated signals in the detector is explained as a consequence of the beating between the zero and first order perturbation probe solutions.

4.2.1 Field representations for probe and pump

The probe field, which is a continuous-wave (cw) propagating from the origin of the fibre (z=0) towards its end (z=L), can be represented as a sum over all the modes sustained by the fibre:

$$\bar{e}_{\omega_s}(t,x,y,z) = \Re e\left\{\overline{E}_{\omega_s}(t,x,y,z)\, e^{j\omega_s t}\right\} = \Re e\left\{\sum_m \tilde{A}_m(t,z)\, \overline{\Gamma}_m(x,y)\, e^{-j\int_0^z \beta_m^s dz}\, e^{j\omega_s t}\right\} \tag{1}$$

where the subscript *s* stands for probe, $\tilde{A}_m(t,z)$ is a slowly varying complex pulse amplitude, $\overline{\Gamma}_m(x,y)$ is the normalised field pattern of mode *m*, ω_S is the central frequency of the probe laser, and $\beta_m^s (= \beta_m(\omega_s, z))$ are the modal propagation constants at ω_S.The finite line-width of the laser is taken into account by supposing that $\tilde{A}_m(t,z)$ are stochastic processes. When the laser light enters the fibre it excites the several propagating modes according to the equations: $\tilde{A}_m(t,0) = A_m U_s(t)$, where A_m is a complex deterministic amplitude depending on the mode, and $U_S(t)$ is a stationary process, common for all modes, and which depends on the

characteristics of the probe laser. A model of random phase ($U_s(t) = e^{j\Phi_s(t)}$) with Lorentzian spectrum will be used to describe the laser. Its corresponding autocorrelation function is:

$$R_s(\tau) = E\left[U_s(t+\tau)U_s^*(t)\right] = e^{-\frac{\tau}{\tau_{coh}^s}} \tag{2}$$

where E accounts for ensemble average over realisations of the random process and τ_{coh}^s is the coherence time for the probe laser.

The pump, which is a pulse propagating from the end of the fibre (z=L) towards its origin (z=0), can be represented:

$$\bar{e}_{\omega_p}(t,x,y,z) = \Re e\left\{\bar{E}_{\omega_p}(t,x,y,z)\, e^{j\omega_p t}\right\} = \Re e\left\{\sum_m \tilde{P}_m(t,z)\,\bar{\Gamma}_m(x,y)\, e^{-j\int_z^L \beta_m^p dz}\, e^{j\omega_p t}\right\} \tag{3}$$

where the subscript p stands for pump and $\beta_m^p (=\beta_m(\omega_p, z))$ are the modal propagation constants at ω_p. Now, $\tilde{P}_m(t,L) = P_m\, S(t)\, U_p(t)$, where P_m is again a complex deterministic amplitude depending on the mode, $S(t)$ is an adequate deterministic pulse shape and $U_p(t)$ accounts for the stochasticity of the pump laser which will be independent with respect to the probe.

Selecting a convenient normalisation for the field patterns, the instantaneous power W_m carried by the mode m can be calculated as:

$$W_m(t,z) = E\left(\left|\tilde{A}_m(t,z)\right|^2\right) \tag{4}$$

where E stands again for ensemble average.

4.2.2 Propagation equations and nonlinear polarisation

By substituting the field representations (1), (3) into the general Maxwell propagation equations with the inclusion of a nonlinear polarisation term and carrying out the scalar product with a generic mode field pattern $\overline{\Gamma}_m(x,y)$, the propagation problem for the probe wave is transformed into the following system of first order partial differential equations [15] that extends the system in Equation 8 (Chapter 3):

$$\left(\frac{\partial \tilde{A}_k(t,z)}{\partial z}+\beta_k'^{s}(z)\frac{\partial \tilde{A}_k(t,z)}{\partial t}\right)=-j\frac{\omega_s}{4}e^{j\int_0^z \beta_k^t dz}\int\overline{\Gamma}_k^*(x,y)\cdot\overline{\Pi}_{\omega_s}^{nl}(t,x,y,z)\,dx\,dy \tag{5}$$

where $\beta_k'^{s}(z)$ is the inverse of the group velocity for mode k and $\overline{\Pi}_{\omega_s}^{nl}(t,x,y,z)$ is the complex amplitude at the probe wavelength of the nonlinear polarisation responsible for the interaction of pump and probe. Our study involves long pump pulses (several nanoseconds) and very highly monochromatic laser sources. For the lengths of fibre that we are addressing (around 1 km), both group velocity dispersion ($\beta_m'' \approx 0$) and losses in the fibre have been neglected simplifying considerably the propagation equations (5) [16]. Similar equations (except for the opposite direction of propagation) can be obtained for the propagation of the pump pulse.

As the central frequencies of probe and pump are different (ω_S and ω_P), nonlinear polarisations at several wavelengths will be induced. We will neglect transient nonlinear effects and the longitudinal components of the field along the fibre. Taking into account the glass isotropy and the electronic origin of the polarisation [16], the x and y components of the nonlinear polarisation at the probe wavelength ω_s are [17]:

$$\Pi_{\omega_S}^{x(y)}=\frac{3}{2}\varepsilon_o\chi_{xxxx}\left\{E_{\omega_p}^{x(y)}E_{\omega_p}^{x(y)*}E_{\omega_s}^{x(y)}+\frac{1}{3}\left(E_{\omega_p}^{x(y)}E_{\omega_p}^{y(x)*}E_{\omega_s}^{y(x)}+E_{\omega_p}^{y(x)}E_{\omega_p}^{x(y)*}E_{\omega_s}^{y(x)}+E_{\omega_p}^{y(x)}E_{\omega_p}^{y(x)*}E_{\omega_s}^{x(y)}\right)\right\} \tag{6}$$

where all the coefficients have been expressed in terms of χ_{xxxx} which, for silica glass has a value of 2.5 10^{-22} m^2/V^2. Similar reasoning gives the following results for the nonlinear polarisation amplitude at the pump wavelength:

$$\Pi_{\omega_p}^{x(y)} = \frac{3}{4}\varepsilon_o \chi_{xxxx}\left\{E_{\omega_p}^{x(y)}E_{\omega_p}^{x(y)*}E_{\omega_p}^{x(y)} + \frac{1}{3}\left(E_{\omega_p}^{x(y)}E_{\omega_p}^{y(x)*}E_{\omega_p}^{y(x)} + E_{\omega_p}^{y(x)}E_{\omega_p}^{x(y)*}E_{\omega_p}^{y(x)} + E_{\omega_p}^{y(x)}E_{\omega_p}^{y(x)*}E_{\omega_p}^{x(y)}\right)\right\} \tag{7}$$

Substituting the nonlinear polarisation terms (6) in equation (5), the propagation equations for the probe modes are obtained:

$$\frac{\partial \tilde{A}_k(t,z)}{\partial z} + \beta_k'^{s}(z)\frac{\partial \tilde{A}_k(t,z)}{\partial t} = -j\sum_{mnl}\left\{\gamma_s \tilde{P}_m(t,z)\tilde{P}_n^*(t,z)\tilde{A}_l(t,z)e^{-j\int_z^L(\beta_m^p-\beta_n^p)\delta}\, e^{-j\int_0^z(\beta_l^s-\beta_k^s)\delta}\, \frac{1}{A_{eff}^{mnlk}}\right\} \tag{8}$$

with γ_s given by:

$$\gamma_s = 3\pi\frac{\chi_{xxxx}}{\varepsilon_o n_{eff}^2 c\lambda_s} \tag{9}$$

where n_{eff} is an average modal refractive index, which depends on the modes *m, n, l* and *k*. We ignore this dependence because it only gives rise to second order effects. A_{eff}^{mnlk} is an effective area defined by the overlap integral among several mode field patterns. If we define:

$$I_{mnlk}^{\alpha\beta\gamma\delta} = \frac{\int \Gamma_m^{\alpha}\Gamma_n^{\beta*}\Gamma_l^{\gamma}\Gamma_k^{\delta*}\,dx\,dy}{\int \Gamma_m^{\alpha}\Gamma_m^{\alpha*}\,dx\,dy \int \Gamma_n^{\beta}\Gamma_n^{\beta*}\,dx\,dy \int \Gamma_l^{\gamma}\Gamma_l^{\gamma*}\,dx\,dy \int \Gamma_k^{\delta}\Gamma_k^{\delta*}\,dx\,dy} \tag{10}$$

where α, β, γ and δ can take the values *x, y*; then the effective area is given by:

$$\frac{1}{A_{eff}^{mnlk}} = I_{mnlk}^{xxxx} + I_{mnlk}^{yyyy} + \frac{1}{3}\left(I_{mnlk}^{xxyy} + I_{mnlk}^{yyxx} + I_{mnlk}^{xyxy} + I_{mnlk}^{xyyx} + I_{mnlk}^{yxyx} + I_{mnlk}^{yxxy}\right) \tag{11}$$

The calculation of $I_{mnlk}^{\alpha\beta\gamma\delta}$ does not depend on the normalisation chosen for the field patterns. For later purposes, it is convenient to define $\Delta\beta_{mnlk}(z)$, which is a measure of the mismatch among the propagation constants of the modes *m, n, l* and *k*:

$$\Delta\beta_{mnlk}(z)=\left(\beta_m^p-\beta_n^p\right)-\left(\beta_l^s-\beta_k^s\right) \tag{12}$$

Analogously, using (7) the propagation equations for the pump modes can be derived:

$$\frac{\partial\widetilde{P}_k(t,z)}{\partial z}-\beta_k'^p(z)\frac{\partial\widetilde{P}_k(t,z)}{\partial t}=+\frac{j}{2}\sum_{mnl}\left\{\gamma_p\,\widetilde{P}_m(t,z)\widetilde{P}_n^*(t,z)\widetilde{P}_l(t,z)e^{-j\int_z^L\Delta\beta_{mnlk}^p\delta}\frac{1}{A_{eff}^{mnlk}}\right\} \tag{13}$$

where γ_p is defined in a similar way to γ_S, and $\Delta\beta_{mnlk}^p$ is defined differently to $\Delta\beta_{mnlk}$, because now all the modes belong to the pump and are co-propagating, so that:

$$\Delta\beta_{mnlk}^p(z)=\beta_m^p-\beta_n^p+\beta_l^p-\beta_k^p \tag{14}$$

In equation (13) we have neglected any effect that the probe could induce on the propagation of the pump pulse.

4.2.3 Solution of the propagation equations

Firstly, we will solve the propagation equations for the pump pulse. The modes of a high birefringence fibre, which are almost linearly polarised, are strongly preserved in their propagation. The large difference between their propagation constants makes the random coupling among modes a very inefficient process (Section 3.1.2) so that those nonlinear terms in equation (13) with $\Delta\beta_{mnlk}^p$ (14) distinct from zero are not effective in coupling the modes. These terms would only be important when the pump power is so high that the nonlinear phase modulation compensates the phase difference induced by the unequal propagation constants of the modes, giving rise to polarisation ellipse rotation [16,18,19] or polarisation instability [20,21]. Only terms with $\Delta\beta_{mnlk}^p$ equal to zero, which are responsible for self and cross-phase

modulation, will be relevant in our case, i.e. those with $m=n$ and $l=k$ or with $m=k$ and $n=l$. The simplified propagation equation for the pump is now:

$$\frac{\partial \widetilde{P}_k(t,z)}{\partial z} - \beta_k'^{P}(z)\frac{\partial \widetilde{P}_k(t,z)}{\partial t} = +\frac{j}{2}\gamma_P\left\{\left|\widetilde{P}_k(t,z)\right|^2 \frac{1}{A_{eff}^{kkkk}} + \sum_{m(\neq k)}\left|\widetilde{P}_m(t,z)\right|^2\left(\frac{1}{A_{eff}^{mmkk}}+\frac{1}{A_{eff}^{kmmk}}\right)\right\}\widetilde{P}_k(t,z) \tag{15}$$

When more than the two fundamental modes are propagating along the fibre, special care must be taken when neglecting the cross terms as will be discussed in Section 4.3.2. If the pump fields at the beginning of the fibre $\widetilde{P}_k(t,0)$ are known (initial conditions), the integration of equation (15) gives the following expression for the propagation of the pump pulse:

$$\widetilde{P}_k(t,z) = \widetilde{P}_k\left(t-\int_z^L \beta_k'^{P}\delta, L\right)\; e^{-j\frac{\gamma_P}{2}\int_z^L\left\{\widetilde{P}_k\left(t-\int_z^L \beta_k'^{P}\delta, L\right)^2 \frac{1}{A_{eff}^{kkkk}} + 2\sum_{q(\neq k)}\widetilde{P}_q\left(t-\int_\eta^L \beta_q'^{P}\delta-\int_z^\eta \beta_k'^{P}\delta, L\right)^2 \frac{1}{A_{eff}^{qqkk}}\right\}d\eta} \tag{16}$$

where we have used δ for a generic differential element.

After substituting the solution for the pump (16) in (8), we integrate the probe equation. The situation now is different from the pump propagation case because the phase matching condition for coupling between different probe modes can be verified and power is exchanged among them. The pump generates a dynamic polarisation grating that couples the probe modes while it moves along the fibre. However, the coupling will be rather weak, so that a perturbative scheme is suitable for the solution of the equation. Using standard perturbation theory, the probe wave is described in first order approximation:

$$\widetilde{A}_k(t,z) \;\approx\; \widetilde{A}_k^0(t,z) \;+\; \widetilde{A}_k^1(t,z) \tag{17}$$

where $\widetilde{A}_k^0(t,z)$ and $\widetilde{A}_k^1(t,z)$ satisfy the following equations:

$$\frac{\partial \widetilde{A}_k^0(t,z)}{\partial z} + \beta_k'^{s}(z)\frac{\partial \widetilde{A}_k^0(t,z)}{\partial t} = H_k(t,z)\widetilde{A}_k^0(t,z) \tag{18}$$

$$\frac{\partial \tilde{A}_k^1(t,z)}{\partial z} + \beta_k'^s(z)\frac{\partial \tilde{A}_k^1(t,z)}{\partial t} = H_k(t,z)\tilde{A}_k^1(t,z) + G_k\left(t,z,\left\{\tilde{A}_m^0(t,z)\right\}\right) \tag{19}$$

The term $H_k(t,z)$ is slowly varying in z, and appears when we set $m=n$ and $l=k$ in the source term of the probe propagation equation (8). This term is responsible for the cross-phase modulation between pump and probe:

$$H_k(t,z) = -j\gamma_s \sum_q \left|\tilde{P}_q(t,z)\right|^2 \frac{1}{A_{eff}^{qqkk}} \tag{20}$$

$\tilde{G}_k(t,z,\{\tilde{A}_m(t,z)\})$ will include the rest of the source terms in the probe propagation equation, and will give rise to the coupling among the probe modes. If we define $[m,n,l]$ to be the set of $\{m,n,l\}$ such that $\{m = n \text{ and } l \neq k\}$ or such that $\{m \neq n\}$, then $\tilde{G}_k(t,z,\{\tilde{A}_m(t,z)\})$ will be:

$$G_k\left(t,z,\left\{\tilde{A}_m\right\}\right) = -j\sum_{[mnl]}\left\{\gamma_s \tilde{P}_m(t,z)\tilde{P}_n^*(t,z)\tilde{A}_l(t,z)e^{-j\int_z^L(\beta_m^p-\beta_n^p)\delta}\, e^{-j\int_0^z(\beta_l^s-\beta_k^s)\delta}\frac{1}{A_{eff}^{mnlk}}\right\} \tag{21}$$

Some of the terms in (21) are null when linearly polarised modes are assumed. The solution of equation (18) when an initial probe field $\tilde{A}_k(t,0)$ is launched into the fibre at z=0 gives for $\tilde{A}_k^0(t,z)$:

$$\tilde{A}_k^0(t,z) = \tilde{A}_k^0\left(t-\int_0^z \beta_k'^s\delta, 0\right)\; e^{-j\gamma_s\int_0^z \sum_q \left|\tilde{P}_q(t-\int_z^L \beta_q'^p\delta-\int_\eta^z \beta_k'^s\delta, L)\right|^2 \frac{1}{A_{eff}^{qqkk}}d\eta} \tag{22}$$

$\tilde{A}_k^1(t,z)$ is now calculated by solving equation (19) with null initial conditions. It can be expressed as an integral extended to the pump-probe interaction length, which is illustrated in a space-time diagram in Figure 2. While $\tilde{A}_k^0(t,z)$ represents the propagation of the initially launched probe light subject to cross-phase modulations from the pump, $\tilde{A}_k^1(t,z)$ represents the scattering from one mode to other due to nonlinear induced coupling.

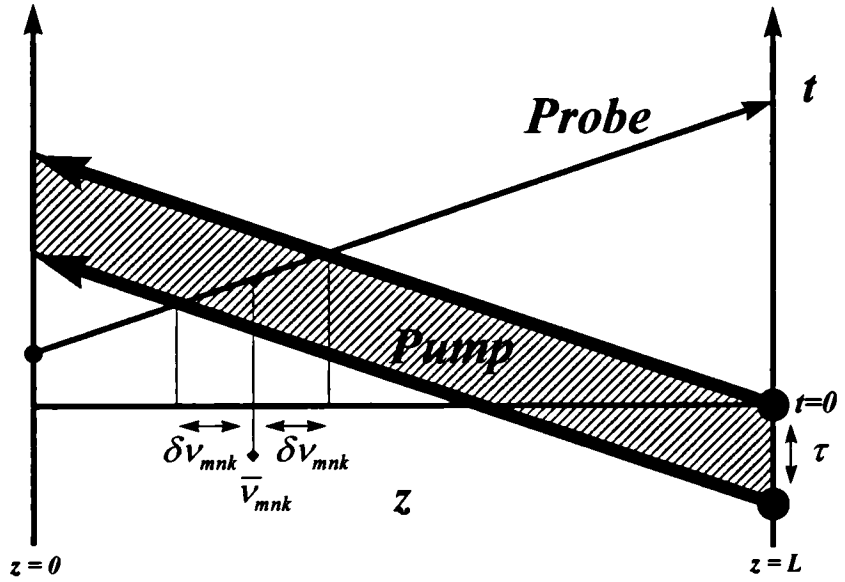

Figure 2. Space-time diagram which illustrates the action of the pump on the probe.

Our main interest is the time evolution of the instantaneous power of the probe wave at the detector. If a mode k is filtered before the detector (with a polariser and a spatial filter), the measured power according to (4) will be:

$$W_k(t) = E\left(\left| \tilde{A}_k^0(t,L) + \tilde{A}_k^1(t,L) \right|^2 \right) \approx \left| A_k \right|^2 + \mathrm{Re}\left\{ E\left(2\,\tilde{A}_k^1(t,L)\,\tilde{A}_k^{0*}(t,L) \right) \right\} \quad (23)$$

where A_k is the complex deterministic amplitude of mode k (Section 4.2.1) and the ensemble average for $\left|\tilde{A}_k^0(t,L)\right|^2$ was calculated taking into account (2). The second term in (23) has been evaluated by first calculating the ensemble average and then carrying out the space integration which solves (19), assuming that the two lasers were statistically independent and described by a random phase model with autocorrelations R_p and R_s given by (2).

For simplicity, we suppose that the pump pulse shape function $S(t)$ is a square function of amplitude unity and time spread τ. The product of the shape functions restricts the interval of integration, which is given by the overlap of the pump pulses of the interacting modes m and n. If we define an average group velocity for every pair of modes (m,n) $\bar{\beta}_{mn}^{\prime p}$ ($=(\beta_m^{\prime p} + \beta_n^{\prime p})/2$) and also a parameter which accounts for the group velocity difference between the modes m

and n $\delta\beta'^{p}_{mn}$ ($=\left|\beta'^{p}_{m}-\beta'^{p}_{n}\right|/2$), then the midpoint value of the integration interval $\bar{v}_{mnk}$ and its half-width δv_{mnk} could be approximated, supposing uniform group velocity along the fibre, by the expressions:

$$\begin{aligned}\bar{v}_{mnk} &\approx L-\frac{t-\frac{\tau}{2}}{\bar{\beta}'^{p}_{mn}+\beta'^{s}_{k}}\\ \delta v_{mnk} &\approx \frac{\frac{\tau}{2}}{\bar{\beta}'^{p}_{mn}+\beta'^{s}_{k}}-\frac{\delta\beta^{p}_{mn}\left(t-\frac{\tau}{2}\right)}{\left(\bar{\beta}'^{p}_{mn}+\beta'^{s}_{k}\right)^{2}}\end{aligned} \tag{24}$$

where it can be appreciated that the integration interval decreases with time due to the walk-off between the modes. The instantaneous power detected in mode k (17) yields:

$$\begin{aligned}W_k(t) \;=\; &\left|A_k\right|^2 \;+\\ &+\;\mathrm{Re}\left\{-4\,j\,\gamma_s\sum_{[mnl]}\left[P_m\,P_n^{*}\,A_l\,A_k^{*}\;\;R_p\left(\int_{v_{mnk}}^{L}\left(\beta'^{p}_{m}-\beta'^{p}_{n}\right)\delta\right)\;\;R_s\left(\int_{0}^{v_{mnk}}\left(\beta'^{s}_{l}-\beta'^{s}_{k}\right)\delta\right)\right.\right.\\ &\left.\left.e^{-j\delta\beta^{p}_{mn}(L-v_{mnk})}\;\;e^{-j\int_{v_{mnk}}^{L}(\beta^{p}_{m}-\beta^{p}_{n})\delta}\;\;e^{-j\int_{0}^{v_{mnk}}(\beta^{s}_{l}-\beta^{s}_{k})\delta}\;\;\frac{1}{A^{mnlk}_{eff}}\right.\right.\\ &\left.\left.\frac{1}{\left(\Delta\beta_{mnlk}(\bar{v}_{mnk})+\delta\beta^{p}_{mn}-\delta\beta^{s}_{lk}\right)}\;\;\sin\left(\left(\Delta\beta_{mnlk}(\bar{v}_{mnk})+\delta\beta^{p}_{mn}-\delta\beta^{s}_{lk}\right)\delta v_{mnk}\right)\right]\right\}\end{aligned} \tag{25}$$

where $\Delta\beta_{mnlk}$ was defined in (12) and $\delta\beta^{p}_{mn}$ is a small shift in the pump propagation constants due to nonlinear phase modulations:

$$\delta\beta^{p}_{mn}=\frac{\gamma_p}{2}\left\{\left|P_m\right|^2\frac{1}{A^{mmmm}_{eff}}+2\sum_{q(\neq m)}\left|P_q\right|^2\frac{1}{A^{qqmm}_{eff}}-\left|P_n\right|^2\frac{1}{A^{nnnn}_{eff}}-2\sum_{q(\neq n)}\left|P_q\right|^2\frac{1}{A^{qqnn}_{eff}}\right\} \tag{26}$$

and $\delta\beta^{s}_{lk}$ is given by the expression:

$$\delta\beta_{lk}^{s} = \gamma_s \left\{ \sum_q |P_q|^2 \frac{1}{A_{eff}^{qqll}} - \sum_q |P_q|^2 \frac{1}{A_{eff}^{qqkk}} \right\} \tag{27}$$

This is the main result of the analysis. It can be observed that because of the time variation of $\bar{\nu}_{mnk}$ (24), oscillating frequency modulated signals will appear in the detector. The interpretation of (25) is straightforward: every pair of pump modes *m* and *n* generate by interference a birefringence grating through the Kerr effect which couples some light from the probe mode *l* to the probe mode *k*. To know the overall power coupled to mode *k*, a summation of the contributions from all the possible pump induced gratings (*m,n*) and all the possible probe modes *l* is performed. For each set of numbers (*mnlk*), there is a frequency modulated signal in the detector whose instantaneous frequency can be calculated by carrying out the time derivative of the phase of the exponential in the former expression:

$$\omega_{mnlk}(t) = -\frac{d\phi_{mnlk}(t)}{dt} = \left(\Delta\beta_{mnlk}(\bar{\nu}_{mnk}) + \delta\beta_{mn}^{p} \right) \frac{1}{\bar{\beta}_{mn}^{lp} + \beta_k^{ls}} \tag{28}$$

It is clear that the instantaneous frequency depends on the local birefringence along the fibre.

The coupling term in equation (25) can be written in terms of a *sinc* function. This is due to the particular choice of a square pump pulse shape. Other pulse shapes, such as a gaussian for example, will apodise the side lobes of the coupling spectrum.

4.3 APPLICATIONS

4.3.1 Fundamental modes

If both pump and probe propagate along the high birefringence fibre in the two orthogonal fundamental modes: *1* (polarised along the x axes) and *2* (polarised along the y axes), equation (25) describes the possible interactions between them. Selecting the mode *2* of the probe beam through a polariser at the exit of the fibre, only two terms among all the [*mnl*] possible combinations give a non null contribution to the beating signal: (*1,2,1*) and (*2,1,1*). This can be proved by assuming linearly polarised modes in the overlap integrals for the calculation of the effective area (11). When the pump power is equally launched in the two pump modes, both $\delta\beta_{mn}^{p}$ and $\delta\beta_{lk}^{s}$ will be null. Defining an effective refractive index for each

mode n_{eff}^{m} $(= \beta_m(\omega)\, c / \omega)$ and also neglecting the birefringence dispersion of the fibre, the two frequencies will be:

$$\omega_{1212} \approx \frac{n_{eff}^{1} - n_{eff}^{2}}{2\,\overline{n}_{eff}} \left(\omega_p - \omega_s\right) = \frac{\Delta n_{eff}^{12}}{2\,\overline{n}_{eff}} \left(\omega_p - \omega_s\right) \tag{29}$$

$$\omega_{2112} \approx \frac{n_{eff}^{1} - n_{eff}^{2}}{2\,\overline{n}_{eff}} \left(\omega_p + \omega_s\right) = \frac{\Delta n_{eff}^{12}}{2\,\overline{n}_{eff}} \left(\omega_p + \omega_s\right) \tag{30}$$

where Δn_{eff}^{12} is the birefringence between modes *1* and *2* and $\overline{n}_{eff}$ is an average effective refractive index between the two modes. It is clear that ω_{1212} is much smaller than ω_{2112}. As these two beat signals are small oscillations over a background constant level, we can also define a visibility for each of them. If we are operating in the coherent range of the sources and the walk-off between modes is negligible for the length of fibre used, then the following expression holds for the visibility of the term *(m,n,l,k)*:

$$V_{mnlk} = \gamma_s \left| \frac{P_m\, P_n\, A_l}{A_k} \right| \frac{1}{A_{eff}^{mnlk}} \left(\frac{c}{\overline{n}_{eff}}\, \tau \right) sinc\left(\frac{\omega_{mnlk}\, \tau}{2\pi} \right) \tag{31}$$

where the *sinc* function is defined as $sinc(x)=sin(\pi x)/(\pi x)$.

Usually, the signal associated with the modes *(2,1,1,2)* has very low visibility because the high value of the frequency ω_{2112} makes the sinc function null. This frequency will be observed only when the birefringence of the fibre is weak. Experimentally, it was observed in Ref. [7], although not explicitly stated. In high birefringence fibres, the signal associated with the modes *(1,2,1,2)* will be predominant. In general, the coupling terms in (25) for which the modes of the pump are in the same order as the modes of the probe ($m=l$, $n=k$) correspond to phase matched interactions and will be predominant in high birefringence fibres.

4.3.2 Several low order modes

Now, we suppose that several low order modes propagate along a high birefringence elliptical core fibre. As we discussed in Section 3.1.2, the LP_{11} mode of weakly-guiding circular-core

fibres consists of four degenerate modes. For strongly guiding elliptical core fibres this degeneracy is lifted and the modes can be grouped into two pairs, (even-LP_{11}) and (odd-LP_{11}), with different cut-off wavelengths [26,22]. The operating wavelength of the fibre can be selected so that only the first of these pairs of modes are guided, namely the (even-LP_{11}) pair. The modes thus propagating in the fibre are the fundamental modes ${}_xLP_{01}$(*1*) and ${}_yLP_{01}$ (*2*) and the higher order modes even-${}_xLP_{11}$ (*3*) and even-${}_yLP_{11}$ (*4*). Due to the non-degeneracy among the mode propagation constants, these modes maintain their identity as they propagate along the fibre. Differential losses between the fundamental and the higher order modes have been measured to be as small a 0.3 dB/km [23]. Also, the inter-modal group delay, which causes walk-off among the modes, can be minimised through an adequate choice of the operating wavelength [22,27,28]. As the birefringence between the fundamental modes *1* and *2* (Δn_{eff}^{12}) is usually different from the birefringence between the higher order modes *3* and *4* (Δn_{eff}^{34}), the approximation made in (19) in which we neglected coupling among the pump modes is valid, and our former analysis holds.

If both pump and probe excite the four lower order modes of the fibre, then the possible phase matched ($m=l$, $n=k$) couplings among them are shown in Figure 3. As $\delta\beta_{mn}^{p}$ and $\delta\beta_{lk}^{s}$ are very small for symmetric launching and can be neglected, the signal visibilities will be given by (31) and the derived frequencies by the following expression (similar to (29)):

$$\omega_{mnmn} \approx \frac{n_{eff}^{m} - n_{eff}^{n}}{2\,\bar{n}_{eff}} \left(\omega_p - \omega_s\right) = \frac{\Delta n_{eff}^{mn}}{2\,\bar{n}_{eff}} \left(\omega_p - \omega_s\right) \qquad (32)$$

Figure 4 shows one possible arrangement where two detectors are separately exposed to the fundamental (*1*) and higher order mode (*3*) by suitably filtering the probe beam. There are three derived frequencies associated with each mode. However, those frequencies arising from coupling between different spatial modes will be an order of magnitude higher in value in an elliptical-core fibre because of the short intermodal beatlength (large Δn_{eff}^{mn}) and therefore will be associated with a much weaker visibility because of the large argument of the *sinc* function in equation (31). These frequencies are represented in Figure 3 by dashed lines.

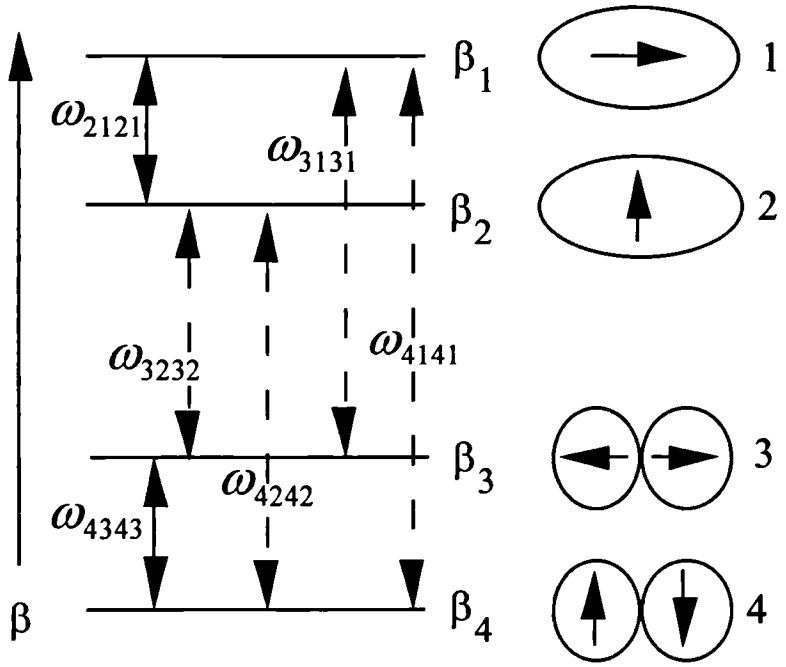

Figure 3. Propagation constants of the first four nondegenerate modes in an elliptical-core fibre and the possible Kerr derived frequencies.

This scheme has the potential to measure the variations along the fibre of two external perturbations simultaneously. As two frequencies (ω_{2121} and ω_{4343}) are detected, and each of them depends on the two external parameters with a certain degree of independence, the magnitude of both perturbations could in principle be determined. It has been experimentally shown, for example, that temperature and strain can be separated by measuring simultaneously both the birefringence between the two fundamental modes (Δn_{eff}^{12}) and the birefringence between the two first higher order modes (Δn_{eff}^{34}) in an elliptical core fibre. The relationship between birefringence and the temperature and strain is expressed through a matrix which is well conditioned and can be inverted [24]. The elements of this matrix have been measured for a variety of elliptical-core fibres by studying the resonant wavelength shifts of mode coupling in rocking filters [29,30] and by polarimetric techniques [31].

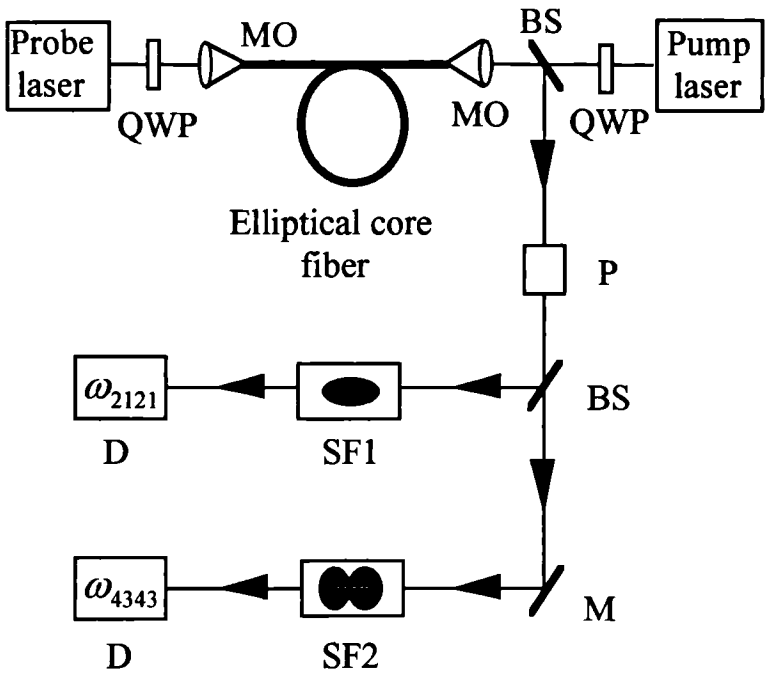

Figure 4. Schematic diagram of the proposed sensor. The polariser is aligned parallel to one of the optical axes of the birefringent fibre. QWP, quarter-waveplate; MO, microscope objective; BS, beamsplitter; P, polariser; SF1, fundamental mode spatial filter; SF2, higher order mode spatial filter; D, detector; M, mirror.

4.4 SYSTEM CONSIDERATIONS

In this section we study the performance of the nonlinearly induced coupling technique in terms of its signal-to-noise ratio. We will focus on the simplest case in which only the fundamental modes are excited in the fibre and the signal associated with the non phase-matched interaction (ω_{2112}) is negligible. The signal detected in the photodiode corresponding to the phase-matched interaction is a frequency modulated signal, with instantaneous frequency given by:

$$f(t) = \frac{\omega_{1212}(t)}{2\pi} = f_c + f_\Delta X(t) \qquad (33)$$

where f_c is the frequency produced by the average background birefringence, and $f_\Delta X(t)$ are the small frequency fluctuations due to changes in birefringence along the fibre induced by the external perturbation X. The sensitivity S_x of the instantaneous frequency to the perturbation X is $S_x = f_\Delta / f_c$. The relation between the time argument of X and the spatial location of the

perturbation (*t-z*) is given in expression (24). If we limit the bandwidth of *X(t)* to B_x, then the fastest spatial periodic perturbation that could be resolved will be:

$$\Delta z = \frac{c}{2\,\overline{n}_{eff}\,B_x} \tag{34}$$

where it was assumed that the pulse width τ was smaller than $1/B_x$ so that the spatial resolution of the distributed sensor was limited by the bandwidth B_x. As the deviation ratio of the frequency modulated probe signal is very low, the bandwidth of the frequency modulated signal B_{FM} is simply related to the bandwidth of the demodulated signal by $B_{FM} = 2\,B_X$.

Let us now calculate the signal-to-noise ratio of the frequency modulated signal. The signal, which is the average of the squared current, can be calculated using the visibility expression (31):

$$S_{FM} = \frac{1}{2}\left(R\,\gamma_s\,|P_1\,P_2\,A_1\,A_2|\,\frac{1}{A_{eff}^{1212}}\left(\frac{c}{\overline{n}_{eff}}\,\tau\right) sinc\left(f_c\,\tau\right)\right)^2 \tag{35}$$

where R is the responsivity of the photodetector, and the ½ term is due to the average of a squared sinusoidal signal. Shot noise will predominate over circuit noise in the detection process because of the large *dc* term in the instantaneous power (25). Consequently, a *pin* photodiode detector (no internal gain) is assumed. The noise, which will be filtered over the bandwidth of the signal B_{FM}, is given by the expression:

$$N_{FM} = 2eR|A_2|^2\,B_{FM} \equiv \mu B_{FM} \tag{36}$$

where e is the electron charge and a noise spectral density μ has been introduced. This noise in the frequency modulated signal will give rise to fluctuations in the instantaneous phase and frequency. Using the theory of FM demodulation [25], the fluctuations of the instantaneous frequency shift σ_f will translate into a maximum resolution for the parameter X:

$$\Delta X = \frac{\sigma_f}{f_\Delta} = \sqrt{\frac{\mu\,B_X^3}{3\,S_{FM}}}\;\frac{1}{f_c\,S_X} \tag{37}$$

As the denominator of (37) depends on the product ($f_c\tau\ sinc\ (f_c\tau)$), the resolution with respect to the parameter X is optimised when:

$$f_c\tau \approx \frac{1}{2} \tag{38}$$

The resolution with respect to the parameter X will also improve as $M^{-1/2}$ when M successive repetitions of the experiment are averaged.

A numerical example for a typical system design is presented below. The theoretical predictions agree well with the experimental data presented in Ref. [9]. We suppose that the laser wavelengths are close to 630 nm, and that the fibre has a birefringence between fundamental modes of 1.5 10^{-4} (equivalent to a beatlength of 4 mm). Let us fix the spatial resolution to 1m, so that the bandwidth B_X is 100MHz. We can also set the pump pulse width τ to 5 ns, smaller than $1/B_x$, so that the centre frequency f_c is 100 MHz according to (38). This means that the wavelength separation between pump and probe has to be 1.25 nm.

The signal-to-noise ratio for the frequency modulated signal increases with both pump and probe powers. Other competing nonlinear effects limit the maximum powers for pump and probe. In the case of the pump pulse, the stimulated Raman scattering limits the pump power roughly to 1 W. For the probe, it is the backward Brillouin stimulated scattering which limits the probe power to several mW. An effective length for the sensor of 450 m (attenuation of 10dB/km) was assumed in the calculations. Safe launched powers would be 0.5 W in each pump mode and 1mW in each probe mode.

The visibility of the frequency modulated signal can be calculated through (31) and yields 1%. In this calculation an effective area A_{eff}^{1212} of 18 μm^2, which corresponds to a modal area of 3μm^2, has been assumed. S_{FM} is calculated through (35) giving 15 μA^2 if a responsivity of 0.5A/W is assumed for the photodiode.

The shot noise spectral density μ is 1.6 10^{-10} $\mu A^2\,Hz^{-1}$ (36). If we suppose a noise equivalent power (NEP) of 4 pA $Hz^{-1/2}$ for the photodiode, then the circuit noise spectral density is $1.6{\cdot}10^{-11}\mu A^2\,Hz^{-1}$, which is one order of magnitude smaller than the shot noise. N_{FM} will be

0.03 μA^2, so that the signal-to-noise ratio for the frequency modulated signal is 27 dB, which is higher than the typical FM demodulation threshold of 10 dB. This figure could be compared with the signal-to-noise ratio of other techniques. For Raman backscattering, for example, a single shot signal-to-noise ratio of 8 dB is typically achieved when the Raman scattered light from a pump laser operating at 633 nm and with peak power 10 W is detected in an APD with responsivity 0.5 A/W and gain of 100.

If the external parameter to measure is temperature, the sensitivity S_T is 3 10^{-4} $^{\circ}C^{-1}$. The temperature resolution per single shot of the pump laser will be 60 °C and 900 pulses are needed to achieve a temperature resolution of 2 °C. One of the advantages of using birefringence sensors is their ability to measure also other external parameters such as strain. For strain, the sensitivity S_ε is 2 10^{-3} $m\varepsilon^{-1}$ so that for the former 900 pulses a strain resolution of 300 $\mu\varepsilon$ would be achieved.

The overall length of the sensor is limited by three factors: loss of coherence among the pump or probe modes, walk-off among the modes or reduction of the strength of the interaction due to losses in the fibre. In our example, the more restrictive of these three is the reduction of power due to losses, which limit the overall length of the sensor to several hundred meters. If the wavelength of operation had been longer, the sensor range could have been extended approximately to one kilometre. Walk-off and loss of coherence among the modes would have then been the most limiting factors.

4.5 CONCLUSION

As a summary, we have analysed the Kerr-induced nonlinear coupling in several pump-probe distributed sensing architectures. We have derived expressions for the coupling efficiencies among the different modes and also for the frequencies generated when the wavelengths of pump and probe differ. The application of these architectures to distributed sensing has also been discussed, showing their potential advantages. First, the improved signal-to-noise ratio with respect to other backscattering techniques; second, the ability of birefringence based sensors to measure both temperature and strain; and third, the possibility of simultaneous measurement of several external parameters by using more complex schemes.

REFERENCES

[1] F. Parvaneh, M. Farhadiroushan, R. Thomas, R. Feced, V.A. Handerek, A.J. Rogers. "Demonstration and potential of distributed temperature sensors using the frequency derived technique". Progress in optical fibre sensors and their applications. IEE, London, November 1995.

[2] F. Parvaneh, M. Farhadiroushan, R. Thomas, R. Feced, V.A. Handerek, A.J. Rogers. "Recent progress in distributed temperature sensing using the frequency derived technique". Optical Fiber Sensors (OFS-11), Sapporo (Japan), May 1996.

[3] R. Feced, S.E. Kanellopoulos, M. Farhadiroushan, V.A. Handerek, A.J. Rogers. "Analysis of optical Kerr effect induced coupling among polarization modes in high-birefringence optical fibers". Optics Communications, Vol. 143, pp. 268-278, November 1997.

[4] A.J. Rogers. "Polarization-optical time domain reflectometry: a technique for the measurement of field distributions". Applied Optics, Vol. 20, No. 6, 1060-1074, March 1981.

[5] M.C. Farries, A.J. Rogers. "Distributed sensing using stimulated Raman action in a monomode optical fibre". Proceedings of the 2nd International Conference on Optical Fibre Sensors, pp. 121-132, Stuttgart 1984.

[6] T. Valis, R. D. Turner and R. M. Measures. "Distributed fiber optic sensing based on counterpropagating waves". Applied Optics, Vol. 28, No. 11, pp. 1984-1990, 1989.

[7] F. Parvaneh, L.C.G. Valente, V.A. Handerek, A.J. Rogers. "Forward-scatter frequency-derived distributed optical-fibre sensing using the optical Kerr effect". Electronics Letters, Vol. 28, No. 12, pp. 1080-1082, June 1992.

[8] F. Parvaneh, V.A. Handerek, A.J. Rogers. "Frequency derived remote measurement of birefringence in polarization maintaining fiber by using the optical Kerr effect". Optics Letters, Vol. 17, No. 19, pp. 1346-1348, October 1992.

[9] F. Parvaneh, M. Farhadiroushan, V.A. Handerek, A.J. Rogers. "High resolution optical fibre distributed sensor based on the frequency-derived technique". Electronics Letters, Vol. 38, No. 24, pp. 2263-2264, November 1996.

[10] W. Zhao, E. Bourkoff. "Distributed fiber sensing by using nonlinearly induced polarization coupling". Optics Letters, Vol. 17, No. 12, pp. 856-858, June 1992.

[11] W. Zhao, E. Bourkoff. "Nonlinear polarization coupling and its application to high resolution distributed fiber sensing", IEEE Journal Quantum Electronics, Vol. 29, No. 7, pp. 2198-2210, July 1993.

[12] T. Horiguchi, T. Kurashima, M. Tateda. "Tensile strain dependence of Brillouin frequency shift in silica optical fibres". IEEE Photonics Technology Letters, Vol. 1, No. 5, pp. 107-108, May 1989.

[13] D. Culverhouse, F. Farahi, C.N. Pannel, D.A. Jackson. "Potential of stimulated Brillouin scattering as sensing mechanism for distributed temperature sensors". Electronics Letters, Vol. 25, No. 14, pp. 913-914, July 1989.

[14] S.U. Ahmed, V.A. Handerek, A. J. Rogers. "Phase matched polarization coupling in high birefringence fibers through the optical Kerr effect". Optics Letters, Vol. 17, No. 9, pp. 643-645, May 1992.

[15] A.D. Boardman, G.S. Cooper. "Power dependent polarization of optical pulses". Journal Optical Society America B, Vol. 5, No. 2, pp. 403-418, February 1988.

[16] G. P. Agrawal. "Nonlinear Fibre Optics", pp. 177-179. Academic Press, 1989.

[17] P.N. Butcher, D. Cotter. "The elements of nonlinear optics", pp. 24-25. Cambridge University Press, 1990.

[18] A. Owyoung, R.W. Hellwarth, N. George. "Intensity-induced changes in the optical polarizations in glasses". Physical Review B, Vol. 5, No. 2, pp. 628-632, January 1972.

[19] H.G. Winful. "Self-induced polarization changes in birefringent optical fibers". Applied Physics Letters, Vol. 47, No. 3, pp. 213-215, August 1985.

[20] R. Daino, G. Gregori, S. Wabnitz. "New all optical devices based on third order nonlinearity of birefringent fibers". Optics Letters, Vol. 11, No. 1, pp. 42-44, January 1986.

[21] H. Winful. "Polarization instabilities in birefringent nonlinear media: application to fiber optic devices". Optics Letters, Vol. 11, No. 1, pp. 33-35, January 1986.

[22] A. Kumar, R.K. Varshney. "Propagation characteristics of dual-mode elliptical-core optical fibers". Optics Letters, Vol. 14, No. 15, pp. 817-819, August 1989.

[23] G. Kotrotsios, O. Parriaux, F. Cochet. "Mode-holding capability of dual mode fibers". Optics Letters, Vol. 15, No. 7, pp. 360-362, April 1990.

[24] A.M. Vengsarkar, W.C. Michie, L. Jankovic, B. Culshaw, R.O. Claus. "Fiber optic dual technique sensor for simultaneous measurement of strain and temperature". Journal of Lightwave Technology, Vol. 12, No. 1, pp. 170-177, January 1994.

[25] A. B. Carlson. "Communication Systems", pp. 328-337. McGraw Hill International Edition, 1986.

[26] R.B. Dyott. "Composition of LP_{11} modes in elliptical cored fibre". Electronics Letters, Vol. 30, No. 12, pp. 993-994, June 1994.

[27] R.B. Dyott, J.R. Cozens, D.G. Morris. "Preservation of polarisation in optical-fibre waveguides with elliptical cores". Electronics Letters, Vol. 15, No. 13, pp. 380-382. June 1979.

[28] W.V. Sorin, B.Y. Kim, H.J. Shaw. "Phase-velocity measurements using prism output coupling for single and few-mode optical fibers". Optics Letters, Vol. 11, No. 2, pp. 106-108. February 1986.

[29] S.E. Kanellopoulos, V.A. Handerek, A.J. Rogers. "Simultaneous strain and temperature sensing employing photogenerated in-fibre gratings". Optics Letters, Vol. 20, No. 3, pp. 333-335, February 1995.

[30] S.E. Kanellopoulos, V.A. Handerek, A.J. Rogers. "Simultaneous strain and temperature sensing employing a photogenerated polarisation coupler and low-order modes in an elliptically cored optical fibre". Electronics Letters, Vol. 30, No. 21, pp. 1786-1787, October 1994.

[31] S.Y. Huang, J.N. Blake, B.Y. Kim. "Perturbation effects on mode propagation in highly elliptical core two-mode fibers". Journal of Lightwave Technology, Vol. 8, No. 1, pp. 23-33, January 1990.

Chapter 5

APPLICATION OF NOISE-INITIATED BRILLOUIN SCATTERING TO DISTRIBUTED SENSING

In this chapter, we describe the use of Noise-Initiated Brillouin Scattering (NIBS) in optical fibres for simultaneous distributed measurement of strain and temperature [1-3]. The chapter starts with a review of Brillouin scattering in optical fibres (Section 5.1) and its application to distributed sensing (Section 5.2). Then, the theoretical analysis is presented (Section 5.3). We discuss the growth of the Stokes and antiStokes NIBS signals and their dependence on strain and temperature. A method to compensate the nonlinear NIBS growth is proposed and the signal to noise ratio of the technique is also evaluated. Experiments carried out at King's College [1-5] showed good agreement with the predictions of the former analysis (Section 5.4).

5.1 BRILLOUIN SCATTERING IN OPTICAL FIBRES

Brillouin scattering is a nonlinear effect which results from the interaction of optical radiation with the acoustic vibrations of the medium [6]. Thermally excited sound waves generate fluctuations in the refractive index of the medium through the photoelastic effect, giving rise to moving gratings that scatter the incident optical radiation. This phenomenon is called the spontaneous Brillouin scattering. Also, two optical waves propagating along different directions can generate, through electrostriction, a grating which produces coupling between them. This is called stimulated Brillouin scattering. While spontaneous Brillouin scattering does not require the presence of a second optical wave (probe), two optical waves (pump and probe) are necessary for stimulated Brillouin scattering. However, if there are no probe photons initially in the medium, spontaneously scattered photons can act as a seed for stimulated scattering. We call this mechanism Noise-Initiated Brillouin Scattering (NIBS).

These concepts are explained more naturally in terms of the quantum mechanical formalism, where the scattering processes are viewed as particle-like interactions among photons and acoustic phonons. There are two types of Brillouin scattering processes: Stokes and antiStokes. In the Stokes process, an incident photon is scattered into a frequency down-shifted Stokes photon, with the simultaneous creation of an acoustic phonon (Figure 1.A). The probability for this process to occur is proportional to:

$$\text{Prob (Stokes)} \propto n_L (n_B + 1)(n_S + 1) \qquad (1)$$

where n_L is the number of photons in the incident pump mode, n_B is the number of phonons in the relevant acoustic mode and n_S is the number of photons in the Stokes probe mode. It can be seen that this probability is non-null even if initially there are no probe photons (spontaneous emission). In the antiStokes process, on the other hand, the incident photon is scattered into a frequency up-shifted photon with concomitant annihilation of an acoustic phonon (Figure 1.B). The probability of this process is proportional to:

$$\text{Prob (antiStokes)} \propto n_L (n_B)(n_A + 1) \qquad (2)$$

where n_A is the number of photons in the antiStokes probe mode. To calculate the photon dynamics during a Brillouin scattering interaction, the inverse processes to those represented in

Figure 1 have also to be taken into account. This will be done in a more systematic way in section 5.3.

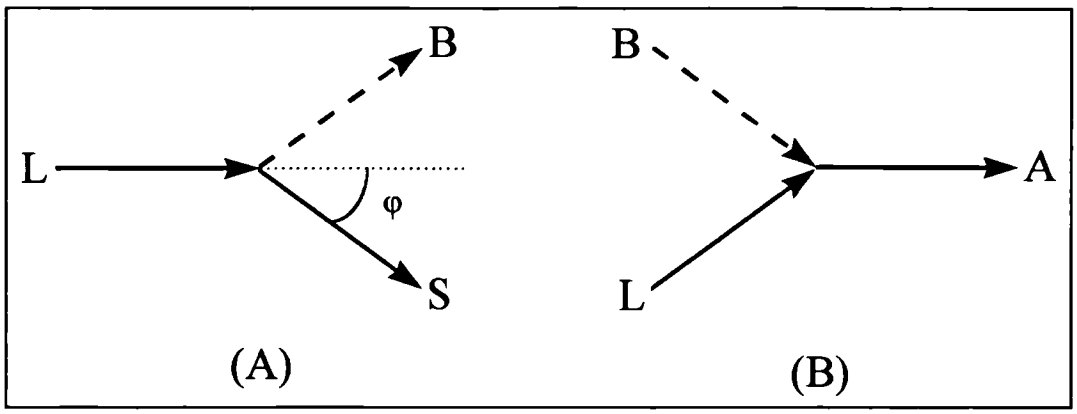

Figure 1. Illustration of Stokes and antiStokes Brillouin scattering processes. L: pump photon, S: Stokes photon, B: acoustic phonon, A: antiStokes photon, and φ, scattering angle.

5.1.1 Conservation laws

Efficient Brillouin scattering only occurs when the optical and acoustic modes involved in the interaction satisfy the relations imposed by the laws of conservation of energy and momentum. In a bulk medium, each optical or acoustic mode is characterised by its propagation constant $\bar{k}$ and its corresponding polarisation. From these parameters, the angular frequency ω of the mode is calculated by means of a dispersion relation. For the Stokes process, the conservation equations are:

$$\begin{aligned} \omega_L &= \Omega_B + \omega_S \\ \bar{k}_L &= \bar{q}_B + \bar{k}_S \end{aligned} \qquad (3)$$

where ω_L, Ω_B and ω_S are the angular frequencies of the pump photon, the acoustic phonon and the Stokes photon respectively, and $\bar{k}_L, \bar{q}_B$ and $\bar{k}_S$ are their corresponding propagation constants. From (3), the Brillouin frequency shift Ω_B can be calculated as a function of the scattering angle φ between the directions of propagation of the incident and the Stokes scattered photons:

$$\Omega_B = 2v_A\left|\bar{k}_L\right|\sin(\varphi/2) \qquad (4)$$

where v_A is the acoustic velocity of the medium. Analogous considerations could be made for the antiStokes scattering process.

Equation (4) seems to indicate that the conservation laws can only be verified in optical fibres for the backscattering geometry, i.e. for φ equal to π. Ippen and Stolen [7] were the first to observe stimulated Brillouin scattering in optical fibres and confirmed the validity of (4). However, other researchers have also observed Brillouin scattering in the forward direction (φ=0) [8,9,10]. A study of the optical and acoustic field modes in guided structures is necessary to clarify the allowed Brillouin scattering processes in optical fibres.

The propagation modes in a waveguide are characterised by a continuous scalar propagation constant along the axial direction (k) and two discrete numbers which specify the transverse field. The first of these numbers usually indicates the number of angular nodes (*n*), while the second gives the number of radial nodes (*m*). In addition, acoustic fields can have three polarisations (one mainly longitudinal and two mainly transversal) while optical fields can only have two polarisations (mainly transversal). For a given set of the former mode parameters, a dispersion equation allows calculation of the mode angular frequency ω.

The conservation laws in the guided wave case can be expressed, for the Stokes process, by the following scalar equations:

$$\begin{aligned} \omega_L &= \Omega_B + \omega_S \\ k_L &= q_B + k_S \end{aligned} \qquad (5)$$

plus a non-null condition for a transversal overlap integral among the acoustic and optical mode fields involved in the scattering process. In a single mode fibre, only acoustic fields with *n*=0 or *n*=2 satisfy this last condition and are effective for Brillouin scattering [11]. It has been theoretically shown that the strongest interaction is produced for the backscattering geometry ($\varphi=\pi$) and that the acoustic modes involved in this case are the longitudinal L_{0m} [12,11]. If the acoustic speed in the fibre core is higher than that in the cladding, the acoustic wave is not guided by the core and a secondary Brillouin resonance can be observed due to longitudinal acoustic cladding modes [12]. On the contrary, if the acoustic modes are guided in the core,

then the L_{0m} modes that verify the conservation law ($q_B = 2k_L$) have well separated angular frequencies Ω_B^m. In this case, several resonances corresponding to the different acoustic frequencies Ω_B^m will be observed in the Brillouin backscattering spectrum [11].

In a single mode fibre, forward Brillouin scattering implies a null propagation constant for the acoustic phonon involved (q_B=0). However, this does not necessarily mean that the associated Brillouin shift is also null. It has been shown that radial (R_{0m}) and mixed torsional-radial (TR_{2m}) acoustic modes scatter the incident light in the forward direction with non-null frequency shifts [8]. For a dual mode optical fibre supporting the LP_{01} and LP_{11} modes, a new phase matching condition for forward scattering arises [9-10]. In this case, the acoustic propagation constant for the phonon involved is different from zero ($q_B \neq 0$) and the scattering process is due to flexural acoustic modes F_{11} (n=1).

5.1.2 Brillouin scattering spectrum

The spectrum of the Brillouin scattered light provides information about the elastic and acoustic properties of optical fibres [13]. The Brillouin frequency shift is proportional to the velocity of the acoustic mode involved in the interaction (4). For the usual case of scattering in the backward direction, the velocity v_A of the relevant longitudinal acoustic mode is [14]:

$$v_A = \sqrt{\frac{E(1-\kappa)}{\rho(1+\kappa)(1-2\kappa)}} \qquad (6)$$

where E is the fibre Young modulus, ρ is its density and κ is the Poisson ratio. For incident light with a wavelength of 1.55 μm, the Brillouin frequency shift of the scattered light is 11.1GHz. These figures enable the calculation of the acoustic velocity, which yields a value of 5.96 km/s [15].

Acoustic phonons have a finite lifetime (T_B) which is governed by various scattering mechanisms. Since the acoustic waves decay as $\exp(-t/T_B)$, the Brillouin spectrum exhibits a Lorentzian line-shape. Its full-width half-maximum (FWHM) $\Delta\nu_B$ (in Hz) or γ (in rad/s), can be related to the phonon lifetime T_B (in s) and to the acoustic attenuation Γ (in m^{-1}) through the expressions:

$$\Delta\nu_B = \frac{\gamma}{2\pi} = \frac{1}{\pi T_B} = \frac{v_A \Gamma}{\pi} \tag{7}$$

The attenuation of acoustic waves in glasses is closely connected to their thermal conductivity properties and has been extensively studied [16-20,13]. There exist two main phonon scattering mechanisms in optical fibres. The first one is due to static imperfections produced by density inhomogeneities or fluctuations in the elastic constants along the glass. This scattering mechanism is only important at very low temperatures. The second mechanism, more important at high temperatures (room temperature), is due to the anharmonicity of the elastic response of the medium. This anharmonicity is characterised by the Grueneisen constant ξ, which relates the relative change in angular frequency of an acoustic mode with propagation constant $\bar{q}$ to the fractional change in volume of the glass δ:

$$\frac{\Delta\Omega_B(\bar{q})}{\Omega_B(\bar{q})} = -\xi\,\delta \tag{8}$$

The absorption process of a sound wave can be described as follows. An incident sound wave modulates the elastic properties of the medium and, through (8), also modulates the frequencies of the thermally-excited phonons. As a result, the thermal phonons are brought to a non-equilibrium state. The frequency of the majority of these thermal phonons is of the order of $K\theta/h$ (where K is the Boltzmann constant, θ is the glass temperature and h is the Planck constant), which is much bigger than the frequency of the phonons involved in Brillouin scattering. The thermal phonons relax then towards equilibrium by means of three-phonon scattering processes, with simultaneous absorption of the sound phonons. The Brillouin linewidth, $\Delta\nu_B$, depends on the dynamics of this relaxation process, and at high temperatures is given by the expression [16-18]:

$$\Delta\nu_B = \frac{\xi^2 \theta\, C_V\, \Omega_B^2\, \tau}{8\pi\, \rho\, v_A^2} \tag{9}$$

where θ is the glass temperature, C_V is the glass specific heat (per unit volume), and τ is the relaxation time for the thermal phonons. Expression (9) is valid for $\Omega_B\tau<<1$, which is usually satisfied at high temperatures. In optical fibres, the Brillouin linewidth has been measured to be typically 40MHz at a wavelength of 1.5 μm [21]. It can be observed in (9) that the Brillouin

linewidth, $\Delta\nu_B$, is proportional to the thermal conductivity of the glass κ_{th} ($\kappa_{th}=1/3\cdot C_V\cdot v_A^2\cdot\tau$). Since the thermal conductivity κ_{th} is inversely proportional to temperature, the Brillouin linewidth is not expected to be very temperature dependent at high temperatures [16-20]. Measurements in optical fibres at high temperatures [22] showed that the Brillouin linewidth exhibited a small linear decrease with temperature, with a slope of -0.1 MHz/°C. Also, equation (9) shows that the Brillouin linewidth is proportional to the square of the Brillouin frequency shift (9), a fact which has been experimentally confirmed for optical fibres [21].

5.1.3 Applications and limitations of Brillouin scattering in optical fibres

Stimulated Brillouin scattering is an important limitation for the power handling capacity of optical fibres in communication links. The use of narrow linewidth lasers to combat chromatic dispersion has the negative effect of setting a limit to the maximum permissible transmitted power [23]. Smith was the first to study theoretically the threshold power for stimulated Brillouin scattering in low loss optical fibres [24], deriving the following expression for the threshold power P_L:

$$P_L \approx 20\frac{A}{g_B L_{eff}} \qquad (10)$$

where A is the optical field modal area, g_B is the Brillouin gain coefficient [25], and L_{eff} is the effective interaction length between the incident and the scattered light [25]. Once this limit is surpassed, the optical signal is strongly depleted.

Several schemes have been proposed for the suppression of stimulated Brillouin scattering in optical fibres [26]. The most obvious solution is to increase the laser linewidth either by modulating a narrow band laser or simply by selecting a broad band laser. In this case, the Brillouin gain g_B is reduced by the ratio between the laser linewidth and the Brillouin linewidth [23, 27]. An alternative solution is to induce a variation of the Brillouin frequency shift Ω_B along the fibre, so as to limit the effective interaction length L_{eff}. This can be achieved by periodically straining a single fibre, by using a fibre with nonuniform core dopant concentration [28], or by splicing sections of different fibres one after the other. Another solution mentioned in the literature is the use of optical isolators to avoid the growth of Brillouin scattering [29].

Brillouin scattering, on the other hand, can also be used for practical applications. Continuous wave Brillouin lasers with low power threshold have been demonstrated [30]. Also, Brillouin tunable narrow bandwidth amplifiers have been implemented, for instance, to recover the carrier signal in coherent optical transmission systems [31]. The bandwidth of these Brillouin amplifiers has been extended by modulating the pump laser [32]. The use of Brillouin amplifiers for channel selection in wavelength division multiplexed (WDM) systems has also been demonstrated [33]. A different set of applications are those related with characterisation of optical fibres. Brillouin scattering has been used instead of the Rayleigh scattering in optical time domain reflectometers (OTDR) to monitor the losses along fibre links [34]. Also, the Brillouin frequency shift can provide information about the composition and concentration of the fibre dopants [35,36,11,26]. Forward Brillouin scattering has been used to measure variations in the outer diameter of the fibre by monitoring the spacing among the scattered modes [37]. Finally, the application of Brillouin scattering to distributed optical fibre sensing is very promising and has received a wide attention recently. This application will be the subject of the rest of the chapter.

5.2 BRILLOUIN SCATTERING FOR DISTRIBUTED SENSING

Brillouin scattering has been successfully used for distributed sensing in optical fibres. The most popular approach exploits the fact that the Brillouin frequency shift ν_B varies linearly with strain [38] and temperature [39,40]. From (4), the Brillouin frequency shift ν_B can be expressed as:

$$\nu_B = \frac{\Omega_B}{2\pi} = \frac{2\, n\, v_A}{\lambda_L} \tag{11}$$

where n is the refractive index of the core of the fibre and λ_L is the free-space wavelength of the pump light. The coefficients $C_{\nu\varepsilon}$ and $C_{\nu\theta}$ that relate the Brillouin frequency shift to strain, ε_z, and temperature, θ, have been measured to be [38,40,4]:

$$\begin{aligned} \delta\nu_B &= C_{\nu\varepsilon}\,\delta\varepsilon_z + C_{\nu\theta}\,\delta\theta \\ C_{\nu\varepsilon} &= 48\ \text{kHz}/\mu\text{strain} \\ C_{\nu\theta} &= 1.10\ \text{MHz}/^{\circ}\text{K} \end{aligned} \tag{12}$$

The dependence of the Brillouin shift on strain and temperature is mainly due to variations in the magnitude of the elastic constants, which result in a corresponding change in the acoustic velocity [38,19,20,13]. Also, fibre coatings can induce thermal strain in fibres due to a mismatch between their thermal expansion coefficients and that of glass. Depending on the specific coating, this effect can cause an apparent increase in the $C_{v\theta}$ coefficient [41].

Two groups of system architectures have been proposed so far to perform distributed measurements. The first group, called Brillouin Optical Time Domain Analysis (BOTDA), makes use of stimulated Brillouin scattering and requires a pump-probe configuration. Its main advantage is the high signal-to-noise ratio that pump-probe schemes are able to achieve. On the other hand, the drawback of BOTDA is that it requires two counterpropagating beams with a frequency difference equal to the Brillouin shift. The second group, called Brillouin Optical Time Domain Reflectometry (BOTDR) relies on spontaneous Brillouin scattering and has the advantage that only access to one end of the fibre is required. The systems presented so far suffer from strain and temperature cross-sensitivity problems. More recently, we described a technique based on noise-initiated Brillouin scattering that solves this problem, permitting the simultaneous distributed measurement of strain and temperature along the fibre.

5.2.1 Pump-probe architectures: BOTDA

In this architecture [42], the pump is usually a highly coherent pulse of light and the probe, which counterpropagates with respect to the pump, is a continuous wave from a very coherent tunable laser. The frequency of the probe laser is scanned along the Stokes band of the pump light Brillouin scattering spectrum. For each frequency, a time domain trace is acquired. Once the frequency scan has been completed, the variations of the Brillouin gain spectrum along the fibre can be determined. From these, the Brillouin shift and, consequently, the distribution of strain or temperature can be mapped along the fibre. In a first experiment, Horiguchi [42] achieved a temperature resolution of 3°C with a spatial resolution of 100 m for a total sensing length of 1.2 km. Later, Jackson et al [43] reported a system with 1°C temperature resolution and 100 m spatial resolution with a sensing range of 22 km, proving the suitability of Brillouin based sensors for long range applications. Also, it has been shown that the spatial resolution could be substantially improved by using pump pulses with duration similar to the phonon lifetime (≈10 ns), which sets the ultimate limitation. In this transient regime, the Brillouin gain is reduced and the scattering spectrum broadened, losing accuracy in the measurements. A best spatial resolution of 1 m has been reported with the BOTDA technique [44].

One of the main problems of the gain BOTDA technique is that depletion of the pump pulse due to stimulated emission [43] limits the overall sensing range. A solution to this issue was to shift the continuous probe wave to the antiStokes scattering band of the pump pulse [45]. In this case, the continuous wave signal is attenuated and the pulsed signal amplified. This technique was called loss BOTDA. A system with 1°C temperature resolution, 5 m spatial resolution and 32 km sensing range was initially demonstrated [45], extending later its sensing range to 51 km [72].

Another problem of BOTDA is the fluctuation in the Brillouin gain along the fibre induced by local mismatch between the pump and probe polarisations [46]. This effect is usually taken into account by means of a polarisation factor that reduces the Brillouin gain, and varies from 0, when the polarisations are orthogonal, to 1, when they are parallel. Due to the random evolution of the polarisation along a low birefringence fibre, it has been shown that this factor takes values from 1/3 to 2/3 when the pump-probe interaction length is much longer than the fibre beatlength [46-48]. This means that although there could be fluctuations in the received Brillouin signal, complete polarisation induced fading will not occur. It has also been shown [47] that it is possible to find an optimum for the pump and probe launching polarisations that maximise the Brillouin signal everywhere along the fibre. If, on the other hand, the pump pulsewidth is smaller than the fibre's beatlength, then the polarisation factor can take any value from 0 to 1 and complete polarisation fading will occur for certain positions along the fibre. In this case, it will be necessary to rotate by 90° either the pump or the probe polarisations in order to retrieve the information from these zones [47].

Usually, the implementation of pump-probe architectures involves the use of two lasers. Recently, a system with pulsed pump and probe beams, both generated by a single laser, has been demonstrated [49]. The probe pulses were modulated by means of an electro-optic modulator and the spatial information was obtained through control of the delay between the pump and probe pulses. This configuration does not suffer from depletion problems. The system achieved 0.25°C of temperature resolution and 45 m of spatial resolution for a sensing range of 1.4 km.

5.2.2 Noise-initiated Brillouin scattering: BOTDR

In this approach the Brillouin scattered light is generated through spontaneous emission along the fibre and, consequently, no probe beam is necessary. Two issues complicate considerably the design of the BOTDR detection scheme. On one hand, the backscattered BOTDR signal levels at the receiver are much lower than those in BOTDA. On the other, spectral filtering of the BOTDR signal has to be performed to identify the central frequency of the Brillouin spectrum. Two alternative solutions have been proposed so far. The first relies on coherent optical detection followed by low pass electrical filtering. In the second, the signal is optically filtered (with an optical interferometer) and then directly detected.

Implementation of the first type of detection scheme requires the generation of coherent light at two frequencies separated only by the Brillouin frequency shift. The beam with higher frequency is modulated in pulses and then launched into the fibre. The second beam acts as local oscillator for the coherent detection of the backscattered Stokes signal. In the first demonstration of BOTDR, two lasers (one of them tunable in frequency) were used to generate these optical beams [50]. A temperature resolution of 6°C, with 100 m spatial resolution was achieved for a sensing range of 11.5 km. In a second configuration that only needed the use of one laser, the frequency of the laser pulses was controlled by the number of times that they circulated through an acousto-optic Bragg cell [51]. Another idea proposed to generate these two optical signals with one laser was to select two adjacent modes from an appropriate multimode laser [52]. Finally, a different scheme based on three wave mixing has been demonstrated [53]. It consists in the mixing of the laser and Stokes optical signals with a high frequency electrical local oscillator in a photoconductive mixer. However, no distributed measurements have been performed with the last two schemes. All these coherent detection schemes suffer from the well known polarisation fading problems, which can be attenuated by radomizing the polarisation of the reference laser light [54].

The second detection scheme requires optical filtering of the scattered radiation by means, for example, of a Fabry-Perot interferometer prior to its direct detection. The noise performance of the detection system has to be optimised to be able to measure accurately the weak scattered signals. Special care has to be taken to avoid excessive losses in the optical interferometer, and also to overcome its potential instability and long term drifts.

5.2.3 Simultaneous strain and temperature measurement

All the systems described so far were unable to differentiate strain effects on the fibre from temperature variations. A first idea to overcome this cross-sensitivity problem was to deploy the fibre in such a way that only some sections are subjected to strain, while the rest of the fibre is free from its influence [73]. However, this special deployment of the fibre is difficult to achieve in most applications, so alternative solutions have been sought.

Recently, a second approach has been proposed. The idea is to measure not only the Brillouin shift but also the spontaneously Brillouin scattered power along the fibre. If the dependence of the Brillouin scattered power on strain and temperature is different from that of the Brillouin shift, then both effects could be discriminated [55-56]. This dependence has been recently measured [55,4,57,3] showing the feasibility of this technique.

Distributed measurements of spontaneously Brillouin scattered power have been demonstrated either by using Fabry-Perot [55] or Mach-Zehnder [58] interferometers to discriminate for the Brillouin signal. It has also been shown that the effect of fibre losses can be corrected by normalising the Brillouin signal against a Rayleigh OTDR trace [59]. These systems, however, did not spectrally resolve the Brillouin scattered radiation and, consequently, were unable to discriminate temperature from strain.

The first system capable of measuring distributions of temperature and strain simultaneously has been recently developed at King's College [5,3,2,74]. In the next section we will treat several theoretical aspects related to this approach. First we will study the growth of the Stokes and antiStokes NIBS power and its dependence on strain and temperature [2-5]. Also, we will propose a method to compensate the nonlinear NIBS growth and to optimise the signal-to-noise ratio of the sensor [1,3]. In Section 5.4, some experiments that corroborate the predictions of the previous analysis will be presented [1-5].

5.3 SIMULTANEOUS DISTRIBUTED MEASUREMENT OF STRAIN AND TEMPERATURE FROM NOISE-INITIATED BRILLOUIN SCATTERING: THEORY

Recently, it has been demonstrated that it is possible to resolve strain and temperature effects in optical fibres by simultaneously measuring the power and frequency shift of noise-initiated Brillouin scattering (NIBS) [4,5,1-3]. In this section, we present a full analysis of this technique. In particular, we study the growth of noise-initiated Stokes and antiStokes Brillouin

signals and investigate their dependence on strain and temperature. Our objective is to derive an equation similar to (12) for the dependence of the Brillouin scattered power P_B^{norm} (to be defined later) on strain, ε_z, and temperature, θ:

$$\frac{\delta P_B^{norm}}{P_B^{norm}} = C_{P\varepsilon}\delta\varepsilon_z + C_{P\theta}\delta\theta \qquad (13)$$

Equations (12) and (13) allow calculation of the strain and temperature from measurement of the frequency shift and Brillouin scattered power provided the ratio $C_{v\varepsilon}\ C_{P\theta}\ /\ C_{v\theta}C_{P\varepsilon}$ is different from unity. We shall determine theoretically the coefficients $C_{P\varepsilon}$ and $C_{P\theta}$ and compare them with experimental results that will be presented in the next section.

A major potential difficulty of this approach is that the growth of the Noise Initiated Brillouin Scattering (NIBS) depends very nonlinearly on the power of the pump pulse. As the laser power fluctuates in time, and also the pump pulse energy decreases as it propagates along the fibre (due to fibre losses and depletion effects), an adequate normalisation becomes necessary. We will show that an effective Brillouin power P_B^{lin}, which is linear with respect to the pump power, can be defined in terms of the Stokes and antiStokes NIBS powers. P_B^{lin} will coincide with both the Stokes and antiStokes NIBS powers in the spontaneous linear regime and its use can be extended well into the nonlinear regime by mathematically combining the values of the Stokes and antiStokes powers. Normalisation of P_B^{lin} against the Rayleigh backscattered power will provide the normalised Brillouin power P_B^{norm} appearing in equation (13), which is independent of the pump power and only depends on the local strain and temperature.

As we are now free to use high input powers to generate Brillouin signals into the nonlinear regime, it is important to determine what input power gives the highest signal-to-noise ratio (SNR). We will see that the NIBS field statistics have an important impact on the SNR performance of the sensor. We find that, for a given detection bandwidth, the antiStokes SNR increases with input power while the Stokes SNR decreases with increased input power. The overall effect on P_B^{lin}, when shot and circuit noise are also considered, is that the SNR can be maximised for a given detection bandwidth with an appropriate choice of the Brillouin gain factor.

The noise initiation of Brillouin scattering (NIBS) is a purely quantum mechanical effect. T. von Foerster and R. J. Glauber have studied the related phenomenon of Raman amplification of Stokes signals using the quantum mechanical formalism [60]. An equivalent semiclassical approach was proposed by R. W. Boyd and coworkers to study the growth of the Stokes NIBS [61]. The quantum features of the problem were introduced in their model through adequate Langevin noise functions that account for the acoustic phonon fluctuations that act as seeds for the NIBS growth. The analysis we present follows the lines of [60], but is adapted for the Brillouin case, and is extended to consider the dynamics of growth of the antiStokes NIBS. The results obtained for the Stokes case agree with those in [61]. The new aspects considered, related to the growth of the antiStokes NIBS, are essential for the linearisation of the Brillouin power as will be discussed in section 5.3.2. The analysis also describes the statistical properties of the NIBS radiation, which will determine the fundamental limitations for the signal to noise ratio performance of the sensor. In section 5.4 we will present experimental measurements that support the predictions of this analysis.

5.3.1 Description of the photon and phonon fields and their interaction

Brillouin scattering involves the nonlinear interaction between the pump light, the acoustic phonons of the medium, and the frequency shifted Stokes and antiStokes photons. In this section, we describe these fields and their interaction from a quantum mechanical viewpoint. We will assume that the optical fibre is single mode at the wavelength of operation and that the problem can be considered spatially unidimensional (being z the axis of propagation). As the two orthogonal polarisation components can be treated independently, we will assume for simplicity that the pump light is linearly polarised.

5.3.1.a Pump Light

The pump light is assumed to be a highly coherent, linearly polarised laser pulse. Its electric field will be described classically by the scalar function $\Sigma_L^r(z,t)$:

$$\Sigma_L^r(z,t) = \Sigma_L(z,t) + \Sigma_L^*(z,t) = \widetilde{\Sigma}_L(z,t)\, e^{-j\omega_L t} + \widetilde{\Sigma}_L^*(z,t)\, e^{j\omega_L t} \qquad (14)$$

where the superscript r stands for real field, $\Sigma_L(z,t)$ is the complex analytical field, ω_L is the laser angular frequency and * stands for complex conjugate. The pump light power will be

assumed to be sufficiently low so that its depletion due to Brillouin saturation effects is negligible in the time scale of the laser pulse-width. Figure 2 illustrates the propagation of the pump pulse in a space-time diagram (z,t). The striped area represents the region where $\left|\tilde{\Sigma}_L(z,t)\right|$ is not null. It can be appreciated that the pulse is launched into the far end of the fibre (z=L) at t=0, and has a duration T. Due to our previous assumptions of negligible depletion and low loss fibre, $\left|\tilde{\Sigma}_L(z,t)\right|$ is slowly attenuated along the fibre, being essentially constant in the scale of the interaction length vT/2 (where v is the speed of light in the fibre).

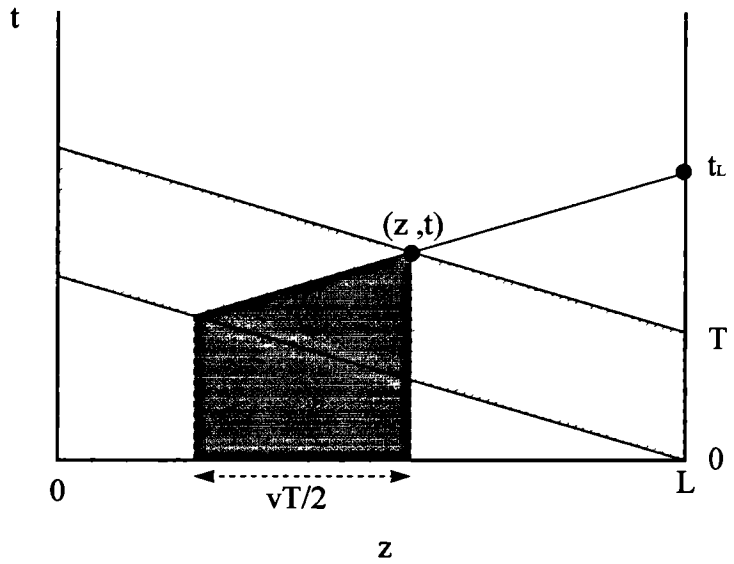

Figure 2. Illustration of the pump pulse propagation (striped area) in a space-time diagram. The shaded area represents the integration area for (31) and (34).

5.3.1.b Electrical field operator for the Brillouin scattered radiation

The Brillouin scattered radiation will be described through its quantum electric field operator in the Heisenberg picture. As the pump light is linearly polarised and the fibre medium is isotropic, the scattered field will also be linearly polarised, with the same polarisation than the pump field [62]. With the unidimensional approximation, the scalar electric field operator $\hat{E}^h$ can be expressed as:

$$\hat{E}^h(z,t) = \hat{E} + \hat{E}^+ = \sum_k j\sqrt{\frac{\hbar\omega_k}{2LA\varepsilon}}\,\hat{a}_k(t)\,e^{jkz} + h.c. \qquad (15)$$

where ^ stands for operator, the superscript h for hermitic operator, and both + and h.c. for hermitic conjugate operator. k, which takes the values $2\pi m/L$ (with m an integer), is the label for the mode with propagation constant k and angular frequency ω_k, with $\hat{a}_k$ as its corresponding annihilation operator. $\hbar$ is the Planck constant; L is the fibre length; A is the effective transverse area, and ε the fibre core permitivity. $\hat{E}$ is the annihilation part of the field operator, while $\hat{E}^+$ is the creation part. The hamiltonian of the electromagnetic field can be written in the usual way:

$$\hat{H}_{photon} = \sum_k \hbar\omega_k \, \hat{a}_k^+ \hat{a}_k \tag{16}$$

5.3.1.c Acoustic field operator

We will only consider Brillouin scattering due to the longitudinal acoustic phonons in the fibre. The longitudinal acoustic strain operator $\hat{S}^h$ is:

$$\hat{S}^h(z,t) = \frac{\partial \hat{u}^h}{\partial z} = \hat{S} + \hat{S}^+ = \sum_q jq \sqrt{\frac{\hbar}{2\rho LA\Omega_q}} \, \hat{b}_q(t) \, e^{jqz} + h.c. \tag{17}$$

where $\hat{u}^h$ is the displacement operator, q labels the phonon mode of propagation constant q ($=2\pi m/L$ with m integer) and angular frequency Ω_q. $\hat{b}_q$ is its corresponding annihilation operator. $\hat{S}$ is the annihilation part of the field operator, while $\hat{S}^+$ is the creation part. ρ is the fibre density. Ω_q is related to $|q|$ through the acoustic velocity v_A:

$$v_A = \frac{\Omega_q}{|q|} \tag{18}$$

Analogously to (16), the hamiltonian for the phonon field is:

$$\hat{H}_{phonon} = \sum_q \hbar\Omega_q \, \hat{b}_q^+ \hat{b}_q \tag{19}$$

5.3.1.d Brillouin interaction

The interaction between the pump light, the Brillouin scattered field, and the phonon field is usually described through a change in the medium permitivity due to the photoelastic effect [63]. The corresponding perturbation in the electromagnetic energy operator will constitute the interaction hamiltonian $\hat{H}_{int}$ [60]:

$$\hat{H}_{int} = \int_V \delta\hat{\varepsilon}_{xx}\, \Sigma_L^r\, \hat{E}^h\, dV = \int_V -\varepsilon_o n^4 p_{12}\, \hat{S}^h\, \Sigma_L^r\, \hat{E}^h\, dV \qquad (20)$$

where $\delta\hat{\varepsilon}_{xx}$ is the change of permitivity operator, ε_o is the vacuum permitivity, n the medium refractive index ($=\sqrt{\varepsilon/\varepsilon_o}$), p_{12} is the photoelastic constant that couples the longitudinal strain to transversal changes in permitivity, and the volume V is equal to A·L. The elementary Brillouin processes, which involve annihilation or creation of photons and phonons (Section 5.1), are described when (20) is expanded with (14), (15) and (17).

5.3.1.e Phonon damping. Langevin noise operators

As a result of Brillouin scattering processes, the phonon thermal equilibrium population is perturbed. The phonon system, however, relaxes towards its equilibrium state through several mechanisms, the most important of them being anharmonic phonon-phonon scattering processes (Section 5.1.2). We are going to describe this relaxation by assuming that each phonon mode is linked to a reservoir that damps the phonon population to its equilibrium state. Using the standard approach [64], the evolution of the annihilation mode operators $\hat{b}_q$ when they are linked to a reservoir, is given by the equation:

$$\frac{d\hat{b}_q}{dt} = \left(-j\Omega_q - \frac{\gamma_q}{2}\right)\hat{b}_q + \hat{\Gamma}_q(t) \qquad (21)$$

where γ_q is the damping constant and $\hat{\Gamma}_q(t)$ the associated Langevin noise operator, which is delta correlated:

$$\left\langle \hat{\Gamma}_q^+(t)\,\hat{\Gamma}_{q'}(t')\right\rangle = \gamma_q\,\langle n\rangle\,\delta(t-t')\,\delta_{qq'} \tag{22}$$

where <> means average over the thermal reservoirs. <n> is the thermal equilibrium population given by the Bose-Einstein distribution. At room temperature (θ = 300 °K) and for the Brillouin angular frequency shift Ω_B corresponding to a λ_L of 1.55 μm (1), <n> is approximately equal to $K\theta/\hbar\Omega_B$, which has a value of 555 (where K was the Boltzmann constant).

By differentiating (17) with respect to time, and substituting (21) in it, we obtain the following equation for the evolution of the annihilation part of the strain operator :

$$\frac{\partial \hat{S}(z,t)}{\partial t} = \left(-j\Omega_B - \frac{\gamma}{2}\right)\hat{S} + \hat{L}(z,t) \tag{23}$$

where only those mode operators $\hat{b}_q$ with Ω_q approximately equal to Ω_B have been considered to be relevant for the description of the Brillouin scattered radiation, and γ is their corresponding damping constant. $\hat{L}(z,t)$ is a new Langevin noise operator with correlation functions:

$$\left\langle \hat{L}^+(z,t)\,\hat{L}(z',t')\right\rangle = \frac{\hbar\Omega_B}{2\rho v_A^2 A}\gamma\,\langle n\rangle\,\delta(t-t')\,\delta(z-z') \tag{24}$$

and:

$$\left\langle \hat{L}(z,t)\,\hat{L}^+(z',t')\right\rangle = \frac{\hbar\Omega_B}{2\rho v_A^2 A}\gamma\,(\langle n\rangle+1)\,\delta(t-t')\,\delta(z-z') \tag{25}$$

Equation (23) describes the damping of the acoustic phonons. The quantum fluctuations associated with this damping are the seed for the NIBS. It is important to point out that the pump pulse-width T that will be used for the sensing application is much bigger than the phonon damping time ($\gamma T >> 1$), so as to be far from the transient regime.

5.3.2 Equations of motion for the field operators and their solution

The Stokes and antiStokes interaction processes involve different sets of acoustic phonon modes. While in the Stokes processes the phonon involved copropagates with the pump light ($q<0$), in the antiStokes processes the phonon counterpropagates with respect to it ($q>0$). As we have also assumed that the pump light can be described classically and that its power remains approximately constant in the length scale of the pulse interaction length ($vT/2$), the equations of motion for the Stokes and antiStokes field operators are weakly coupled and can be solved independently. Consequently, we will carry out two parallel analysis for the growth of the Stokes and antiStokes NIBS.

5.3.2.a Equations of motion

The Heisenberg equations of motion are derived by calculating the relevant commutators between the field operators (15) and (17) and the hamiltonians (16), (19) and (20). The damping term and the Langevin noise operator that appear in (23) can be added afterwards to the equation of motion for the acoustic strain operator. The coupled equations of motion for the forward propagating ($k>0$) Stokes field operator $\hat{E}_S$ and the acoustic strain operator $\hat{S}$ are:

$$\frac{\partial \hat{E}_S(z,t)}{\partial t} = -v\frac{\partial \hat{E}_S(z,t)}{\partial z} - j\chi\frac{\omega_S}{2\varepsilon}\Sigma_L(z,t)\,\hat{S}^+(z,t) \tag{26}$$

$$\frac{\partial \hat{S}^+(z,t)}{\partial t} = \left(j\Omega_B - \frac{\gamma}{2}\right)\hat{S}^+(z,t) + \hat{L}^+(z,t) + j\chi\frac{\Omega_B}{2\rho v_A^2}\Sigma_L^*(z,t)\,\hat{E}_S(z,t) \tag{27}$$

where only those mode operators with angular frequency approximately equal to ω_s ($= \omega_L - \Omega_B$) are important for the description of the Stokes field operator and χ is defined as:

$$\chi = -\varepsilon_o n^4 p_{12} \tag{28}$$

A similar reasoning gives the following equations of motion for the antiStokes case:

$$\frac{\partial \hat{E}_A(z,t)}{\partial t} = -v\frac{\partial \hat{E}_A(z,t)}{\partial z} - j\chi\frac{\omega_A}{2\varepsilon}\Sigma_L(z,t)\,\hat{S}(z,t) \tag{29}$$

$$\frac{\partial \hat{S}(z,t)}{\partial t} = \left(-j\Omega_B - \frac{\gamma}{2} \right) \hat{S}(z,t) + \hat{L}(z,t) - j\chi \frac{\Omega_B}{2\rho v_A^2} \Sigma_L^*(z,t)\, \hat{E}_A(z,t) \qquad (30)$$

where $\hat{E}_A$ is the antiStokes field operator and ω_A (= $\omega_L+\Omega_B$) is the antiStokes angular frequency.

It can be appreciated that the electrical field operator (annihilation part) is coupled in the Stokes case to the creation part of the acoustic strain operator, while in the antiStokes case is coupled to its annihilation part. This reflects the differences between the two processes. Also, the difference in sign of the last term of (30) with respect to the corresponding term in (27) is responsible for the different evolution of any probe signals launched at the Stokes or antiStokes frequencies. While the Stokes probe signal would be amplified, the antiStokes would be attenuated.

5.3.2.b Solution for the field operators

The equations of motion can be solved by use of the Laplace transform method [65]. If initially there are no Stokes or antiStokes probe photons in the medium (as is the case for our sensor), we can neglect the effect of the initial field operators and consider only the contribution that comes from the Langevin noise operators. By inspection of Figure 2, the field operator at the space-time point (L,t_L) will be the same than that at the point (z,t), which is calculated in the Stokes case as [60,61,65]:

$$\hat{E}_S(z,t) = \int_0^{T/2} dt' \int_0^{\infty} dt''\, \hat{V}_S^+(z - vt', t - t' - t'')\, e^{-\left(\frac{\gamma}{2} + j\omega_S\right)t''}\, I_0\left[2\kappa\sqrt{t't''}\right] \qquad (31)$$

where $\hat{V}_S^+(z,t)$ is:

$$\hat{V}_S^+(z,t) = -j\chi \frac{\omega_S}{2\varepsilon} \tilde{\Sigma}_L(z,t)\, e^{j\omega_L t}\, \hat{L}^+(z,t) \qquad (32)$$

and κ is:

$$\kappa^2 = \chi^2 \frac{\Omega_B \omega_S}{4\rho v_A^2 \varepsilon} \left|\tilde{\Sigma}_L(z,t)\right|^2 \tag{33}$$

where I_0 is the modified Bessel function of zero order. The integration area is the shaded region in Figure 2, where it can be appreciated that we have made the approximation of extending the integration of the t'' variable to ∞ due to the decaying term $\exp(-\gamma t''/2)$ and the fact that $\gamma T >> 1$.

We have carried out a parallel analysis for the calculation of the antiStokes field operator:

$$\hat{E}_A(z,t) = \int_0^{T/2} dt' \int_0^{\infty} dt'' \, \hat{V}_A(z - vt', t - t' - t'') \, e^{-\left(\frac{\gamma}{2} + j\omega_A\right)t''} \, J_0\left[2\kappa\sqrt{t't''}\right] \tag{34}$$

where now $\hat{V}_A(z,t)$ is:

$$\hat{V}_A(z,t) = -j\chi \frac{\omega_A}{2\varepsilon} \tilde{\Sigma}_L(z,t) \, e^{j\omega_L t} \, \hat{L}(z,t) \tag{35}$$

and κ is given by (33) with the substitution of ω_S for ω_A and J_0 is the Bessel function of zero order.

5.3.3 Field intensity, optical power and spectral power density

5.3.3.a Field intensity and optical power

The Stokes and antiStokes average field intensities ($I_{S,A}$) at the space-time point (L,t_L) can be expressed in terms of the previous field operators solutions (31) and (34) as:

$$I_{S,A}(L,t_L) = \left\langle \hat{E}^+_{S,A}(L,t_L) \, \hat{E}_{S,A}(L,t_L) \right\rangle = \left\langle \hat{E}^+_{S,A}(z,t) \, \hat{E}_{S,A}(z,t) \right\rangle \tag{36}$$

These average field intensities $I_{S,A}$ are related to the average Stokes and antiStokes optical powers $P_{S,A}$ through the expression [66]:

$$P_{S,A}(z,t) = 2\varepsilon A v \, I_{S,A}(z,t) \tag{37}$$

Evaluation of (37) and (36) for the Stokes optical power P_S yields [60,61]:

$$P_S = \frac{\hbar\omega_S(\langle n\rangle + 1)}{2}\gamma\, G\, e^{G}\left(I_0(G) - I_1(G)\right) \tag{38}$$

where I_0 and I_1 are the modified Bessel functions and the gain parameter G [67] is given by:

$$G = \frac{\kappa^2}{\gamma}T \tag{39}$$

Following a similar treatment, we have calculated the average antiStokes power P_A to be:

$$P_A = \frac{\hbar\omega_A\langle n\rangle}{2}\gamma\, G\, e^{-G}\left(I_0(G) + I_1(G)\right) \tag{40}$$

5.3.3.b Field autocorrelation and optical power spectral density

Both the Stokes and antiStokes optical fields are stationary. By inspection of Figure 3, the field autocorrelations $R_{S,A}(\tau)$ at the far end of the fibre (z=L) are defined as:

$$R_{S,A}(\tau) = \left\langle \hat{E}^{+}_{S,A}(L, t_L + \tau)\, \hat{E}_{S,A}(L, t_L)\right\rangle = \left\langle \hat{E}^{+}_{S,A}\left(z - v\frac{\tau}{2}, t + \frac{\tau}{2}\right)\hat{E}_{S,A}(z,t)\right\rangle \tag{41}$$

The optical power spectral densities $\Phi_{S,A}(\omega)$ are related to the Fourier transform of $R_{S,A}(\tau)$ through an expression analogous to (37). When $\gamma T >> 1$, the Stokes optical power spectral density $\Phi_S(\omega)$ is (Appendix) [61]:

$$\Phi_S(\omega) = \hbar\omega_S(\langle n\rangle + 1)\left(e^{\frac{2\left(\frac{\gamma}{2}\right)^2 G}{\left(\frac{\gamma}{2}\right)^2 + (\omega-\omega_S)^2}} - 1\right) \tag{42}$$

Similar calculations for the antiStokes optical power spectral density, $\Phi_A(\omega)$, yield:

$$\Phi_A(\omega) = \hbar\omega_A \langle n \rangle \left(1 - e^{\frac{-2\left(\frac{\gamma}{2}\right)^2 G}{\left(\frac{\gamma}{2}\right)^2 + (\omega-\omega_A)^2}} \right) \tag{43}$$

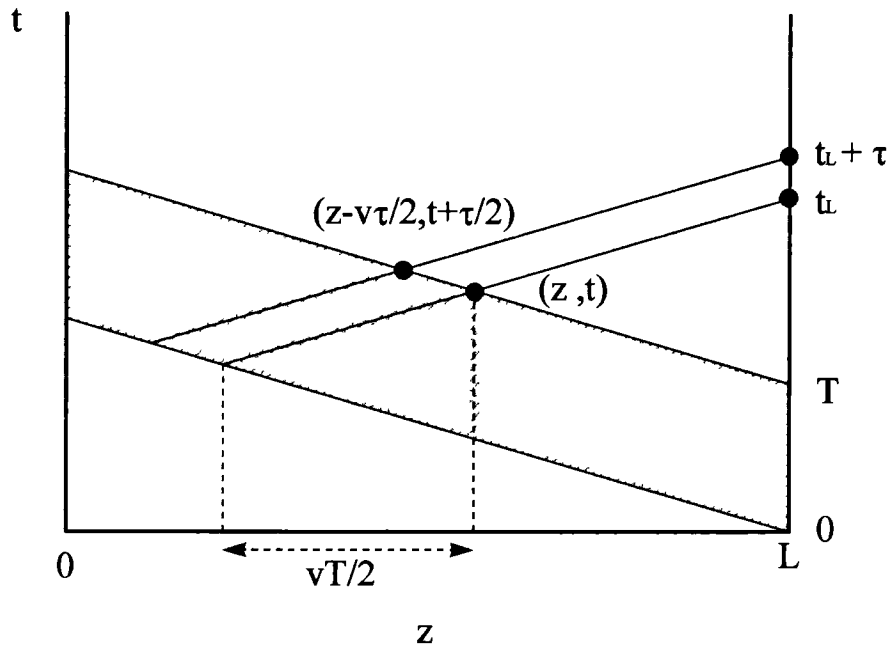

Figure 3. Space-time points involved in the calculation of the field autocorrelation. Each pair of points is connected through characteristics lines of (26) and (29).

5.3.3.c Asymptotic behaviour of the Stokes and antiStokes optical powers

From (39), it can be seen that the gain parameter G is proportional to the pump pulse power. For low pump powers, the Stokes and antiStokes optical powers are linear with G and approximately equal:

$$P_S \approx P_A \approx \frac{\hbar\omega_L \langle n \rangle}{2} \gamma\, G \tag{44}$$

However, for higher pump powers the NIBS growth is very nonlinear and the evolution of the Stokes optical power very different from that of the antiStokes. In the limit of high G, the Stokes optical power is approximately:

$$P_S \approx \frac{\hbar\omega_S\langle n\rangle}{2}\gamma\, e^{2G}\,\frac{1}{8\sqrt{2\pi G}} \tag{45}$$

while the antiStokes optical power is approximately:

$$P_A \approx \frac{\hbar\omega_A\langle n\rangle}{2}\gamma\,\frac{2\sqrt{G}}{\sqrt{2\pi}} \tag{46}$$

These results are explained naturally from the optical power spectral densities expressions (42) and (43). In the Stokes case, the maximum Stokes power spectral density is proportional to exp(2G) when G is high. However, it can be shown that its effective bandwidth decreases as $\sqrt{G}$. This behaviour is reflected in (45). For the antiStokes case, on the other hand, the parenthesis term in (43) saturates to 1, but the effective bandwidth increases as $\sqrt{G}$ as is described by (46).

5.3.4 Linearised Brillouin power and its dependence on strain and temperature

5.3.4.a Linearisation

As discussed in the introduction to Section 5.3, we define now an effective Brillouin power, P_B^{lin}, that is linear with respect to the pump power and is equal to the Stokes and antiStokes powers in the linear regime (44):

$$P_B^{lin} = \frac{\hbar\omega_L\langle n\rangle}{2}\gamma\, G \tag{47}$$

P_B^{lin} can be calculated in an exact way from measurement of P_S and P_A with the help of equations (38) and (40). The procedure would be as follows: G is evaluated from the ratio P_S/P_A and its substitution in either (38) or (40) retrieves the remaining term of (47) ($\hbar\omega_L\langle n\rangle\gamma\,/\,2$). A useful approximate formula to calculate P_B^{lin} from P_S and P_A is:

$$P_B^{lin} \approx \frac{P_S P_A \ln\left(\frac{P_S}{P_A}\right)}{P_S - P_A} \tag{48}$$

This expression would be exact if the effective Stokes and antiStokes spectral bandwidths did not change with G or, alternatively, if the Stokes and antiStokes fields were spectrally filtered in the centre of their spectrum. The use of equations (38), (40), (47), and (48) as theoretical fits for experimental data will be illustrated in Section 5.4.

5.3.4.b P_B^{lin} *dependence on strain and temperature*

We are now in a position to look for the strain and temperature dependence of P_B^{lin}. Using equations (28), (33) and (39), we rewrite (47) in terms of more fundamental magnitudes, substituting, where possible, the measurable Brillouin shift ν_B defined in (11):

$$P_B^{lin} = \frac{\pi^2 n^7 p_{12}^2 c}{\rho A} \frac{T P_P}{\lambda_L^4} \frac{K\theta}{\nu_B^2} \tag{49}$$

where P_P is the power of the pump pulse. We can safely ignore the strain and temperature dependence of all the terms except those of θ and ν_B in the last fraction of (49) and write:

$$P_B^{lin} = \frac{\eta\theta}{\nu_B^2} \tag{50}$$

where η is a constant that can be determined with the knowledge of the terms in (49) or by means of a calibration measurement. Equation (50) shows that measurement of the Brillouin shift, ν_B, and of the linear effective Brillouin power, P_B^{lin}, determines the temperature θ. Substitution into (12) then yields the strain ε_z. We can also express these findings in terms of the coefficients used in (13). We find $C_{P\varepsilon} = -9\ 10^{-4}$ % /$\mu\varepsilon$ and $C_{P\theta} = 0.32$ % /°K at 0 $\mu\varepsilon$ and 300 °K. We stated earlier that it would be possible to measure the strain and temperature simultaneously provided $C_{\nu\varepsilon}C_{P\theta} / C_{\nu\theta}C_{P\varepsilon}$ differs from unity. Using the above theory, we expect $C_{\nu\varepsilon}C_{P\theta} / C_{\nu\theta}C_{P\varepsilon}$ to be -18, and hence predict that the recovery of ε_z and θ from P_B^{lin} and ν_B is a well-conditioned problem. If the pump power is noticeably attenuated as it propagates along the

fibre, it will be necessary to normalise P_B^{lin} against the Rayleigh backscattered power (which has negligible strain and temperature dependence and is proportional to the local power along the fibre) and use the resulting P_B^{norm}. The reasoning regarding the strain and temperature dependence of P_B^{lin} will hold identically for P_B^{norm}.

5.3.5 Field intensity noise and electrical power spectral density

5.3.5.a Field intensity noise

The statistical properties of the NIBS radiation have an important impact in the sensor performance. The features of the NIBS field intensity noise can be described by the fourth-order correlation of the electrical field. Due to the thermal-noise origin of the scattered field, Wick's theorem allows the calculation of this fourth-order field correlation function in terms of second-order correlation functions. The field intensity autocorrelation $\Re_{S,A}(\tau)$ can be expressed as:

$$\begin{aligned}\Re_{S,A}(\tau) &= \left\langle \hat{E}^+(L,t_L)\,\hat{E}^+(L,t_L+\tau)\,\hat{E}\,(L,t_L+\tau)\,\hat{E}\,(L,t_L)\right\rangle = \\ &= \left\langle \hat{E}^+(L,t_L)\,\hat{E}\,(L,t_L)\right\rangle\left\langle \hat{E}^+(L,t_L+\tau)\,\hat{E}\,(L,t_L+\tau)\right\rangle + \\ &\quad + \left\langle \hat{E}^+(L,t_L)\,\hat{E}\,(L,t_L+\tau)\right\rangle\left\langle \hat{E}^+(L,t_L+\tau)\,\hat{E}\,(L,t_L)\right\rangle = \\ &= I_{S,A}^2 + R_{S,A}(\tau)\,R_{S,A}(-\tau)\end{aligned} \tag{51}$$

where we have omitted the subscripts S or A in the field operators. This result was expected from the gaussian statistics of NIBS [60]. From (51), it can be seen that the variance of the field intensity is equal to the average field intensity squared. This will constitute an important source of noise in the detection process.

5.3.5.b Spectral power density of the detected electrical current

We can characterise the optical detector by its responsivity R ($=e\eta\bar{g}/\hbar\omega_L$; with e, electron charge; η, quantum efficiency and $\bar{g}$, average gain of the detector); its random gain g and excess noise factor F; and its response in current to one photon detection $i_R(t)=e\cdot g\cdot h(t)$, where

h(t) is such that $\int_0^\infty h(t)dt$ equals 1. Taking into account the statistics of the optical field (51), the spectral power density of the detected electrical current $\Psi_{S,A}(\omega)$ is [68]:

$$\Psi_{S,A}(\omega) = R^2 P_{S,A}^2 \delta\left(\frac{\omega}{2\pi}\right) + R^2 |H(\omega)|^2 \int_{-\infty}^{\infty} \Phi_{S,A}(\omega+\omega')\Phi_{S,A}(\omega')\frac{d\omega'}{2\pi} + \\ + \quad e\,R\,\bar{g}\,F\,P_{S,A}\,|H(\omega)|^2 \tag{52}$$

where $H(\omega)$ is the Fourier transform of h(t). The first term in (52) is the average current power detected, the second term represents the noise induced by the field statistics and the third term is the shot noise. The last two terms constitute the fundamental noise limitations of the detection process and depend on the selected detection bandwidth.

The field statistics induced noise is band-limited, and its bandwidth depends on the G parameter (39, 45, 46). For a broad detection bandwidth, the whole noise spectral power density is integrated and the detected signal-to-noise ratio (SNR), neglecting the shot noise contribution, tends to one. As the detection bandwidth is reduced, the noise spectral power density is filtered and the SNR improves.

Using (52), we can calculate the SNR of the Stokes and antiStokes NIBS as a function of the detection bandwidth B (one-sided) for different values of the parameter G (Figures 4 and 5). We assume that the pump pulse-width is such that $\gamma T >> 1$, a free-space wavelength λ_L of 1.55 μm, a Brillouin shift ν_B of 11.25 GHz, a full-width half-maximum for the Brillouin optical spectrum $\gamma/2\pi$ of 37 MHz, and a value of 555 for the phonon thermal population $\langle n \rangle$ at 300°K. We also neglect the excess noise factor F and gain $\bar{g}$ of the photo-detector and take R equal to 1 A/W, a typical value for InGaAs devices.

The SNR for the detected Stokes NIBS is shown in Figure 4. For a given B, we observe that the SNR deteriorates as G increases, due to a progressive reduction of the Brillouin effective bandwidth (45). At low values of G (≈0.01), the shot noise is not negligible, becoming an added source of deterioration for the SNR, which drops under one for high values of B. The SNR for the detected antiStokes NIBS (Figure 5) shows a different behavior. In this case, the SNR improves as G increases, due to the spectral broadening of the antiStokes NIBS. As in the Stokes case, at low G, the shot noise becomes noticeable.

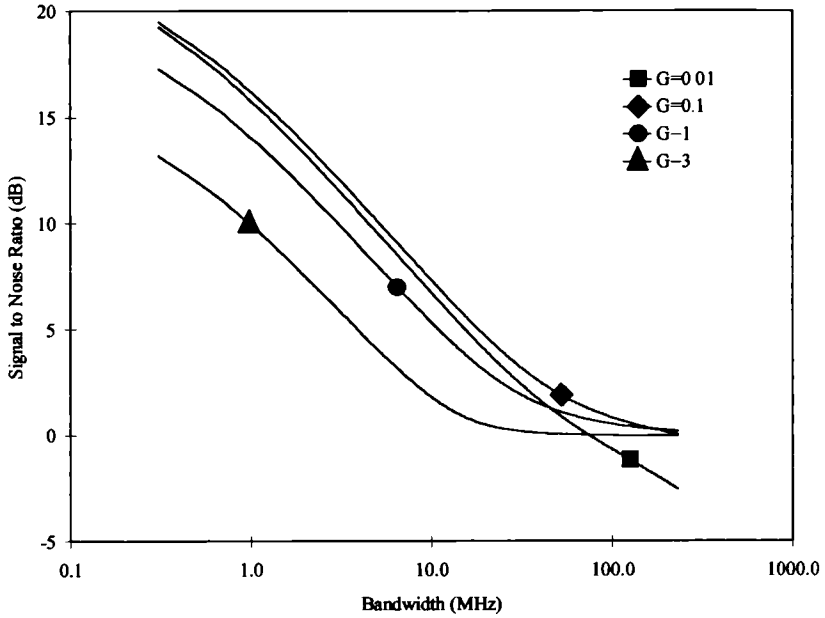

Figure 4. SNR of the Stokes NIBS after detection.

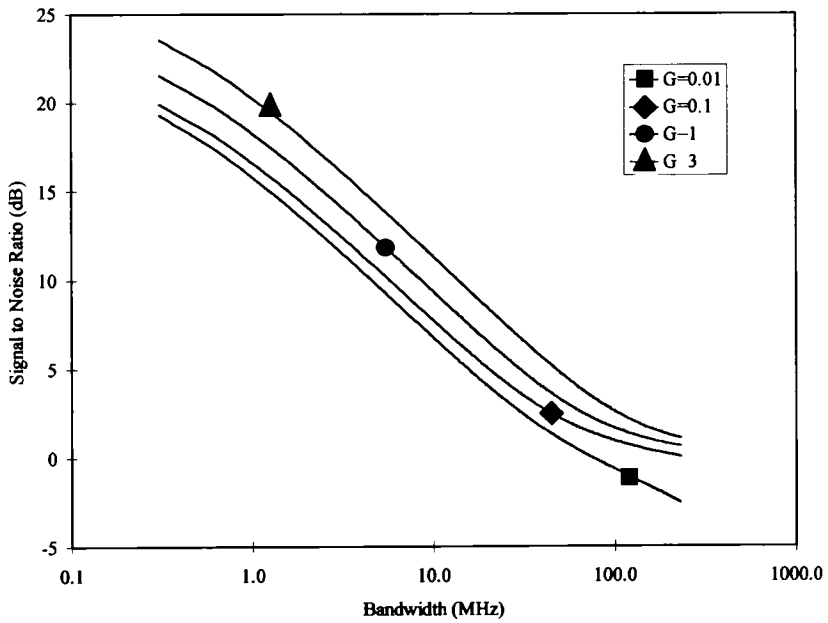

Figure 5. SNR of the antiStokes NIBS after detection.

5.3.5.c Spatial resolution and signal-to-noise ratio performance of the sensor

The sensor spatial resolution depends both on the pump pulse-width T and on the detector's bandwidth B. If we match the detector's bandwidth to the pump pulse-width ($B \approx 1/2T$) [69], then the spatial resolution δz for the system is:

$$\delta z = \frac{vT}{2} \tag{53}$$

From (52), it is seen that the one-sided effective bandwidth (in Hz) of the field statistics induced noise is approximately $\gamma/2\pi$ for low values of the G. The ratio between the noise effective bandwidth and the detection bandwidth B gives the improvement in SNR due to the detector's filtering action. As this ratio is proportional to γT, the use of $\gamma T >> 1$ has the beneficial effect of an improved SNR, at the expense of poorer spatial resolution.

The best achievable spatial resolution is limited by the phonon lifetime T_B ($\approx 2/\gamma \approx 10$ns). When the pump pulsewidth T is comparable to T_B, the Brillouin gain is reduced and the resulting spectrum is broadened, causing the power and frequency shift measurement to deteriorate. A spatial resolution of 1m has been recently reported working in this transient regime [44].

5.3.5.d Circuit noise and optimum G

So far, we have only considered the fundamental noise limitations due to field statistics and shot noise. The circuit noise acts as an added source of noise which degrades the performance of the sensor at low values of the G parameter. To evaluate its effect, we have calculated the signal to noise ratio of the effective Brillouin power P_B^{lin} as a function of G for different detection bandwidths B assuming a noise-equivalent-power (NEP) for the detector of 0.1 $pW/\sqrt{Hz}$ (Figure 6). We also supposed that the Brillouin linearisation process was carried out by use of formula (38).

Figure 6 shows that whilst the circuit noise is dominant at low values of G, at high G the SNR is limited by the field statistics noise. It can be seen that there is a bandwidth-dependent optimum value for G where the SNR is maximised. The optimum G is around the region where the Brillouin process begins to be significantly nonlinear, hence validating the use of P_B^{lin} (see Figure 9 discussed later). If a detector with in-buit gain was used (such an avalanche photo-diode) the optimum G would be shifted towards lower values. This effect will be offset against

any additional noise sources, such as noise associated with the amplified spontaneous emission in any optical amplifiers used, which would push the optimum G towards higher values.

From the SNR we can calculate the errors in the determined strain and temperature using (12) and (13). The accuracy of the measured Brillouin shift (12), ν_B, is proportional to $SNR^{-1/4}$. [44,50]. However, for the experimental system developed at King's College, the limiting source of error is due to the accuracy of the power measurement through equation (13). Using Figure 6 we calculate that the minimum number of measurements required to achieve a distributed mapping with 5m spatial resolution (10 MHz detection bandwidth), a temperature resolution of 1 °C and a strain resolution of 20 μstrain is 10^5. For the current non-optimised system at King's College, this would take an acquisition time of 15 minutes for a distributed measurement over a 1 km length.

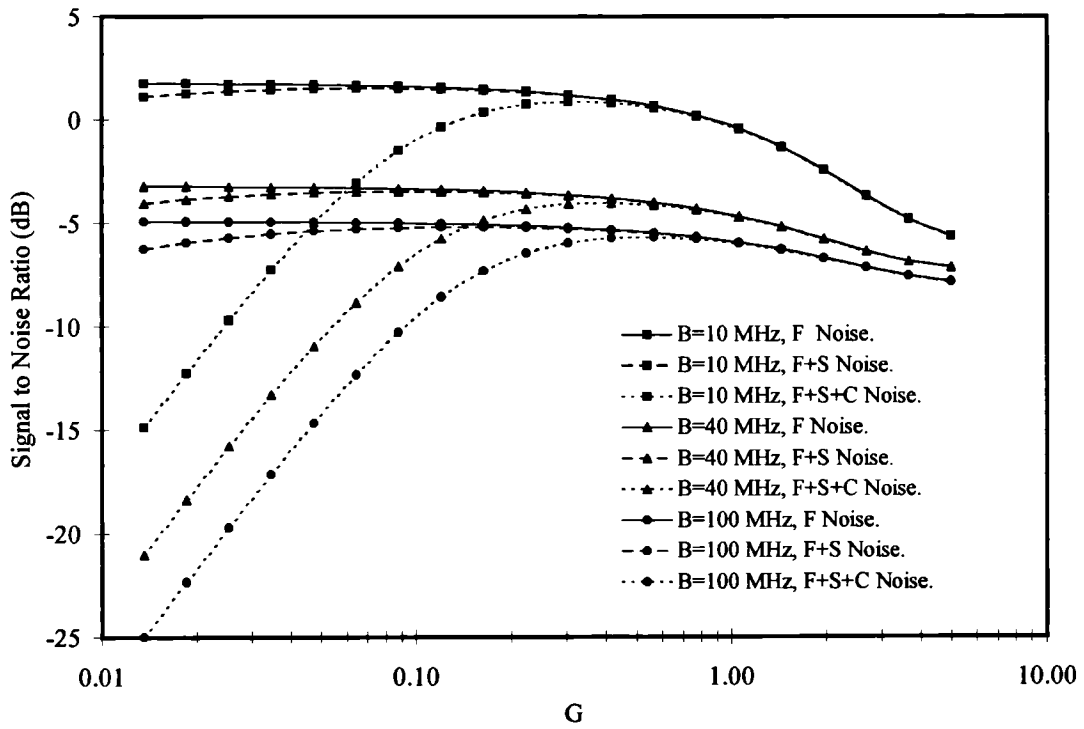

Figure 6. SNR of the linearised Brillouin power as a function of G for different detection bandwidths B. F: field statistics, S: shot, C: circuit.

5.4 EXPERIMENTS

Several experiments that support the predictions of the previous analysis have been carried out at King's College [4-5,1-3]. In particular, two experimental arrangements were constructed; the first a continuous wave (CW) system used to determine the accuracy of the theory described above, and the second a pulsed system to conduct distributed simultaneous strain and temperature measurements. The system is represented in Figure 7.

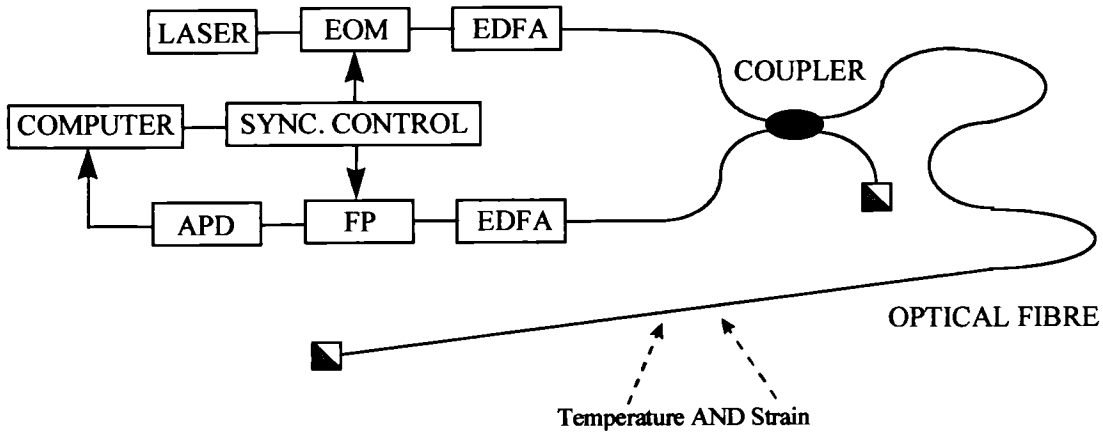

Figure 7. Experimental system. EOM: Electro-optic modulator, EDFA: Erbium-doped fibre amplifier, FP: Fabry-Perot, APD: Avalanche-photodiode, SYNC: Synchronisation.

5.4.1 CW experiments

For the CW measurements, light from a 1553nm distributed feedback laser (DFB) with a 15MHZ linewidth was amplified by an erbium-doped amplifier (EDFA) to powers between 4.4mW and 25.0mW, and sent into the test fibre via a 3dB coupler. The test fibre was a length of standard telecommunication fibre that was single mode at 1550nm, and had a GeO_2 doped core. The backscattered signal was amplified by 14 dB by a second EDFA before being spectrally analysed by a Fabry-Perot (FP) interferometer with a 9.7GHz free spectral range (FSR) and a finesse of 195 (50MHz resolution). The FSR of the FP was less than the Brillouin frequency shift (approximately 11GHz), causing aliasing of the Stokes, Rayleigh and antiStokes signals. The resulting signal was collected on a computer, where the amplitudes and frequencies of the peaks were determined. To improve the performance of the system, each measured Brillouin spectrum was aligned with respect to the central dominant Rayleigh peak. This procedure corrected for any long term drifts in the FP spectral response. As the FP

bandwidth is larger than the Brillouin linewidth (50MHz > 37MHz), the measured peak amplitudes can be taken as an accurate measure of the integrated Brillouin powers.

5.4.1.a Linearisation of the Brillouin scattered power

Two experiments were conducted using the CW arrangement. In the first experiment [1,3], input light with powers between 1.5mW and 11mW (after the coupler) was launched into a 4.3km test fibre to test the predictions of Section 5.3.4.a that linearity between an effective Brillouin power and the pump power could be produced. In this experiment the EDFA amplifying the backscattered signal was not used. Brillouin spectra for the various input powers are shown in Figure 8. The variation of the Brillouin powers with G is shown in Figure 9. It can be seen that the theoretical plots achieve excellent agreement with the experimental plots, and that P_B^{lin} is linear with G up to the maximum value of G that we could obtain. The approximate form of P_B^{lin} (48) is valid up to moderate values of G ($G < 0.8$). The theory lines were derived from (38), (40), (47) and (48) using common normalisation terms.

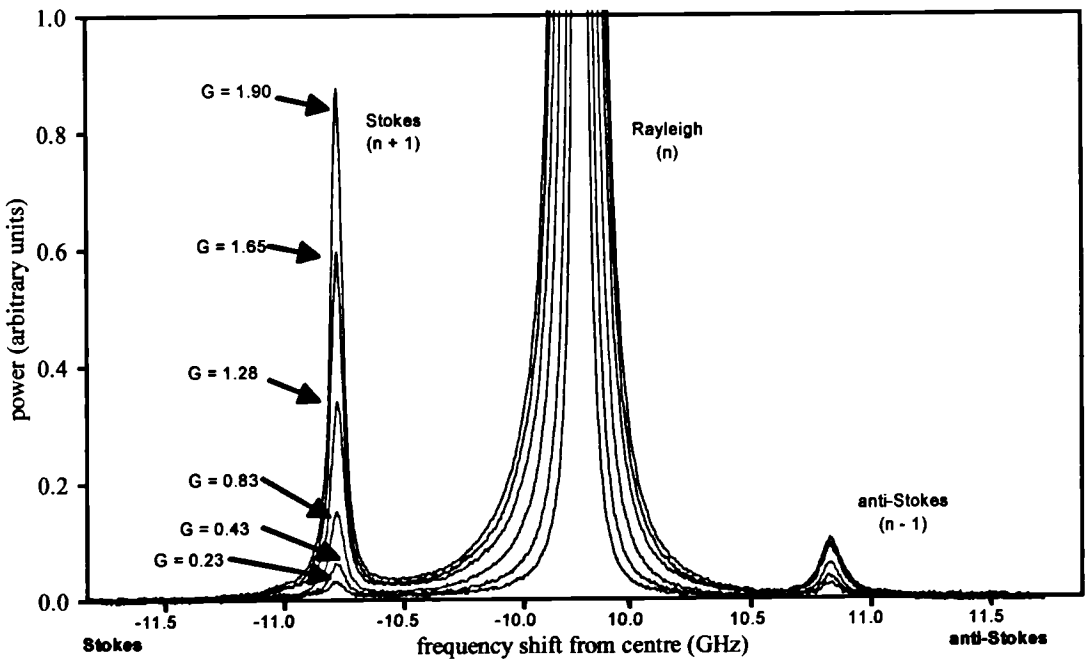

Figure 8. Brillouin spectra for various values of G.

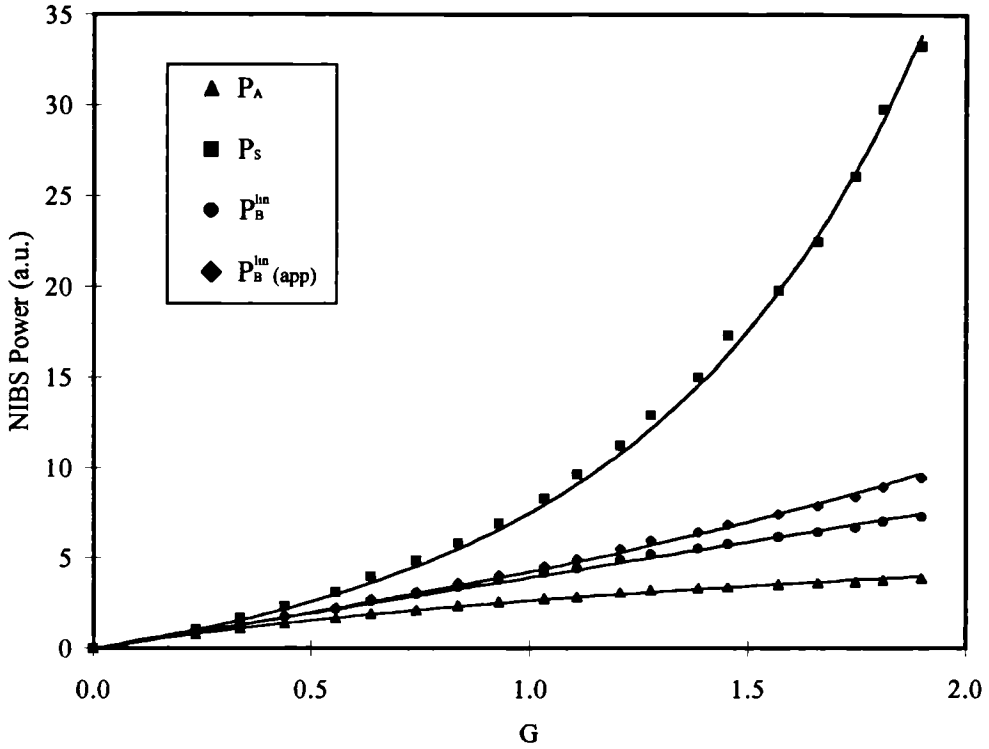

Figure 9. Experimental values for the Stokes power, P_S; antiStokes power, P_A; linearised Brillouin power, P_B^{lin}; and linearised Brillouin power approximated with (48), P_B^{lin}(app); for different values of G. The continuous lines are theoretical fits using (38), (40), (47) and (48) respectively.

5.4.1.b Strain and temperature dependence of the integrated Brillouin scattered power

In the second experiment, the equations (12) and (49) that predict the strain and temperature dependence of the Brillouin signal were tested [4,3]. For the temperature measurement, 4.3 km of test fibre were immersed in a water bath held at various temperatures, and an input power of 4.5mW was used. For the strain measurement, a 50m test fibre was subjected to various strains via a system of pulleys, and the input power was 23mW. The EDFA in the backscattered arm was used for both the temperature and strain measurements. Figures 10 and 11 show plots of P_B^{lin} and Brillouin frequency shift versus temperature and strain respectively. The theory lines shown in Figures 10 and 11 show the predicted dependence of P_B^{lin} on temperature and strain given by (50), with the constant η chosen to obtain best fit. The good agreement between theory and experiment gives us justification to use (50) and (12) for the determination of temperature and strain.

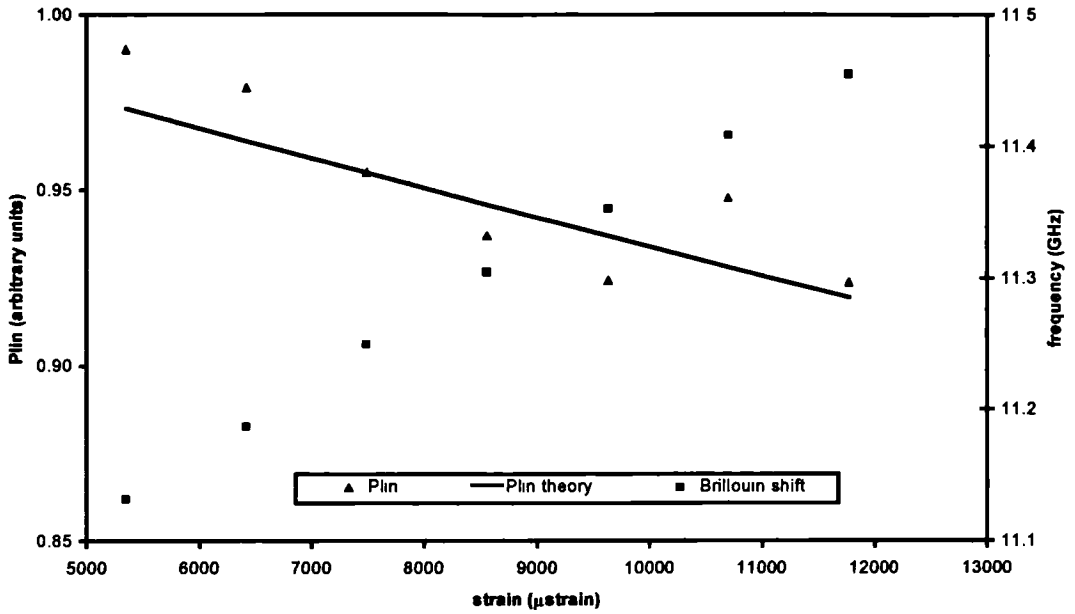

Figure 10. Brillouin frequency shift and P_B^{lin} versus strain. The theoretical plot uses (50) with η chosen so as to produce best fit.

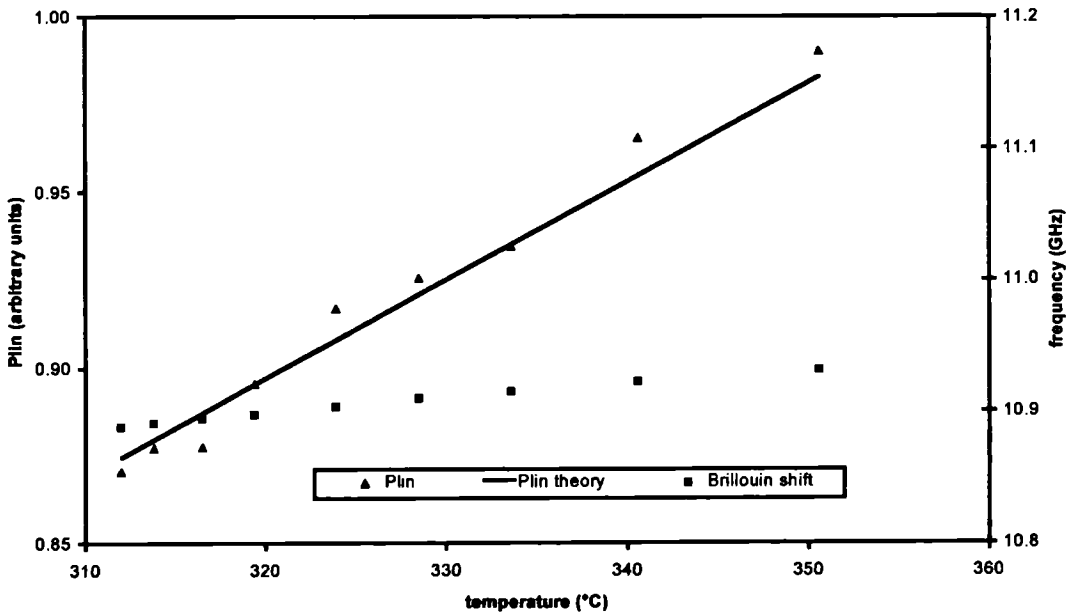

Figure 11. Brillouin frequency shift and P_B^{lin} versus temperature. The theoretical plot uses (50) with η chosen so as to produce best fit. Figures 10 and 11 are plotted over the same y-scale for ease of comparison.

We can also express these results in terms of the coefficients that appear in (12) and (13), which we list below:

$C_{\nu\varepsilon} = 0.0483 \pm 0.0004$ MHz/μstrain,

$C_{\nu\theta} = 1.10 \pm 0.02$ MHz/°C,

$C_{P\varepsilon} = -(7.7 \pm 1.4) \cdot 10^{-4}$ %/μstrain,

$C_{P\theta} = 0.36 \pm 0.06$ %/°C,

where the power coefficients are given in terms of a percentage relative to the power at 300°K and 0 μstrain. The experimentally determined $C_{P\varepsilon}$ and $C_{P\theta}$ agree within errors with the predicted values and the experimental ratio $C_{\nu\varepsilon}C_{P\theta}/C_{\nu\theta}C_{P\varepsilon}$ =-21 compares favourably with the predicted value of -18. These results have been confirmed by measurements carried out by other groups [55,57].

5.4.2 Distributed measurements

Finally, some preliminary experiments demonstrated the feasibility of this technique for simultaneous distributed measurement of strain and temperature [5,2-3]. For these measurements, light from an external cavity laser with 100 kHz linewidth and 1553 nm wavelength was modulated by an electro-optic modulator in pulses of 400ns. These pulses were subsequently optically amplified to peak powers of about 100 mW. The pulse duration limited the spatial resolution of the system to 40m. The backscattered signal was detected in this case by an avalanche photo-diode (APD) with 38 MHz bandwidth. By collecting a series of OTDR traces and simultaneously scanning the FP, the Brillouin scattered radiation was resolved both spatially and spectrally.

A test fibre was subjected to various strains and temperatures along its length. The distribution of strain and temperature for the first 500m of fibre is shown in Figure 13. The total length of the fibre, 4.3km, limited the pulse repetition interval (excitation cycle) to 50 μs.

Figure 12 shows the linearised Brillouin powers and frequency shifts measured along the first 500m of fibre. The achieved SNR was lower than that theoretically expected due to the use of

non-optimal components in the system. In particular, the excessive losses in the detection scheme made necessary the use of an optical amplifier at the receiver, contributing additional noise to the detector (amplified spontaneous emission, ASE noise). The strain and temperature distributions derived from previous measurements are shown in Figure 13. It can be observed that some cross-sensitivity problems between strain and temperature appeared for abrupt changes in strain or temperature along the fibre. These problems were due to the inability of the present processing routine to measure accurately the total scattered power for broadened Brillouin spectra. The strain and temperature resolutions were estimated by calculating the standard deviation of the measured values for a section of fibre with uniform strain and temperature. The strain resolution obtained was 100μstrain, and the temperature resolution was 4°C. The overall measurement time was 1 hour and the total length of the fibre was 4.3 km. These results are promising, and a considerable improvement is expected with more suitable components. The reader is referred to [3,5] for a more detailed discussion about the distributed measurement tests performed on the system.

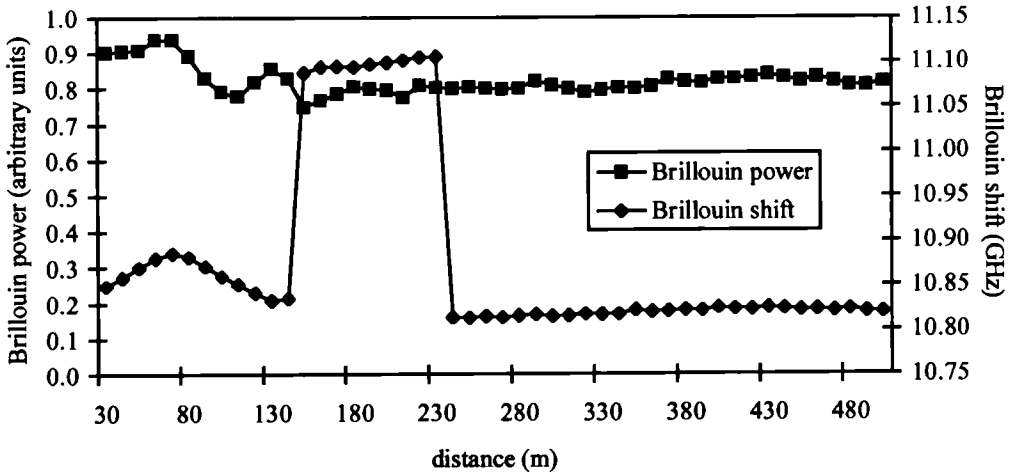

Figure 12. Evolution of the integrated Brillouin scattered power and frequency shift along the first 500m of the test fibre.

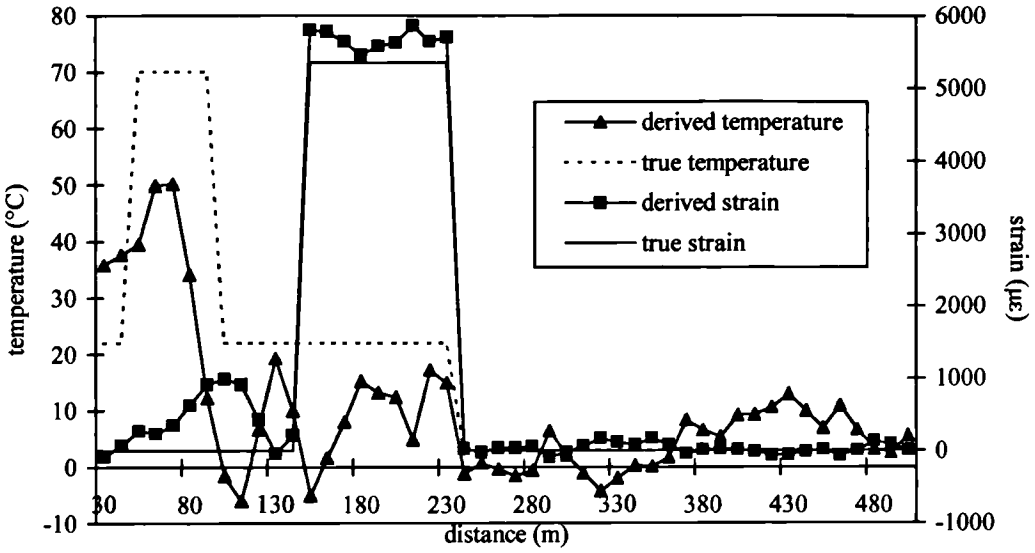

Figure 13. True and derived strain and temperature distributions along the first 500m of the test fibre.

APPENDIX

From (31) and (41), the Stokes field autocorrelation is given (neglecting constants terms) by:

$$R_S(\tau) = \int_0^{\frac{T-\tau}{2}} dt' \int_0^{\infty} dt'' \; e^{-2\gamma t'} \; e^{\gamma \tau} \; e^{j\omega_s \tau} \; I_0\left(2\kappa\sqrt{t\left(t'+|\tau|\right)}\right) I_0\left(2\kappa\sqrt{\left(t'+\frac{|\tau|}{2}\right)t''}\right) \tag{A1}$$

The Fourier transform of (A1) can be expressed after a change of variables as:

$$R_S(\omega) = 2\Re\text{eal}\left\{\int_0^{\frac{T}{2}} dt' \int_0^{\frac{T-t'}{2}} d\tau \int_0^{\infty} dt'' e^{-2\gamma t'} \; e^{-\gamma\tau} e^{-j(\omega-\omega_s)\tau} I_0\left(2\kappa\sqrt{t'\left(t''+\tau\right)}\right) I_0\left(2\kappa\sqrt{\left(t'+\frac{\tau}{2}\right)t''}\right)\right\} \tag{A2}$$

Due to the two decaying exponential functions, the integrand only contributes significantly for small values of t'' and τ (of the order of $1/\gamma$). As we have also assumed that $\gamma T >> 1$, we can make the following two approximations: first, we neglect the second order term $t''\tau/2$ in the argument of the second Bessel function, and second, we extend the second integral to infinite. With these approximations, the integral can be readily solved [70,71] to give (42) [61]. Analogous considerations could be done for the antiStokes case.

REFERENCES

[1] R. Feced, T.R. Parker, M. Farhadiroushan, V.A. Handerek, A.J. Rogers. "Power measurement of noise-initiated Brillouin scattering in optical fibres for sensing applications". Accepted for publication in Optics Letters.

T.R. Parker, R. Feced, M. Farhadiroushan, V.A. Handerek, A.J. Rogers. "Linearisation of noise-initiated Brillouin backscattered power for simultaneous strain and temperature measurement". 4th Optical fibre measurement conference. NPL, Teddington (UK), October 1997.

[2] T.R. Parker, M. Farhadiroushan, R. Feced, V.A. Handerek, A.J. Rogers. "Simultaneous distributed strain and temperature sensing using noise-initiated Brillouin scattering ". 12th Optical Fiber Sensors Conference, Williamsburg, Virginia (USA). October 1997.

[3] T.R. Parker, M. Farhadiroushan, R. Feced, V.A. Handerek, A.J. Rogers. "Simultaneous distributed measurement of strain and temperature from noise initiated Brillouin scattering in optical fibres". Accepted for publication in IEEE Journal of Quantum Electronics.

[4] T.R. Parker, M. Farhadiroushan, V.A. Handerek, A.J. Rogers. "Temperature and strain dependence of the power level and frequency of spontaneous Brillouin scattering in optical fibres". Optics Letters, Vol. 22, No. 11, pp. 787-789, June 1997.

[5] T.R. Parker, M. Farhadiroushan, V.A. Handerek, A.J. Rogers. "A fully-distributed simultaneous strain and temperature sensor using spontaneous Brillouin backscatter". IEEE Photonics Technology Letters, Vol. 9, No. 7, pp. 979-981, July 1997.

[6] G.P Agrawal. "Nonlinear fiber optics", pp. 264. Academic Press, 1989.

[7] E.P. Ippen, R.H. Stolen. "Stimulated Brillouin scattering in optical fibers". Applied Physics Letters, Vol. 21, No. 11, pp. 539-541, December 1972.

[8] R.M. Shelby, M.D. Levenson, P.W. Bayer. "Guided acoustic-wave Brillouin scattering". Physical Review B, Vol. 31, No. 8, pp. 5244-5252, April 1985.

[9] P.St.J. Russell, D. Culverhouse, F. Farahi. "Experimental observation of forward stimulated Brillouin scattering in dual-mode single-core fibre". Electronics Letters, Vol. 26, No. 15, pp. 1195-1196, July 1990.

[10] P.St.J. Russell, D. Culverhouse, F. Farahi. "Experimental observation of forward stimulated Brillouin scattering in dual-mode single-core fibre". IEEE Journal of Quantum Electronics, Vol. 27, No. 3, pp. 836-842, March 1991.

[11] N. Shibata, K. Okamoto, Y. Azuma. "Longitudinal acoustic modes and Brillouin-gain spectra for GeO_2- doped-core single-mode fibers". Journal Optical Society of America B, Vol.6, No. 6, pp. 1167-1174, June 1989.

[12] P.J. Thomas, N.L. Rowell, H.M. van Driel, G.I. Stegeman. "Normal acoustic modes and Brillouin scattering in single-mode optical fibers". Physical Review B, Vol. 19, No. 10, pp. 4986-4998, May 1979.

[13] D. Heiman, D.S. Hamilton, R.W. Hellwarth. "Brillouin scattering measurements on optical glasses". Physical Review B, Vol. 19, No.12, pp. 6583-6592, June 1979.

[14] S.P. Timoshenko, J.N. Goodier. "Theory of elasticity", Chapter 14. McGraw-Hill, 1970.

[15] G.P Agrawal. "Nonlinear fiber optics", pp. 265. Academic Press, 1989.

[16] H.E. Bommel, K. Dransfeld. "Excitation and attenuation of hypersonic waves in quartz". Physical Review, Vol. 117, No. 5, pp. 1245-1252, March 1960.

[17] T.O. Woodruf, H. Ehrenreich. "Absorption of sound in insulators". Physical Review, Vol. 123, No. 5, pp. 1553-1559, September 1961.

[18] A. S. Pine. "Brillouin scattering study of acoustic attenuation in fused quartz". Physical Review, Vol. 185, No. 3, pp. 1187-1193, September 1969.

[19] J.A. Bucaro, H.D. Dardy. "High-temperature Brillouin scattering in fused quartz". Journal of Applied Physics, Vol. 45, No. 12, pp. 5324-5329, December 1974.

[20] J. Pelaous, R. Vacher. "Thermal Brillouin scattering in crystalline and fused quartz from 20 to 1000°C". Solid State Communications, Vol. 18, No.5, pp. 657-661, 1976.

[21] Y. Azuma, N. Shibata, T. Horiguchi, M. Tateda. "Wavelength dependence of Brillouin-gain spectra for single-mode optical fibres". Electronics Letters, Vol. 24, No. 5, pp. 250-252, March 1988.

[22] T. Kurashima, T. Horiguchi, M. Tateda. "Thermal effects of Brillouin gain spectra in single-mode fibers". IEEE Photonics Technology Letters, Vol. 2, No. 10, pp. 718-720, October 1990.

[23] D. Cotter. "Stimulated Brillouin scattering in monomode optical fiber". Journal of Optical Communications, Vol. 4, No. 1, pp. 10-19, 1983.

[24] R.G. Smith. "Optical power handling capability of low loss optical fibers as determined by stimulated Raman and Brillouin scattering". Applied Optics, Vol. 11, No. 11, pp. 2489-2494. November 1972.

[25] G.P Agrawal. "Nonlinear fiber optics", pp. 265. Academic Press, 1989.

[26] K. Shiraki, M. Ohashi, M. Tateda. "SBS threshold of a fiber with a Brillouin frequency shift distribution". Journal of Lightwave Technology, Vol. 14, No. 1, pp. 50-57, January 1996.

[27] G.P Agrawal. "Nonlinear fiber optics", pp. 267. Academic Press, 1989.

[28] X.P. Mao, R.W. Tkach, A.R. Chraplyvy, R.M. Jopson, R.M. Derosier. "Stimulated Brillouin threshold dependence on fiber type and uniformity". IEEE Photonics Technology Letters, Vol. 4, No. 1, pp. 66-68, January 1992.

[29] Y. Takushima, T. Okoshi. "Suppression of stimulated Brillouin scattering using optical isolators". Electronics Letters, Vol. 28, No. 12, pp. 1155-1157, June 1992.

[30] K.O. Hill, B.S. Kawasaki, D.C. Johnson. "CW Brillouin laser". Applied Physics Letters, Vol. 28, No. 10, pp. 608-609, May 1976.

[31] C.G. Atkins, D. Cotter, D.W. Smith, R. Wyatt. "Application of Brillouin amplification in coherent optical transmission". Electronics Letters, Vol. 22, No. 10, pp. 556-558, May 1986.

[32] N.A. Olsson, J.P. Van der Ziel. "Fibre Brillouin amplifier with electronically controlled bandwidth". Electronics Letters, Vol. 22, No. 9, pp. 488-490, April 1986.

[33] A.R. Chraplyvy, R.W. Tkach. "Narrowband tunable optical filter for channel selection in densely packed WDM systems". Electronics Letters, Vol. 22, pp.1084-1085, 1986.

[34] T. Horiguchi, M. Tateda. "Optical-fiber-attenuation investigation using stimulated Brillouin scattering between a pulse and a continuous wave". Optics Letters, Vol. 14, No. 8, pp. 408-410, April 1989.

[35] R.W. Tkach, A.R. Chraplyvy, R.M. Derosier. "Spontaneous Brillouin scattering for single-mode optical-fibre characterisation". Electronics Letters, Vol. 22, No. 19, pp.1011-1013, September 1986.

[36] N. Shibata, R.G. Waarts, R.P. Braun. "Brillouin-gain spectra for single-mode fibers having pure-silica, GeO_2-doped, and P_2O_5-doped cores". Optics Letters, Vol. 12, No. 4, pp. 269-271, April 1987.

[37] M. Ohashi, N. Shibata, K. Shiraki. "Fibre diameter estimation based on guided acoustic wave Brillouin scattering". Electronics Letters, Vol. 28, No. 10, pp. 900-902, May 1992.

[38] T. Horiguchi, T. Kurashima, M. Tateda. "Tensile strain dependence of Brillouin frequency shift in silica optical fibres". IEEE Photonics Technology Letters, Vol. 1, No. 5, pp. 107-108, May 1989.

[39] D. Culverhouse, F. Farahi, C.N. Pannel, D.A. Jackson. "Potential of stimulated Brillouin scattering as sensing mechanism for distributed temperature sensors". Electronics Letters, Vol. 25, No. 14, pp. 913-914, July 1989.

[40] T. Kurashima, T. Horiguchi, M. Tateda. "Thermal effects of Brillouin gain spectra in single-mode fibers". IEEE Photonics Technology Letters, Vol. 2, No. 10, pp. 718-720, October 1990.

[41] T. Kurashima, T. Horiguchi, M. Tateda. "Thermal effects on the Brillouin frequency shift in jacketed optical silica fibers". Applied Optics, Vol. 29, No. 15, pp. 2219-2222, May 1990.

[42] T. Kurashima, T. Horiguchi, M. Tateda. "Distributed-temperature sensing using stimulated Brillouin scattering in optical silica fibers". Optics Letters, Vol. 15, No. 18, pp. 1038-1040, September 1990.

[43] X. Bao, D.J. Webb, D.A. Jackson. "Characteristics of Brillouin gain based distributed temperature sensors". Electronics Letters, Vol. 29, No. 17, pp. 1543-1544, August 1993.

[44] T. Horiguchi, K. Shimizu, T. Kurashima, M. Tateda, Y. Koyamada. "Development of a distributed sensing technique using Brillouin scattering". Journal of Lightwave Technology, Vol. 13, No. 7, pp. 1296-1302, July 1995.

[45] X. Bao, D.J. Webb, D.A. Jackson. "32-km distributed temperature sensor based on Brillouin loss in an optical fiber". Optics Letters, Vol. 18, No. 18, pp. 1561- 1563, September 1993.

[46] T. Horiguchi, M. Tateda, N. Shibata, Y. Azuma. "Brillouin gain variation due to a polarization-state change of the pump or Stokes fields in standard single-mode fibers". Optics Letters, Vol. 14, No. 6, pp. 329-331, March 1989.

[47] X. Bao, J. Dhliwayo, N. Heron, D.J. Webb, D.A. Jackson. "Experimental and theoretical studies on a distributed temperature sensor based on Brillouin scattering". Journal of Lightwave Technology, Vol. 13, No. 7, pp. 1340-1348, July 1995.

[48] M.O. van Deventer, A.J. Boot. "Polarization properties of stimulated Brillouin scattering in single-mode fibers". Journal of Lightwave Technology, Vol. 12, No. 4, pp. 585-590, April 1994.

[49] M. Nikles, L. Thevenaz, P.A. Robert. "Simple distributed fiber sensor based on Brillouin gain spectrum analysis". Optics Letters, Vol. 21, No. 10, pp.758-760, May 1996.

[50] T. Kurashima, T. Horiguchi, H. Izumita, S. Furukawa, Y. Koyamada. "Brillouin optical-fiber time domain reflectometry". IEICE Transactions Communications, Vol. E76-B, No. 4, pp. 382-389, April 1993.

[51] K. Shimizu, T. Horiguchi, Y. Koyamada. "Measurement of distributed strain and temperature in a branched optical fiber network by use of Brillouin optical time-domain reflectometry". Optics Letters, Vol. 20, No. 5, pp. 507-509, March 1995.

[52] J. Czarske, H. Muller. "Heterodyne detection technique using stimulated Brillouin scattering and a multimode laser". Optics Letters, Vol. 19, No. 19, pp. 1589-1591, October 1994.

[53] N.N. Ghogomu, J.K.A. Everard. "Coherent photoconductive detection of Brillouin scattering for Brillouin sensing". Electronics Letters, Vol. 31, No. 18, pp. 1606-1607, August 1995.

[54] T. Kurashima, M. Tateda, T. Horiguchi, Y. Koyamada. "Performance improvement of a combined OTDR for distributed strain and loss measurement by randomizing the reference light polarisation state". IEEE Photonics Technology Letters, Vol. 9, No. 3, pp. 360-362, March 1997.

[55] P.C. Wait, T.P. Newson. "Landau-Placzek ratio applied to distributed fibre sensing". Optics Communications, Vol. 122, pp. 141-146, January 1996.

[56] T.R. Parker, M. Farhadiroushan, V.A. Handerek, A.J. Rogers. "Simultaneous measurement of spontaneous Brillouin scattering amplitude and frequency as a function of temperature". Proceedings 11th Optical Fibre Sensors Conference, pp.662, Sapporo (Japan). May 1996.

[57] K. de Souza, P.C. Wait, T.P. Newson. "Characterisation of strain dependence of the Landau-Placzek ratio for distributed sensing". Electronics Letters, Vol. 33, No. 7, pp.615-616, March 1997.

[58] K. de Souza, G.P. Lees, P.C. Wait, T.P. Newson. "Diode-pumped Landau-Placzek based distributed temperature sensor utilising an all-fibre Mach-Zehnder interferometer". Electronics Letters, Vol. 32, No. 23, pp.2174-2175, November 1996.

[59] P.C. Wait, T.P. Newson. "Reduction of coherent noise in the Landau-Placzek ratio method for distributed fibre optic temperature sensing". Optics Communications, Vol. 131, pp. 285-289, November 1996.

[60] T. von Foerster, R.J. Glauber. "Quantum theory of light propagation in amplifying media". Physical Review A, Vol. 3, No. 4, pp. 1484-1511, April 1971.

[61] R.W. Boyd, K. Razazewski, P. Narum. "Noise initiation of stimulated Brillouin scattering". Physical Review A, Vol. 42, No. 9, pp. 5514-5521, November 1990.

[62] H.Z. Cummins, P.S.Schoen. "Laser Handbook", Section E1, p. 1046. Edited by F.T Arecchi, E.O. Schulz-Dubois. North-Holland, Amsterdam, 1972.

[63] C.L. Tang. "Saturation and spectral characteristics of the Stokes emission in the stimulated Brillouin process". Journal of Applied Physics, Vol. 37, No. 8, pp. 2945-2955, July 1966.

[64] W.H. Louisell. "Quantum statistical properties of radiation", pp. 418-443. John Wiley & Sons, Wiley Classics, 1990.

[65] M.G. Raymer, J. Mostowski. "Stimulated Raman scattering: unified treatment of spontaneous initiation and spatial propagation". Physical Review A, Vol. 24, No. 4, pp. 1980-1993, October 1981.

[66] L. Mandel, E. Wolf. "Optical coherence and quantum optics", pp. 483 and 580. Cambridge University Press, 1995.

[67] 2G is equal to the more commonly used term $g_B P_o L_{eff}/A_{eff}$, where in our case L_{eff} is half the pulsewidth, e.g. G.P Agrawal. "Nonlinear fiber optics", pp. 268, Academic Press, 1989.

[68] L. Mandel, E. Wolf. "Optical coherence and quantum optics", pp. 708-712. Cambridge University Press, 1995.

[69] A.B. Carlson, "Communication Systems", pp. 101-103, McGraw Hill International, 1986.

[70] M. Abramowitz, I.A. Stegun. "Handbook of mathematical functions", Chapters 9, 11 and 29, Dover Publication, 1970.

[71] R. Spiegel, L. Abellanas. "Formulas y tablas de matematica aplicada", Chapter 31, McGraw-Hill, 1988.

[72] X. Bao, D.J. Webb, D.A. Jackson. "Recent progress in experiments on Brillouin loss based distributed sensor". 10th Optical Fiber Sensors Conference, pp. 506-509, 1994.

[73] X. Bao, D.J. Webb, D.A. Jackson. "Combined distributed temperature and strain sensor based on Brillouin loss in an optical fiber". Optics Letters, Vol. 19, No. 2, pp. 141-143, January 1994.

[74] M. Farhadiroushan, T.R. Parker. "Distributed strain and temperature measurement system". UK Patent Application: 9626099.7, 1996.

Chapter 6

CONCLUSIONS

In this thesis we have investigated the use of several nonlinear optical effects for distributed optical fibre sensing. In particular, we have considered the use of Raman scattering, the optical Kerr effect, and Brillouin scattering, identifying the strengths and limitations of each of these techniques. We have also studied some aspects related to the fabrication of polarisation gratings in high-birefringence optical fibres.

6.1 RAMAN SCATTERING

Monitoring of the spontaneously scattered Raman light in an ODTR backscattering architecture is a powerful technique for distributed measurement of temperature. There exist several commercial systems that map temperature over long distances (several kilometres) with a spatial resolution of one metre. Our aim was to demonstrate the potential of Raman scattering to perform distributed measurements with very high spatial resolution (few centimetres) for short range applications.

We showed that a time-correlated single photon counting (TC-SPC) detection scheme gives optimum signal-to-noise ratio (SNR) for this type of measurements and that practical systems can be implemented. The typical performance of one such system yields a spatial resolution of 10 cm with a temperature resolution of 2°C for a measurement time of 1 minute and a sensing length of 20 m. This performance, achieved by maximising the power throughput and also by use of very fast electronics, approaches the fundamental limitations of the TC-SPC technique. Due to the pile-up effect, a further increase of the power throughput would give rise to distortions in the OTDR traces, degrading the SNR response. The problem of measuring distributions of high temperatures (550°C) has also been discussed. Apart from the sensitivity degradation at high temperatures inherent to the Raman scattering process, further measurement errors could be caused by temperature dependent variations of the differential losses between the Stokes and antiStokes signals. This is a consequence of the physical transformations suffered by hermetically coated fibres at elevated temperatures.

Measurement of the spontaneous Raman scattering by means of the TC-SPC technique is also a practical solution to overcome the dead-zone problem in high spatial resolution OTDR schemes. OTDR systems with minimum dead-zone will be necessary to map the losses along short-haul optical networks with large density of components.

The next step towards improved very high spatial resolution DART sensors follows naturally. We have carried out calculations that indicate that a regime intermediate between the single-photon counting and the analogue-photon detection would give better performance than any of the two extreme cases. If the recovery-time of both the detector and the timing-electronics is reduced so that it lasts for only a few time channels, then several photons could be detected and timed per incident laser pulse launched into the fibre. This would allow us to increase the detection probability per channel, leading to a significant improvement of the measurement

time. Although several systems based on this principle (Multi-Photon Counting) have been reported, they are not yet suitable for very high resolution measurements owing to their coarse timing-resolution (>4ns) and, also, to the long dead-time and "after pulse" effects in the detector. However, they show how future technical advances could lead towards very high spatial resolution real-time DART sensors.

6.2 KERR EFFECT

The second nonlinear optical effect considered was the optical Kerr effect. In this case, the sensing principle is based on phase matched coupling, induced by an intense pump pulse between the polarisation modes of a counter-propagating CW probe beam in a high birefringent fibre. This technique allows mapping of the local birefringence along a polarisation preserving fibre and can be used for distributed measurements of either strain or temperature. The enhanced SNR of pump-probe schemes permits a short measurement time (seconds) for distributed measurements with moderate spatial resolutions (one metre).

In this thesis, we have analysed the Kerr-induced nonlinear mode coupling in elliptical-core fibres for its use in distributed sensing applications. We have derived expressions for the coupling efficiencies and also for the magnitude of the frequencies generated at the detector. The analysis indicates that this type of sensor will be useful in those applications that need fast mapping of sensing lengths of a few hundred metres with a moderate spatial resolution (one metre). The ability of birefringence based sensors to measure both temperature and strain permits the design of architectures that would be able to discriminate between them. We have proposed one possible scheme that relies on nonlinear coupling among the modes of an elliptical-core fibre that supports several low-order modes. It still remains a challenge to implement such a system in a cost-effective way.

6.3 BRILLOUIN SCATTERING

The last nonlinear optical effect considered was noise-initiated Brillouin scattering in optical fibres. The frequency shift of the Brillouin scattered radiation is sensitive to both the local strain and temperature along the fibre. Many sensing systems based on this fact have been previously reported.

Our aim was to show that measurement of both the spectrum and the integrated power of the Brillouin scattered radiation enables simultaneous distributed measurement of strain and temperature. Brillouin sensing systems will be very appropriate for mapping strain and temperature over long distances (tens of kilometres) with a spatial resolution of several metres. We have demonstrated a novel processing technique that compensates the nonlinear growth of Brillouin scattering. A SNR analysis indicated that the main source of noise is that associated with the statistics of the field itself, and that the optimum point of operation for the distributed sensor was at gain values in the nonlinear Brillouin growth regime, emphasising the importance of our compensation procedure.

Initial experiments have confirmed the enormous potential of this technique. However, the present experimental system needs to be optimised in various aspects. The selection of more adequate optical components would permit an improved power throughput along the system. This will make unnecessary the use of the optical amplifier in the detection scheme, reducing the noise associated with its ASE. This is an ongoing activity at King's College and important improvements are expected in short term.

6.4 STATIC POLARISATION GRATINGS

In this thesis, we have also studied several aspects related to static polarisation gratings in polarisation preserving fibres. Firstly, we carried out experiments that corroborate some of the predictions of the depletion model for photo-induced birefringence. In particular, we have confirmed the negative sign for the photo-induced birefringence and the angular dependence of the coupling strength. Also, we have demonstrated a technique that permits fabrication of polarisation gratings with tailored spectral responses.

Finally, we have investigated the effects that the fabrication procedure has on the mechanical properties of UV photo-induced devices. We have observed a large increase in the axial stress of UV exposed fibres, and also a degradation of their mechanical strength. These observations indicate that the core of germanium-doped optical fibres transforms into a more compact structure when is exposed to UV radiation. The consequences of these structural transformations for the mechanical reliability of photo-induced devices is of practical importance, specially in sensing applications where the fibre could be subjected to large strains.

6.5 FINAL CONCLUSION

The use of nonlinear optical effects for distributed sensing offers a variety of sensing configurations that can provide a practical solution in many different applications. If the measurand is temperature, Raman scattering provides an attractive solution for both long-haul applications and also for high spatial resolution short-haul applications. For distributed measurement of strain, birefringence (Kerr) and Brillouin scattering based systems are very appropriate.

Present efforts are directed towards the development of a robust distributed sensor that can measure both temperature and strain simultaneously, an area that has attracted great interest. Distributed measurement of spectrally resolved noise-initiated Brillouin scattering seems to be the most suitable technique for this purpose, and first experimental systems have been recently demonstrated.

Although there are already several Raman-based systems commercially available, most of the other techniques studied in this thesis are still at the research stage. We hope that this thesis will contribute to the future development and widespread use of distributed sensing systems based on nonlinear optical effects.

LIST OF PUBLICATIONS

Journal papers:

[1] R. Feced, M.P. Edwards, S.E. Kanellopoulos, N.H. Taylor, V.A. Handerek. "Mechanical strength degradation of UV exposed optical fibres". Electronics Letters Vol. 33, No. 2, pp. 157-159, January 1997.

[2] R. Feced, M. Farhadiroushan, V.A. Handerek, A.J. Rogers. "Advances in high resolution distributed sensing using the time-correlated single photon counting technique". IEE Proceedings in Optoelectronics, Vol. 144, No. 3, pp. 183-188, June 1997.

[3] R. Feced, M. Farhadiroushan, V.A. Handerek, A.J. Rogers. "A high spatial resolution distributed optical fiber sensor for high temperature measurements". Review of Scientific Instruments (AIP), Vol. 68, No. 10, pp. 3772-3776, October 1997.

[4] R. Feced, S.E. Kanellopoulos, M. Farhadiroushan, V.A. Handerek, A.J. Rogers. "Analysis of optical Kerr effect induced coupling among polarisation modes in high-birefringence optical fibers". Optics Communications, Vol. 143, pp. 268-278, November 1997.

[5] R. Feced, M. Farhadiroushan, V.A. Handerek. "Zero dead-zone OTDR with high spatial resolution for short haul applications". IEEE Photonics Technology Letters, Vol. 9, No. 8, pp. 1140-1142, August 1997.

[6] R. Feced, T.R. Parker, M. Farhadiroushan, V.A. Handerek, A.J. Rogers. "Power measurement of noise-initiated Brillouin scattering in optical fibres for sensing applications". Accepted for publication in Optics Letters (January 1998).

[7] T.R. Parker, M. Farhadiroushan, R. Feced, V.A. Handerek, A.J. Rogers. "Simultaneous distributed measurement of temperature and strain from noise-initiated Brillouin scattering in optical fibres". Accepted for publication in IEEE Journal of Quantum Electronics (April 1998).

Conference papers:

[8] V.A. Handerek, S.E. Kanellopoulos, R. Feced, J.Croucher. "Evaluation of shape-birefringent fibres for sensing systems employing photogenerated polarization couplers". Optical fibre gratings and their applications. IEE, London, January 1995.

[9] F. Parvaneh, M. Farhadiroushan, R. Thomas, R. Feced, V.A. Handerek, A.J. Rogers. "Demonstration and potential of distributed temperature sensors using the frequency derived technique". Progress in optical fibre sensors and their applications. IEE, London, November 1995.

[10] F. Parvaneh, M. Farhadiroushan, R. Thomas, R. Feced, V.A. Handerek, A.J. Rogers. "Recent progress in distributed temperature sensing using the frequency derived technique". Optical Fiber Sensors (OFS-11), Sapporo (Japan), May 1996.

[11] R. Feced, M. Farhadiroushan, P. Rodriguez, V.A. Handerek, A.J. Rogers. "Advances in high resolution distributed sensing using a time-resolved photon counting technique". SPIE 2838, 105-113 (1996). Denver (USA), August 1996.

[12] R. Feced, M. Farhadiroushan, V.A. Handerek, A.J. Rogers. "High temperature testing of a high spatial resolution distributed optical fibre temperature sensor". Optical techniques for smart structures and structural monitoring. IEE, London, February 1997.

[13] K.W. Raine, R. Feced, S.E. Kanellopoulos, V.A. Handerek, A. Parker. "High resolution stress profiling of UV exposed optical fibres". 4th Optical fibre measurement conference. NPL, Teddington (UK), October 1997.

[14] R. Feced, M. Farhadiroushan, V.A. Handerek. "A high spatial resolution zero dead-zone OTDR". 4th Optical fibre measurement conference. NPL, Teddington (UK), October 1997.

[15] M. Farhadiroushan, R. Feced, V.A. Handerek, A.J. Rogers. "Evaluation of a high spatial resolution distributed optical fiber sensor for high temperatures applications". 12th Optical Fiber Sensors Conference, Williamsburg, Virginia (USA). October 1997.

[16] T.R. Parker, M. Farhadiroushan, R. Feced, V.A. Handerek, A.J. Rogers. "Simultaneous distributed strain and temperature sensing using noise-initiated Brillouin scattering ". 12th Optical Fiber Sensors Conference, Williamsburg, Virginia (USA). October 1997.

[17] T.R. Parker, R. Feced, M. Farhadiroushan, V.A. Handerek, A.J. Rogers. "Linearisation of noise-initiated Brillouin backscattered power for simultaneous strain and temperature measurement". 4th Optical fibre measurement conference. NPL, Teddington (UK), October 1997.

[18] R. Feced, S.E. Kanellopoulos, R.A. Griffin, V.A. Handerek. "Polarisation dependence of photo-induced birefringence and its application to fabrication of tailored polarisation filters". Bragg grating, Photosensitivity, and Poling in Glass Fibers and Waveguides Topical Meeting (OSA), Williamsburg, Virginia (USA). October 1997.